THÈSE

En vue de l'obtention du

DOCTORAT DE L'UNIVERSITÉ DE TOULOUSE

Délivré par :

Institut National Polytechnique de Toulouse (Toulouse INP)

Discipline ou spécialité :

Dynamique des Fluides

Présentée et soutenue par :

M. LORIC TORRES

le jeudi 7 décembre 2023

Titre :

Simulation numérique directe de l'ébullition en microgravité

Ecole doctorale :

Mécanique, Energétique, Génie civil, Procédés (MEGeP)

Unité de recherche :

Institut de Mécanique des Fluides de Toulouse (IMFT)

Directeur(s) de Thèse :

MME CATHERINE COLIN

M. SÉBASTIEN TANGUY

Rapporteurs :

M. STEPHANE ZALESKI, UNIVERSITE SORBONNE

M. YOHEI SATO, INSTITUT PAUL SCHERRER

Membre(s) du jury :

M. MARC MEDALE, UNIVERSITE AIX-MARSEILLE 1, Président

M. GUILLAUME BOIS, CEA SACLAY, Membre

MME ANNAFEDERICA URBANO, ISAE-SUPAERO, Membre

MME CATHERINE COLIN, TOULOUSE INP, Membre

M. SÉBASTIEN TANGUY, UNIVERSITE TOULOUSE 3, Membre

M. THIERRY ONDARCUHU, TOULOUSE INP, Membre

À mon père,

Abstract

Prediction of heat transfer in nucleate boiling remains an open problem. CFD allows to perform simulations at industrial scales, but requires to model the wall heat transfer. The most advanced models are based on the heat flux partitioning between the latent heat due to the bubble vaporization and the sensible heat directly transferred to the liquid. They require a good prediction of the bubble growth rate, detachment diameter, which can be obtained with DNS. This thesis focus on such simulations.

The solver $\mathcal{DIVA}$ has been developed at the IMFT and provides accurate simulations of bubble growth in contact line and micro-layer regimes. However, the contact line, which is the bubble interface in contact with the wall, requires a specific attention. This region is subject of significant heat flux and large variation of the contact angle. Several models have been developed to account for it. Yet to our knowledge, no clear coupling methodology between DNS and micro-region model has been proposed in the past. In this work, a coupling between these different scales is proposed. An implicit coupling has been developed between the micro-region model and the DNS, and required a deep computational work. This coupling is presented in a generic manner and can be done regardless of the chosen micro-region model. The convergence of the results is demonstrated in comparison with the RUBI experiment, developed for the study of boiling on an isolated site in microgravity, on board of the International Space Station. The configuration setup allows the measurement of wall temperatures and local heat fluxes through infrared thermography. These measurements are synchronized with bubble growth visualizations by high-speed camera. The coupling, along with the appropriate micro-region model, has significantly improved bubble growth predictions.

Afterwards, a study of heat transfer between a superheated wall and a fluid in microgravity has been conducted. Without buoyancy, the bubble stays attached to the wall and thus the investigation is easier. Therefore, the study enables a better understanding of the parameters involved in the micro-region model. The prediction of bubble growth rates has been improved, and the physics at stake at the contact line is better apprehended.

Résumé

La prédiction des transferts de chaleur en ébullition nucléée est un problème ouvert. La CFD permet des simulations a échelle industrielle, mais nécessite des modélisations de ces transferts. Aujourd'hui, les modèles les plus élaborés sont basés sur une partition du flux de chaleur entre chaleur latente due à la vaporisation des bulles et chaleur sensible due au transfert direct de la chaleur vers la phase liquide. Ils nécessitent cependant une bonne prédiction des taux de croissance des bulles et de leur diamètre de détachement, qui peut être obtenue par simulation DNS. C'est ce que l'on propose de faire dans cette thèse.

En DNS, les coûts de calculs pour des simulations à échelle industrielle étant très importants, les calculs sont réalisés sur des bulles uniques en vue d'enrichir la modélisation pour des simulations de type RANS à grande échelle. Développé à l'IMFT, le code $\mathcal{DIVA}$ permet de simuler la croissance de bulle en régime de ligne de contact et de micro-couche. Néanmoins, l'étude détaillée des phénomènes de ligne de contact, point d'accroche de l'interface de la bulle à une paroi surchauffée, nécessite une attention particulière. Appelée micro-région, elle est le siège de flux de chaleur très importants, et de fortes variations de la courbure de l'interface. Plusieurs modèles semi-analytiques existent pour l'appréhender. Mais à l'heure actuelle, les simulations DNS ne permettent pas de prendre en compte l'intégralité des effets décrits par ces modèles. Dans le cadre de ce travail, un couplage entre ces différentes échelles est proposé.

Un travail numérique a été effectué afin d'établir un couplage implicite d'un modèle de micro-région avec la DNS. Celui-ci est présenté de manière générique, et peut être fait peu importe le modèle de micro-région choisi. La convergence des résultats est démontrée, en comparaison avec l'expérience RUBI, développée pour l'étude de l'ébullition sur site isolé en microgravité à bord de la station spatiale internationale. Le dispositif permet la mesure de la température de paroi et des flux de chaleur locaux par thermographie infrarouge. Ces mesures sont synchronisées avec des visualisations de la croissance des bulles par caméra rapide. Le couplage, associé au modèle de micro-région idoine a permis une large amélioration des prédictions de croissance de bulle.

Par la suite, l'étude des transferts de chaleur entre une paroi surchauffée et un fluide en microgravité a été effectuée. En l'absence de gravité, la bulle reste accrochée à sa paroi et la croissance peut être observée plus facilement. Ainsi, cette étude permet une meilleure compréhension des paramètres impactant le modèle de micro-région, et leur meilleure prise en compte dans la prédiction des taux de croissance de bulles. La physique en jeu à micro-échelle à la ligne de contact est également mieux maîtrisée.

Remerciements

Si seul mon nom signe ce manuscrit, il m'aurait été impossible de mener cette thèse sans un grand nombre de personnes que j'ai eu la chance de côtoyer au cours de cette aventure. À travers ces quelques lignes, je souhaiterais leur témoigner ma reconnaissance.

Dans un premier temps, mes remerciements vont à mes directeur·trices de thèse. Merci à toustes les deux de m'avoir accordé la confiance de mener ce projet et de m'avoir accompagné tout du long. Catherine, pour ta bienveillance, ta disponibilité, et la pertinence de tout ce que tu as pu (m')apporter durant ces trois années. Sébastien, pour tes conseils, ton optimisme, ton avis au quotidien sur mon approche numérique. Je pense notamment à cette fameuse journée du 21 janvier 2022 durant laquelle tu n'avais vraiment pas envie de corriger tes copies, que tu as préféré passer dans mon bureau et pendant laquelle on a mis en place un concept qui se trouve être au centre de ma thèse. Enfin, Annafederica, pour ton aide sur le code et pour ta curiosité sans limite qui m'a encouragé à explorer des directions inattendues. Merci à toustes les trois pour le soutien et l'encadrement que vous m'avez offerts. Je suis fier d'avoir pu vivre cette expérience avec vous.

Je souhaiterais également adresser mes remerciements aux membres du jury pour avoir accepté d'évaluer le fruit de ce travail, pour la pertinence de leurs remarques et la discussion qui s'en est suivie.

Merci à toustes les permanent·es de l'IMFT pour les discussions scientifiques (et parfois moins), en particulier à Rémi et Wladimir pour la bonne balade à vélo ! Marie-Hélène, je suis reconnaissant pour ta gentillesse et ton engagement à faciliter le quotidien des doctorant·es contre les (trop) nombreuses difficultés administratives.

Vient à présent le tour des doctorant·es, post-doctorant·es, stagiaires et celle·eux passé·es par le labo. À commencer par la *Team* DIVA, et mon quatrième encadrant de thèse, *debugger*, *master* du code, psy, mais avant tout - et surtout ! - ami, Guillaume. Merci pour ta présence, ton aide et ton amitié. J'espère continuer à parler de sciences (et pas que) avec toi autour d'un (plusieurs) verre(s). À ma camarade de thèse Marie (qui me devance de deux semaines), avec qui j'aurais partagé mon bureau tout du long. Merci pour ton soutien, pour les galères communes, les rires et les ragots... Je souhaite également bon courage aux futurs docteurs de DIVA: Léo, Sergiu, Gauthier, et, plus tard, Maxence.

Un immense merci ensuite aux *coushifts* pour les discussions (plutôt interruptions) de travail quotidiennes. Aujourd'hui, je pourrais faire la présentation des travaux d'Antoine ou de Rémi, tout le monde n'y verrait que du feu. C'est ça aussi l'expérience de thèse, faire trois thèses à trois, et profiter du vécu des autres. Merci pour ces années où votre point de vue m'a bien aidé plus d'une fois, mais aussi et surtout pour les cafés, les pizzas, les Rummikubs dans la piscine, et tout ce qui n'a pas trait à la thèse et a rendu le quotidien agréable. Antoine, je ne serai plus là pour critiquer tes figures, n'en profite pas pour faire n'importe quoi. Pour le quotidien, je n'oublie sûrement pas Gautier et Corentin, que ce soit pour les conversations course à pied, jeux de société, les restos du vendredi *etc.* ... Bon courage à tous les quatre pour vos soutenances à venir.

De manière générale, je salue tous les doctorant·es et post-docs de l'IMFT pour l'ambiance

géniale qui y règne. Je n'ai pas été le plus présent, mais c'était un plaisir de, parfois, boire un coup, ou de *Geoguesser* avec quelques-uns d'entre vous un midi par semaine. Je suis reconnaissant envers Julie, Léa et Mathilde, pour votre travail pendant le projet recherche. Sur les trois, j'ai bien compris que deux n'aimaient pas la thermique (promis, je ne dénoncerai personne). J'espère quand même que ça vous aura plu.

Quick word for Johannes, my german collegue of Darmstadt, performing the same stuff as I did for 3 years. It was a pleasure complaining about RUBI with you. Despite completely different methods, we always agree on which stuff doesn't work. I wish you good luck for the last year, and nice weather for your surf/ski sessions.

Je remercie ensuite toustes celle·eux qui ont été là tout le long. Benoît, pour ta présence quotidienne, Damien, pour les quelques tours à l'aventure dans les Pyrénées. Merci Marta d'être là depuis un petit bout de chemin, pour ton soutien inconditionnel et ta disponibilité dès que j'en ressentais le besoin. Je vous sais gré à toustes les trois pour les nombreuses (mais plus si régulières) soirées saucisson-coinche-tartiflette/*fajitas*.

Au groupe Toulousaings, dont certain·es déjà cité·es, pour les occupations du dimanche, les *week-ends* surfs, randos, raquettes, jeux de société, concerts ou quelque autre occupation qui m'a sorti de la morosité des fins de semaines.

À d'autres Ensmatiques que je ne voudrais surtout pas perdre de vue. Merci Benjamin pour les soirées *Geoguessr*, MK ou autres; pour les concerts qu'on a pu faire, et pour être le pilier d'organisation du groupe. Aux autres Kassos pas encore mentionné·es, Maxime, Flavie, Marc pour la déconnexion que me procure votre présence. Et pour m'avoir fait trottiner un peu à Madrid quand même. Merci à vous, infiniment.

Aux skieur·ses, Victor, Marine, Baptiste. J'espère pouvoir vous re-rejoindre au plus vite. En m'attendant, ne vous perdez pas sur les pistes, et envoyez-moi un saucisson de Savoie !

Enfin, merci à Justine d'avoir été là tout du long. Merci pour ta présence, ton soutien au quotidien malgré la distance. Merci d'arriver à toujours trouver les mots justes. À ton tour maintenant de mener ton doctorat, durant lequel j'espère être là pour toi comme tu as pu l'être pour moi.

À ma famille, selon laquelle j'ai fait des bubulles sur mon ordi pendant trois ans. Ma mère, pour ton soutien, pour m'avoir permis de faire ce que je souhaitais. Mes sœurs, la Docteure (celle qu'on appellera Docteur en tout cas). Pour tes conseils lecture (promis j'avance, mais je lis pas aussi vite que toi !), la visite Montpelliéraine et les restos quand tu viens à Toulouse. Et la petite, qui court plus vite que moi maintenant. Merci pour les conseils course et kiné (que je n'applique pas), pour le séjour Raphaëlois. Tu seras très bientôt dans le coin, on pourra peut-être enfin finir la randonnée au Valier. Merci à ma grand-mère pour le soutien sous forme culinaire, et pour le repos que me procure chacune de mes venues à Carcassonne. Merci pour tes connaissances qui me profitent régulièrement dans mes mots-fléchés !

Cette thèse est, d'une manière ou d'une autre, pour mon père, parti trop tôt. Je crois qu'une de ses raisons d'être est, aussi, que tu sois fier de moi.

Contents

1 Introduction **1**
- 1.1 Previous experimental results . . . 3
  - 1.1.1 Experimental observation of micro-layers . . . 4
  - 1.1.2 Similar experiments without micro-layer . . . 6
  - 1.1.3 Weightlessness experiments . . . 7
  - 1.1.4 RUBI experiment . . . 8
- 1.2 Numerical methods . . . 10
  - 1.2.1 Methods for interface tracking . . . 10
  - 1.2.2 Methods for continuity at the interface crossing . . . 11
  - 1.2.3 Modeling of the contact line . . . 12
- 1.3 Simulation of bubble growth . . . 13
  - 1.3.1 Nucleate boiling regime . . . 13
  - 1.3.2 Bubble growth in micro-layer regime . . . 15
- 1.4 Boiling at the micro-region scale . . . 16
  - 1.4.1 Micro-layer or micro-region ? . . . 16
  - 1.4.2 Criterion for regime transition . . . 17
- 1.5 Outline of the thesis . . . 19

2 Numerical methods **21**
- 2.1 Governing equations . . . 22
  - 2.1.1 Mass conservation . . . 22
  - 2.1.2 Momentum balance . . . 23
  - 2.1.3 Energy conservation . . . 24
- 2.2 Numerical Methods . . . 25
  - 2.2.1 Interface localization . . . 25
  - 2.2.2 Ghost Fluid Method . . . 26
  - 2.2.3 Projection Algorithm . . . 29
  - 2.2.4 Extrapolations of the fields . . . 31
  - 2.2.5 Discretization for the numerical schemes . . . 32
- 2.3 Validation case: Scriven bubble growth . . . 33
- 2.4 Conclusion on the Numerical Methods . . . 35

3 Microregion Models **37**
- 3.1 Stephan's model . . . 38
- 3.2 Mathieu's model . . . 42
  - 3.2.1 Perfectly-wetting fluid . . . 45
  - 3.2.2 Partially-wetting fluid . . . 46
- 3.3 Janeček and Nikolayev's model: quick overview . . . 50
- 3.4 Parametric Analysis . . . 51
  - 3.4.1 Impact of the microscopic contact angle . . . 51
  - 3.4.2 Impact of the slip length . . . 52

3.4.3 Impact of the interfacial resistance . . . 53
3.4.4 Impact of the contact line velocity . . . 56
3.4.5 Impact of the shot parameter . . . 56
3.5 Conclusion on micro-region models . . . 59

4 Micro-region coupling with DNS **61**
4.1 Implementation of the conjugated heat transfer . . . 62
4.2 Micro-region coupling in the wall . . . 64
4.3 Micro-region coupling in the fluid domain . . . 67
4.3.1 Incorporation in a single cell at the contact line - DNS LMR . . . 67
4.3.2 Integrated in the volumic divergence term - DNS IMR . . . 68
4.3.3 Spread at the interface - DNS SMR . . . 70
4.3.4 Choice of the accurate spreading length for DNS-SMR . . . 73
4.3.5 Heat Balance in the dihedral . . . 74
4.4 Validation case: Multiscale Boiling experiment (RUBI) . . . 77
4.4.1 Simulation setup . . . 77
4.4.2 Limitations of the experiment . . . 78
4.4.3 Comparison with the experimental results . . . 79
4.5 On the importance of the model dependency on the physical properties . . . 82
4.5.1 Qualitative influence of the accommodation coefficient . . . 83
4.5.2 Qualitative influence of the thermal conductivity ratio λ_w/λ_{liq} . . . 85
4.6 Conclusion of the coupling between micro-region and DNS . . . 87

5 Results of nucleate boiling with micro-region **89**
5.1 Parametric analysis . . . 90
5.1.1 Configuration setup . . . 92
5.1.2 Parameters studied and ranges of variation . . . 93
5.2 Results . . . 94
5.2.1 Evolution of the equilibrium diameter . . . 94
5.2.2 Evolution of the contact line superheat and micro-region fluxes . . . 97
5.2.3 Construction of the correlation for R_{eq} . . . 101
5.2.4 Study of the Nusselt number . . . 104
5.2.5 Global variations . . . 107
5.3 Limitations for non-static configurations . . . 107
5.4 Conclusion of the chapter . . . 110

6 Outlooks: Simulation of boiling in micro-layer regime **111**
6.1 Experiment of Bucci . . . 112
6.1.1 Configuration setup . . . 112
6.1.2 Simulation results . . . 114
6.2 Conclusion on micro-layer simulations . . . 119

Conclusion and outlooks **121**

A Analytical solution of the temperature of two walls with heat source at the interface **123**

B Analytical solution of the bubble equilibrium radius in microgravity **127**

C Physical Properties **129**

D Post treatment of the infrared camera of RUBI **131**

Chapter 1

Introduction

Contents

1.1 Previous experimental results 3
1.1.1 Experimental observation of micro-layers 4
1.1.2 Similar experiments without micro-layer 6
1.1.3 Weightlessness experiments 7
1.1.4 RUBI experiment 8
1.2 Numerical methods 10
1.2.1 Methods for interface tracking 10
1.2.2 Methods for continuity at the interface crossing 11
1.2.3 Modeling of the contact line 12
1.3 Simulation of bubble growth 13
1.3.1 Nucleate boiling regime 13
1.3.2 Bubble growth in micro-layer regime 15
1.4 Boiling at the micro-region scale 16
1.4.1 Micro-layer or micro-region ? 16
1.4.2 Criterion for regime transition 17
1.5 Outline of the thesis 19

Nucleate boiling is encountered in many industrial applications. 85% of the electricity in the world is produced from vapor generators. Numerous studies have been carried out by the nuclear industry since the 1960's, motivated by safety issues. Boiling may occur in accidental situations, for example in the case of a lost of coolant accident, with a strong depressurization of the Pressurized Water Reactor. In this configuration, nucleate boiling can quickly transit to film boiling, leading to the damage of fuel cell rods. In these situations it is crucial to be able to predict the heat transfer in nucleate boiling regimes, which motivated a lot of experimental studies and the development of numerical simulation tool such as the code Neptune-CFD in France. On the other hand, the nucleate boiling regime is an efficient way to increase the heat transfer coefficient by comparison to single-phase convection. Liquid-vapor flows have long been used to cool electronic components in compact devices, such as cell phones, laptops. In larger heat exchangers, nucleate boiling is a good candidate for an efficient cooling. But care has to be taken to avoid reaching the critical heat flux, corresponding to a large amount of vapor in direct contact with the wall, acting as an insulator and leading to large wall temperature increase and a destruction of the wall.

Nucleate boiling has also been investigated for space applications. In rocket launchers, the cryogenic propellants are stored liquid in tanks, just below their saturation temperature. Due to

solar radiation and dissipation of the engines, nucleate boiling occurs and increases the pressure inside the tanks. To prevent overpressure in the tanks from happening, propellant has to be released, reducing the time of the mission. The fuel ejected being lost, it has implications for the flight and must be avoided as much as possible. Moreover, as a result of the enhancements of satellites' embedded electronics, they dissipate much heat (up to 10-100 W/cm^2) and require effective cooling while minimizing weight. Thus the prediction of nucleate boiling heat transfer is of crucial importance for the sizing of theses devices.

These studies led to numerous correlations and empirical relations to predict the heat flux induced by phase change at large scales. Such results are valid within a range of parameters defined by the experimenter, and do not predict the general process of boiling. They cannot be used out of the parameter ranges of the study. However, the large number of parameters involved, often entangled with each other, adds to the complexity of the prediction and explains why correlations have been used.

Nowadays, the most advanced CFD models of boiling at industrial scales are based on the heat flux partitioning at the wall between the latent heat due to the bubble vaporization and the sensible heat directly transferred to the liquid through convection, conduction and quenching:

$$q''_{\mathrm{w}} = S_{\mathrm{dry}} q''_{\mathrm{vap}} + S_{\mathrm{liq}} \left(q''_{\mathrm{convection}} + q''_{\mathrm{boiling}} + q''_{\mathrm{quenching}} \right) \tag{1.1}$$

With S_{dry} and S_{liq} the area fraction covered by vapor and liquid, respectively. These models were introduced by Kurul & Podowski [1], and later improved by Basu [2, 3] to account for bubble sliding and merging in convective boiling. Recent studies have been performed, such as Richenderfer who experimentally analysed with infrared images the heat flux at the surface of a heated substrate [4]. Figure 1.1 displays snapshots of the infrared and B&W cameras. The partition between the dry area heat flux, and the evaporation heat flux can be directly deduced via the adequate post-treatment.

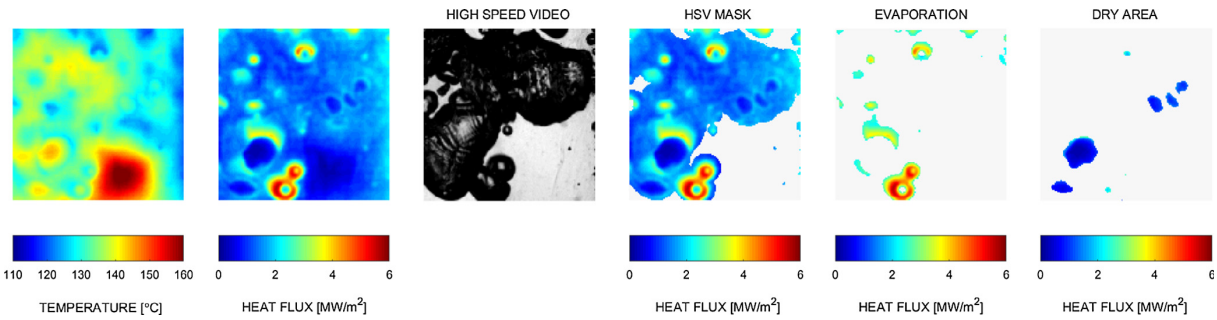

Figure 1.1: Temperature and heat flux field; B&W image; flux partition between evaporation and dry conduction; image from [4].

The heat partitioning is a major concern for nuclear applications, where the prediction of the critical heat flux is crucial. These models provide an accurate description of the different boiling regimes. Figure 1.2 shows the heat flux partitioning as observed by Baglietto [5].

For low superheat, the heat flux comes exclusively from the forced convection in the liquid. As the temperature increases, nucleation occurs and the boiling process highly contributes to the heat transfer. As bubbles detach from the wall, the quenching increases as well and cools down the wall. In case of convective boiling, the sliding of bubbles also contributes to the heat transfer. A transition occur at the critical heat flux (CHF). After this point, the heat transfer drastically drops since the wall is blanketted by vapor, and the convection in vapor if much less efficient for the cooling of the wall.

These models are used in industrial codes such as NEPTUNE_CFD, co-developed by EDF and the CEA for the simulations of Pressurized Water Reactors or on ANSYS Fluent for various applications. However, these models, used for large simulations, require inputs such as the

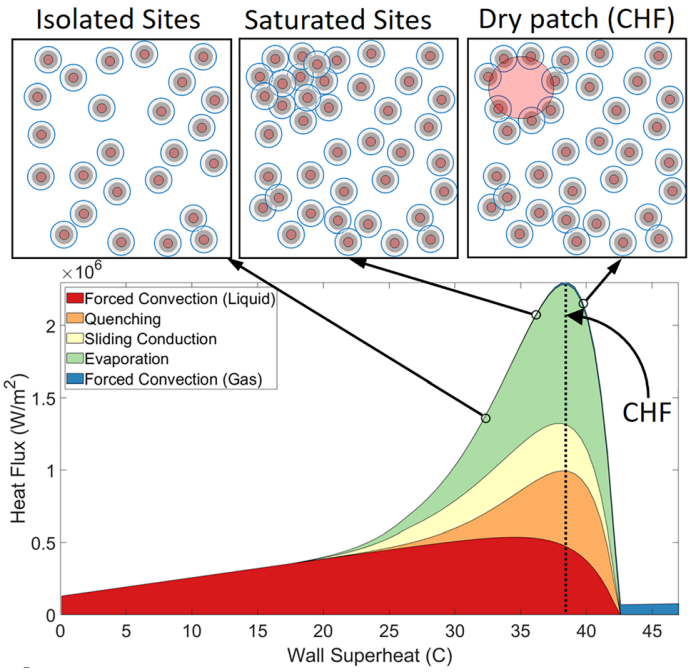

Figure 1.2: Evolution of the heat flux partition with temperature. Image from Baglietto [5]

bubble growth rate, detachment diameter and frequency, and the nucleation site density of the wall. These parameters can be obtained by experiments or Direct Numerical Simulations, at the scale of the single bubble. The understanding of the largest scales depends on the knowledge of the physics underlying in the bubble growth.

1.1 Previous experimental results

Several experimental studies began in the 1950's to investigate on the growth rate of steam bubbles and motivated the developments of theoretical models. For a single bubble, numerous evaluation for the growth rate has been established, and are summarized in [6]. With the assumption of a thin thermal boundary layer around the bubble, the energy balance can be written

$$\rho_{\text{vap}} L_{\text{vap}} 4\pi R^2 \dot{R} = 4\pi R^2 \lambda_{\text{liq}} \left.\frac{\mathrm{d}T_{\text{liq}}}{\mathrm{d}r}\right|_R \simeq 4\pi R^2 \lambda_{\text{liq}} \frac{T_0 - T_{\text{vap}}}{\delta_t} \tag{1.2}$$

with $\delta_t \simeq \sqrt{\alpha_{\text{liq}} t}$, the thickness of the thermal boundary layer. After integration, the following equation is obtained:

$$R(t) = 2C \times \text{Ja} \sqrt{\alpha_{\text{liq}} t} \tag{1.3}$$

With $\text{Ja} = \frac{\rho_{\text{liq}} C_{p,\text{liq}} \Delta T}{\rho_{\text{vap}} L_{\text{vap}}}$ the Jakob number. The value of $C = \sqrt{\frac{3}{\pi}}$ is obtained by Plesset & Zwick [7] for high Jakob numbers. Forster & Zuber's approximation [8] was $C = \sqrt{\frac{\pi}{2}}$ for the same conditions of Jakob. Scriven [9], without the assumption of thin thermal layer, define C as a function of the Jakob number. It can be demonstrated that

$$\dot{R} = \text{Ja} \times f(\text{Ja}) \sqrt{\frac{\alpha_{\text{liq}}}{t}} \tag{1.4}$$

with $f(\text{Ja})$ a function of the Jakob number which can be detailed as follows:

$$f(\mathrm{Ja}) = \frac{F}{2\mathrm{Ja}^2} \quad \text{with F given by} \quad \mathrm{Ja} = F\exp\left(\frac{3F}{2}\right)\int_1^\infty \frac{1}{x^2}\exp\left(-\frac{F}{x}-\frac{Fx^2}{2}\right)\mathrm{d}x \tag{1.5}$$

For high Jakob number, the function $f(\mathrm{Ja})$ tends to $\sqrt{\frac{3}{\pi}}$, which is consistent with the result of Plesset & Zwick. Scriven results were confirmed by numerical simulation of Legendre et al [10].

In 1970, Mikic & Rohsenhow [11] used the development of Scriven, and account for the non-uniform temperature field, which is the case with solid heater. Moreover, the presence of the wall leads to truncated bubble, which are accounted for by Mei [12]. The geometrical parameter c_m is defined as the ratio between the contact line radius r_{cl} and the bubble radius R, $c_m = r_{\mathrm{cl}}/R$, and therefore

$$R(t) = \frac{c_m}{f(c_m)}\frac{\mathrm{Ja}}{c_1\sqrt{\mathrm{Pr}}}\sqrt{\alpha_{\mathrm{liq}}t} \tag{1.6}$$

with $\mathrm{Pr} = \frac{\nu}{\alpha}$ the Prandtl number, and c_1 a constant extracted from numerous data sets which can be related by

$$c_1 = \left[\left(0.4134\mathrm{Ja}^{0.1655}\right)^{-6} + \left(1-0.1e^{-0.0005\mathrm{Ja}}\right)^{-6}\right]^{-1/6} \tag{1.7}$$

Numerous experiments were conducted with bubbles nucleated above a superheated plate. We can cite Zuber [13], who investigated the heat transfer coefficient for isolated bubbles, and found similarities between the flow regimes of bubble departing from a surface and the updraught of turbulent natural convection. A large study of boiling on heated plates is carried out by Van Stralen [14, 15, 16], for pure liquid and binary mixture. The analysis is led on bubble detaching. The growth rate, departure frequency are compared to experimental data and correlations are made.

Such correlations are empirically established, and are valid for specific fluids and ranges of parameters. Extrapolations on different fluid properties are not accurate, but sometimes used when no better predictive method is available. Therefore, more advanced measurements techniques have been devised to enhance predictions and delve into smaller scales for a better understanding of the mechanisms involved in nucleate boiling.

1.1.1 Experimental observation of micro-layers

Numerous experiments have been carried out last decades to visualize bubbles growth due to superheating. They were mainly conducted with water for the sake of simplicity, and because of the growing interest in the nuclear applications, which use water as working fluid. Van Stralen [14, 15, 16] observed a liquid layer between the bubble interface and the superheated wall, which is called the micro-layer. His study is performed with water and binary mixtures. Large bubbles can be observed. In 1969, Cooper & Lloyd, with toluene and isopropyl alcohol, noticed the micro-layer as well [17]. Its thickness is measured of about one to ten micrometers, and this layer is the location of high heat transfer. Empirical laws are established, and the micro-layer thickness evolution is evaluated to

$$\delta \propto \sqrt{\nu_{\mathrm{liq}}t} \tag{1.8}$$

More precise study can be performed with micro-electro-mechanical systems (MEMS). Yabuki [18, 19] investigated on the micro-layer thickness, which is observed to decrease with the initial superheat. It was estimated that around 50% of the overall evaporation is due to the

micro-layer contribution. This value is found to be slightly independent on the wall superheat. This observation differs from Utaka's [20], who, for nearly similar micro-layer contribution, found it quasi linearly dependent on the superheat. Micro-layer evaporation can also be studied with infrared camera, as did Gerardi et al [21]. With spatial resolution of 100 µm, they compared their experiment to old models and correlations, which they found great agreements with. Bucci conducted micro-layer experiments with infrared and high speed cameras as well [22]. A heat flux map distribution evolution with time has been established, and provide crucial information on the micro-layer length and thickness.

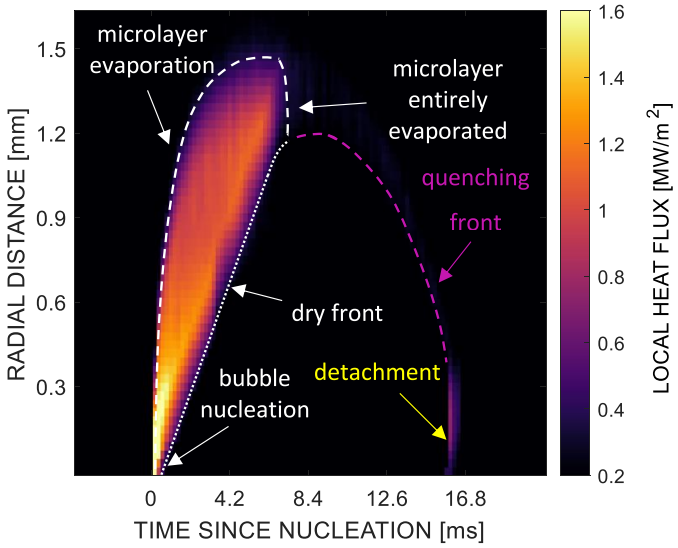

Figure 1.3: Temporal evolution of the heat flux distribution radially away from the nucleation site. Image from [22].

In figure 1.3, the heat flux associated to micro-layer is of about 1 MW/m^2, whereas the heat flux of the dry area is an order of magnitude lower. The transition between the high and low values of flux allow to spot the contact line.

Moreover, interferometry can be performed to measure micro-layer thickness, as the pioneer work of Jawurek [23]. Gao [24] corrected the coefficient of Cooper's equation (1.8).

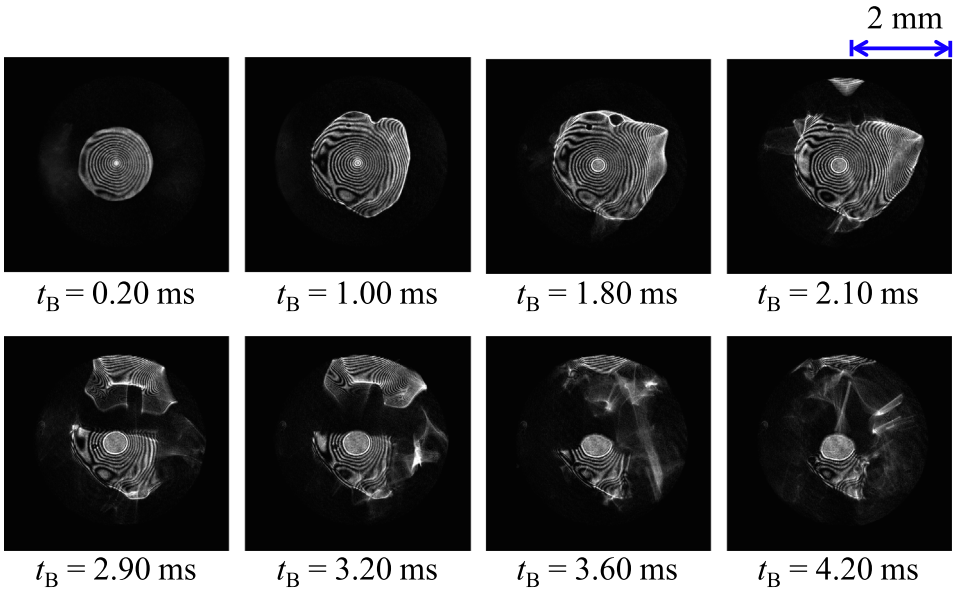

Figure 1.4: Interferometry images from Chen [25]. $q'' = 433$ kW/m^2, shooting rate 10000 fps.

Chen [25] measured, for different heat flux, the evolution of the micro-layer length and thickness. Figure 1.4 displays the distribution of interferometric fringes, which is post processed to deduce the micro-layer properties. Especially, it has been observed that its length decreases with the heat flux and therefore the micro-layer disappear faster, due to the more intense evaporation.

More recently, Tecchio [26] used white-light interferometry (WLI). Despite the limitation in slope (especially in the micro-layer rim), the micro-layer length and thickness are measured more accurately. The dynamics is found to be governed by surface tension and viscosity. The different methods developed for micro-layer visualization, have been recently discussed by Kossolapov [27].

However, his investigation [28] highlighted that this micro-layer occurs only with relatively low pressure when water is used as the working fluid. Above 3 bars, the micro-layer vanishes. At the same time, similar experiments have been carried out and lead to different observations. Mainly conducted with refrigerants, a micro-layer is not systematically observed.

1.1.2 Similar experiments without micro-layer

Chen [29] observed the heat flux during nucleation and growth phase for FC-72. For low superheat, the heater remains partially wetted during the bubble detachment, while for higher superheat, the liquid quickly evaporates and leaves the heater completely dry afterwards. No micro-layer is observed.

Demiray & Kim [30] and and Henry [31] used MEMS sensors and controlled the wall temperature with heaters which size are between 0.8×0.8mm (9 cells) to 2.7×2.7mm (96 cells). The setup is displayed in figure 1.5. Very high heat flux are measured.

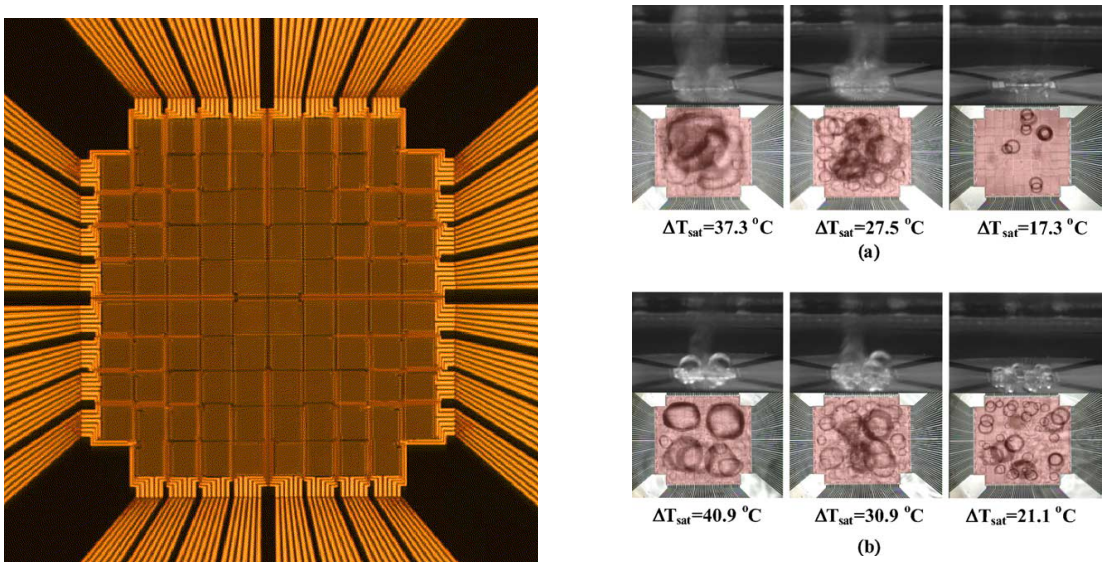

Figure 1.5: left: Picture of the 96 arrays heater; right:boiling pictures at high-g (a) $T_{\text{sub}} = 8°\text{C}$, $T_{\text{bulk}} = 55°\text{C}$; (b) $T_{\text{sub}} = 31°\text{C}$, $T_{\text{bulk}} = 28°\text{C}$. Both pictures from Henry [31].

Moghaddam [32] was able to look at the different contributions involved in the evaporation of successive bubbles, and highlight the dependency on the boiling regimes. Indeed, a large impact on the waiting time between successive bubble is observed, and hence on the departure diameter and frequency, which need to be accurately know for heat transfer predictions. Similar analysis is carried out with unencapsulated liquid crystals (TLCs) by Sodtke [33]. It provides high resolution for the thermal field below the substrate, and allows to highlight the temperature variations entailed by the contact line motion. However, restrictions in the measurements and low frequency response of the system lead researchers to used IR camera instead. Dry spots are

hotter than wet ones, so the thermal gradients can be observed, as well as heat flux. With such device, Wagner & Stephan [34] showed that the contribution of the heat flux near the contact line is between 10-30% depending on the fluid.

These experiments, performed with refrigerants on ground, lead to small bubbles which quickly detach from the heated wall. Observations are difficult to carry out, and the effects of gravity (buoyancy forces on the vapor phase, natural convection...) often hinders a precise comprehension of the fundamental principles underlying nucleate boiling. For that reason, experiments in microgravity have been conducted through parabolic flights or onboard of the International Space Station.

1.1.3 Weightlessness experiments

It is well known that buoyancy is a dominant mechanism in nucleate boiling. Empirical correlations of bubble departure or detachment frequency are, obviously, gravity dependent. Moreover, nucleate boiling is of utmost importance in space applications for which the management of liquid propellant in micro-gravity is critical, or for cooling systems for space applications. In the absence of buoyancy forces, the bubble behavior is different since it does not detach from the heating wall. The vapor could end up blanketing the heated wall and inducing significant heat flux. For these two reasons, intensive studies on boiling in micro-gravity have been carried out. Such experiments provide observations on long time ranges, which allow more accurate description of the phenomena involved in nucleate boiling.

Since 1960, microgravity experiments have been conducted as part of the NASA Space Program. Using drop towers, Siegel [35] replicated microgravity conditions for a few seconds and investigated nucleate pool boiling with varying fluids and a heated wall. Straub [36] studied the effects of surface tension and Maragoni convection on nucleate boiling using a heated wire or a heated plate.

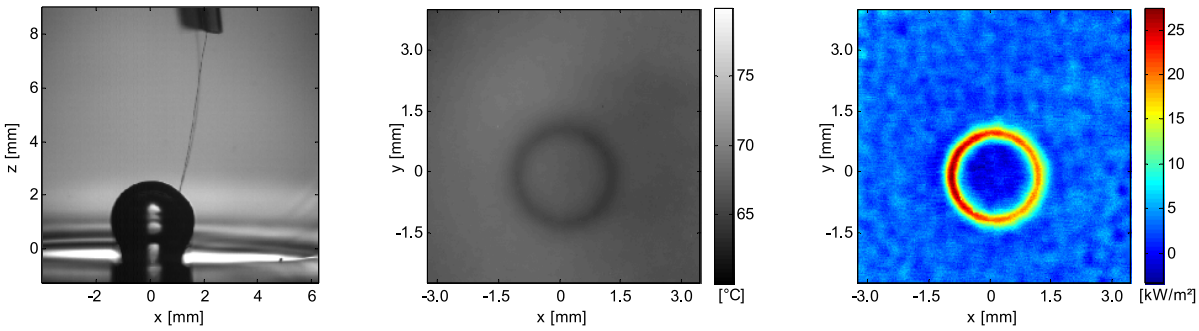

Figure 1.6: B&W picture from side, temperature and heat flux field from below the bubble, in low-gravity. Images from Schweizer [37].

Since 2000, numerous experiments have been carried out to examine wall temperature in nucleate boiling during parabolic flights. Ohta [38] used a transparent heater to visualize the bubble's foot growth from below, and used thermal sensors to measure the temperature. Schweizer & Stephan [39] studied multiple detachments in reduced gravity. The bubble departure frequency is decreased, and detachment diameter increased. Figure 1.6 shows B&W and infrared image of the bubble. Very high contact line heat flux is observed, with no micro-layer. More recently, researchers have been investigating new methods to artificially detach a bubble from a heated wall in microgravity conditions. One such method is the use of an electric field, which was studied by Di Marco et al [40] during parabolas. The electric field creates body forces on the vapor, inducing the departure of the bubble for a critical radius size and enhancing heat transfer at the bubble foot, thereby delaying the boiling crisis. However this effect is less pronounced at high heat fluxes. Another method is the use of a shear flow, which was studied by Duhar [41] in terrestrial gravity to drag the bubble away from the heat source. The different forces acting

on the bubble during growth were analyzed theoretically and compared to experimental data. A correlation of the departure diameter as a function of the Jakob number and the liquid flow velocity is established. However, the impact on the bubble growth is Reynolds dependent and thus challenging to evaluate.

Lebon [42], with the BIOMAN experiment, investigated on isolated bubble detachment with and without shear flow. This encompassed the initial concepts of the RUBI experiment (Reference mUltiscale Boiling Investigation), which was launched onboard of the International Space Station in july 2019.

1.1.4 RUBI experiment

In order to improve the understanding in heat and mass transfer at the bubble scale, the RUBI experiment has been designed. It is the fruit of the collaboration between 13 research groups in 7 countries, and was designed in order to study nucleate pool boiling in microgravity, and with shear flow and an electric field. The Reference mUltiscale Boiling Investigation is an international experiment launched in july 2019 in the International Space Station. A scheme is shown in figure 1.7.

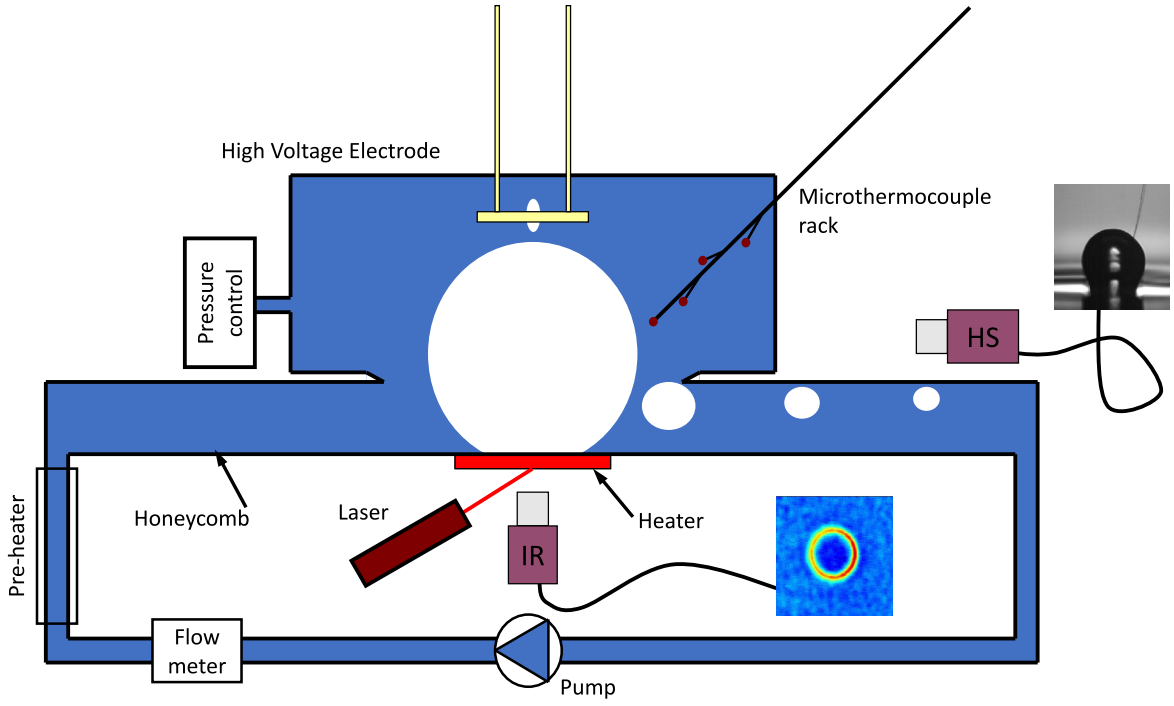

Figure 1.7: RUBI experiment. Copyright ESA

The system consists in a closed loop and a chamber of $40 \times 40 \times 40$ mm^3 where the nucleate boiling occurs. The fluid is FC-72 (N-perfluorohexane), which properties are described in Table C.1 for two different saturation conditions operated in the ISS. A solid Chromium substrate at the interface between the fluid and the Saphirre wall carries an electric current and induces Joule effect. Thus, a thermal layer expands in the fluid during a specific time t_{wait}. At this time, a laser pulse (20 ms) is sent below the Sapphire plate (which is transparent), and locally raises the temperature so that the nucleation occurs in an artificial cavity of 50 µm radius, with a L-shape. Once the nucleation site is activated, the laser is no longer required to trigger the next bubbles, since the shape of the cavity maintains a vapor embryo after the bubble departure. Two cameras provide an ongoing monitoring of the whole phenomenon: an infrared camera, below the transparent plate observes the temperature of the wall; and a black & white high speed camera (500 Hz) records the bubble from the side, and tracks its shape evolution and velocity.

Several parameters can be shifted to change the operational conditions, such as the pressure, subcooling temperature, substrate heat flux, electric field or velocity of the shear flow if so. In addition, thermal sensors collect continuously both liquid and vapor temperature in various locations. More details on the RUBI can be found in [43]. Thus, 3440 different experiments have been operated during 2 campaigns between 2019 and 2021. Each configuration is performed three times, with one baseline experiment done periodically to assure the reproductibility and the absence of degradation. Four main configurations can be considered, and are displayed in figure 1.8:

- Without shear flow or electric field. In microgravity, the bubble grows and reaches an equilibrium diameter when the evaporation at its foot is balanced with the condensation at its top due to the subcooling. This has not been observed in RUBI due to the short experimental time (10 s).
- With a shear flow: an input flow is generated with a pump, and cross a honeycomb structure. The bubbles detach from the wall if the drag overcomes the surface forces and the bubble slides along the wall.
- With an electric field. It generates a surface force at the interface which induces the bubble detachment.
- With shear flow and electric field.

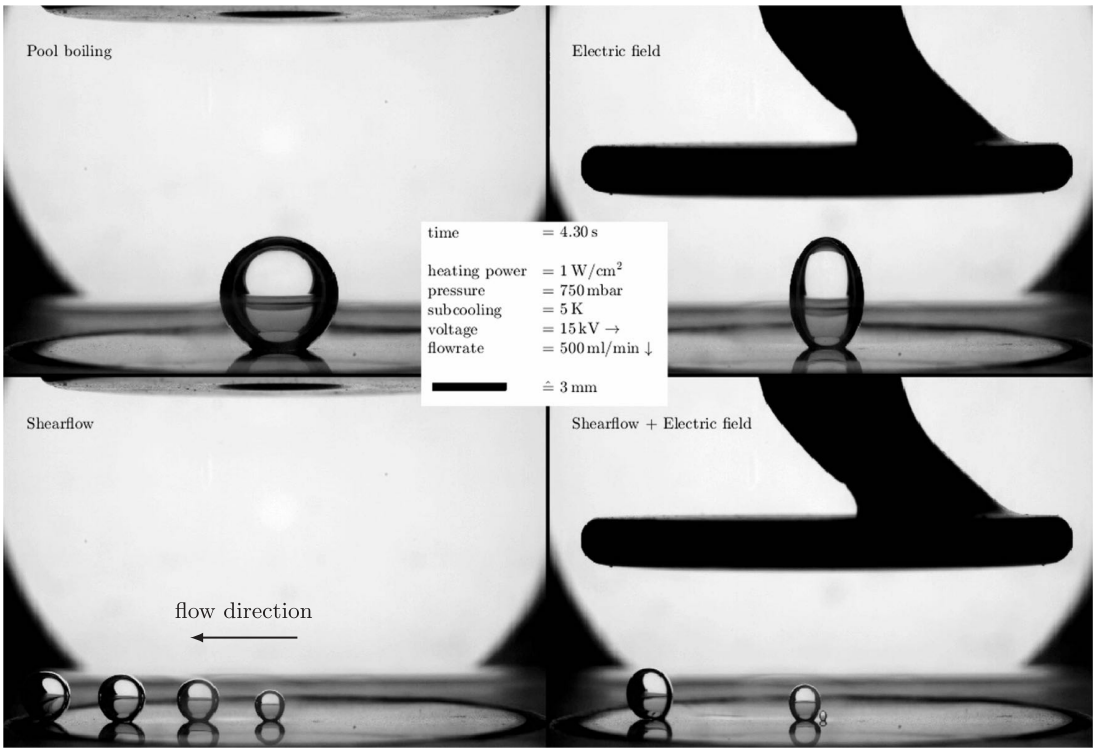

Figure 1.8: B&W pictures of the 4 different configurations and the associated bubble shapes. Images from [43].

Post-processing has been performed on the B&W images and the IR camera to come up with the diameter evolution, the apparent contact angle and the thermal field on the substrate. A short detail of the post-processing work is described in Appendix D. A post-treated IR image is displayed in figure 1.9.

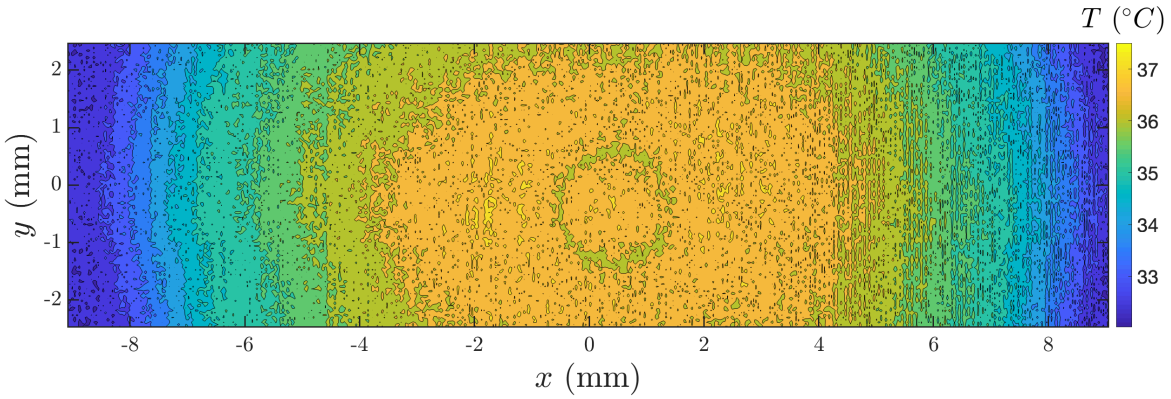

Figure 1.9: Raw image of the substrate. The cold ring depict the cooling of solid domain by the contact line.

1.2 Numerical methods

We now take interest in the methods used for the numerical simulations of boiling.

1.2.1 Methods for interface tracking

Many issues must be addressed to perform effective numerical simulations of boiling. The scales involved are about $\sim 1 - 10$ mm for the usual bubble diameter. Complete descriptions of large applications are prohibitively expensive, since DNS of single to few bubbles are already computationally demanding. Direct Numerical Simulations of nucleate pool boiling have been performed by the late 90's, with the pioneering works of and Son & Dhir [44]. Several methods are developed to account for two-phase-flows. Especially, an accurate description and localization of the liquid/vapor interface is required. Among them, the Markers-and-Cells (MAC) is a Lagrangian method that has been developed Harlow et al [45] (see figure 1.10).

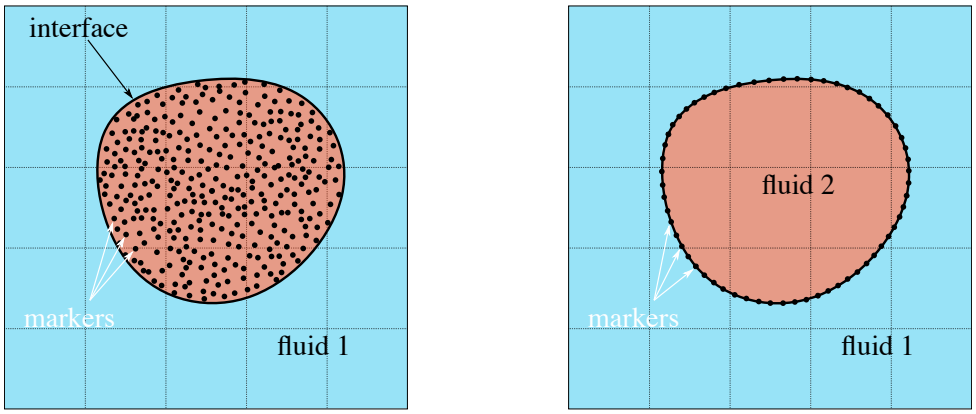

Figure 1.10: Markers-and-Cells (left) and Front Tracking (right) methods

It uses markers spread in the liquid domain which enable to distinct both phases. As an improvement of the MAC, the front-tracking is introduced by Daly [46], and allows to reduce the number of trackers to have only at the interface. Implemented by Glimm [47], it was later improved by Juric [48] and by Popinet & Zaleski [49]. Especially, a better treatment of the surface tension, comparison with theoretical solutions are enhanced and the spurious currents vanished. The front-tracking method allows to perform simulations of nucleate boiling dealing with complex interfaces and to free from the simplifying hypothesis of spherical interface for computation.

On the other side, Eulerian methods have also been developed. The Volume of Fluid method (VOF) has been initiated by Hirt et al [50]. It uses a stationary mesh in which a Color Function C is defined to account for the fluid fraction, its value is defined as 1 in the liquid, 0 in a the vapor, and a value in-between if the cell is crossed by the interface (see figure 1.11, left). The function is advected by the local velocity field $\mathbf{v}$ with

$$\frac{\partial C}{\partial t} + \mathbf{v} \cdot \nabla C = 0 \tag{1.9}$$

The VOF method provide accurate mass conservation, but specific interface reconstruction algorithm are required for the calculation of the curvature. This method is currently one of the most popular, and has been improved by the years [51, 52]. The Level Set Method (LSM) is introduced by Osher & Sethian [53, 54]. The tracking is performed through a continuous distance function to the interface ϕ (see figure 1.11). This function is advected at every time step, and a reinitialisation step improves the stability as described by [55]. A more detailed description is developed in chapter 2. It has especially been used for liquid/vapor two-phase flows [56] as well as flames [57], and can handle multiple chemical compound tracking.

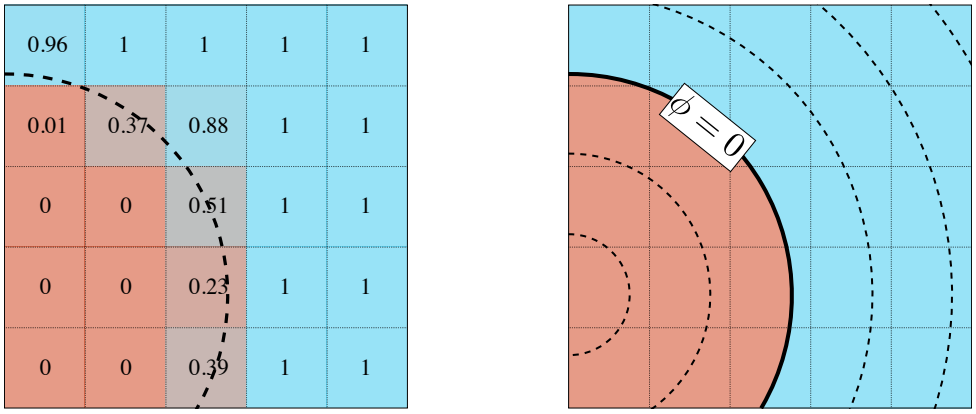

Figure 1.11: Volume of Fluid (left) and Level Set (right) Methods

Once the interface is precisely localized, the conservation equations can be computed. However, issues in terms of mass conservation can be encountered. Scardovelli et al pusblished a more exhaustive review of all these methods [58].

1.2.2 Methods for continuity at the interface crossing

In multiphase flows, discontinuities of the fields must be captured at interfaces. The computational cells crossed by the interface are difficult to define, and their computation is even more challenging. Scardovelli et al [58] developed the Delta Function Method (DFM), which stems on smoothing the physical properties in the vicinity of the interface with a δ function. The discontinuity is spread out and varies over several cells. The computation of the conservation equations in this region remains unchanged. On the opposite, the Ghost Fluid Method (GFM) initiated in [59] uses this discontinuity to add jump conditions on conservation equations. On each side of the interface, ghost cells are generated in order to simulate liquid cells in the vapor phase and vapor cells in the liquid phase. This method will be described further, in part 2.2.2. High order schemes for velocity, pressure and temperature uses these ghost cells for gradient computation, and prevent discontinuity to alter the results. Lalanne et al [60] proved that DFM and GFM are formally identical. However, Tanguy et al [61] demonstrated that GFM computation provides more accurate results than DFM for nucleate boiling simulations. Comparison of bubble growth rate with analytical results are better, and velocity fields are improved. With these works in last decades and more recently [62, 63], huge progress in scientific computing has been achieved.

1.2.3 Modeling of the contact line

The interface is the location of discontinuity between the liquid and the vapor phases. The triple interface between liquid, vapor and solid is even more complex. The viscous dissipation tends toward infinity in the momentum equation [64]. To alleviate the hydrodynamic singularity, a solution is proposed by Dussan [65], who proposes the use of a slip length at nano-scale. Moreover, when in contact with thermally conductive walls, a thermal singularity is also observed. A model developed by Wayner [66] is often used, with an interfacial thermal resistance to regulate the infinite flux entailed by a temperature discontinuity. Numerous numerical models have been developed to characterize the phenomena taking place in this highly specific area, leveraging the hydrodynamic and thermal singularity [67, 68, 69, 70]. They will be decribed in detailed in chapter 3, but a quick overview is given below.

Micro-region models

The baseline of such models is the intermolecular forces between the wall and the fluid, which require specific handling. Moreover, usual Navier-Stokes equations are computed on mesh size of micrometers, and are insufficient to capture phenomena at scales of about tens to hundreds of nanometers. Therefore, the use of a specific analytical model is required to depict the phenomena that occur. Nowadays and despite the increasing interest in micro-region models, the means and methods to characterize them is an open problem. Indeed, these very low scales phenomena cannot be directly observed by experiments. Only the more large scale effects, such as variation in the apparent contact angle or heat flux at the contact line can be directly observed. Raj et al [71] investigated on the contact angle variation of FC-72 with the superheat, and compared with the result of Stephan's model [67]. The evolution displays similar tendency despite difficulty in the curvature measurements. Global conclusions are difficult to draw on which model is valid or not since there are uncertainties in the measurements.

In [67], Stephan & Busse introduced a model based on a 2D analysis. The authors exploited results of Wayner [66], and assumed the existence of an adsorbed film formed by the liquid of a grooved heat pipe, which is a very thin liquid layer where the intermolecular forces are strong enough to alter the saturation properties of the fluid, making it non-evaporating. These forces can be depicted with a disjoining pressure, modeled through a Hamaker constant. Moreover, the interface displays an internal resistance to mitigate the evaporation as suggested by Schrage [72]:

$$R_\Gamma = \frac{2-f}{2f}\frac{T_{\text{sat}}\sqrt{2\pi R_g T_{\text{sat}}}}{\rho_{\text{vap}} L_{\text{vap}}^2} \tag{1.10}$$

with f the accommodation coefficient, depending on the fluid properties. This interfacial resistance is often regarded as an equivalent liquid thickness $\lambda_{\text{liq}} R_\Gamma$, as in the heat flux equation:

$$q'' = \lambda_{\text{liq}} \frac{T_{\text{w}} - T_\Gamma}{\delta + \lambda_{\text{liq}} R_\Gamma} \tag{1.11}$$

with δ the thickness of the liquid film. Although, this heat flux remains important because of the proximity of the heated wall, and generates high evaporation rate in the vicinity of the contact line.

Mathieu [68] improved this analytical model by considering the liquid flow equation in a wedge, and relaxed the singularity at the contact line with the lubrication hypothesis. He introduced the slip length [65] to account for the contact line motion. His model can also be applied to partially wetting fluid, where the adsorbed film is absent and a microscopic contact angle is considered. Such a case is shown in figure 1.12. As this case is more usual, it has been used for the numerical study of boiling based on RUBI experimental results. Nikolayev and Janeček [69, 73] used the same elements as Stephan and Mathieu, and considered the

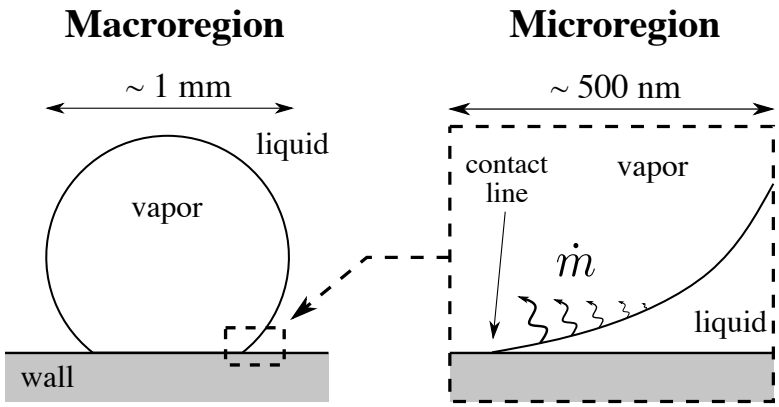

Figure 1.12: Macro and micro-region, for a partially-wetting fluid since there is no adsorbed film.

contribution of the recoil pressure due to high heat flux, the Marangoni effect caused by the surface tension, and accounted for the contact line velocity in the flow equation. Moreover, the interaction with the wall has been studied analytically and the model has been integrated to simulations in [73]. Despite some differences between the models, they globally display the same tendencies.

Coupling with DNS

If micro-region models provide local heat flux and apparent contact angle, such low scale results cannot be directly computed into DNS solver. A coupling of the micro-region to the CFD simulations is required through a subgrid model. Kunkelmann proposed one in his thesis [74]. The micro-region is not solved on a fixed length, and he defined a transition region to make the link between the micro and the DNS scales. Yet, the handling of the associate heat flux remains complex due to the very high values. Batzdorf [75] proposed to spread the micro-region contribution along the whole bubble interface to smooth the process. Son et al [76] distribute it as a source term in the mass conservation. With the micro-region heat flux, the comparisons between DNS and experiments are improved.

However to our knowledge, no implicit coupling between micro-region model and DNS fully describes the treatment required at the contact line. Simulations have accounted for the heat flux all along the interface, or in the whole bubble, but therefore do not simulate the contact line accurately, since the liquid flow feeding the contact line evaporation is not accounted for.

1.3 Simulation of bubble growth

1.3.1 Nucleate boiling regime

Despite the availability of computational resources that enable high-cost calculations, Direct Numerical Simulations are most of the time restricted to single (or a few) bubble simulations. Nevertheless, the numerical methods developed these recent years enable to perform simulations of nucleate boiling with confidence. Son et al [44] studied the growth and departure of a bubble from a heated wall. Comparisons with the experiment of Siegel revealed the importance of the micro-region model to correctly capture the growth rate. However, Huber et al [77] reached identical results without micro-region modelling but with thinner meshes. The diameter evolution is shown in figure 1.13. A study of the bubble growth rate is carried out for high macroscopic contact angle (water) and low Jakob number (Ja).

Nucleate boiling is studied in different configurations [76, 78], with an interesting match with experiments. Moreover, Shin et al [79] performed 3-dimensional simulations of single bubble

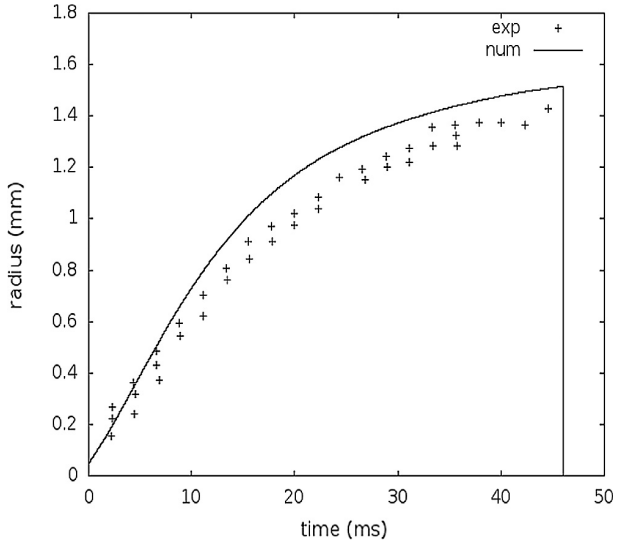

Figure 1.13: Numerical vs experimental results, from [77].

detaching from a superheated wall, see figure 1.14. Great agreement is found with experimental data, as the Nusselt is identical to the results of [80].

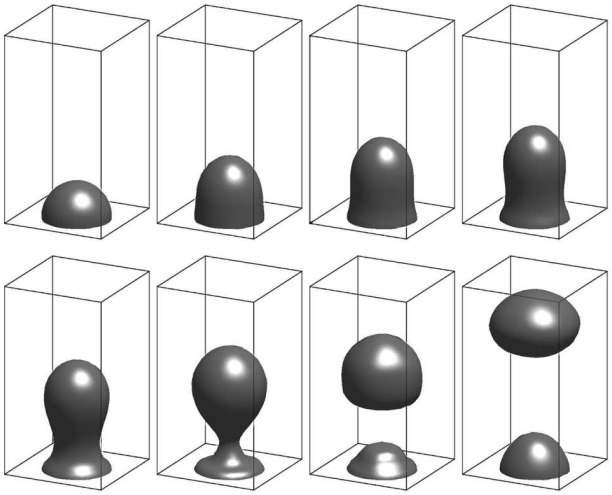

Figure 1.14: 3D simulations of [79].

Moreover, the computation of two-phase flows creates a singularity at the contact line, since the wall temperature is different from the saturation temperature of the interface. The wall properties are often disregarded despite their great importance. Mann studied the influence of the wall thermal conductivity on a single bubble growth accounting for the micro-region model [81]. By increasing the solid conductivity, two antagonist effects are observed which mitigate the effect of the micro-region on the global bubble growth. It is straightforward that the greater the wall thermal conductivity, the greater the temperature of the solid and hence the contact line temperature. This leads to greater micro-region heat flux. However, a greater wall temperature increases the contact angle and thus the liquid film is thicker, which lowers the conductive flux further from the contact line. Yet, this study focus on a single bubble growth. The effects of the successive departures, and the renucleation criterion is investigated in [82]. It is observed that the bubble departure diameter decreases with the thermal conductivity, whereas the growth time increases. Indeed, the waiting time between the take-off of a bubble and the nucleation of the following one is significantly shortened with the solid thermal conductivity. Therefore, the thermal boundary layer in the liquid at the bubble nucleation is colder than with low wall

conductivity and the bubble grows in a less favourable environment.

Nucleate pool boiling in microgravity conditions is investigated in [83]. A water bubble attached on a heated wall, in a subcooled liquid is simulated at equilibrium state, since condensation and evaporation are balanced. The bubble diameter at equilibrium and the growth time are studied, and an analytical correlation with the Jakob number and the contact angle is established. Moreover, the ratio between the solid and the liquid thermal conductivity is found to be of great impact on the heat flux, and so on the equilibrium state. A low solid thermal conductivity induces a drop in the wall temperature because the interface tends to impose its temperature to the contact line in the absence of micro-region model. The opposite result may be expected for high solid thermal conductivity, with a micro-region coupling.

1.3.2 Bubble growth in micro-layer regime

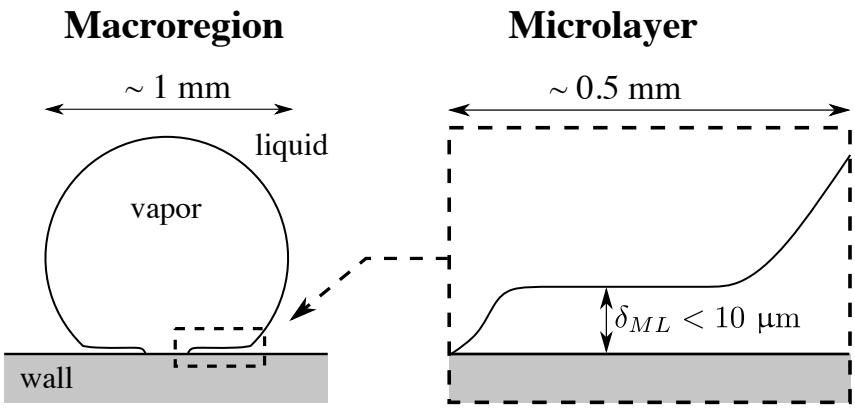

Figure 1.15: Micro-layer description

When the local superheat at the wall is high enough, the bubble grows too fast for the contact line to dewet, which generates the deposition of a thin liquid film below the bubble, known as micro-layer (see figure 1.15). The transition between the contact line and the micro-layer regimes is investigated in several works [84, 85]. Snapshots of two bubble in contact line and micro-layer regimes are displayed on Fig. 1.16.

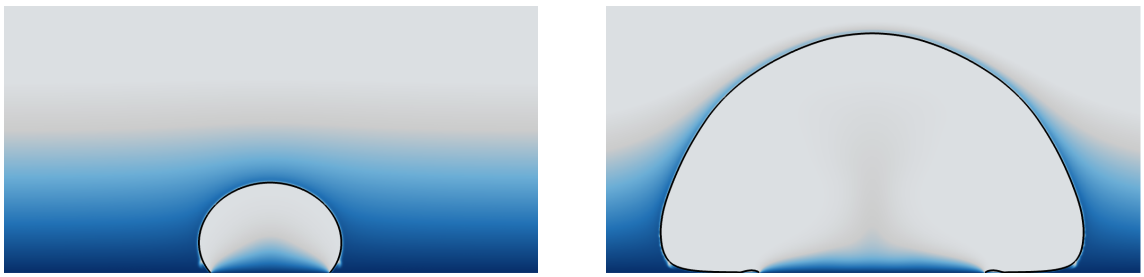

(a) Ja = 21 (b) Ja = 61

Figure 1.16: Contact line (left) and micro-layer (right) regimes. Images from Urbano et al [84]

Due to the thickness of the micro-layer of about 1-5 µm, the numerical simulations are challenging. Chen [86] and Sato [87], used the assumption of initial slope of Utaka [88] to avoid computing the micro-layer, and defined a model for the depletion which matches with the experiments of [89] and [20]. With refined simulation, Guion [90] proposed correlations and models for the layer slope and contact angle depending on Bond and Capillary numbers.

The micro-layer is also studied within the framework of pulsating heat pipes. Zhang & Nikolayev [91, 92] investigated on the liquid meniscus motion. Due to a ridge in the vicinity of the contact line, the micro-layer thickness and more generally, dynamics, is found to be nearly

independent on the initial contact angle, and accurately described by lubrication theory coupled with conductive heat transfer through the liquid film. If a global model is difficult to establish due to the numerous phenomena and physics involved, the effect of evaporation is quantified, and an analytical expression can be set for the dewetting speed.

The influence of considering the thermal field in the wall is studied in [93]. Simulations with different wall properties display high discrepancies. Hänsch et al [94] show the major importance of considering conjugate heat transfer as well. Indeed, the bubble growth is largely overestimated if a constant wall temperature is assumed.
In more recent simulations, authors are willing to couple element of gas kinetic theory (used in micro-region formulation, such as the interfacial resistance) to direct numerical simulation of micro-layer. Hänsch [94] estimated necessary to account for thermal resistance in micro-layer regime for water since it is equivalent to a conductive resistance of $\sim$ 4 µm, which is the thickness of the layer. Bureš [85] also discussed about the adequate choice for the value of the accommodation coefficient. In [95], a complete simulation of the micro-layer is performed, and a consistent range of f for the interfacial resistance has been established to fit with the experimental results of Bucci [22].

1.4 Boiling at the micro-region scale

1.4.1 Micro-layer or micro-region ?

Within the literature previously introduced, two distinct phenomena have been highlighted, both involving high heat flux. The first is the micro-layer, thin liquid film trapped between the interface and the superheated wall, and is a few micrometer thick and up to millimeter long. On the other hand, some studies do not observe micro-layers, but rather local heat flux in the vicinity of the contact line. These phenomena have been considered as equivalent, and were mixed-up until the study of Fischer [96].

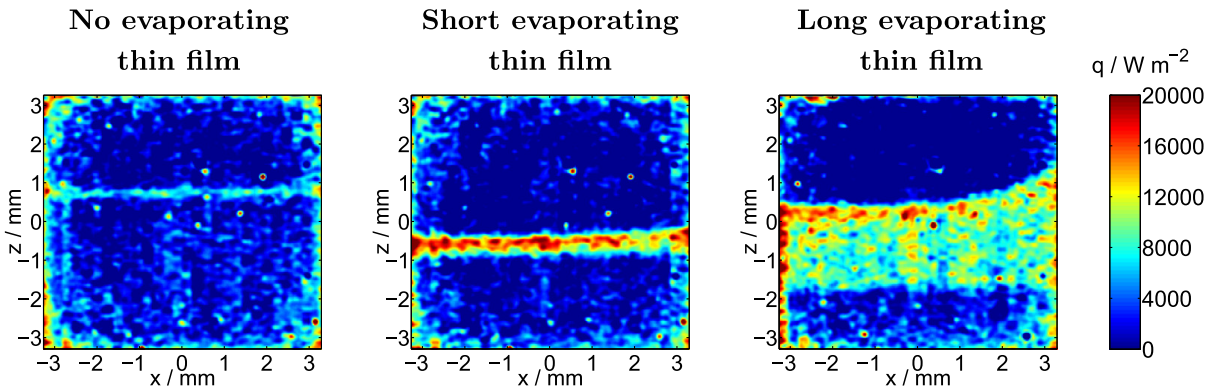

Figure 1.17: Infrared images of the heat flux at the substrate, from [96]. High heat flux are still spotted at the contact line.

In [96], the authors investigated on the transition from the contact line to the micro-layer regime by artificially imposing the contact line motion. With increasing velocities, the micro-layer is developed (see figure 1.17, middle and right) and is an area of very high heat transfer. Yet, the highest heat flux always occur in the vicinity of the contact line, where the liquid film is the thinnest. Considering a stationary thin film, a dimensionless parameter A is defined

$$A = \frac{\mathrm{Ja}}{\mathrm{PrRe}} = \frac{\text{evaporating mass flux}}{\text{deposited mass flux}} \tag{1.12}$$

as a function of the Jakob number Ja, the Prandtl number Pr and the Reynolds number $\mathrm{Re} = \frac{\rho v L}{\mu}$. For large values of A, the contact line heat transfer is dominant, whereas small values indicate a micro-layer heat transfer dominant mode. Such observation demonstrates that this contact line heat flux observed for refrigerant is a different phenomenon from the micro-layer. Thus, a contact line heat flux is always considered, but can be hidden if a micro-layer is present. An experiment with the same aim was used by Schweikert [97] to differentiate the regimes with a rotating test cell to impose the contact line velocity. A frontier was drawn and the impact of the superheat and contact line velocity is studied. A scaling law of the micro-layer thickness with $\mathrm{Ca}^{2/3}$ is established, whereas the film length is $\mathrm{Ca}^{5/3}$ dependent, which is consistent with Landau & Levich law [98].

These studies definitely differentiate the micro-region, highlighted by the contact line heat flux, from the micro-layer visible on a larger extent. In contact line regime, the micro-region is always present, but is hidden in the high heat flux area when in micro-layer regime.

1.4.2 Criterion for regime transition

Only few studies have focus on the transition between the two mentioned boiling regimes. Schweikert [97], already cited above, set a criterion on a critical contact line velocity above which a micro-layer is formed:

$$v_{\mathrm{cl,crit}}^{\mathrm{Schweikert}} = 3.12 \times 10^{-3} \Delta T^{1.44} \tag{1.13}$$

On the other hand, Urbano [84] performed several simulations varying the fluid properties (surface tension, viscosity) and the wall superheat through the Jakob number. Contact line and micro-layer regimes were obtained, see figure 1.16. A transition between the two regimes is described by a correlation based on both superheat (through the Jakob number) and contact line velocity (through the Capillary number):

$$\left(\frac{\theta_{\mathrm{app}} - \theta_0}{313}\right)^3 \leq \mathrm{JaCa} \tag{1.14}$$

With $\mathrm{Ca} = \frac{\mu_{\mathrm{liq}} v_{\mathrm{cl}}}{\sigma}$, and $\theta_0 = 5°$.

Recently, Bureš used both studies to create a new correlation. In [97], the authors considered FC-72, and since Stephan's micro-region model provides the following fit

$$\theta_{\mathrm{app,Stephan}} = 9.37 \times \Delta T^{0.54} \tag{1.15}$$

Equation (1.13) can be written

$$v_{\mathrm{cl,crit}}^{\mathrm{Schweikert}} = 8.00 \times 10^{-6} \theta_{\mathrm{app,Stephan}}^{2.67} \tag{1.16}$$

Which displays a power-law dependency on $\theta^{2.67}$, close to the Cox-Voinov law in θ^3.

The correlation of Urbano is also arranged under some assumption. We consider that an estimation of v_{cl} for the first instants of the bubble is given by the expansion velocity

$$v_{\mathrm{cl}} \approx \frac{q''}{\rho_{\mathrm{vap}} L_{\mathrm{vap}}} \tag{1.17}$$

And the wall heat flux q'' can be written as

$$q'' = \lambda_{\mathrm{liq}} \frac{\Delta T}{\delta_{\mathrm{KC}}} \tag{1.18}$$

With δ_{KC} the Kays-Crawford free convection boundary layer thickness [99], used in by Urbano as initial condition of the simulations. Then, the capillary number can be written as

$$\mathrm{Ca} = \frac{\mu_{\mathrm{liq}}\alpha_{\mathrm{liq}}}{\sigma}\frac{\mathrm{Ja}}{\delta_{\mathrm{KS}}} \tag{1.19}$$

Which lead to the modified correlation

$$\left(\frac{\theta_{\mathrm{app}} - \theta_0}{313}\right)^3 \leq \frac{\mu_{\mathrm{liq}}\alpha_{\mathrm{liq}}}{\sigma}\frac{\mathrm{Ja}^2}{\delta_{\mathrm{KS}}} \tag{1.20}$$

The frontier is established with the Jakob number and the contact angle only.

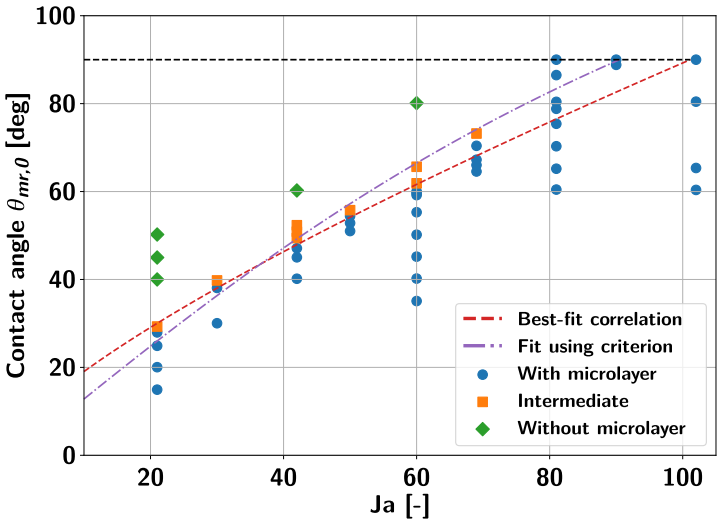

Figure 1.18: Correlation by Bureš [85] on the results of Urbano [84].

These correlations are valid for $\mathrm{Ja} \leq 75$, which is equivalent to $\Delta T \leq 25$ K for water. This is the case for most of the industrial applications.

Therefore, experimental and numerical results have been used and are able to capture the transition between contact line and micro-layer regimes. This observation is consistent with Zhang & Nikolayev [91, 92], who concluded that the dewetting is induced by evaporation. The behavior of the micro-layer is similar to a dewetting film, driven by capillary mechanism.

However, it should be noted that the simulations of Urbano do not account for micro-region model. In this micro-layer where the hydrodynamics must be accurately solved, a coupling with the nano-scales would induce a liquid flow towards the contact line for evaporation. It may be expected that micro-region considerations change the hydrodynamics, and impact on the transition from the contact line to micro-layer regime.

1.5 Outline of the thesis

In the present chapter, a quick presentation of prior research works on nucleate boiling has been provided, from early experimental studies to more recent simulations. The difficulty to carry out research works are largely due to the complexity of the methods required for numerical simulations or to the sophisticated devices needed to accurately characterize what occurs at the contact line.

Two major phenomena have been introduced in this chapter. First, the micro-layer, which occurs at "large" scale since it can be observed with different measurements methods, and which occurs in specific configurations largely documented. Nowadays, only few authors have performed a full simulation of the micro-layer, despite the continuous development of more efficient numerical methods and the increase of computing performance. On the other hand, the micro-region is a phenomenon at smaller scales, as it cannot be directly observed, and which effect on larger scales are complex to quantify, despite the continuous improvements of technical capabilities. As a consequence, several issues can be raised from the previous observations.

The local phenomenon at the contact line derives from the hydrodynamic and thermal conditions in its vicinity as much as it impacts them. The existing works deduce a heat flux from a wall temperature, but the coupling between a micro-region model and a DNS solver has never been clearly addressed. Therefore, the issue of (i) how to adapt the solid/fluid boundary at the contact line (ii) how to handle the micro-region outputs inside the DNS must be tackled.

Only few experiments provide valuable data of the global impact of the micro-region on bubble growth. Since only these large scale evidences can be observed, how to ensure the nano-scale variations described by the models are accurate?

Micro-region and micro-layer are two distinct phenomena acting at different scales, and have long been mixed-up due to the same observable effects. With numerical simulations, can we quantify on the impact of the micro-region on the micro-layer ? A transition criterion which has been obtained through simulations do not consider the micro-region. Could it hasten/delay the micro-layer formation ?

Therefore, the aim is to focus on both phenomena, and have a better understanding of what is involved and how to predict their influence on the overall bubble growth and the global heat transfer generated. Then, the work carried out in this thesis will be presented as follows:

- The first part is dedicated to the numerical and mathematical background of the in-house code $\mathcal{DIVA}$. The governing equations, computational methods to accurately account for phase change, interface tracking and hydrodynamics will be introduced.
- The second part will focus on some micro-region models and their specificities. The assumptions, basis and limit of the models will be presented, and the models compared. The impact of the numerous parameters involved is studied, and the main differences between models highlighted.
- Afterwards, the coupling between the micro-region model and the DNS solver is detailed. Different methods are introduced, and the choice for the most adequate is being discussed, with accuracy and convergence arguments. Validation tests are performed.
- Then, numerical results of simulations with model will be presented. Its influence on the overall bubble growth described, and the comparison with different setup will be performed. In particular, we will focus on the nucleate boiling regime, in cases of low superheat ($<\sim$15 K). A parametric study will be conducted to quantify the influence of the micro-region model, the solid thermal conductivity and all the major parameters in micro-gravity conditions. Finally, a case with more important superheat, leading to micro-layer will be shown as an outlook.

Chapter 2

Numerical methods

In this chapter, a global overview to accurately simulate two-phase flows is provided. The first section will tackle the conservation equations and the jump conditions at the liquid/vapor interface. Afterwards, the numerical methods and solvers to compute them are detailed. A specific focus is given on the Level-Set method for the tracking of the interface, and on the Ghost Fluid method to capture the discontinuities at the interface. Finally, a validation case, based on Scriven's test case will also be simulated to ensure the consistency of the algorithm and methods described.
In the scope of this work, all these methods are used in the solver $\mathcal{DIVA}$, developed at IMFT. The MPI version of the code allows to perform large calculations on supercomputers, crucial for expensive configurations such as micro-layer simulations.

Contents

2.1 Governing equations 22
2.1.1 Mass conservation 22
2.1.2 Momentum balance 23
2.1.3 Energy conservation 24
2.2 Numerical Methods 25
2.2.1 Interface localization 25
2.2.2 Ghost Fluid Method 26
2.2.3 Projection Algorithm 29
2.2.4 Extrapolations of the fields 31
2.2.5 Discretization for the numerical schemes 32
2.3 Validation case: Scriven bubble growth 33
2.4 Conclusion on the Numerical Methods 35

2.1 Governing equations

In this section, the main equations used for two-phase flows are developed. A specific focus on the interface jumps is provided.

2.1.1 Mass conservation

For a flow with no mass creation, the mass of the fluid in a finite volume V is

$$m(\mathbf{x},t) = \iiint_{V(t)} \rho(\mathbf{x},t)\,\mathrm{d}\mathcal{V} \tag{2.1}$$

The Reynolds transport theorem is applied to the previous equation

$$\frac{d}{dt}\left(\iiint_{V(t)} \rho(\mathbf{x},t)\,\mathrm{d}\mathcal{V}\right) = \iiint_{V(t)} \left(\frac{\partial \rho}{\partial t} + \nabla\cdot(\rho\mathbf{v})\right)\mathrm{d}\mathcal{V} = 0 \tag{2.2}$$

This equation is null for every volume V. Thus, we obtain a mass conservation equation:

$$\frac{\partial \rho}{\partial t} + \nabla\cdot(\rho\mathbf{v}) = 0 \tag{2.3}$$

Due to the low velocity and low temperature variations considered in the whole study, the flow is assumed incompressible and therefore equation (2.3) is simplified into :

$$\nabla\cdot\mathbf{v} = 0 \tag{2.4}$$

The previous equation is valid for both liquid and vapor phases, but it cannot described the interface velocity, where a velocity jump needs to be accounted for due to phase change.

To calculate the jump, a mass balance is performed on a control volume $\mathcal{V}$. A discontinuity surface Σ separates the liquid volume V_{liq} from the vapor volume V_{vap}. The outer surfaces are noted S_{liq} and S_{vap}.

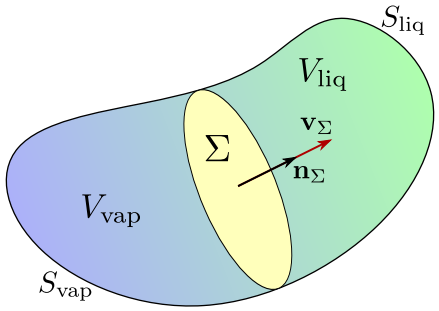

Figure 2.1: Discontinuity Σ in a volume $\mathcal{V}$

We use equation (2.2) and developed it in 6 terms:

$$\begin{aligned}\frac{d}{dt}\left(\iiint_{V(t)} \rho(\mathbf{x},t)\,\mathrm{d}\mathcal{V}\right) = &\cancel{\iiint_{V_{\mathrm{liq}}} \frac{\partial \rho}{\partial t}\,\mathrm{d}\mathcal{V}} + \oiint_{S_{\mathrm{liq}}-\Sigma} \rho_{\mathrm{liq}}(\mathbf{v}\cdot\mathbf{n})\,\mathrm{d}S - \oiint_{\Sigma} \rho_{\mathrm{liq}}(\mathbf{v}_\Sigma\cdot\mathbf{n}_\Sigma)\,\mathrm{d}\Sigma \\ &+ \cancel{\iiint_{V_{\mathrm{vap}}} \frac{\partial \rho}{\partial t}\,\mathrm{d}\mathcal{V}} + \oiint_{S_{\mathrm{vap}}-\Sigma} \rho_{\mathrm{vap}}(\mathbf{v}\cdot\mathbf{n})\,\mathrm{d}S + \oiint_{\Sigma} \rho_{\mathrm{vap}}(\mathbf{v}_\Sigma\cdot\mathbf{n}_\Sigma)\,\mathrm{d}\Sigma\end{aligned} \tag{2.5}$$

We then suppose that the balance is verified in V_{liq} and V_{vap}. It remains:

$$\oiint_{\Sigma} \left(\rho_{\mathrm{vap}}(\mathbf{v}_{\mathrm{vap}}-\mathbf{v}_\Sigma)\cdot\mathbf{n}_\Sigma - \rho_{\mathrm{liq}}(\mathbf{v}_{\mathrm{liq}}-\mathbf{v}_\Sigma)\cdot\mathbf{n}_\Sigma\right)\mathrm{d}S = 0 \tag{2.6}$$

By noticing that $\dot{m} = -\rho_{\text{liq}}(\mathbf{v}_{\text{liq}} - \mathbf{v}_\Sigma)\cdot\mathbf{n}_\Sigma = -\rho_{\text{vap}}(\mathbf{v}_{\text{vap}} - \mathbf{v}_\Sigma)\cdot\mathbf{n}_\Sigma$, and integrating on smaller surfaces, we have:

$$[\mathbf{v}]_\Sigma = -\dot{m}\left[\frac{1}{\rho}\right]_\Sigma \mathbf{n}_\Sigma \tag{2.7}$$

Where $[g]_\Sigma = g_{\text{vap}} - g_{\text{liq}}$ is the jump operator at the interface, for a given field g. The normal velocity is discontinuous because of the mass transfer at the interface. It could be emphasized that the velocity jump in the tangential direction is zero, due to viscous effect which impose no-slip at the interface.

2.1.2 Momentum balance

Newton's second law states that variation of momentum is caused by the external forces acting on the considered system. For nucleate boiling, variation of pressure and temperature are weak. The flow can be considered incompressible, and therefore be described by the usual Navier-Stokes equation:

$$\rho\left(\frac{\partial \mathbf{v}}{\partial t} + (\mathbf{v}\cdot\nabla)\mathbf{v}\right) = -\nabla p + \nabla\cdot(2\mu\bar{\bar{D}}) + \rho\mathbf{g} \tag{2.8}$$

In microgravity conditions, the last term of (2.8) is null. Similarly as in 2.1.1, the pressure jump at the interface needs to be accounted for. We consider the stress tensor $\bar{\bar{S}} = -p\bar{\bar{I}} + 2\mu\bar{\bar{D}}$, with $\bar{\bar{D}}$ the strain-rate tensor, defined as

$$\bar{\bar{D}} = \frac{1}{2}\left(\nabla\mathbf{v} + \nabla^T\mathbf{v}\right) \tag{2.9}$$

Then, in the absence of gravity, the integral momentum balance equation is

$$\frac{d}{dt}\left(\iiint_V \rho\mathbf{v}\,\mathrm{d}\mathcal{V}\right) = -\oiint_S \sigma\kappa\mathbf{n}\,\mathrm{d}S + \oiint \bar{\bar{S}}\cdot\mathbf{n}\,\mathrm{d}S \tag{2.10}$$

With κ the local curvature. The left side, similarly as in the mass balance, is split into 6 terms:

$$\begin{aligned}\frac{d}{dt}\left(\iiint_V \rho\mathbf{v}\,\mathrm{d}\mathcal{V}\right) = &\iiint_{V_{\text{liq}}} \frac{\partial\rho_{\text{liq}}\mathbf{v}_{\text{liq}}}{\partial t}\,\mathrm{d}\mathcal{V} + \oiint_{S_{\text{liq}}-\Sigma} \rho_{\text{liq}}\mathbf{v}_{\text{liq}}(\mathbf{v}_{\text{liq}}\cdot\mathbf{n})\,\mathrm{d}S - \oiint_\Sigma \rho_{\text{liq}}\mathbf{v}_{\text{liq}}(\mathbf{v}_\Sigma - \mathbf{v}_{\text{liq}})\cdot\mathbf{n}_\Sigma\,\mathrm{d}\Sigma \\ &+ \iiint_{V_{\text{vap}}} \frac{\partial\rho_{\text{vap}}\mathbf{v}_{\text{vap}}}{\partial t}\,\mathrm{d}\mathcal{V} + \oiint_{S_{\text{vap}}-\Sigma} \rho_{\text{vap}}\mathbf{v}_{\text{vap}}(\mathbf{v}_{\text{vap}}\cdot\mathbf{n})\,\mathrm{d}S + \oiint_\Sigma \rho_{\text{vap}}\mathbf{v}_{\text{vap}}(\mathbf{v}_\Sigma - \mathbf{v}_{\text{vap}})\cdot\mathbf{n}_\Sigma\,\mathrm{d}\Sigma\end{aligned} \tag{2.11}$$

And the last term of the right hand side of equation (2.10) split into 4 terms:

$$\oiint_S \bar{\bar{S}}\cdot\mathbf{n}\,\mathrm{d}S = \oiint_{S_{\text{liq}}} \bar{\bar{S}}_{\text{liq}}\cdot\mathbf{n}\,\mathrm{d}S + \oiint_\Sigma \bar{\bar{S}}_{\text{liq}}\cdot\mathbf{n}_\Sigma\,\mathrm{d}S + \oiint_{S_{\text{vap}}} \bar{\bar{S}}_{\text{vap}}\cdot\mathbf{n}\,\mathrm{d}S - \oiint_\Sigma \bar{\bar{S}}_{\text{vap}}\cdot\mathbf{n}_\Sigma\,\mathrm{d}S \tag{2.12}$$

If we assume the momentum balance is verified in both V_{liq} and V_{vap}, it remains:

$$\oiint_\Sigma \left[-\rho_{\text{vap}}\mathbf{v}_{\text{vap}}(\mathbf{v}_{\text{vap}} - \mathbf{v}_\Sigma) + \rho_{\text{liq}}\mathbf{v}_{\text{liq}}(\mathbf{v}_{\text{liq}} - \mathbf{v}_\Sigma)\right]\cdot\mathbf{n}_\Sigma\,\mathrm{d}\Sigma = \oiint_\Sigma (\bar{\bar{S}}_{\text{liq}} - \bar{\bar{S}}_{\text{vap}})\cdot\mathbf{n}_\Sigma\,\mathrm{d}\Sigma - \oiint_\Sigma \sigma\kappa\mathbf{n}_\Sigma\,\mathrm{d}\Sigma \tag{2.13}$$

Thus, we obtain:

$$[\rho\mathbf{v}(\mathbf{v} - \mathbf{v}_\Sigma)]_\Sigma = \left[\bar{\bar{S}}\cdot\mathbf{n}\right]_\Sigma + \sigma\kappa \tag{2.14}$$

By splitting $\bar{\bar{S}}$ and noticing

$$[\rho \mathbf{v}(\mathbf{v} - \mathbf{v}_\Sigma)]_\Sigma = \dot{m}^2 \left[\frac{1}{\rho}\right]_\Sigma \tag{2.15a}$$

$$\mathbf{n}_\Sigma \cdot \left[2\mu \bar{\bar{D}} \cdot \mathbf{n}_\Sigma\right] = 2\mu \frac{\partial v_n}{\partial n} \tag{2.15b}$$

We finally obtain the pressure jump condition:

$$[p]_\Sigma = \sigma\kappa + 2\left[\mu \frac{\partial v_n}{\partial n}\right]_\Sigma - \dot{m}^2 \left[\frac{1}{\rho}\right]_\Sigma \tag{2.16}$$

$$\left[2\mu \mathbf{t}_\Sigma \cdot \bar{\bar{D}} \cdot \mathbf{n}_\Sigma\right]_\Sigma = 0 \tag{2.17}$$

If the surface tension is constant, the tangential stress is constant along the interface (or equal in both liquid and vapor phases), thus no jump is required in equation (2.17). This is the case if Maragoni convection is negligible, and if the interface is neither contaminated by surfactant or considered as elastic, or in the absence of non-condensable gas in the vapor phase. This is assumed in this whole study.

2.1.3 Energy conservation

In our case, the boiling of a pure liquid into its pure vapor is investigated. The transformation is considered isobaric, therefore the energy conservation based on the variable enthalpy h is written:

$$\rho\left(\frac{\partial h}{\partial t} + \mathbf{v} \cdot \nabla h\right) = \nabla \cdot (\lambda \nabla T) \tag{2.18}$$

In the present study, all physical properties can be considered constant since nucleate boiling involves moderate temperature variations ($\Delta T < 20$ K). Therefore, the enthalpy variation with temperature is

$$h(T) - h_0 = C_p(T - T_0) \tag{2.19}$$

which is valid for both perfect gas and liquid. It leads to

$$\rho C_p\left(\frac{\partial T}{\partial t} + \mathbf{v} \cdot \nabla T\right) = \nabla \cdot (\lambda \nabla T) \tag{2.20}$$

With phase change, the interface energy balance is

$$[-\lambda \nabla T \cdot \mathbf{n}]_\Sigma = \dot{m}(L_{\text{vap}} + (C_{p,\text{liq}} - C_{p,\text{vap}})(T_{\text{sat}} - T_\Sigma)) \tag{2.21}$$

Equation (2.21) states that the heat flux between the liquid and the vapor phases is used to both set the liquid and vapor temperatures to T_{sat} and to vaporize/condense with $\dot{m}$. In case of boiling and with liquid in its pure vapor, away from the micro-region, the interface temperature remains equal to the saturation temperature:

$$T_{\text{liq},\Sigma} = T_{\text{vap},\Sigma} = T_\Sigma = T_{\text{sat}} \tag{2.22}$$

Therefore, the contribution of heating both phases is negligible, thus the previous equation is simplified in

$$[-\lambda \nabla T \cdot \mathbf{n}]_\Sigma = \dot{m} L_{\text{vap}} \tag{2.23}$$

The heat flux provided by the liquid and the vapor phases is equal to the heat associated to the evaporation process.

In 2D, the discontinuity surface Σ is the liquid/vapor interface, a line we denote as Γ for the whole study. $\mathbf{n}_\Gamma$ is the normal vector to the interface, pointing from the vapor towards the liquid. The three jump conditions become :

$$\begin{cases} [\mathbf{v}]_\Gamma = -\dot{m}\left[\frac{1}{\rho}\right]_\Gamma \mathbf{n} & \text{(2.24a)} \\ [p]_\Gamma = \sigma\kappa + 2\left[\mu\frac{\partial v_n}{\partial n}\right]_\Gamma - \dot{m}^2\left[\frac{1}{\rho}\right]_\Gamma & \text{(2.24b)} \\ [-\lambda\nabla T\cdot\mathbf{n}]_\Gamma = \dot{m}L_{\text{vap}} & \text{(2.24c)} \\ & \text{(2.24d)} \end{cases}$$

These jump conditions must be captured to accurately describe two-phase flows.

2.2 Numerical Methods

In this section, the main numerical methods are now described.

2.2.1 Interface localization

To track the interface for a two-phase flow, the $\mathcal{DIVA}$ solver uses the Level-Set Method (LSM), initially developed by Osher [53]. A function ϕ is computed in the whole domain, (see figure 2.2) and is the signed distance to the interface:

$$\phi(\mathbf{x}(t),t) = \begin{cases} \text{dist}(\mathbf{x},\Gamma(t)) & \text{if } \mathbf{x}(t)\in\Omega^+ \\ 0 & \text{if } \mathbf{x}(t)\in\Gamma \\ -\text{dist}(\mathbf{x},\Gamma(t)) & \text{if } \mathbf{x}(t)\in\Omega^- \end{cases} \tag{2.25}$$

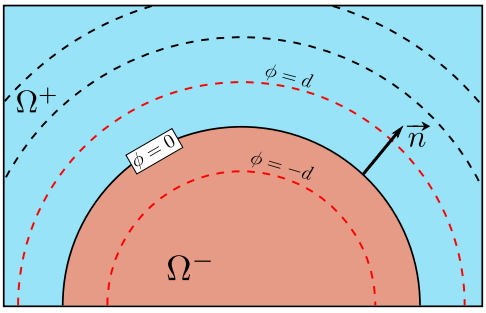

Figure 2.2: Level Set Function for a circular interface

The distance is set positive in the liquid phase (Ω^+) and negative in the vapor phase (Ω^-). The motion of the interface is computed with the interface velocity $\mathbf{v}_\Gamma$ with the following equation:

$$\frac{\partial\phi}{\partial t} + \mathbf{v}_\Gamma\cdot\nabla\phi = 0 \tag{2.26}$$

The interface velocity can be calculated with both liquid and vapor velocities

$$\mathbf{v}_\Gamma = \mathbf{v}_{\text{liq}} + \frac{\dot{m}}{\rho_{\text{liq}}}\mathbf{n} = \mathbf{v}_{\text{vap}} + \frac{\dot{m}}{\rho_{\text{vap}}}\mathbf{n} \tag{2.27}$$

In practise, for droplet configuration, the definition based on the liquid properties is preferred, whereas bubble configuration will be based on vapor properties. Moreover, Sussman [55] suggests to add a reinitialization equation to preserve the signed distance property. He defined ϕ_{new} the modified distance function, and τ a fictional time step. He then solves

$$\frac{\partial \phi_{\text{new}}}{\partial \tau} = \text{sign}(\phi)(1 - |\nabla \phi|) \tag{2.28}$$

Afterwards, ϕ takes the values set by ϕ_{new}. Despite the absence of physical sense, it provides a better stability in the computation. However, as it could slightly move the 0-level (corresponding to the interface location), some spurious interface displacement can be observed, hence a mass non-conservation of the method. This drawback is corrected with a subcell resolution described by Min [100].

With the ϕ function, the normal vector and curvature computation are straightforward :

$$\mathbf{n} = \frac{\nabla \phi}{\|\nabla \phi\|} \tag{2.29a}$$

$$\kappa = -\nabla \cdot \mathbf{n} \tag{2.29b}$$

Moreover, the level-set boundary condition is also used to impose the contact angle between the fluid and the wall. Most of the time in simulation of nucleate boiling, the wall is considered as perfectly flat and without roughness, therefore the contact angle is not supposed to vary with time or with position. A simple Neumann condition is imposed at the wall :

$$\nabla \phi \cdot \mathbf{n}_{\text{w}} = \cos \theta \tag{2.30}$$

With θ the contact angle and $\mathbf{n}_{\text{w}}$ the normal vector to the wall, pointing towards the fluid. Without further assumptions, the contact angle is set constant, and experimental values are used. Later on with micro-region coupling, the dependence of the angle on the local superheat and velocity at the contact line will lead to temporal evolution, described in Chapter 3.

2.2.2 Ghost Fluid Method

The equations previously described are based on the concept of jump at the interface, which is a discontinuity complex to account for with usual numerical schemes. Indeed, most of them rely on smooth variations and gradients to work efficiently. To maintain continuity in the equations, the Ghost Fluid Method, initially introduced by Fedkiw [59], proposes to model ghost cells on each side of the interface. High-order numerical schemes need to take into account the cells in the vicinity. Near the interface, the neighbouring cells may be in the opposite phase and have different properties. As a result, gradient computations are not reliable. These ghost cells are computed in both liquid and vapor phases to ensure the fields continuity.

The situation is described in figure 2.3. We have two domains Ω^- and Ω^+, where the function g is defined. The jump is noted $[g] = g^+ - g^-$. The interface is located between x_i and x_{i+1}. For the cells in its vicinity (usually three), real cells values ($\bullet$) and ghost cells values ($\circ$) are generated. In the present case, the calculation of g_i at time step $n+1$ (in vapor phase Ω^-) requires values of g_{i-2}, g_{i-1}, g_i, g^{G}_{i+1} and g^{G}_{i+2} at time step n.

Let's consider a 1D problem of the function g, with a diffusion coefficient β, and discontinuities of the function and its first derivative:

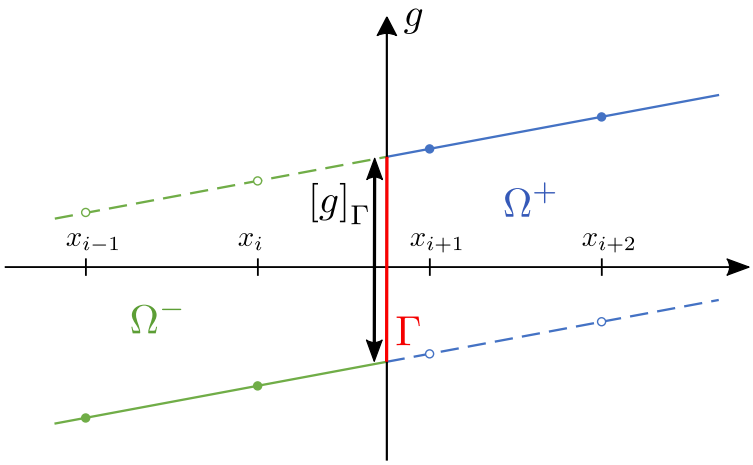

Figure 2.3: Interface jump of the function g with the GFM. Real cells (•), Ghost cells (○)

$$\begin{cases} \dfrac{d}{dx}\left(\beta\dfrac{dg}{dx}\right) & = h(x) \\ [g]_\Gamma & = a_\Gamma(x) \\ \left[\beta\dfrac{dg}{dx}\right]_\Gamma & = b_\Gamma(x) \end{cases} \tag{2.31}$$

First case: $a_\Gamma \neq 0$, $b_\Gamma = 0$, $\beta^+ = \beta^- = 1$

With a second order finite difference scheme, we have

$$\frac{d}{dx}\left(\frac{dg}{dx}\right)_i = \frac{\left.\frac{dg}{dx}\right|_{i+1/2} - \left.\frac{dg}{dx}\right|_{i-1/2}}{\Delta x} = \frac{\frac{g_{i+1}-g_i}{\Delta x} - \frac{g_i-g_{i-1}}{\Delta x}}{\Delta x} = h_i \tag{2.32}$$

If we consider cells away from the interface, all the meshes involved are in the same phase. If the interface is located between the cells i and $i+1$, the schemes can be written as

$$\frac{\frac{g^+_{i+1}-g^-_i}{\Delta x} - \frac{g^-_i-g^-_{i-1}}{\Delta x}}{\Delta x} = h_i \tag{2.33}$$

The numerical scheme will not be accurate, since g^+_{i+1} is in a different phase compared to the other points. The ghost fluid method proposes to substitute it by the ghost value:

$$g^{-,\mathrm{G}}_{i+1} = g^+_{i+1} - a_\Gamma \tag{2.34}$$

which leads to

$$\frac{\frac{g^{-,\mathrm{G}}_{i+1}-g^-_i}{\Delta x} - \frac{g^-_i-g^-_{i-1}}{\Delta x}}{\Delta x} = h_i \tag{2.35}$$

If we switch back to the known value, we have

$$\frac{\frac{g^+_{i+1}-g^-_i}{\Delta x} - \frac{g^-_i-g^-_{i-1}}{\Delta x}}{\Delta x} = h_i + \frac{a_\Gamma}{\Delta x^2} \tag{2.36}$$

The jump on the function is operated through a term on the right-hand side.

Second case: $a_\Gamma \neq 0$, $b_\Gamma \neq 0$, $\beta^+ = \beta^- = 1$

Now, we consider that the interface crosses between i and $i+1/2$, in equation (2.32), the flux can be written with the ghost value:

$$\left.\frac{dg}{dx}\right|_{i+1/2}^{-,\mathrm{G}} = \left.\frac{dg}{dx}\right|_{i+1/2}^{+} - b_\Gamma \tag{2.37}$$

And so we substitute the value in the equation:

$$\frac{d}{dx}\left(\frac{dg}{dx}\right)_i = \frac{\left.\frac{dg}{dx}\right|_{i+1/2}^{-,\mathrm{G}} - \left.\frac{dg}{dx}\right|_{i-1/2}^{-}}{\Delta x} \tag{2.38}$$

Again, we change with the known value:

$$\frac{d}{dx}\left(\frac{dg}{dx}\right)_i = \frac{\left.\frac{dg}{dx}\right|_{i+1/2}^{+} - \left.\frac{dg}{dx}\right|_{i-1/2}^{-} - b_\Gamma}{\Delta x} \tag{2.39}$$

Then, the scheme is the same as in equation 2.35

$$\frac{\left.\frac{dg}{dx}\right|_{i+1/2}^{+} - \left.\frac{dg}{dx}\right|_{i-1/2}^{-} - b_\Gamma}{\Delta x} = \frac{\frac{g_{i+1}^{-,\mathrm{G}} - g_i^-}{\Delta x} - \frac{g_i^- - g_{i-1}^-}{\Delta x} - b_\Gamma}{\Delta x} \tag{2.40}$$

And at the end, we obtain

$$\frac{\frac{g_{i+1}^+ - g_i^-}{\Delta x} - \frac{g_i^- - g_{i-1}^-}{\Delta x}}{\Delta x} = h_i + \frac{a_\Gamma}{\Delta x^2} + \frac{b_\Gamma}{\Delta x} \tag{2.41}$$

The jump on the derivative is accounted for with a second term on the right-hand side. A better precision is obtained if we consider subcell resolution of the interface.

General case: $a_\Gamma \neq 0$, $b_\Gamma \neq 0$, $\beta^+ \neq \beta^-$, **with subcell resolution**

Let's consider the distance between the cells and the interface. For an interface between cells i and $i+1$, we note $\theta\Delta x$ the distance between i and Γ, and $(1-\theta)\Delta x$ between Γ and $i+1$. The jump conditions become

$$\beta^+ \frac{g_{i+1}^+ - g_\Gamma^+}{(1-\theta)\Delta x} - \beta^- \frac{g_\Gamma^- - g_i^-}{\theta\Delta x} = b_\Gamma \tag{2.42a}$$

$$g_\Gamma^+ = g_\Gamma^- + a_\Gamma \tag{2.42b}$$

We modify equation (2.32):

$$\frac{d}{dx}\left(\beta\frac{dg}{dx}\right)_i = \frac{\beta_{i+1/2}^+ \left.\frac{dg}{dx}\right|_{i+1/2} - \beta_{i-1/2}^- \left.\frac{dg}{dx}\right|_{i-1/2}}{\Delta x} = \frac{\beta^- \frac{g_\Gamma^- - g_i^-}{\theta\Delta x} - \beta^- \frac{g_i^- - g_{i-1}^-}{\Delta x}}{\Delta x} = h_i \tag{2.43}$$

We isolate g_Γ^- by changing the jump on the derivative:

$$g_\Gamma^- = \frac{\beta^+\theta g_{i+1}^+ + \beta^-(1-\theta)g_i^- - a_\Gamma\beta^+\theta - b_\Gamma\theta(1-\theta)\Delta x}{\beta^+\theta + \beta^-(1-\theta)} \tag{2.44}$$

We inject in equation (2.43), which leads to

$$\frac{d}{dx}\left(\beta\frac{dg}{dx}\right)_i = \frac{\hat{\beta}\frac{g_{i+1}^+ - g_i^-}{\Delta x} - \beta^-\frac{g_i^- - g_{i-1}^-}{\Delta x}}{\Delta x} = h_i + b_\Gamma\frac{\hat{\beta}(1-\theta)}{\beta^+\Delta x} + a_\Gamma\frac{\hat{\beta}}{\Delta x^2} \tag{2.45}$$

With $\hat{\beta}$ the local interpolation of diffusion coefficient, defined as

$$\hat{\beta} = \frac{\beta^+\beta^-}{\beta^+\theta + \beta^-(1-\theta)} \tag{2.46}$$

The discontinuity of the diffusion coefficient is accounted for with this local interpolation, and the jumps on the function and its derivatives lead to a singular source term in the right hand side of equation (2.45).

2.2.3 Projection Algorithm

Solving the hydrodynamics

The following method is introduced by [57], in order to solve the whole set of conservation equations, and accounting for the jump conditions. The computation of a temporary velocity field is required to solve the pressure and temperature fields. This temporary velocity field is then corrected to consider the null divergence in a incompressible flow.

The first step of the algorithm is to calculate the temporary field:

$$\mathbf{v}^* = \mathbf{v}^n - \Delta t\left(\mathbf{v}^n\cdot\nabla\mathbf{v}^n - \frac{\nabla\cdot(2\mu\bar{\bar{D}}^n)}{\rho^{n+1}} - \mathbf{g}\right) \tag{2.47}$$

The discretization of the deformation tensor $\bar{\bar{D}}$ can be found in [101]. Vapor and liquid velocities are extended on both sides with the Ghost Fluid Method presented above. First, the liquid velocity is computed:

$$\mathbf{v}_{\text{liq}}^* = \begin{cases} \mathbf{v}^* & \text{if } \phi^{n+1} > 0 \\ \mathbf{v}^* + \dot{m}^n\left[\frac{1}{\rho}\right]_\Gamma\mathbf{n}_\Gamma & \text{if } \phi^{n+1} < 0 \end{cases} \tag{2.48}$$

$\dot{m}^n$ is known from the previous iteration, developed in equation (2.63). Afterwards, the velocity is computed the same way in the vapor:

$$\mathbf{v}_{\text{vap}}^* = \begin{cases} \mathbf{v}^* - \dot{m}^n\left[\frac{1}{\rho}\right]_\Gamma\mathbf{n}_\Gamma & \text{if } \phi^{n+1} > 0 \\ \mathbf{v}^* & \text{if } \phi^{n+1} < 0 \end{cases} \tag{2.49}$$

Then, the pressure field is computed:

$$\text{If } \phi > 0,\ \nabla\cdot\left(\frac{\nabla p^{n+1}}{\rho_{\text{liq}}^{n+1}}\right) = \frac{\nabla\cdot\mathbf{v}_{\text{liq}}^*}{\Delta t} \tag{2.50a}$$

$$\text{If } \phi < 0,\ \nabla\cdot\left(\frac{\nabla p^{n+1}}{\rho_{\text{vap}}^{n+1}}\right) = \frac{\nabla\cdot\mathbf{v}_{\text{vap}}^*}{\Delta t} \tag{2.50b}$$

$$\left[p^{n+1}\right]_\Gamma = \sigma\kappa \tag{2.50c}$$

The final velocity field is then corrected with the pressure gradient:

$$\mathbf{v}^{n+1} = \mathbf{v}^* - \frac{\Delta t}{\rho}\left(\nabla p^{n+1} - \left(\sigma\kappa - \dot{m}^2\left[\frac{1}{\rho}\right]_\Gamma\right)\delta_\Gamma\mathbf{n}_\Gamma\right) \tag{2.51}$$

Velocity and pressure fields have been obtained by solving the mass and momentum equations. Tanguy et al [102] suggest to add an extension by computing a ghost pressure field to improve precision. This step is crucial for droplets, where the mass loss can be important. However for bubbles the enhancement is expensive in computational time compared to the precision gain and will not be used in the present work.

Thermal computation

To account for the phase change, the $\mathcal{DIVA}$ solver uses the GFTSB (Ghost Fluid Thermal Solver for Boiling) developed by [56]. The energy equation is solved in both liquid and vapor phases to obtain the temperature field:

$$\text{If } \phi > 0,\ \rho_{\text{liq}} C_{p,\text{liq}} T^{n+1} - \Delta t \nabla \cdot (\lambda_{\text{liq}} \nabla T^{n+1}) = \rho_{\text{liq}} C_{p,\text{liq}} \left(T^n - \Delta t \left(\mathbf{v}_{\text{liq}} \cdot \nabla T^n_{\text{liq}} \right) \right) \tag{2.52a}$$

$$\text{If } \phi < 0,\ \rho_{\text{vap}} C_{p,\text{vap}} T^{n+1} - \Delta t \nabla \cdot (\lambda_{\text{vap}} \nabla T^{n+1}) = \rho_{\text{vap}} C_{p,\text{vap}} \left(T^n - \Delta t \left(\mathbf{v}_{\text{vap}} \cdot \nabla T^n_{\text{vap}} \right) \right) \tag{2.52b}$$

In the specific case of boiling, the system is solely composed by pure liquid and vapor, and the phase change occurs only at saturation. This situation differs from evaporation, where a pure liquid is vaporized into a mixture of gas. Therefore, for nucleate boiling, the Dirichlet condition is imposed at the interface, and the temperature is set equal to the saturation temperature $T_\Gamma = T_{\text{sat}}$ via the method developed by Gibou [103]. Let's write the heat equation in 2D, with the Dirichlet condition:

$$\begin{cases} \alpha \dfrac{\partial T}{\partial t} - \nabla \cdot (\beta \nabla T) = f \\ T_\Gamma = g \end{cases} \tag{2.53}$$

We can discretize equation (2.53) into

$$\alpha T^{n+1} - \Delta t \nabla \cdot (\beta \nabla T^{n+1}) = \alpha T^n + \Delta t f^n \tag{2.54}$$

The decomposition with finite volume method is applied on a mesh (i, j) of volume $\mathcal{V}_{i,j}$. The thermal gradient are computed at the half-mesh distance $i \pm \frac{1}{2}$ and $j \pm \frac{1}{2}$.

$$\begin{aligned} \alpha T^{n+1}_{i,j} \mathcal{V}_{i,j} - \Delta t \Bigg(& -\beta_{i,j-\frac{1}{2}} \frac{T^{n+1}_{i,j} - T^{n+1}_{i,j-1}}{\Delta y_{j-1}} \Delta x_{i-\frac{1}{2}} + \beta_{i+\frac{1}{2},j} \frac{T^{n+1}_{i+1,j} - T^{n+1}_{i,j}}{\Delta x_i} \Delta y_{j-\frac{1}{2}} + \\ & \beta_{i,j+\frac{1}{2}} \frac{T^{n+1}_{i,j+1} - T^{n+1}_{i,j}}{\Delta y_j} \Delta x_{i-\frac{1}{2}} - \beta_{i-\frac{1}{2},j} \frac{T^{n+1}_{i,j} - T^{n+1}_{i-1,j}}{\Delta x_{i-1}} \Delta y_{j-\frac{1}{2}} \Bigg) = \left(\alpha T^n_{i,j} + \Delta t f^n_{i,j} \right) \mathcal{V}_{i,j} \end{aligned} \tag{2.55}$$

If the interface crosses between (i, j) and $(i + 1, j)$, the variable $T_{i+1,j}$ is in the other phase, and the Dirichlet condition must be used. The ghost temperature is used:

$$\frac{T_{i+1,j} - T_{i,j}}{\Delta x_i} \rightarrow \frac{T^{\text{G}}_{i+1,j} - T_{i,j}}{\Delta x_i} \tag{2.56}$$

This $T^{\text{G}}_{i+1,j}$ is computed with the Dirichlet condition at the interface. Indeed, we can compute a distance ϵ of the mesh $(i + 1, j)$ from the interface:

$$\epsilon = \frac{|\phi_{i,j}|}{|\phi_{i,j}| + |\phi_{i+1,j}|} \tag{2.57}$$

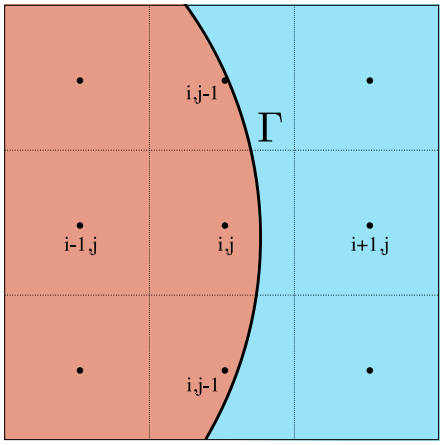

Figure 2.4: Mesh points, red is the vapor, blue the liquid

Then, a second order solution for $T^{\mathrm{G}}_{i+1,j}$ leads to

$$T^{\mathrm{G}}_{i+1,j} = \frac{T_\Gamma + (\epsilon - 1)T_{i,j}}{\epsilon} \tag{2.58}$$

The term $\frac{T_{i+1,j} - T_{i,j}}{\Delta x_i}$ in equation (2.55) becomes $\frac{T_\Gamma - T_{i,j}}{\epsilon \Delta x_i}$, and the interface temperature has been imposed. The linear system of the solver can easily handle this discretization, since we obtain symmetric matrices which are solved with efficient matrix inversion methods.

2.2.4 Extrapolations of the fields

At the liquid/vapor interface, accurate values of temperature are required for the calculation of the mass flow rate field. To have a better computation of the liquid and vapor temperature values, ghost fields are generated in the vicinity of the interface, similarly as described above. Aslam [104] developed a methodology to preserve continuity of temperature and its derivatives. Three different extrapolations can be used:

Constant extrapolation In order to create a constant extrapolation of the field g, we solve the following equation:

$$\frac{\partial g}{\partial \tau} \pm H(\pm\phi)\mathbf{n} \cdot \nabla g = 0 \tag{2.59}$$

With τ a fictitious time. If we want to extrapolate from the vapor ($\phi < 0$) to the liquid ($\phi > 0$), the $+$ sign is kept before and in the Heaviside function, and vice-versa. This equation is solved with multiple iterations until convergence is reached, and leads a field which respects the condition $\mathbf{n} \cdot \nabla g = 0$ in the vicinity of the interface. In practise, 25 iterations are ample to obtain an accurate field as shown by Tanguy et al [61], since the values far from the interface are not required. For the sake of stability, the fictitious time τ is set to $\Delta x/4$.

Linear extrapolation Similarly, linear extrapolation can be made, with constant value of the gradient. If we note $g_n = \mathbf{n} \cdot \nabla g$, we solve the following PDE:

$$\frac{\partial g_n}{\partial \tau} \pm H(\pm\phi)(\mathbf{n} \cdot \nabla g_n) = 0 \tag{2.60}$$

Again, multiple iterations lead to $\mathbf{n} \cdot \nabla g_n = 0$. The normal derivative is constant. Afterwards, the field f is extended with the following equation:

$$\frac{\partial g}{\partial \tau} \pm H(\pm\phi)\left(\mathbf{n} \cdot \nabla g - g_n\right) = 0 \tag{2.61}$$

After this step, $\mathbf{n} \cdot \nabla g = g_n$. The normal derivative is constant.

Quadratic extrapolation Quadratic extrapolation provides constant value of the 2nd order derivative $g_{nn} = \mathbf{n} \cdot \nabla^2 g$

The method is similar, at first the PDE of highest order is solved, and follow the first order derivative and then the function.

$$\frac{\partial g_{nn}}{\partial \tau} \pm H(\pm\phi)(\mathbf{n}\cdot\nabla g_{nn}) = 0 \tag{2.62a}$$

$$\frac{\partial g_{n}}{\partial \tau} \pm H(\pm\phi)\left(\mathbf{n}\cdot\nabla g_{n} - g_{nn}\right) = 0 \tag{2.62b}$$

$$\frac{\partial g}{\partial \tau} \pm H(\pm\phi)\left(\mathbf{n}\cdot\nabla g - g_{n}\right) = 0 \tag{2.62c}$$

Then, the value of g_{nn} is extended constant, g_n is linear and g quadratic along the normal $\mathbf{n}$. For the temperature field, as the first derivative is used to compute the mass flow rate, quadratic extension is used. It is defined as the difference between the input liquid thermal flux crossing the interface and the output vapor flux departing from the interface:

$$\dot{m} = \frac{-\lambda_{\text{liq}}\nabla T_{\text{liq}}\cdot\mathbf{n} + \lambda_{\text{vap}}\nabla T_{\text{vap}}\cdot\mathbf{n}}{L_{\text{vap}}} \tag{2.63}$$

The mass flow rate is extended as well to ensure its continuity at the interface. Afterwards, the interface velocity is computed with equation (2.27), and the projection algorithm starts again.

2.2.5 Discretization for the numerical schemes

Temporal discretization

Time step for the algorithm is computed to account for stability requirements for convective and capillary equations.

$$\Delta t_{\text{conv}} = \frac{\Delta x}{\max\|\mathbf{v}\|} \tag{2.64a}$$

$$\Delta t_{\text{cap}} = \frac{1}{2}\sqrt{\frac{\rho_{\text{liq}}\Delta x^3}{\sigma}} \tag{2.64b}$$

Thus, global time step Δt is

$$\frac{1}{\Delta t} = \frac{1}{\Delta t_{\text{conv}}} + \frac{1}{\Delta t_{\text{cap}}} \tag{2.65}$$

For the simulations carried out in the whole study, the viscous terms have been computed with an implicit temporal scheme [105], hence there is no time step restriction related to the viscosity.

Spatial discretization

In both liquid and vapor phases, 5th order WENO (Weighted Essentially Non-Oscillatory) schemes proposed by Borges [106] are used for convective terms and redistance algorithm, due to their stability and accuracy properties. Other spatial derivatives are computed with standard second order finite volume centered schemes. The computation of the linear systems are performed with the BBMG method (Black-Box-MultiGrid), developed by Dendy [107]. This allows to solve efficiently linear systems with highly heterogeneous coefficients. It provides accurate solutions in cases of atomizations [108]. Comparisons with other methods have been performed by MacLachan [109], and computations are shown to be faster with BBMG. In particular, the number of iterations required for convergence shows low dependency on the density jump between the phases, which is a valuable asset. Temporal integration is carried out with second order Runge-Kutta scheme coupling the temporal evolution of all the variables.

2.3 Validation case: Scriven bubble growth

Considering two-phase flows and more specifically boiling, only few analytical results can be obtained. The case described by Scriven is a classical benchmark used for the test of numerical solvers performing phase change. The development has been detailed in section 1.1, and is reminded quickly.

In the perfect case of bubble in a superheated liquid, the growth rate can be calculated with the following equation:

$$\dot{R} = \mathrm{Ja} \times f(\mathrm{Ja}) \sqrt{\frac{\alpha_{\mathrm{liq}}}{t}} \tag{2.66}$$

with $f(\mathrm{Ja})$ a function of the Jakob:

$$f(\mathrm{Ja}) = \frac{F}{2\mathrm{Ja}^2} \quad \text{with F given by} \quad \mathrm{Ja} = F \exp\left(\frac{3F}{2}\right) \int_1^\infty \frac{1}{x^2} \exp\left(-\frac{F}{x} - \frac{Fx^2}{2}\right) \mathrm{d}x \tag{2.67}$$

The solution provided by the solver has been compared to this analytical solution. The fluid considered here is water.

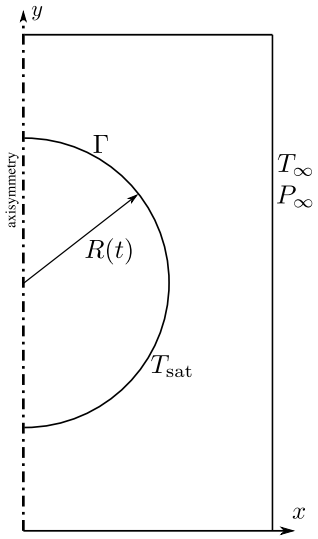

Figure 2.5: Schematic of the configuration of Scriven.

The domain considered here is 6×12 mm^2, axisymmetric. It is composed of 512×1024 cells, the grid is uniform, with cell size of 12 µm. The bubble is initiated in the middle of the domain, with constant temperature inside and at its interface. Gravity is neglected. The temperature and the pressure are imposed at the boundary of the domain. Bubble initial radius is set to $R_0 = 1$ mm. The Jakob number is set to

$$\mathrm{Ja_e} = \frac{\rho_{\mathrm{liq}} C_{p,\mathrm{liq}} (T_\infty - T_{\mathrm{sat}})}{\rho_{\mathrm{vap}} L_{\mathrm{vap}}} = 3 \tag{2.68}$$

which leads to $T_\infty = T_{\mathrm{sat}} + 0.989$ K. Numerical solving with *Matlab* of equation (2.67) gives the value $F = 3.3293$.

Then, the initial temperature is

$$T(r) = \begin{cases} T_{\mathrm{sat}} & \text{if} \quad r \leq R_0 \\ T_\infty - \frac{T_\infty - T_{\mathrm{sat}}}{\mathrm{Ja}} \times g\left(F, \frac{r}{2\sqrt{\alpha_{\mathrm{liq}} t_0}}\right) & \text{if} \quad r > R_0 \end{cases} \tag{2.69}$$

With

$$g\left(F, \frac{r}{2\sqrt{\alpha_{\mathrm{liq}} t_0}}\right) = F \exp\frac{3F}{2} \int_{\frac{r}{2\sqrt{\alpha_{\mathrm{liq}} t_0}}}^\infty \frac{1}{x^2} \exp\left(-\frac{F}{x} - \frac{Fx^2}{2}\right) \mathrm{d}x \tag{2.70}$$

and t_0 the initial theoretical time at which the bubble is generated,

$$t_0 = \frac{R_0^2}{4F^2 \alpha_{\mathrm{liq}}} \tag{2.71}$$

A velocity field is also initiated. It is purely radial:

$$v_r(r) = \begin{cases} 0 \quad \text{if} \quad r \leq R_0 \\ \dfrac{R_0^2}{r^2}\dfrac{dR}{dt}(t_0) \quad \text{if} \quad r > R_0 \end{cases} \tag{2.72}$$

The initial rate of growth is

$$\frac{dR}{dt}(t_0) = F\sqrt{\frac{\alpha_{\text{liq}}}{t_0}} \tag{2.73}$$

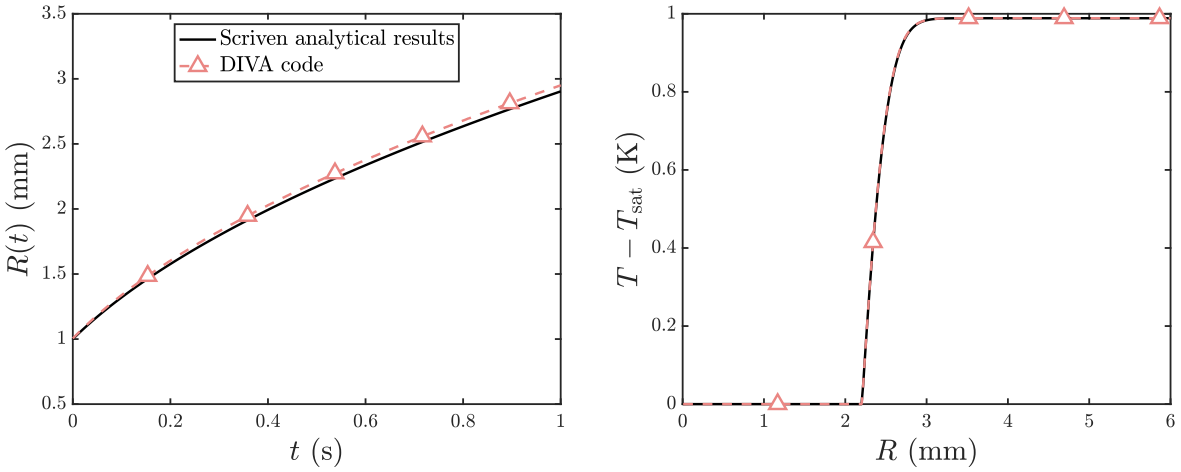

Figure 2.6: Evolution of the bubble radius and temperature field at 0.5 s. The radius has been ajusted on the right plot. Mesh size is 12 µm.

The results of the simulations are shown in figure 2.6. The match on the bubble radius is excellent, even for long time ranges. In this specific case, as the Jakob number is quite low, the thermal layer around the interface is large and accurately solved. This can be observed on the right plot, where the temperature radial profile is perfectly captured. Therefore, the mass flow rate is well computed and the bubble growth rate is correct. This is mainly due to the quadratic extrapolation on the temperature, which provides significant improvements. With only first order extrapolation on the temperature field, Tanguy et al [61] observed up to 15% difference with analytical results at $t = 4t_0$, and the value drops to 2% or high Jakob number with quadratic extrapolation. In the present simulation for the same time, the difference is of 1.76%.

Temperature and velocity profiles are displayed on figure 2.7. The velocities are solely normal to the bubble, with very low values inside the bubble. It increases outside, in the vicinity of the interface where the boiling occurs, due to the velocity jump. In this case, a rather coarse mesh is enough to capture the bubble growth accurately since the thermal layer is thick enough to be correctly simulated. However and as mentioned, more important superheats will likely require thinner meshes.

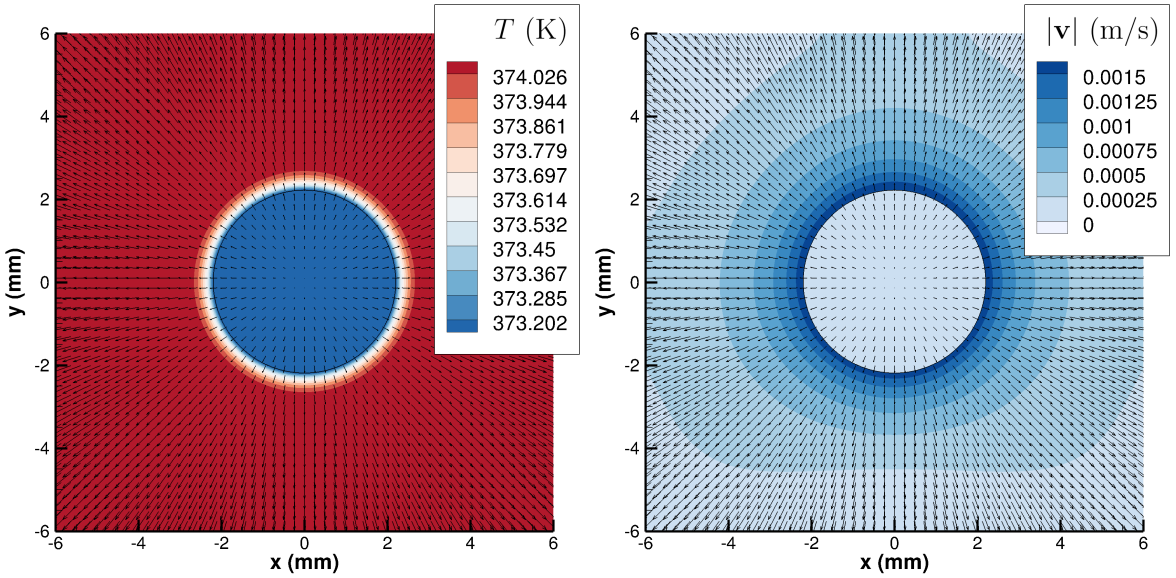

(a) (b)

Figure 2.7: Temperature and velocity fields, for $t = 0.5$ s.

2.4 Conclusion on the Numerical Methods

In this chapter, the fundamental equations and related numerical methods involved in two-phase flows with phase change have been presented.

Many numerical methods are required to capture the hydrodynamics correctly with computation. The Level-Set Method is used for the interface tracking and the curvature definition, which is crucial to be accounted for in the case of bubbles. The Ghost Fluid Method provides an accurate computation of the different fields across the liquid/vapor interface. The equations are solved with a projection algorithm coupled with the thermal solver called GFTSB. The methods described have been validated against a test case, and show good agreement.

However, these equations and methods are inadequate to account for low scale phenomena. Especially, at the contact line, the heat flux and mass flow are not modelled accurately with the equations previously presented. Micro-region models are required, and a literature study of the existing ones is provided in the next chapter.

Chapter 3

Microregion Models

Many previous studies have been performed with the DIVA solver to simulate bubble growth. It has been validated against experimental data in several conditions and particularly for nucleate boiling in normal gravity conditions [77].
However, Navier-Stokes equations applied to phase change do not account for local phenomena at the contact line. They describe the fluid behavior as long as the continuity hypothesis holds. The DNS is inadequate since mesh sizes for usual simulations are far larger than the characteristic length of the micro-region. Several studies have been carried-out, but only larger scale impacts of the micro-region can be observed, such as variations of the apparent contact angle and increase of the local heat flux in the vicinity of the contact line. Direct comparisons with experiments are therefore difficult to perform.
In order to study the global impact of the micro-region, two different models have been implemented and compared in the present chapter: Stephan's [67] and Mathieu's [68] models, which are detailed. A quick overview of Nikolayev & Janeček [69] model, which improved the initial formulation, is also provided.

Contents

3.1 Stephan's model . . . 38
3.2 Mathieu's model . . . 42
3.2.1 Perfectly-wetting fluid . . . 45
3.2.2 Partially-wetting fluid . . . 46
3.3 Janeček and Nikolayev's model: quick overview . . . 50
3.4 Parametric Analysis . . . 51
3.4.1 Impact of the microscopic contact angle . . . 51
3.4.2 Impact of the slip length . . . 52
3.4.3 Impact of the interfacial resistance . . . 53
3.4.4 Impact of the contact line velocity . . . 56
3.4.5 Impact of the shot parameter . . . 56
3.5 Conclusion on micro-region models . . . 59

3.1 Stephan's model

This model developed by Stephan & Busse [67], and derived from the equations of Wayner et al [66]. It provides a set of equations describing the motion of perfectly-wetting and non-polar fluid.

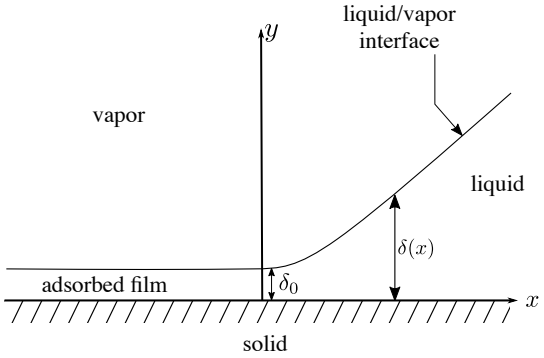

Figure 3.1: Micro-region described by Stephan & Busse [67].

For a perfectly-wetting fluid, a thin and non-evaporating liquid layer (call adsorbed film) is generated, which thickness is about few nanometers. Indeed, the London and Van der Waals intermolecular forces between the wall and the fluid can be taken into account through the disjoining pressure, which is modelled with the following equation:

$$P_d = \frac{A}{\delta^3} \tag{3.1}$$

with A the Hamaker's constant, δ the film thickness. The force associated to the disjoining pressure is inversely proportional to the cube of the film thickness, and quickly drops at the end of the micro-region. This force generates a high increase of the pressure of the fluid, which leads to variation of the saturation properties (especially of the saturation temperature) and prevents the evaporation process.

We define $\Delta P = P_{\text{vap}} - P_{\text{liq}} = \sigma\kappa - \frac{A}{\delta^3}$, with κ the curvature of the interface $\kappa = \frac{\delta''}{(1+\delta'^2)^{3/2}}$

An improvement of the model is raised by Raj [71], and includes the recoil pressure in this equation. It directly depends on the evaporation mass flow rate, and is non-negligible when the wall temperature rises. Janeček [110] estimates its influence on the apparent angle at less than 5% for 20 K superheat for water. Since the superheats considered in this thesis will be lower, we chose to neglect the vapor recoil.

The vapor pressure in the bubble is assumed constant, and the curvature negligible once the angle reaches its macroscopic value, hence we have

$$\frac{d\Delta P}{dx} = -\frac{dP_{\text{liq}}}{dx} = \frac{3A\delta'}{\delta^4} \tag{3.2}$$

On the other hand, the evaporation in the micro-region induces a liquid flow which brings fluid in the evaporating area. For a perfectly-wetting fluid, the momentum equation is simplified into the lubrication equation

$$\frac{d\Delta P}{dx} = -\frac{dP_{\text{liq}}}{dx} = -\mu_{\text{liq}}\frac{d^2v}{dy^2} \tag{3.3}$$

The equation (3.3) is integrated twice, leading to two integrating constant c_1 and c_2:

$$v(y) = \frac{1}{2\mu_{\text{liq}}}\frac{d\Delta P}{dx}y^2 + c_1 y + c_2 \tag{3.4}$$

We set no-slip boundary condition at the wall $v|_{y=0} = 0$, and slip boundary condition at the interface $\frac{dv}{dy}|_{y=\delta} = 0$. We obtain the following equation for the velocity

$$v(y) = -\frac{1}{\mu_{\text{liq}}}\frac{d\Delta P}{dx}(\frac{y^2}{2} - \delta y) \tag{3.5}$$

We assume the whole incoming liquid flow turns into vapor (the adsorbed layer does not evaporate), and then we obtain the evaporating mass flow rate by integrating equation (3.5)

$$\dot{m}_{\text{mic}} = \frac{\rho_{\text{liq}}}{\delta}\int_0^\delta v(y)\,\mathrm{d}y = -\frac{1}{3\nu_{\text{liq}}}\frac{d}{dx}\left(\delta^3\frac{d\Delta P}{dx}\right) \tag{3.6}$$

On the other hand, this evaporation mass flow can be written with a heat conduction equation applied to the liquid film. The heat flux is written as follows

$$q'' = \frac{T_{\text{w}} - T_\Gamma}{\frac{\delta}{\lambda_{\text{liq}}} + R_\Gamma} \tag{3.7}$$

With R_Γ the interfacial resistance defined by Schrage [72].

$$R_\Gamma = \frac{2-f}{2f}\frac{T_{\text{sat}}\sqrt{2\pi R_g T_{\text{sat}}}(\rho_{\text{liq}} - \rho_{\text{vap}})}{\rho_{\text{vap}}\rho_{\text{liq}}L_{\text{vap}}^2} \simeq \frac{2-f}{2f}\frac{T_{\text{sat}}\sqrt{2\pi R_g T_{\text{sat}}}}{\rho_{\text{vap}}L_{\text{vap}}^2} \tag{3.8}$$

f is the accommodation coefficient, which value is $0 \leq f \leq 1$. It accounts for the molecular effects such as reflection or emission of molecules from the liquid-vapor interface. This parameter remains of foremost importance for the calculation of the micro-region superheat and fluxes, since the dependence of the results on f is high. A specific focus is provided in section 3.4. Many experimental works have been carried-out to evaluate its value, but the compilation by Paul [111] shows wide scattering of the results for a single fluid. For instance for water, among four studies, the lowest value is 0.02 and the highest above 0.25.

Moreover, we need do define T_Γ, the local interface temperature. Indeed, its value changes due to the pressure variations. Clausius-Clapeyron relation yields

$$\left.\frac{dP}{dT}\right|_{\text{sat}} = \frac{L_{\text{vap}}\rho_{\text{liq}}\rho_{\text{vap}}}{T_{\text{sat}}(P_{\text{vap}})(\rho_{\text{liq}} - \rho_{\text{vap}})} \tag{3.9}$$

By assuming $\rho_{\text{liq}} - \rho_{\text{vap}} \approx \rho_{\text{liq}}$ as in equation (3.8), and integrating from the interface to the vapor phase,

$$\frac{P_{\text{sat}}(T_\Gamma) - P_{\text{vap}}}{T_\Gamma - T_{\text{sat}}(P_{\text{vap}})} = \frac{L_{\text{vap}}\rho_{\text{vap}}}{T_{\text{sat}}(P_{\text{vap}})} \tag{3.10}$$

From the equality of chemical potential we deduce [112]:

$$P_{\text{sat}}(T_\Gamma) = P_{\text{vap}} + \Delta P\frac{\rho_{\text{vap}}}{\rho_{\text{liq}} - \rho_{\text{vap}}} \approx P_{\text{vap}} + \Delta P\frac{\rho_{\text{vap}}}{\rho_{\text{liq}}} \tag{3.11}$$

And thus

$$T_\Gamma = T_{\text{sat}}(1 + \frac{\Delta P}{\rho_{\text{liq}}L_{\text{vap}}}) \tag{3.12}$$

The heat flux is

$$q'' = \frac{T_\mathrm{w} - T_\mathrm{sat}\left(1 + \frac{\Delta P}{\rho_\mathrm{liq} L_\mathrm{vap}}\right)}{\frac{\delta}{\lambda_\mathrm{liq}} + \frac{2-f}{2f}\frac{T_\mathrm{sat}\sqrt{2\pi R_g T_\mathrm{sat}}}{\rho_\mathrm{vap} L_\mathrm{vap}^2}} \tag{3.13}$$

We assume the whole heat flux in the micro-region contributes to evaporation ($\dot{m}_\mathrm{mic} = \frac{q''_\mathrm{mic}}{L_\mathrm{vap}}$), and thus

$$\frac{T_\mathrm{w} - T_\mathrm{sat}\left(1 + \frac{\Delta P}{\rho_\mathrm{liq} L_\mathrm{vap}}\right)}{\frac{\delta}{\lambda_\mathrm{liq}} + \frac{2-f}{2f}\frac{T_\mathrm{sat}\sqrt{2\pi R_g T_\mathrm{sat}}}{\rho_\mathrm{vap} L_\mathrm{vap}^2}} = -\frac{L_\mathrm{vap}}{3\nu_\mathrm{liq}}\frac{d}{dx}\left(\delta^3 \frac{d\Delta P}{dx}\right) \tag{3.14}$$

The equation (3.14), coupled with (3.3), leads to a fourth order differential equation coupling the local film thickness δ, its derivative δ', the local pressure ΔP, and the heat flux integrated along the wall q' such as , $q' = \int_{l=0}^{x} q''\,\mathrm{d}l$. This equation is split into four first order differential equations:

$$\begin{cases} \dfrac{\partial \delta}{\partial x} = \delta' & \text{(3.15a)} \\ \dfrac{\partial \delta'}{\partial x} = \dfrac{(1+\delta'^2)^{3/2}}{\sigma}(\Delta P - \dfrac{A}{\delta^3}) & \text{(3.15b)} \\ \dfrac{\partial \Delta P}{\partial x} = -\dfrac{3\mu_\mathrm{liq}}{\rho_\mathrm{liq} L_\mathrm{vap}}\dfrac{q'}{\delta^3} & \text{(3.15c)} \\ \dfrac{\partial q'}{\partial x} = \dfrac{T_\mathrm{w} - T_\mathrm{sat}(1 + \frac{\Delta P}{\rho_\mathrm{liq} L_\mathrm{vap}})}{\frac{\delta}{\lambda_\mathrm{liq}} + R_\Gamma} & \text{(3.15d)} \end{cases}$$

Which can be associated with the following boundary conditions:

$$\begin{cases} \delta|_{x=0} = \sqrt[3]{\dfrac{A T_\mathrm{sat}}{\rho_\mathrm{liq} L_\mathrm{vap}(T_\mathrm{w} - T_\mathrm{sat})}} & \text{(3.16a)} \\ \delta'|_{x=0} = 0 & \text{(3.16b)} \\ \Delta P|_{x=0} = \dfrac{A}{\delta_0^3} & \text{(3.16c)} \\ q'|_{x=0} = 0 & \text{(3.16d)} \end{cases}$$

Such a system can be solved with a fourth order Runge-Kutta scheme. The initial thickness of the adsorbed film is computed so that the temperature of the interface is equal to the wall temperature, therefore there is no conduction heat flux at $x = 0$. The initial curvature is set to zero. The pressure is modified by the disjoining pressure, and the integrated heat flux, by definition, is null in $x = 0$.

We can notice that the initial condition is the trivial solution of the equations, which leads to no evolution. In order to avoid it, a perturbation is set on the initial integrated heat flux and the shooting method [113] is used to search for a solution with a constant final curvature (which results in $\delta' = $ constant). The perturbation is adapted with the successive iterations of the algorithm. The variable δ' is used as an intermediate, and we prefer to use the value $\theta = \arctan \delta'$, which gives the value of the contact angle.

Figure 3.2 details the evolution of the variables $\delta, \theta, \Delta P$ and q' for three given wall temperatures. The fluid is FC-72, which properties are listed in Table C.1. The saturation conditions are chosen identical to the article of Raj et al [71]. For the first dozens nanometers, the film thickness and slopes are constant. Indeed, in the adsorbed film the saturation properties are altered since the pressure is very high due to the disjoining pressure, so that the saturation temperature is equal to the wall temperature, hence the zero heat flux in this region. Afterwards,

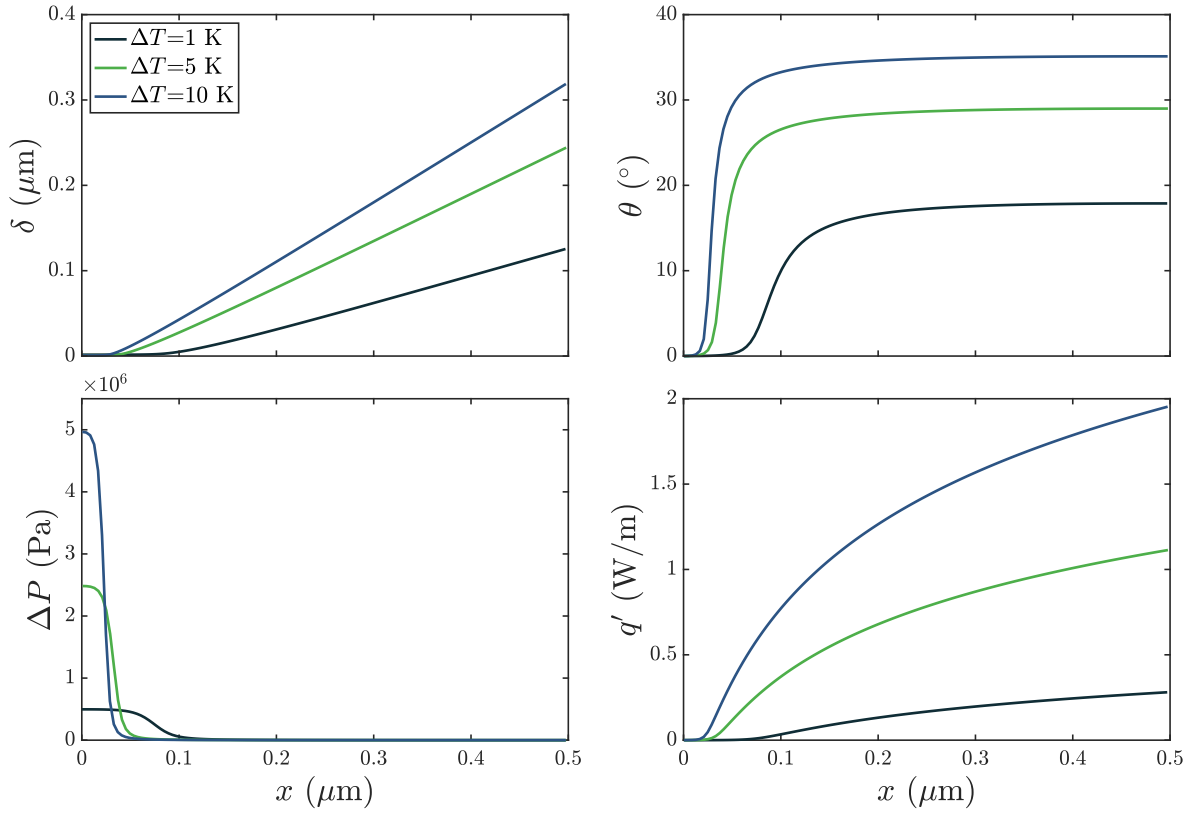

Figure 3.2: Stephan micro-region model for FC-72.

the contact angle quickly increases and leads to the increase of the film thickness. The pressure difference immediately drops because of the $\frac{A}{\delta^3}$ dependence, and the saturation properties return to the ones in the bulk vapor. The only remaining contribution is due to the curvature which is close to zero. Indeed, the contact angle quickly reaches a constant value. The integrated heat flux slows down but continuously increases, although the major contribution was brought by the first hundreds nanometers.

This model provides solutions for usual wall superheat. However, calculation for specific temperatures can last a few seconds or minutes and thus cannot be directly implemented in numerical simulations due to the computational cost enhancement. Kunkelmann [74] suggested the use of numerical correlations for both contact angle and integrated heat flux. He proposes 8th order root series interpolation, which can be resumed in equations (3.17).

$$q' = \sum_{i=1}^{8} \alpha_{q'_i} \Delta T^{1/i} \qquad \theta_{\text{app}} = \sum_{i=1}^{8} \alpha_{\theta_i} \Delta T^{1/i} \tag{3.17}$$

The present correlation with Stephan's model and applied to FC-72, for $\Delta T \in [0.1, 15]$ have been computed. The coefficient are depicted in Table 3.1. Equations for q' and θ_{app} are plotted on figure 3.3.

Table 3.1: Correlation coefficients for 8th order inverse correlation

i	1	2	3	4	5	6	7	8
$\alpha_{q'_i}$	$-1.05.10^{-1}$	$5.08.10^{1}$	$-1.50.10^{3}$	$1.34.10^{4}$	$-4.98.10^{4}$	$8.78.10^{4}$	$-7.30.10^{4}$	$2.30.10^{4}$
α_{θ_i}	4.02	$-3.29.10^{3}$	$1.36.10^{5}$	$-1.40.10^{6}$	$5.64.10^{6}$	$-1.05.10^{7}$	$9.07.10^{6}$	$-2.95.10^{6}$

The evolution of the integrated heat flux q and the apparent contact angle θ_{app} can be seen

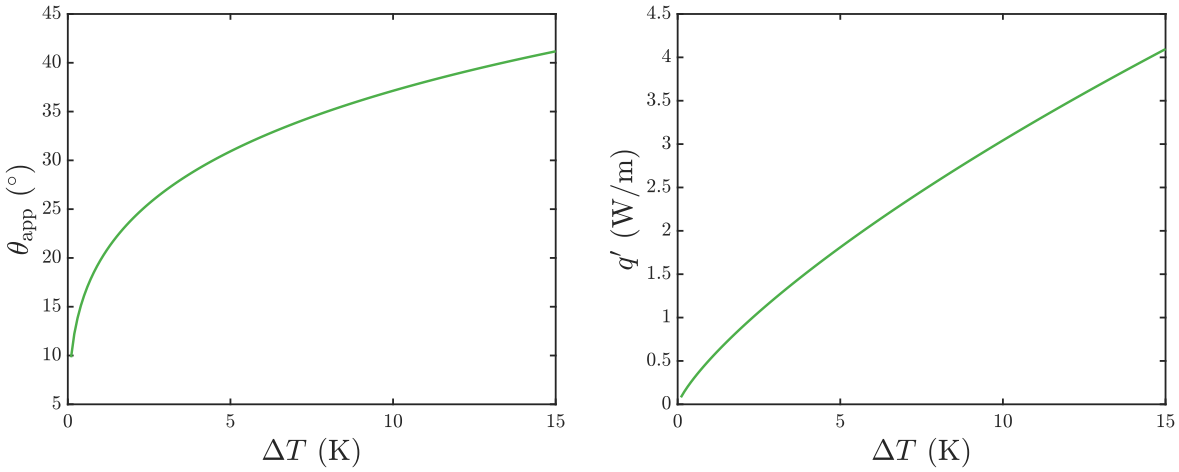

Figure 3.3: Evolution of θ_{app} (ΔT) and q' (ΔT) for Stephan's model. Fluid is FC-72, integration length 2 µm.

in figure 3.3. As one might expect, the integrated heat flux rises with the wall temperature, almost linearly. The apparent contact angle increases with the temperature as well, quickly for low temperature and slower afterwards. Indeed, a high apparent contact angle allows a liquid flow to establish and supply the mass flow rate generated by evaporation at the contact line.

This model has been improved through the years. Especially, the contact line velocity is accounted for by Batzdorf in [75].

3.2 Mathieu's model

This model developed by Mathieu [68] is an improvement of Stephan's one. It accounts for the contact line motion, and allows to study both wetting and non-wetting fluids. Thus and in order to deal with high contact angles, the lubrication equation are not used and the Stokes flow in a wedge is calculated with a stream function. The equations are henceforth integrated along the interface instead of the wall abscissa x. The new curvilinear abscissa is noted s. For a pinned contact line, the velocity component u_r and u_θ in a wedge with an angle α, are as follows [114]:

$$\begin{cases} u_r &= \dfrac{1}{r}\dfrac{q'}{\rho_{\text{liq}} L_{\text{vap}}}\dfrac{2\cos(2(\alpha-\theta)) - 2\cos(2\alpha)}{2\alpha\cos(2\alpha) - \sin(2\alpha)} & \text{(3.18a)} \\ u_\theta &= 0 & \text{(3.18b)} \end{cases}$$

For the sake of the illustration, a typical velocity field based on equations (3.18) can be observed on figure 3.4.

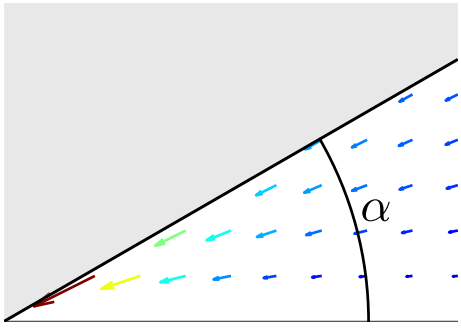

Figure 3.4: Plot of the velocity field, with only source term at the contact line.

From these equations we deduce the pressure field in the wedge:

$$P(r,\theta) = \frac{\mu_{\text{liq}}}{r^2}\frac{q'}{\rho_{\text{liq}}L_{\text{vap}}}\frac{4\cos(2(\alpha-\theta))}{2\alpha\cos(2\alpha)-\sin(2\alpha)} \tag{3.19}$$

In the vapor, the pressure is considered constant. Therefore, by deriving the previous equation along the curvilinear abscissa, and considering $\theta = \alpha$, we obtain the pressure jump variation at the interface

$$\frac{\partial \Delta P}{\partial s} = \frac{\mu_{\text{liq}}}{r^3}\frac{q'}{\rho_{\text{liq}}L_{\text{vap}}}\frac{8}{2\theta\cos(2\theta)-\sin(2\theta)} \tag{3.20}$$

Moreover, Mathieu suggests to add the contact line velocity contribution in the velocity field. If we consider an advancing wall with a velocity v_{w}, it induces two velocity components in the liquid:

$$\begin{cases} u_r &= v_{\text{w}}\dfrac{-\sin(2\alpha-\theta)+\theta\cos(2\alpha-\theta)-\sin\theta+(2\alpha-\theta)\cos\theta}{2\alpha-\sin(2\alpha)} & \text{(3.21a)} \\ u_\theta &= -v_{\text{w}}\dfrac{(2\alpha-\theta)\sin\theta-\theta\sin(2\alpha-\theta)}{2\alpha-\sin(2\alpha)} & \text{(3.21b)} \end{cases}$$

Which is illustrated by figure 3.5.

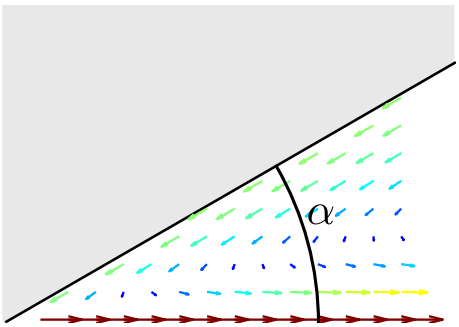

Figure 3.5: Plot of the velocity field, with an receding contact line (or advancing wall with velocity v_{w}), without phase change

Again, we can deduce the pressure field

$$P(r,\theta) = -v_{\text{w}}\frac{\mu_{\text{liq}}}{r}\frac{2\sin\theta+2\sin(2\alpha-\theta)}{2\alpha-\sin(2\alpha)} \tag{3.22}$$

Again, the derivation along s, at $\theta = \alpha$ leads to

$$\frac{\partial \Delta P}{\partial s} = v_{\text{w}}\frac{\mu_{\text{liq}}}{r^2}\frac{4\sin\theta}{2\theta-\sin(2\theta)} \tag{3.23}$$

An advancing wall with velocity v_{w} is equivalent to an receding contact line, thus $v_s = -v_{\text{w}}$. If we consider values positive for v_s when the contact line is advancing, the equation is changed into

$$\frac{\partial \Delta P}{\partial s} = -v_s\frac{\mu_{\text{liq}}}{r^2}\frac{4\sin\theta}{2\theta-\sin(2\theta)} \tag{3.24}$$

Then, the linear combination of the two contributions leads to the following equation

$$\frac{\partial \Delta P}{\partial s} = -\mu_{\text{liq}}\left(-\frac{1}{r^3}\frac{q'}{\rho_{\text{liq}}L_{\text{vap}}}f_V(\theta)+v_s\frac{1}{r^2}f_v(\theta)\right) \tag{3.25}$$

with the functions f_V and f_v:

$$f_V(\theta) = \frac{8}{2\theta\cos(2\theta) - \sin(2\theta)} \underset{\theta\to 0}{\sim} -\frac{3}{\theta^3} + o(\theta^{-3}) \tag{3.26a}$$

$$f_v(\theta) = \frac{4\sin(\theta)}{2\theta - \sin(2\theta)} \underset{\theta\to 0}{\sim} \frac{3}{\theta^2} + o(\theta^{-2}) \tag{3.26b}$$

$$r = \frac{\delta}{\sin(\theta)} \tag{3.26c}$$

Simplifications are valid for low θ values. One can notice that with this simplified formula and for a slip velocity equal to zero, we meet the results of the lubrication theory previously developed in section 3.1:

$$\frac{\partial \Delta P}{\partial s} \underset{\theta\to 0}{\sim} -\frac{3\mu_{\text{liq}}}{\rho_{\text{liq}} L_{\text{vap}}} \frac{q'}{\delta^3} \tag{3.27}$$

However, if a contact line velocity is considered, the viscous stress is found to have a non-integrable singularity. If we keep using the same equations with the no slip-boundary conditions and considering no phase change, from equation (3.25) we deduce

$$\frac{\partial \Delta P}{\partial s} = -\mu_{\text{liq}} v_s \frac{1}{r^2} \frac{4\sin(\theta)}{2\theta - \sin(2\theta)} \tag{3.28}$$

The angle θ is only curvature dependant, then,

$$\frac{\partial \theta}{\partial s} = \frac{1}{\sigma} \Delta P \tag{3.29}$$

Allowing us to write

$$\frac{\partial^2 \theta}{\partial s^2} = -\text{Ca} \frac{1}{r^2} \frac{4\sin(\theta)}{2\theta - \sin(2\theta)} \tag{3.30}$$

With $\text{Ca} = \frac{\mu_{\text{liq}} v_s}{\sigma}$ the capillary number. Equation (3.30) does not provide a consistent value for the microscopic angle, whatever the capillary number. Thus, the motion of the contact line cannot be solved using Navier-Stokes equations coupled with no-slip boundary condition.

An alternative to this modelling is suggested by Dussan, who uses the Navier's condition. Indeed, it was well known that a fluid displays no velocity against a wall (no-slip condition), hence this singularity. However refutations were brought by experiments conducted with rarefied gas, and a solution for modelling was introduced with a slip length. The fluid is supposed to slide on an artificial layer with a thickness l_s.

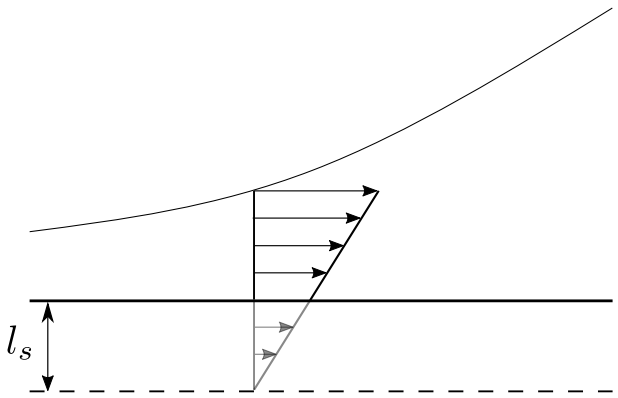

Figure 3.6: Modelling of the slip length.

The value of the slip length is usually about 1×10^{-10} m, and entails a change in the definition of r to account for this length, $r = \frac{\delta+l_s}{\sin(\theta)}$. The influence of this parameter is investigated later.

3.2.1 Perfectly-wetting fluid

For a perfectly-wetting fluid, the assumptions are similar as in Stephan's model. The fluid velocity is calculated with the evaporation mass flow equation at the micro-region scale.

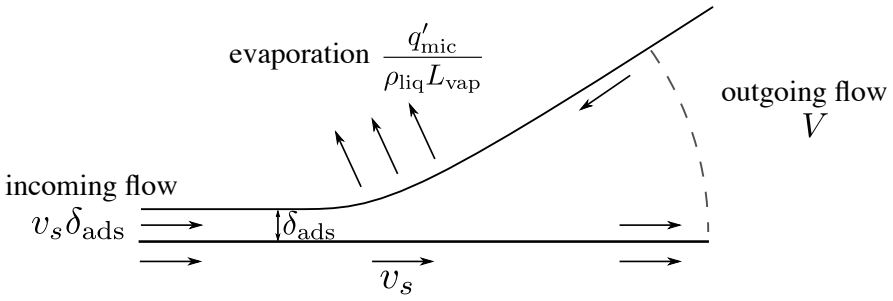

Figure 3.7: Integration of the slip velocity.

Then, the linear mass flow V is the sum of two contributions: the one from the evaporation linear heat flux q'_{mic}, and the one from the slip v_s on a film layer with a thickness δ_{ads}:

$$V = -\frac{q'_{\text{mic}}}{\rho_{\text{liq}}L_{\text{vap}}} + v_s\delta_{\text{ads}} \tag{3.31}$$

The set of equations is identical to Stephan's, with one exception on the integrated heat flux q' equation, where the liquid film thickness is $r\theta$. This allows to compute important contact angles as the lubrication theory is limited in such cases. Similarly, recoil pressure is neglected but should be considered for greater wall superheat.

The set of equations for perfectly-wetting fluid is the following:

$$\begin{cases} \dfrac{\partial x}{\partial s} = \cos(\theta) & \text{(3.32a)} \\ \dfrac{\partial \delta}{\partial s} = \sin(\theta) & \text{(3.32b)} \\ \dfrac{\partial \theta}{\partial s} = \dfrac{1}{\sigma}(\Delta P - \dfrac{A}{\delta^3}) & \text{(3.32c)} \\ \dfrac{\partial \Delta P}{\partial s} = -\mu_{\text{liq}}\left(V\dfrac{1}{r^3}f_V(\theta) + v_s\dfrac{1}{r^2}f_v(\theta)\right) & \text{(3.32d)} \\ \dfrac{\partial q'}{\partial s} = \dfrac{T_{\text{w}} - T_{\text{sat}}(1+\frac{\Delta P}{\rho_{\text{liq}}L_{\text{vap}}})}{\frac{r\theta}{\lambda_{\text{liq}}} + R_\Gamma} & \text{(3.32e)} \end{cases}$$

With the boundary conditions:

$$\begin{cases} x|_{s=0} = 0 & \text{(3.33a)} \\ \delta|_{s=0} = \delta_{\text{ads}}(1+\epsilon) & \text{(3.33b)} \\ \theta|_{s=0} = 0 & \text{(3.33c)} \\ \Delta P|_{s=0} = \Delta P_{\text{shoot}} & \text{(3.33d)} \\ q'|_{s=0} = 0 & \text{(3.33e)} \end{cases}$$

With $\delta_{\text{ads}} = \sqrt[3]{\frac{AT_{\text{sat}}}{L_{\text{vap}}\rho_{\text{liq}}(T_{\text{w}}-T_{\text{sat}})}}$, similar as Stephan's model. Likewise, an initial condition on

pressure needs to be chosen: we use the shooting method and aim a curvature equal to zero at infinity, which can be deduced from the pressure value:

$$\Delta P|_{s_{\text{ext}}} \to 0 \tag{3.34}$$

Iterations are performed to find the appropriate value of ΔP_{shoot} which fulfils the condition (3.34).

A 4th Runge-Kutta scheme is implemented to solve the system, as in section 3.1. It provides values of microscopic angle at the end of the micro-region, integrated heat flux along the interface, the pressure and the film thickness for a perfectly-wetting fluid.

It should be emphasized that the Hamaker constant A used for the disjoining pressure, as well as the accommodation coefficient f, is not precisely known for most of common fluids. The numerous experiments conducted have led to scattered values. Usually, A is chosen equal to 2×10^{-21} J. However, Mathieu highlighted the very weak influence of this parameter on the final macroscopic angle. Variation of many order of magnitude only implies a low modification of the results. As mentioned before and highlighted by Batzdorf [75], the uncertainty on f is far more impacting than on A.

However, this model can only depict the behavior of very specific surfaces, chemically treated to remove any roughness and which enable a isothermal contact angle equal to zero. Yet, this condition is not usually reached. An improvement has to be developed so as to account for a non-zero microscopic contact angle.

Quick description of the shooting method algorithm The algorithm is drawn in figure 3.8. A final integration length L_{int} is set, and an initial value on the pressure (or the parameter used for the shot) is set. The integration process begins, and is performed on intermediate lengths l_i much smaller than L_{int}. The lengths are increased along the process. The first step is to find a solution of the micro-region on a very small length, which fulfils the condition of low final curvature. As long as the initial guess has not fulfils this condition, it is changed with the secant method. Once it has, the process is repeted with a larger integration length. The intermediate values of l_i are increased until the final length L_{int} is reached and fulfils the condition on the curvature. The use of these intermediate integration lengths are of utmost importance, since the process evolution is chaotic.

3.2.2 Partially-wetting fluid

Henceforth, the previous part is modified to study a partially-wetting fluid. A triple line between solid, liquid and vapor phase is then considered. It is characterized by a microscopic contact angle; the adsorbed film vanishes, and so does the disjoining pressure.

Once the Hamaker constant and disjoining pressure removed, only the curvature can induce pressure variations; the flux in equation (3.31) is now only due to the evaporation q'; the equations are now similar as in subsection 3.2.1.

$$\begin{cases} \dfrac{\partial x}{\partial s} = \cos(\theta) & \text{(3.35a)} \\ \dfrac{\partial \delta}{\partial s} = \sin(\theta) & \text{(3.35b)} \\ \dfrac{\partial \theta}{\partial s} = \dfrac{1}{\sigma}\Delta P & \text{(3.35c)} \\ \dfrac{\partial \Delta P}{\partial s} = -\mu_{\text{liq}}\left(-\dfrac{q'}{\rho_{\text{liq}} L_{\text{vap}}}\dfrac{1}{r^3} f_V(\theta) + v_s \dfrac{1}{r^2} f_v(\theta)\right) & \text{(3.35d)} \\ \dfrac{\partial q'}{\partial s} = \dfrac{T_{\text{w}} - T_{\text{sat}}(1 + \frac{\Delta P}{\rho_{\text{liq}} L_{\text{vap}}})}{\frac{r\theta}{\lambda_{\text{liq}}} + R_\Gamma} & \text{(3.35e)} \end{cases}$$

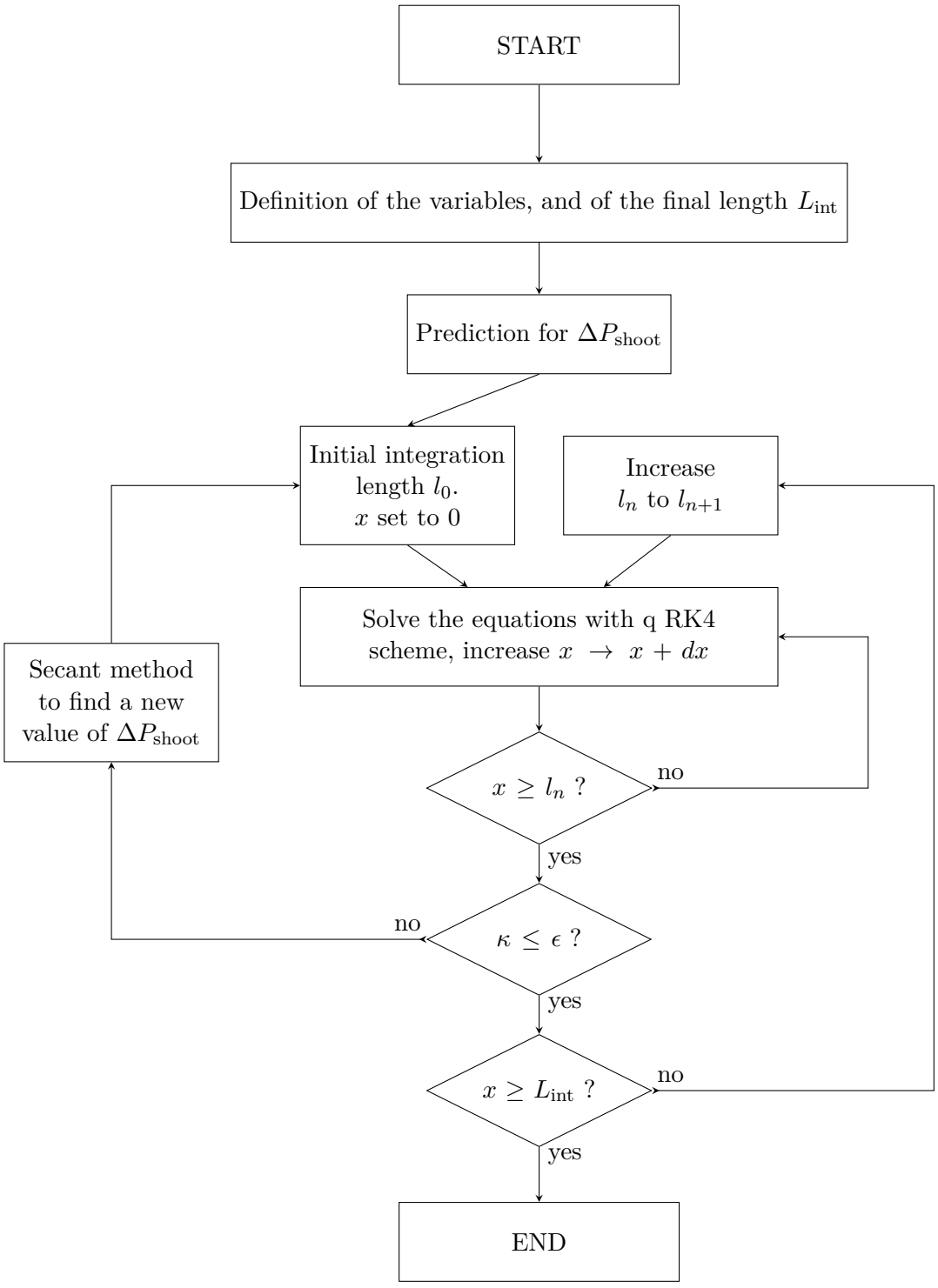

Figure 3.8: Schematic of the algorithm.

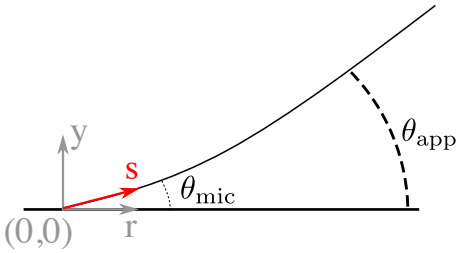

Figure 3.9: Modelling the partially-wetting fluid.

The boundary conditions are:

$$\begin{cases} x|_{s=0} = 0 & \text{(3.36a)} \\ \delta|_{s=0} = 0 & \text{(3.36b)} \\ \theta|_{s=0} = \theta_{\text{mic}} & \text{(3.36c)} \\ \Delta P|_{s=0} = \Delta P_{\text{shoot}} & \text{(3.36d)} \\ q'|_{s=0} = 0 & \text{(3.36e)} \end{cases}$$

Similarly to subsection 3.2.1, the shooting method is used to find the suitable pressure providing the constant curvature at the infinity. Indeed, the initial boundary condition of heat flux and pressure (in the case of a contact line at wall temperature) will lead to the absence of evolution as both (3.35d) and (3.35e) will remain null, as they are lineary dependant of their value. However, the boundary condition on the pressure becomes questionable. With the adsorbed film a null heat flux was required on the boundary due to the non-evaporating film, which is not the case if a contact line is considered. Moreover and similarly as the perfectly wetting fluid, the boundary conditions in terms of pressure and heat flux are solution of the overall equations: if the contact line temperature is equal to the wall temperature, we have

$$\Delta P|_{s=0} = \frac{\rho_{\text{liq}} L_{\text{vap}} (T_{\text{w}} - T_{\text{sat}})}{T_{\text{sat}}} \tag{3.37}$$

However, if several models are based on the temperature continuity at the wall [73, 70, 115], the interfacial resistance in Mathieu's model allows a finite heat flux despite the thermal singularity. Then, the boundary condition on the pressure (which is straightforwardly linked to the temperature) is set free while the boundary condition on the integrated flux is imposed to zero. The parameter used for shooting method is changed. In this case,

$$\Delta P|_{s=0} = \frac{\rho_{\text{liq}} L_{\text{vap}} (T_\Gamma|_{s=0} - T_{\text{sat}})}{T_{\text{sat}}} = \frac{\rho_{\text{liq}} L_{\text{vap}} (T_{\text{cl}} - T_{\text{sat}})}{T_{\text{sat}}} \tag{3.38}$$

With T_{cl} the interface temperature at the contact line, different from the wall temperature T_{w}. This induces the contact line heat flux

$$q''_{\text{cl}} = \frac{T_{\text{w}} - T_{\text{cl}}}{R_\Gamma} \tag{3.39}$$

Therefore, the temperature discontinuity is related to the interfacial resistance. The influence of the interfacial resistance on the heat flux and temperature at the contact line are shown further. A discussion on the influence of the shooting parameter and the initial condition is raised in part 3.4.5.

The results of Mathieu's model are plotted for $\Delta T = 5$ K in figure 3.10, considering wetting fluid ($\theta_{\text{mic}} \approx 0°$) and non-wetting fluid ($\theta_{\text{mic}} = 8°$). They can barely be distinguished. The global behavior is similar as Stephan's model, with the exception of the adsorbed film which is absent. Indeed, it can be seen in figure 3.10 that the transition from the microscopic to the

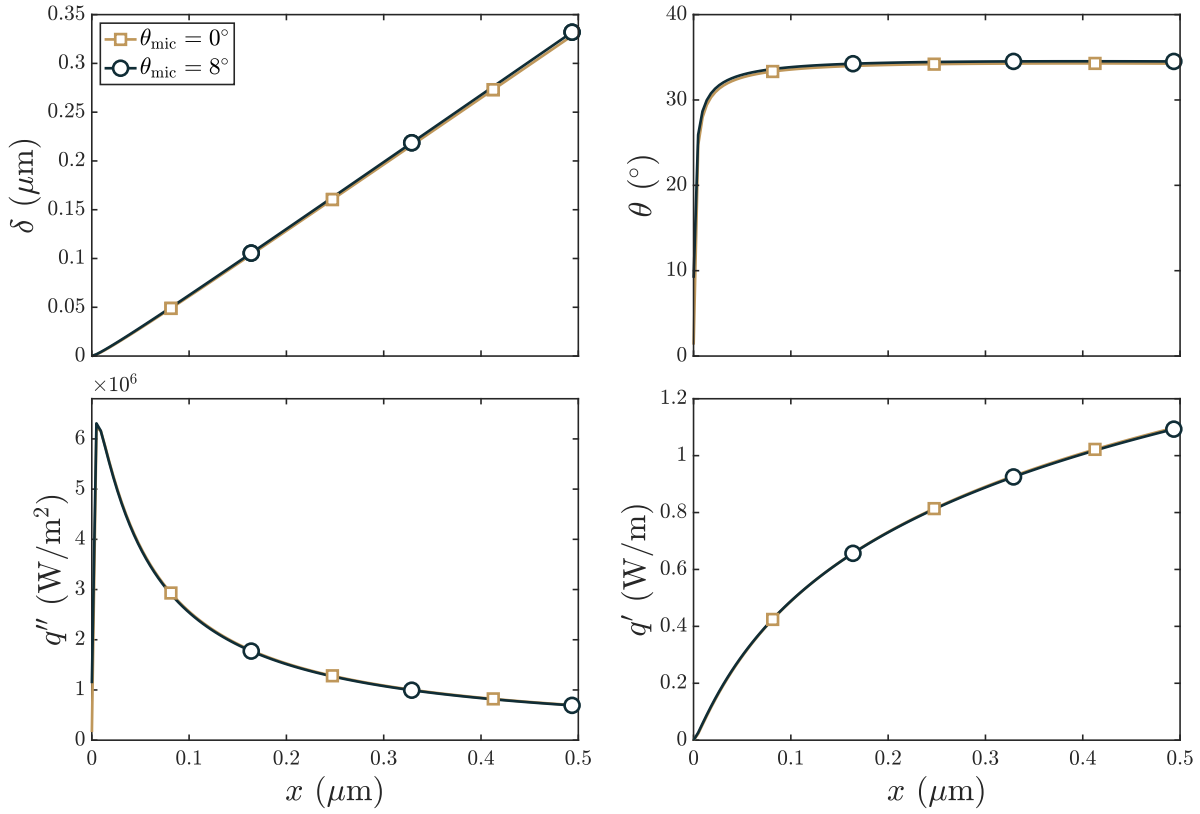

Figure 3.10: Mathieu micro-region model for FC-72, $\Delta T = 5$ K, for wetting and non-wetting microscopic angle.

macroscopic contact angle occurs in about 0.1 µm.

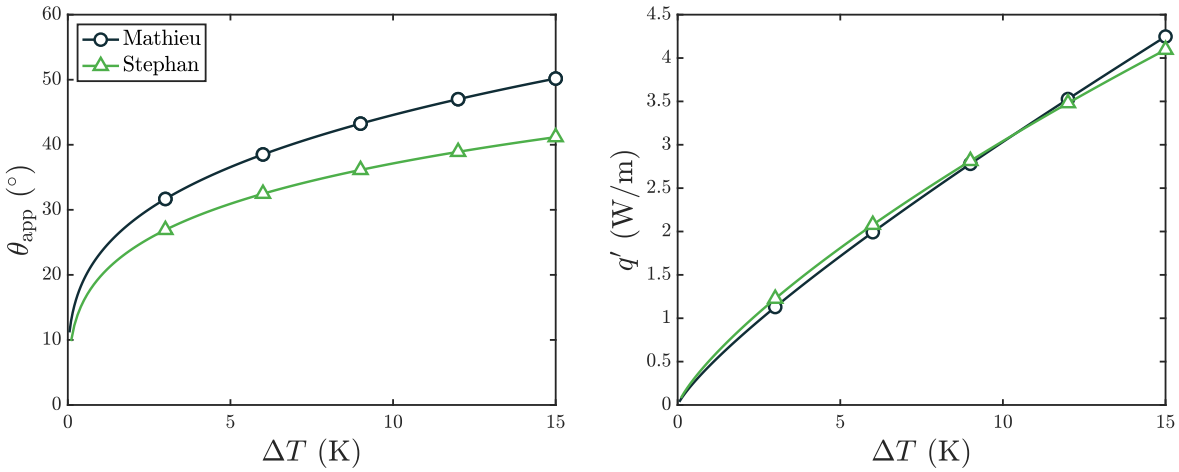

Figure 3.11: Evolution of θ_{app} (ΔT) and q' (ΔT) for Stephan and Mathieu.

The results of Stephan's and Mathieu's models are broadly equivalent in their behavior, and can be seen in figure 3.11. However the values slightly differ for the contact angle. With Mathieu's model, the increase due to the superheat is faster, and leads to 20% difference for

$\Delta T = 15$ K, whereas the integrated heat flux is almost equal for both models.

Thus, the issue is raised in what model has to be chosen for FC-72. Stephan's model has widely been studied and is commonly considered as reliable. Mathieu's is less known but more suitable for partially-wetting fluid. Moreover, one argument in favor of Mathieu's model is the thickness of the supposed adsorbed film for FC-72. Considering equation (3.16a) with $A = 2 \times 10^{-21}$ J and $f = 1$, the thickness δ_0 for a superheat of 5 K would be of 0.95 nm, which is the order of magnitude of the size of the C_6F_{14} molecule. Moreover, this value is meant to decrease with the superheat, which will be the case in the RUBI experiment. As an adsorbed film one molecule thick seems non-realistic, Stephan's model has been abandoned in favor of Mathieu's.

3.3 Janeček and Nikolayev's model: quick overview

Another model has been developed more recently by Janeček and Nikolayev [73, 110, 116, 117, 118]. The partially-wetting case is briefly presented, as it has not been implemented and studied in details. It is based on similar assumptions but adds some physical elements.

The Kelvin effect impact on the interface is slightly different, since the heat flux is directly integrated in the equation, as well as the interfacial resistance :

$$T_\Gamma = T_{\text{sat}} \left(1 + \frac{\Delta P}{\rho_{\text{liq}} L_{\text{vap}}} \right) + \frac{q''}{R_\Gamma} \tag{3.40}$$

Then, as the wall temperature is considered constant equal to T_{w}, the heat flux between the wall and the interface results in

$$q'' = \frac{\lambda_{\text{liq}} (T_{\text{w}} - T_\Gamma)}{\delta} \tag{3.41}$$

The mass flow rate can be calculated, as in Stephan's and Mathieu's models:

$$\dot{m} = \frac{q''}{L_{\text{vap}}} = \frac{1}{L_{\text{vap}}} \frac{T_{\text{w}} - T_{\text{sat}} \left(1 + \frac{\Delta P}{\rho_{\text{liq}} L_{\text{vap}}} \right)}{\frac{\delta}{\lambda_{\text{liq}}} + R_\Gamma} \tag{3.42}$$

Similarly as Stephan's model, the lubrication theory is applied as a small slope is considered along the interface. Neglected in both previous model, the Marangoni effect is considered by Nikolayev & Janeček. Indeed, since the temperature varies along the interface, so does the surface tension, with the following relation:

$$\frac{\mathrm{d}\sigma}{\mathrm{d}x} = -\gamma \frac{\mathrm{d}T_\Gamma}{\mathrm{d}x} \tag{3.43}$$

with $\gamma = \frac{\mathrm{d}\sigma}{\mathrm{d}T}$. Then, the slip length coupled with Marangoni effect, the following equation is obtained:

$$\frac{\mathrm{d}}{\mathrm{d}x} \left[\delta \left(\frac{\delta}{2} + l_s \right) \frac{\mathrm{d}\sigma}{\mathrm{d}x} + \delta^2 \left(\frac{\delta}{3} + l_s \right) \frac{\mathrm{d}\Delta P}{\mathrm{d}x} \right] = \mu_{\text{liq}} \left(v_\Gamma - \frac{\dot{m}}{\rho_{\text{liq}}} \right) \tag{3.44}$$

With v_Γ the interface velocity, which is approximated with

$$v_\Gamma(x) = v_{\text{cl}} \frac{\mathrm{d}\delta}{\mathrm{d}x} \tag{3.45}$$

Then, the interfacial pressure balance is

$$\Delta P = \sigma \kappa \tag{3.46}$$

If the superheat increases, so does the evaporation rate, and then the recoil pressure needs to be considered in equation (3.46), which leads to

$$\Delta P = \sigma\kappa + \dot{m}^2 \left(\frac{1}{\rho_{\text{vap}}^2} - \frac{1}{\rho_{\text{liq}}^2} \right) \tag{3.47}$$

Similarly as with Stephan's and Mathieu's model, a fourth order differential equation is obtained by combining all the elements presented above. The model is slightly different but uses similar assumptions. The boundary conditions have similarities with both models, as we impose an interface temperature equal to the wall temperature at the contact line (which leads to an initial condition on the pressure, detailed in [110]), and a initial heat flux equal to zero.

$$\begin{cases} y|_{x=0} = 0 & \text{(3.48a)} \\ \theta|_{x=0} = \theta_{\text{mic}} & \text{(3.48b)} \\ \Delta P|_{x=0} = \dfrac{\rho_{\text{liq}} L_{\text{vap}} \Delta T}{T_{\text{sat}}} & \text{(3.48c)} \end{cases}$$

The last equation is equivalent to a zero initial heat flux, since it leads to temperature continuity. As last boundary condition, a constant slope as the outlet of the micro-region is considered, and allows to connect the interface profile at micro and macro scales. The set of equations (3.48) is valid for partial wetting, in a case where the contact line velocity is zero. The computation does not require the shooting method, since the system can be analytically solved under some assumptions, with modified Bessel functions. Again, we refer to [73] for implementation and solving details.

Comparisons have been performed by Janeček [110] for FC-72, where the model shows small deviations with Stephan's. The interest of the author in nuclear energy leads its research to use high pressure water, which will not be the case in this study. This model has not been implemented and used, since we believe the assumption of temperature continuity at the contact line is arguable. However, the addition of physical phenomena compared to other models is a valuable asset. In our case, since we only consider low superheat and pure fluids, we assume low influence of the Marangoni effect and recoil pressure on the model.

3.4 Parametric Analysis

As described previously, micro-region models use parameters which values are uncertain. The Hamaker constant for Stephan's model, the slip length for Mathieu's model, but also the accommodation coefficient or the microscopic contact angle for volatile fluids cannot be directly measured (or is difficult to measure) and remain unknown. Thus, a parametric analysis is conducted in the present chapter. The influence of the shooting parameter is also raised.

3.4.1 Impact of the microscopic contact angle

Because of the low scale nature of the microscopic contact angle, it remains difficult to measure it by experiment. Its value with zero superheat is the most accurate which can be used. Moreover, this contact angle also depend on the material surface the bubble or drop is set on. Since the validity of the value is difficult to assess, its influence on the model is investigated.

Results obtained with Mathieu's micro-model have been plotted for superheat temperatures ranging from 0 to 5 K in figure 3.12.

One can observe that the value of the microscopic contact angle has a large influence on the apparent one. However, for a 0° initial angle for both FC-72 and water, the macroscopic contact angle tends to converge toward the 10° result, and so does the flux, see figure 3.13. The higher the microscopic contact angle, the lower the influence of the superheat. For a 5 K superheat in

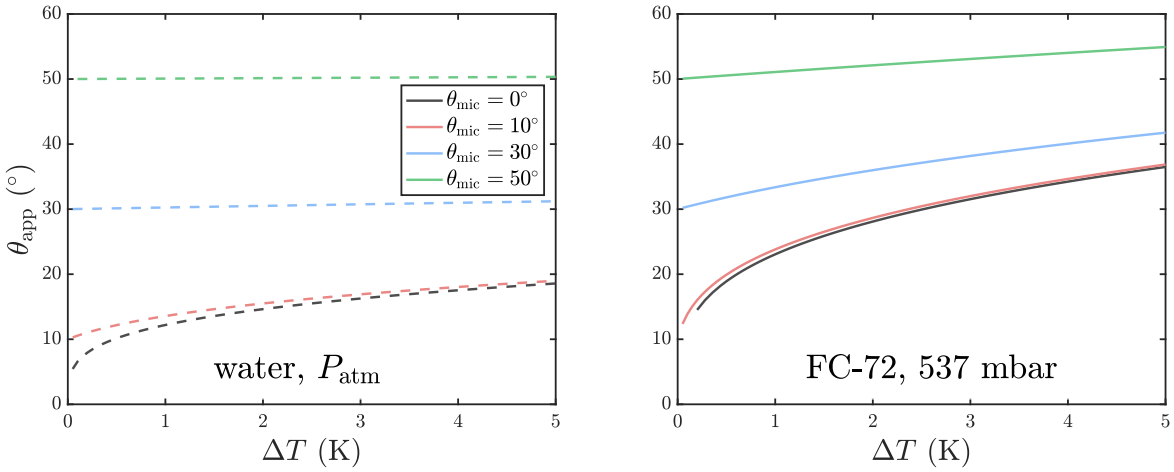

Figure 3.12: Variation of θ_{app}, for water and FC-72. Integration length is 6 μm.

the case of the 50° initial angle, the final angle is 54.3°, whereas for the same superheat and a microscopic angle of 0°, the final angle is 36.5°. The same behavior is observed with water. Therefore, Mathieu's micro-region model leads to similar results between perfectly and partially-wetting fluids with low contact angle, below ∼15° for water at ambient pressure and ∼20° for FC-72 at 537 mbar. This result has already been highlighted in figure 3.10.

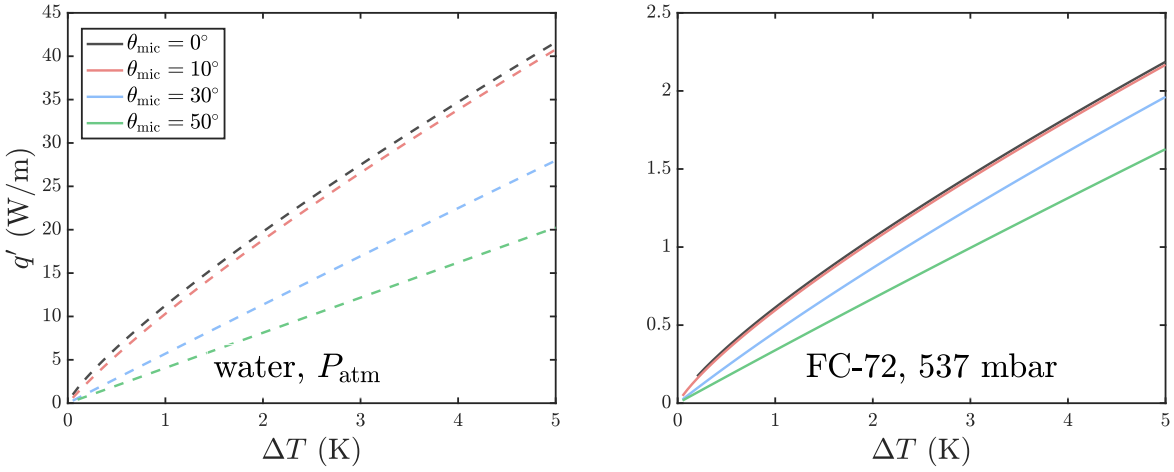

Figure 3.13: Variation of q', for water and FC-72.

This conclusion can be extended to the integrated heat flux. A higher microscopic contact angle leads to a lower heat flux whatever the fluid. With high contact angle, the interface curvature leads to the increase of the liquid film thickness. Then, the conduction heat flux decreases since the thermal gradient drops. As a consequence, the micro-region heat flux is lowered.

3.4.2 Impact of the slip length

In the micro-region model of Mathieu for a partially-wetting fluid, the slip length plays a major role as it removes the hydrodynamic singularity at the contact line, as described previously.

The influence of its value is observed in figure 3.14, the evolution of the film thickness, apparent contact angle and heat fluxes are observed. Increasing the value of the slip length reduces the local curvature for low value of s. This entails a lower value of contact angle and

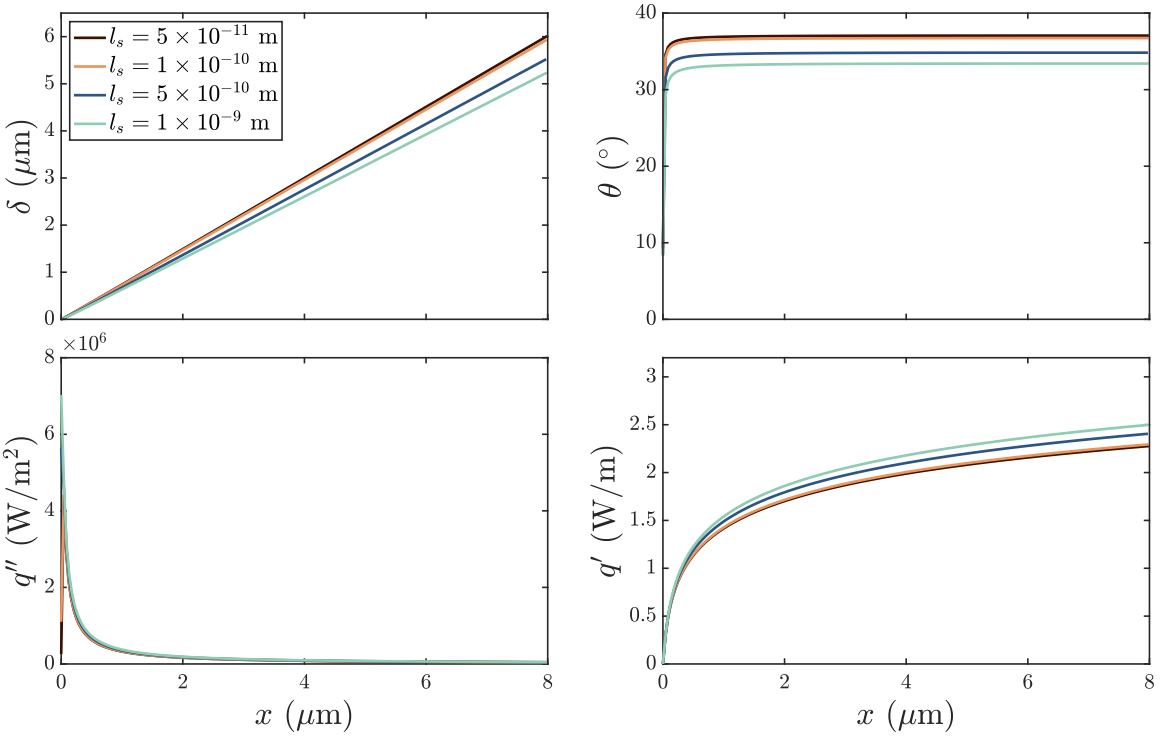

Figure 3.14: Influence of the slip length for FC-72. $f = 0.44$, $\Delta T = 5$ K

higher heat flux. For values below $l_s = 0.1$ nm, the final results of all fields considered become independent of l_s. Therefore, the slip length is chosen equal to 1×10^{-10} m, value often found in the literature, and for which dependency on the results is minimized. Mathieu also observed that a variation of several orders of magnitude on the slip length only leads to a factor two on the apparent contact angle. However and as highlighted by Mathieu, such low values of l_s provide the best fit with experimental data, but are lower than molecular dimensions. Therefore, the physical meaning of the artificial layer the slip length models is open to debate.

3.4.3 Impact of the interfacial resistance

As described in section 3.1, the interfacial resistance plays a prominent role for the micro-region modelling. It is highly dependent on the accommodation coefficient, which illustrates the fraction of the molecules crossing the interface due to vaporization.

In figure 3.15, the interfacial resistance seen as a resistive fluid thickness is plotted. It can be noticed that low values of f lead to high resistance. An accommodation coefficient of 0 would indicate a perfect reflection of the particles on the interface, hence an infinite resistance. Then, it appears that this parameter is critical in the model.

However, this value is not perfectly known and difficult to measure experimentally. Evaporation coefficients are compiled by Paul [111] for several fluids. However, values for FC-72 have not be found in the literature. Figure 3.16 displays the influence of the accommodation coefficient for three different values.

For a given contact line superheat, it can be noticed that variations in the evaporation coefficient do not deeply alter the integrated heat flux contrary to the apparent contact angle. A factor 4 for this coefficient entails 10% difference on the integrated heat flux for a 10 K superheat whereas the apparent contact angle changes from 45° to 30°, hence a 50% difference. However, this major difference in the contact angle entails variations in the bubble shape, which

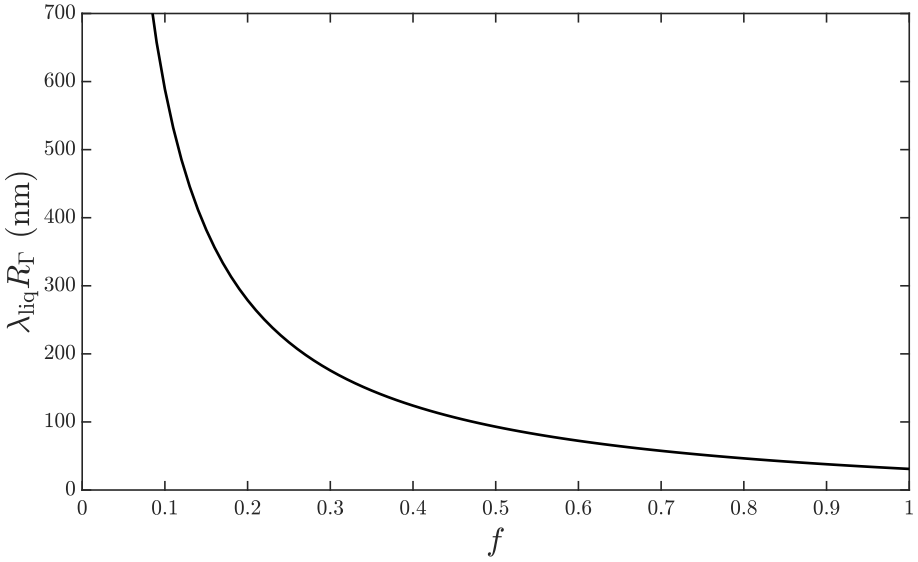

Figure 3.15: Equivalent fluid thickness of the interfacial resistance R_Γ for FC-72

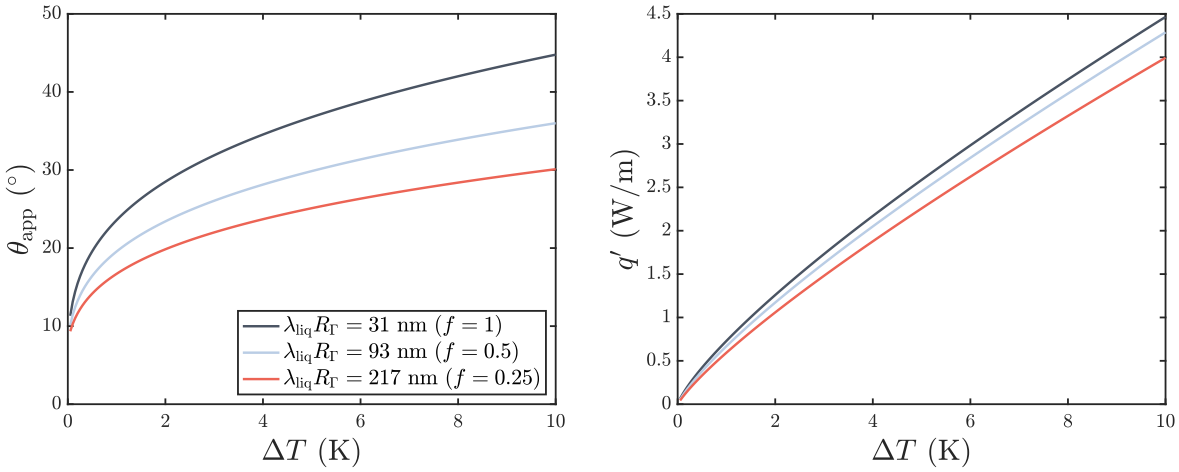

Figure 3.16: Influence of the interfacial resistance on the macroscopic angle and heat flux. Fluid is FC-72, 537 mbar, integration length is 16 µm, $\theta_{\mathrm{mic}} = 8°$

implies a different growth dynamic.

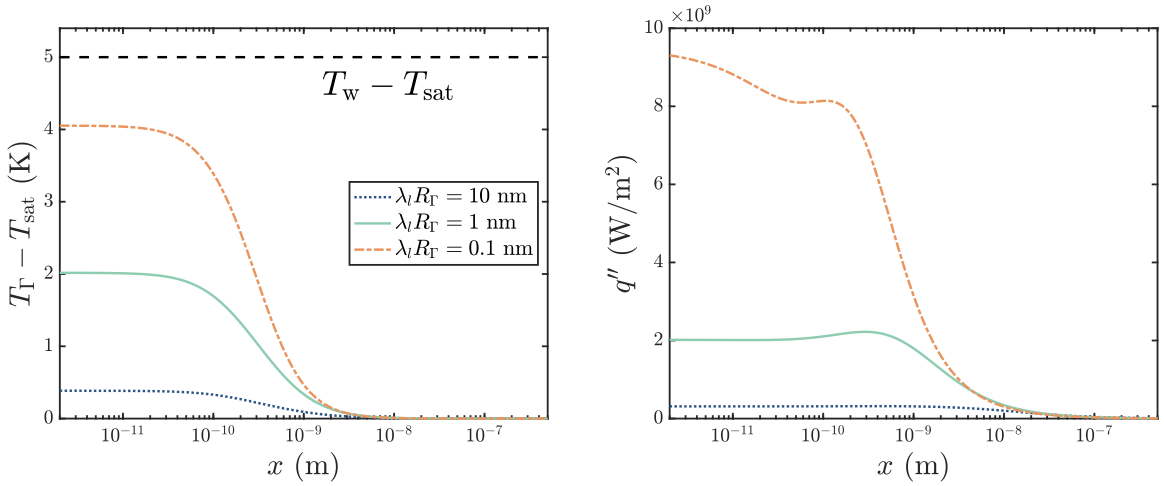

Figure 3.17: Temperature and heat flux evolution at nanoscale. Water, $\Delta T = 5$ K, $\theta_{mic} = 30°$, P_{atm}, $l_s = 0.1$ nm.

In figure 3.17, the temperature of the contact line can be observed as highly dependent on the interfacial resistance. The lower this resistance, the higher the Kelvin effect. As a consequence, the temperature difference between the interface and the wall is reduced, but the heat flux at the contact line is increased.

With a zero interfacial resistance, the interface temperature would tend to the imposed wall temperature, and there would not be a thermal discontinuity anymore.

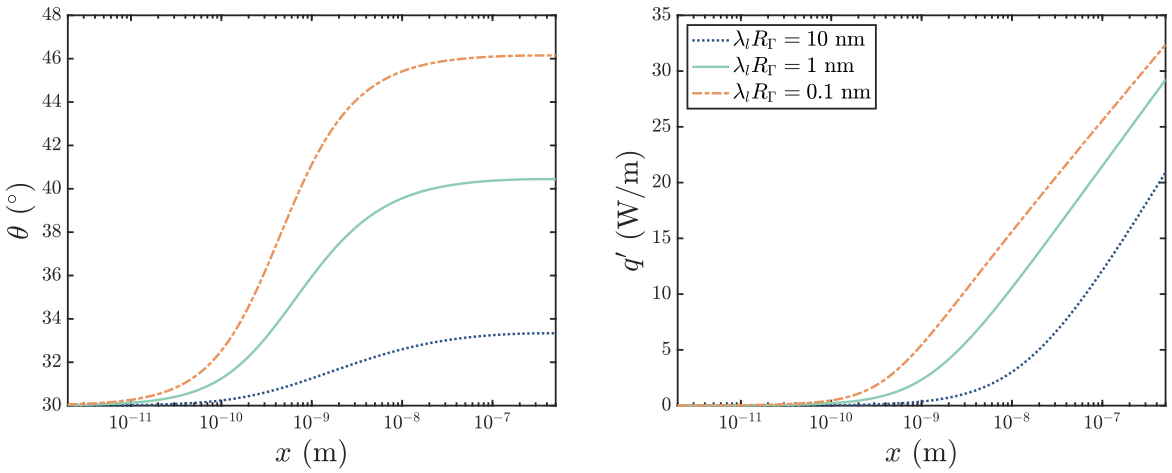

Figure 3.18: Contact angle and integrated heat flux evolution. Same configuration as 3.17

With the increase of integrated heat flux, the contact angle also becomes greater. The outcome of the model, for a 30° microscopic contact angle, displays large differences depending on the value of R_Γ. Between 0.1 nm and 10 nm, the values varies from 46° to 33°, see figure 3.18, left. This entails large differences on the integrated heat flux as well, up to 50% between the two limit cases considered here.

Thus, the interfacial resistance is a parameter of uppermost importance in the integrated model since it induces large variations on the apparent contact angle and heat flux. However, it must be noted that the values considered in this part are intentionally chosen low. Indeed for water with the usual equation (3.8), $\lambda_{liq} R_\Gamma$ the minimum computational value is 31 nm, reached

for $f = 1$. Therefore, the interfacial resistance is never be considered as zero. The influence in the global DNS evolution would be considered further in this manuscript.

3.4.4 Impact of the contact line velocity

As mentioned earlier, the model can account for the contact line velocity in equation (3.32d).

In most of the cases that will be presented in this thesis, we are investigating in the equilibrium state of a bubble, where the contact line is expected to be static. During the growth process in micro-gravity and under low superheat, the contact line velocity is low and is neglected.

However, it is important to highlight that the contact line velocity is expected to be high is some specific configurations. Especially, for cases of high superheat with water, a micro-layer is generated and the dewetting could be very fast. These cases will be quickly tackled in chapter 6.

In the present part, its impact on the local model is investigated.

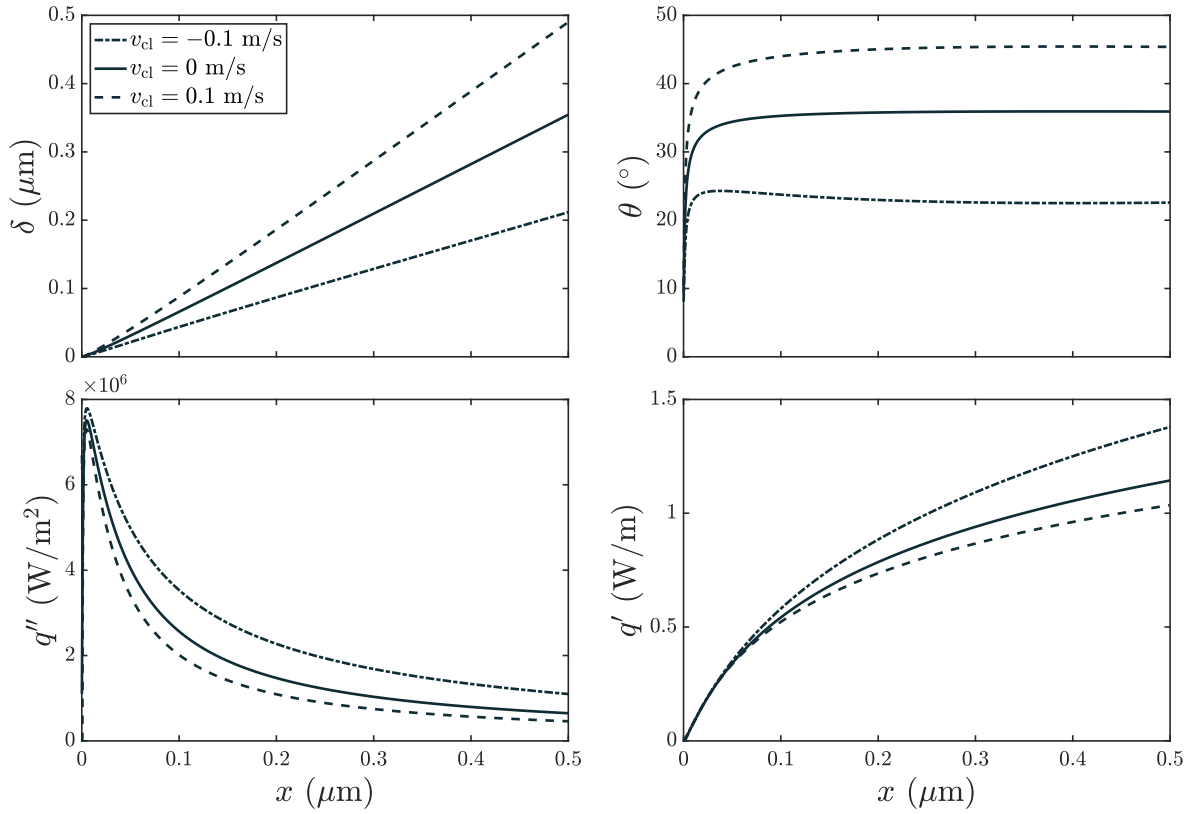

Figure 3.19: Influence of the contact line velocity for FC-72. ΔT=5 K, $f = 1$, $\theta_{mic} = 8°$

One can observe in figure 3.19 that the apparent contact angle is highly dependent on the contact line velocity. For a ΔT of 5 K, the difference between -0.1 m/s and 0.1 m/s is of more than 20°. On the other hand, the heat flux variation is low, especially for advancing contact line (positive velocity). Receding contact line only slightly decreases the heat flux.

Then, the velocity strongly impacts the contact angle. This would have a major influence on micro-layer configurations where high velocity and high superheat are encountered.

3.4.5 Impact of the shot parameter

For the computation of the micro-region model, the shooting method is used to satisfy one boundary condition at the outlet of the micro-region ($\theta = \theta_{app} =$ constante, or $\kappa = 0$).

In Stephan's model, the adsorbed film generates a pressure so that the interface temperature equals the wall temperature. A perturbation is induced on the integrated heat flux to avoid the zero trivial solution. Since the disjoining pressure is not considered with Mathieu's model, no explicit boundary condition on the pressure is set.

As a consequence, two assumptions are available:

- as with Stephan's model, we can assume the continuity between the wall and the interface temperature at the contact line. The pressure is imposed $\Delta P|_{s=0} = \frac{\rho_{\text{liq}} L_{\text{vap}} (T_{\text{w}} - T_{\text{sat}})}{T_{\text{sat}}}$, and an adequate perturbation is iterated with the shooting method on the integrated heat flux at $s = 0$: $q'_{\text{shoot}} \neq 0$.
- Do not assume the temperature continuity; as a consequence we have no information on the value of the pressure at the boundary, and can perform the shooting on this parameter ΔP_{shoot}. We can therefore impose the integrated heat flux is equal to 0 at the boundary, $q'|_{s=0} = 0$. Since the pressure is not imposed, the temperature is discontinuous at the contact line but the heat flux is regulated by the interfacial resistance.

In the present section, the influence of the parameter used for the shooting method is investigated.

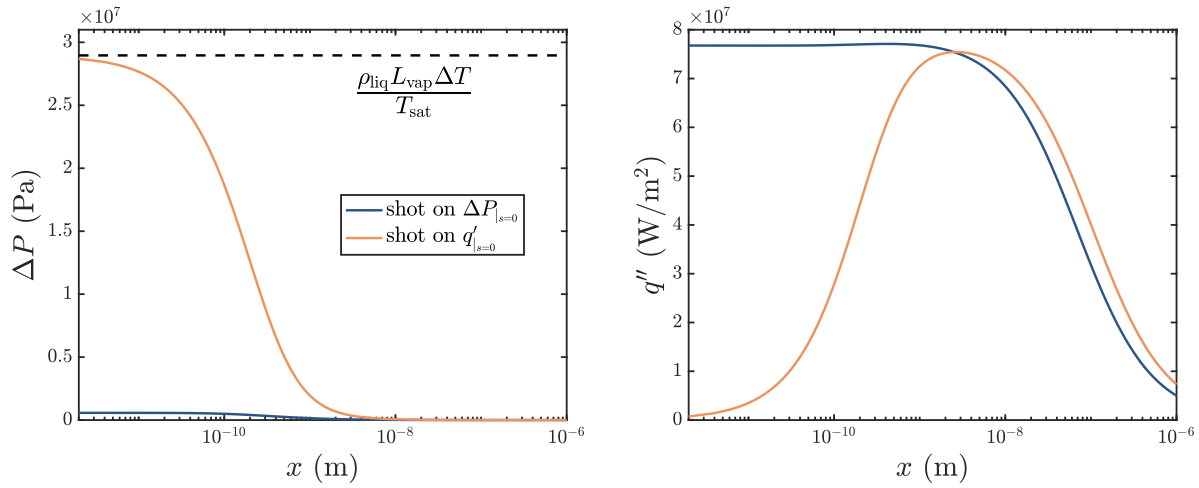

Figure 3.20: Influence of the shooting method.

In figure 3.20 is displayed the heat flux along the wall for a shot in $\Delta P|_{s=0}$ (blue) and for $q'|_{s=0}$ (orange). Both methods using different shooting parameters lead to utterly different results. Indeed, when shooting on the pressure, the boundary value $\Delta P|_{s=0}$ found is much lower than the imposed pressure when we consider that the interface is $T_\Gamma|_{s=0} = T_{\text{sat}}$. Indeed at the boundary, the pressure can be written

$$\Delta P|_{s=0} = \frac{\rho_{\text{liq}} L_{\text{vap}} (T_\Gamma|_{s=0} - T_{\text{sat}})}{T_{\text{sat}}} \tag{3.49}$$

The variation of temperature found is much smaller, and the associate heat flux is non-zero since we observe temperature discontinuity. As a consequence, since the pressure at the boundary is different, so is the temperature at the boundary is different for the two cases studied. If we impose $T_\Gamma|_{s=0} = T_{\text{w}}$, we obtain a zero heat flux initially, but the shooting method imposes a non-zero integrated heat flux with the perturbation. This perturbation may turn out to be non-negligible, whereas it should be zero by definition:

$$q'|_{s=0} = \int_{s=0}^{0} q'' \, \mathrm{d}x \tag{3.50}$$

Since the value of the initial heat flux may be important, the consistency of the shot with the boundary heat flux is arguable. Moreover, the difference in the boundary conditions entails variations on the results after the integration process. The evolution of apparent contact angle and integrated heat flux is displayed in figure 3.21.

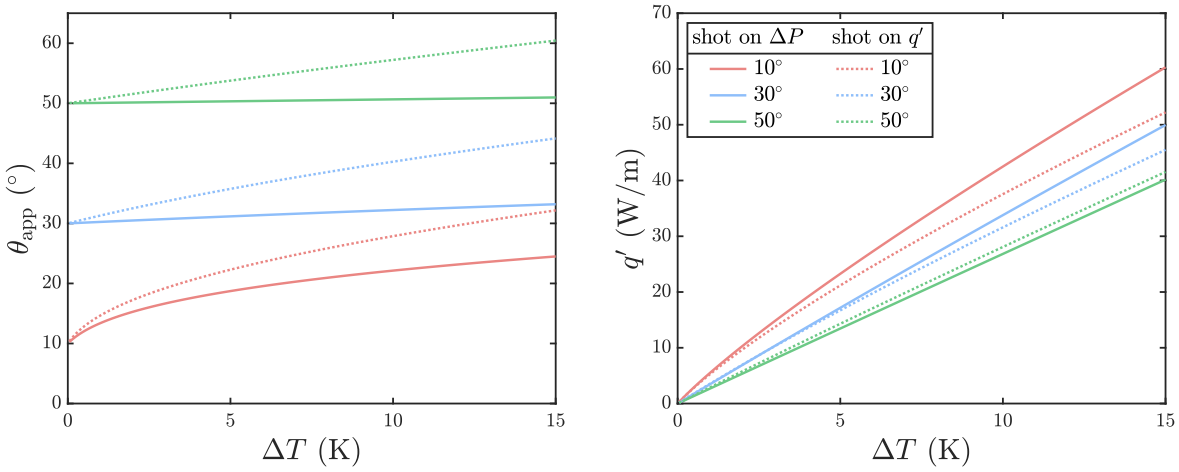

Figure 3.21: Evolution of the apparent contact angle and integrated heat flux with the superheat. Fluid is water, P_{atm}.

If the pressure is imposed at the boundary (we shoot on the integrated heat flux $q'|_{s=0}$), the much larger pressure found by the algorithm also leads to a higher curvature, and therefore a higher apparent contact angle, whatever the microscopic angle. On the other hand, the integrated heat flux variations are smaller.

Thus, the shooting method with the initial heat flux as the shooting parameter leads to greater apparent contact angle, especially for high superheat. Yet, since the boundary condition on the heat flux is found non zero (and more importantly, non negligible), we consider that considering a temperature continuity at the contact line is invalid. Since the interfacial resistance regulates the heat flux, it relaxes the potential infinite heat flux in case of temperature discontinuity. Therefore and for all the micro-region model computations, a free boundary condition for the shooting method will be set on the pressure value (hence, a free temperature at $s = 0$).

3.5 Conclusion on micro-region models

In the present chapter, different micro-region models have been described. The original model from Stephan & Busse is developed in details. Further improvements by Mathieu's, allowed to model partially-wetting fluids by the addition of several elements and modification of the computation and do not assume temperature continuity at the contact line. Afterwards, Nikolayev & Janeček made progress and added new physical elements as the Marangoni effect and link between macro and micro scales through Cox-Voinov equation for taking into account the contact line motion in the modification of the apparent contact angle. In the case of this study with pool boiling with wetting fluids, Mathieu's model will be used.

A parametric analysis has been conducted to investigate on the impact of the parameters of the model on the larger scale. Especially, the impact of interfacial resistance (through the accommodation coefficient f) has been highlighted. Major variations can be induced. The contact line velocity may also have a significant impact. However, the results displayed are theoretical. They are indeed given for a given superheat, velocity, independently from the real conditions. A coupling between the micro-region model and the DNS solver is required to determine which are the actual local superheat and contact line velocity, and therefore the real heat flux and apparent contact angle.

All the results shown above are obtained quickly. For a given fluid and specific superheat, the outputs of the model are obtained within a few minutes. However, it is much more convenient to compute the model beforehand, and to integrate it in the DNS. Next chapter will be dedicated to the coupling between a given model and the DNS solver, as a consequent computational changes are required both in the fluid and the solid domains.

Chapter 4

Micro-region coupling with DNS

A full resolution of this micro-region is not practicable for grid size considerations. Consequently, defining a suitable coupling strategy based on a subgrid resolution of this micro-region is mandatory to perform DNS of nucleate boiling in conditions where a micro-region is involved at the contact line. Several anterior studies have already proposed to couple a DNS solver with such a micro-region model [44, 119, 120, 121]. However, none of these works are fully focused on how to carry out such a non-trivial coupling. Therefore, some pending issues still remain and require additional investigations to understand clearly how this can be achieved in a consistent way.
The coupling is described, and the two majors points detailed: (i) the coupling with the heat conduction solver in the wall (ii) the coupling of the micro-region model with the mass transfer in the DNS.
This chapter is a more complete development of the article [122].

Contents

4.1 Implementation of the conjugated heat transfer 62
4.2 Micro-region coupling in the wall 64
4.3 Micro-region coupling in the fluid domain 67
4.3.1 Incorporation in a single cell at the contact line - DNS LMR 67
4.3.2 Integrated in the volumic divergence term - DNS IMR 68
4.3.3 Spread at the interface - DNS SMR 70
4.3.4 Choice of the accurate spreading length for DNS-SMR 73
4.3.5 Heat Balance in the dihedral 74
4.4 Validation case: Multiscale Boiling experiment (RUBI) 77
4.4.1 Simulation setup 77
4.4.2 Limitations of the experiment 78
4.4.3 Comparison with the experimental results 79
4.5 On the importance of the model dependency on the physical properties 82
4.5.1 Qualitative influence of the accommodation coefficient 83
4.5.2 Qualitative influence of the thermal conductivity ratio λ_w/λ_{liq} 85
4.6 Conclusion of the coupling between micro-region and DNS 87

4.1 Implementation of the conjugated heat transfer

In both nucleate boiling or evaporation of sessile droplet, the thermal field in the substrate must be solved to accurately account for the phase change. Especially, it would be shown later that the temperature of the contact line is one of the driving parameters of the overall bubble growth as the micro-region model depends on it. Therefore, it is required to solve the temperature field. The solid domain is considered static and plane, which allows to avoid using the immersed boundary method. We only compute the thermal field with the energy equation:

$$\rho_{\mathrm{w}} C_{p,\mathrm{w}} \frac{\partial T}{\partial t} = \nabla \cdot (\lambda_{\mathrm{w}} \nabla T) \tag{4.1}$$

The temperature fields are solved separately in the fluid and in the solid domains. At the fluid/solid interface Γ_{w} of normal $\mathbf{n}_{\mathrm{w}}$, the continuity of the heat flux is considered:

$$-\lambda_{\mathrm{w}} \nabla T|_{\Gamma_{\mathrm{w}},\mathrm{w}} \cdot \mathbf{n}_{\mathrm{w}} = -\lambda_{\mathrm{f}} \nabla T|_{\Gamma_{\mathrm{w}},\mathrm{f}} \cdot \mathbf{n}_{\mathrm{w}} \tag{4.2}$$

Equation (4.1) is discretized with finite volume method, and solved with a Gauss-Seidel algorithm. For the sake of the simplicity and computational cost, the wall solver is only partially parallel. The core at the bottom of the fluid domain computes the wall as well, as depicted in figure 4.1.

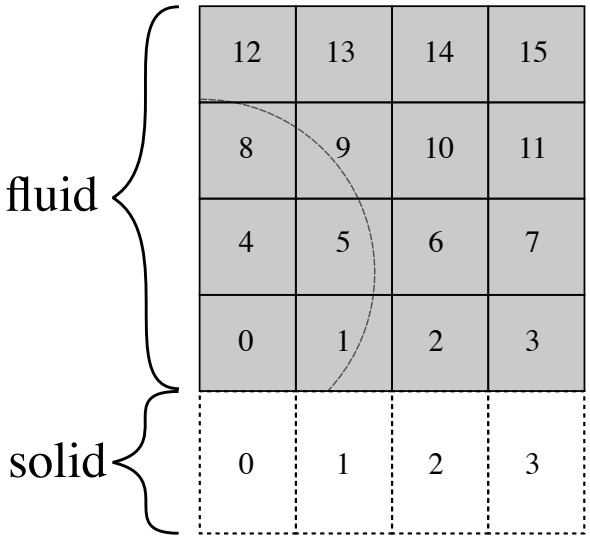

Figure 4.1: Example of a 16 cores distribution for the computation. The cores at the bottom of the fluid also handle the wall.

Thus, in 2D-axisymmetric, for a cell with coordinate index (i, j), the spatial scheme is the following:

$$\begin{aligned} -\frac{\lambda_{\mathrm{w}} r_i \Delta x_i}{\Delta y_j}(T_{i,j}^{n+1} - T_{i,j+1}^{n+1}) - \frac{\lambda_{\mathrm{w}} r_i \Delta x_i}{\Delta y_{j-1}}(T_{i,j}^{n+1} - T_{i,j-1}^{n+1}) - \frac{\lambda_{\mathrm{w}} r_{i+1/2} \Delta y_j}{\Delta x_i}(T_{i,j}^{n+1} - T_{i+1,j}^{n+1}) \\ - \frac{\lambda_{\mathrm{w}} r_{i-1/2} \Delta y_j}{\Delta x_i}(T_{i,j}^{n+1} - T_{i-1,j}^{n+1}) = \frac{\rho C_p V_{i,j}}{dt}(T_{i,j}^{n+1} - T_{i,j}^{n}) \end{aligned} \tag{4.3}$$

Which can be simplified into

$$a_{y_{i,j}}(T_{i,j}^{n+1} - T_{i,j+1}^{n+1}) + a_{y_{i,j-1}}(T_{i,j}^{n+1} - T_{i,j-1}^{n+1}) + a_{x_{i,j}}(T_{i,j}^{n+1} - T_{i+1,j}^{n+1}) + a_{x_{i-1,j}}(T_{i,j}^{n+1} - T_{i-1,j}^{n+1}) + (T_{i,j}^{n+1} - T_{i,j}^{n})\rho C_p V_{i,j} = 0 \quad (4.4)$$

The coefficients a are

$$\begin{aligned} a_{x_{i,j}} &= -\frac{\lambda_{\mathrm{w}} r_{i+1/2} \Delta y_j}{\Delta x_i} dt \\ a_{y_{i,j}} &= -\frac{\lambda_{\mathrm{w}} r_i \Delta x_i}{\Delta y_j} dt \\ V_{i,j} &= r_i \Delta x_i \Delta y_j \end{aligned} \quad (4.5)$$

dt is the time step, and r_i the radial coordinate.

Terms are reorganized:

$$T_{i,j}^{n+1}(\rho C_p V_{i,j} + a_{x_{i,j}} + a_{x_{i-1,j}} + a_{y_{i,j}} + a_{y_{i,j-1}}) - a_{y_{i,j}} T_{i,j+1}^{n+1} - a_{y_{i,j-1}} T_{i,j-1}^{n+1} - a_{x_{i,j}} T_{i+1,j}^{n+1} - a_{x_{i-1,j}} T_{i-1,j}^{n+1} = T_{i,j}^{n} \rho C_p V_{i,j} \quad (4.6)$$

This can be written under its matrix form:

$$\mathcal{A} T^{n+1} = T^n \quad (4.7)$$

With $\mathcal{A}$ a diagonally dominant matrix, which allows efficient computation with a Gauss-Seidel algorithm. In practise, the computation of the solid domain is much faster than the fluid.

The boundary conditions between the fluid and the solid domain are separated with a fluid boundary condition at the bottom ($T_{\mathrm{f},i,0}$), and a solid boundary condition at the top ($T_{\mathrm{w},i,N_y^{\mathrm{w}}+1}$). Their value is straightforward with the continuity of the flux at the solid-fluid interface and lead to the following equations

$$T_{\mathrm{f},i,0}^{n+1} = \frac{2\lambda_{\mathrm{w}}}{\lambda_{\mathrm{w}} + \lambda_{\mathrm{f}}}(T_{\mathrm{w},i,N_y^{\mathrm{w}}}^{n} - T_{i,1}^{n}) + T_{i,1}^{n} \quad (4.8a)$$

$$T_{\mathrm{w},i,N_y^{\mathrm{w}}+1}^{n+1} = \frac{2\lambda_{\mathrm{f}}}{\lambda_{\mathrm{w}} + \lambda_{\mathrm{f}}}(T_{i,1}^{n} - T_{\mathrm{w},i,N_y^{\mathrm{w}}}^{n}) + T_{\mathrm{w},i,N_y^{\mathrm{w}}}^{n} \quad (4.8b)$$

As nucleate boiling simulations involve small time steps due to the capillary time step constraint, this explicit coupling between the boundary conditions of both domains at each temporal iteration gives a satisfactory accuracy in this framework. In the previous equation, λ_{f} is the fluid thermal conductivity, which could be either liquid or vapor. In the absence of micro-region model, the contact line cell has a specific treatment, since the cell is crossed by the interface and both liquid and vapor. The value of the fluid conductivity is computed with the local level-set value,

$$\lambda_f = \begin{cases} \lambda_{liq} & \text{if } \phi_{i,0} > 0 \text{ and } \phi_{i,1} > 0 \\ \lambda_{vap} & \text{if } \phi_{i,0} < 0 \text{ and } \phi_{i,1} < 0 \\ \dfrac{\lambda_{liq}\lambda_{vap}}{\lambda_{vap} \times \xi + \lambda_{liq} \times (1-\xi)} \text{ with } \xi = \dfrac{|\phi_{i,0}|}{|\phi_{i,1}| + |\phi_{i,0}|} & \text{if } \phi_{i,0} > 0 \text{ and } \phi_{i,1} < 0 \\ \dfrac{\lambda_{liq}\lambda_{vap}}{\lambda_{liq} \times \xi + \lambda_{vap} \times (1-\xi)} \text{ with } \xi = \dfrac{|\phi_{i,0}|}{|\phi_{i,1}| + |\phi_{i,0}|} & \text{if } \phi_{i,0} < 0 \text{ and } \phi_{i,1} > 0 \end{cases} \tag{4.9}$$

These explicit boundary conditions enable to connect the solid and fluid domain accurately, in the general case. If the micro-region model is accounted for, the contact line requires a specific handling, and cannot be modelled by Fourier's law between the fluid and the wall. The modifications in the numerical scheme for the coupling with the micro-region model is described in the next section.

4.2 Micro-region coupling in the wall

The micro-region heat flux, as computed with Stephan or Mathieu's model, provides a significant contribution to the global heat flux in the bubble, within a region of size around 100 nm. Such length is too small to be simulated, since it would required even thinner mesh to be accurately captured (variations occur on the first dozens of nanometers). Therefore, the coupling at the contact line between the DNS solver and the micro-region model must be performed.

This coupling is based on the linear relation between the micro-region heat flux and the wall superheat which we chose to approximate for limited ranges of superheat. The micro-region model is integrated on a length equal to the mesh size, so that the heat flux in the contact line cell can be directly substituted by the heat flux calculated. Hence, the coupling with the current mesh can be simply implemented.

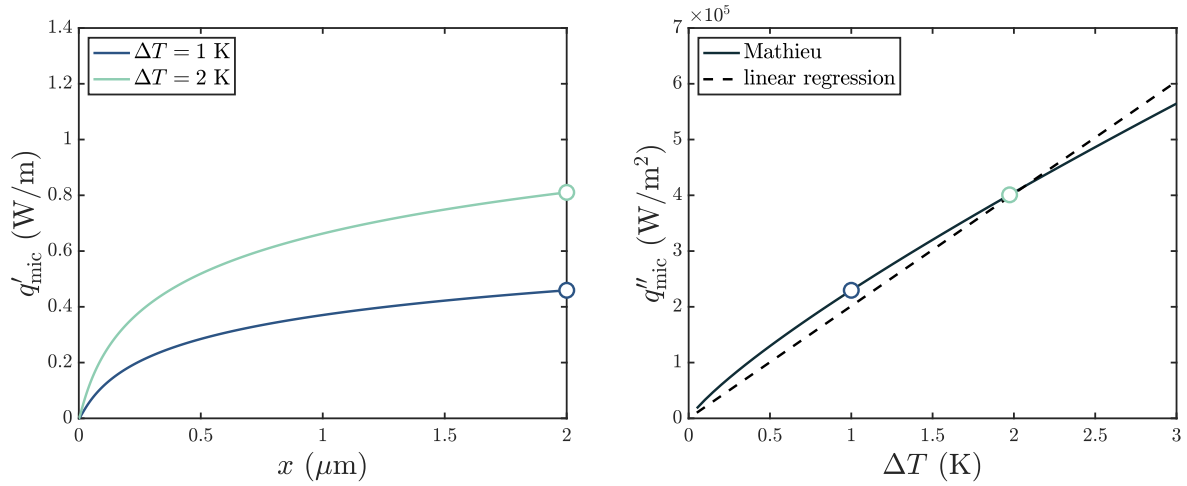

Figure 4.2: Integrated heat flux (left), and linear regression on the average heat flux (right). FC-72, 537 mbar. Integration length is $l_{mic} = 2$ µm.

As a first step, the micro-region flux has been considered a linear function of T_w, the wall temperature, if computed on short wall superheat ranges. This can be assumed on figure 4.2, where the maximal superheat is 3 K and where a linear approximation seems a good start.
We can easily link the micro-region heat flux q'_{mic}, given by the micro-region model integrated on a length l_{mic}, to the micro-region heat flux density q''_{mic}:

$$q''_{\text{mic}} = \frac{q'_{\text{mic}}}{l_{\text{mic}}} \tag{4.10}$$

As we reckon the linearity and we assume the micro-region heat flux is equal to the flux between the last solid mesh and the wall,

$$q''_{\text{mic}} = A'\Delta T + B' = AT_{\text{w}} + B \tag{4.11}$$

$l_{\text{mic}} = 2\ \mu m$		$l_{\text{mic}} = 4\ \mu m$		$l_{\text{mic}} = 8\ \mu m$	
A	B	A	B	A	B
2.0001×10^5	-6.2535×10^7	1.1829×10^5	-3.6986×10^7	6.8893×10^4	-2.1540×10^7

Table 4.1: Values of coefficients A and B of equation (4.11) for different meshes. Calculated for FC-72, 537 mbar, with a microscopic contact angle of 10°, with Mathieu's model for superheat range of 0 to 3 K.

Determining the coefficients A and B requires to perform pre-computations of the micro-region model to generate a data-base from which these coefficients can be extracted. Mathieu's model is integrated on the desired length, here chosen equal to the mesh size. Thus, the values are highly mesh-dependent. Moreover, the heat flux can be written with the temperature derivative:

$$q''_{\text{mic}} = -\lambda_{\text{w}} \left.\frac{\partial T}{\partial y}\right|_{\text{cl}} = \lambda_{\text{w}} \frac{T_{N_y^{\text{w}}} - T_{\text{w}}}{\frac{\Delta y}{2}} \tag{4.12}$$

Then, equations (4.11) and (4.12) can be merged into the following Robin condition:

$$AT_{\text{w}} + \lambda_{\text{w}} \left.\frac{\partial T}{\partial y}\right|_{\text{cl}} = -B \tag{4.13}$$

Afterwards, the wall temperature is a function of the solid cell temperature and the linear regression coefficient only.

$$T_{\text{w}} = \frac{\frac{2\lambda_{\text{w}}}{\Delta y} T_{N_y^{\text{w}}} - B}{\frac{2\lambda_{\text{w}}}{\Delta y} + A} \tag{4.14}$$

Yet, the DNS solver does not use T_{w} for the boundary condition but a solid ghost cell value in the liquid domain instead, twice as far from the last solid mesh than the wall. This is illustrated in figure 4.3. By balancing the flux,

$$q''_{\text{mic}} = \lambda_{\text{w}} \frac{T_{N_y^{\text{w}}} - T_{\text{w}}}{\frac{\Delta y}{2}} = \lambda_{\text{w}} \frac{T_{\text{w}} - T_{N_y^{\text{w}}+1}}{\frac{\Delta y}{2}} = \lambda_{\text{w}} \frac{T_{N_y^{\text{w}}} - T_{N_y^{\text{w}}+1}}{\Delta y} \tag{4.15}$$

The solution of the solid ghost cell temperature $T_{N_y^{\text{w}}+1}$ can be deduced

$$T_{N_y^{\text{w}}+1} = 2T_{\text{w}} - T_{N_y^{\text{w}}} = T_{N_y^{\text{w}}} \left(\frac{\frac{2\lambda_{\text{w}}}{\Delta y} - A}{\frac{2\lambda_{\text{w}}}{\Delta y} + A} \right) - \frac{2B}{\frac{2\lambda_{\text{w}}}{\Delta y} + A} \tag{4.16}$$

Equation (4.16) can then be written as

$$T_{N_y^{\text{w}}+1} = aT_{N_y^{\text{w}}} + b \tag{4.17}$$

With

$$a = \left(\frac{\frac{2\lambda_{\text{w}}}{\Delta y} - A}{\frac{2\lambda_{\text{w}}}{\Delta y} + A} \right) \text{ and } b = -\frac{2B}{\frac{2\lambda_{\text{w}}}{\Delta y} + A} \tag{4.18}$$

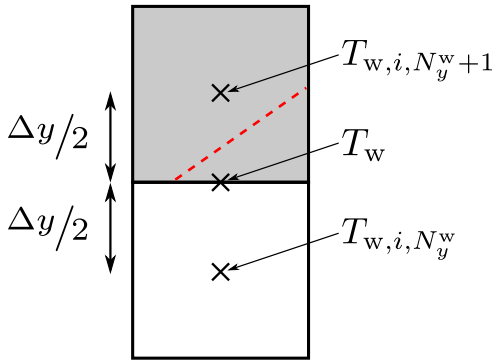

Figure 4.3: Temperature boundary condition for the wall. The interface is illustrated by the red dotted line.

	$l_{\mathrm{mic}} = 2\ \mu m$		$l_{\mathrm{mic}} = 4\ \mu m$		$l_{\mathrm{mic}} = 8\ \mu m$	
λ_{w}	a	b	a	b	a	b
1 W.m^{-1}.K^{-1}	0.667	104.2	0.617	119.6	0.568	135.1
5 W.m^{-1}.K^{-1}	0.923	24.05	0.910	28.25	0.896	32.66
50 W.m^{-1}.K^{-1}	0.992	2.491	0.991	2.945	0.989	3.427

Table 4.2: Values of coefficients a and b of equation (4.18) for different configurations of mesh and solid thermal conductivity. Calculated with coefficient of table 4.1.

The coupling between the micro-region model and the solid heat conduction solver is taken into account through the coefficients a and b which both depend on the solid thermal conductivity λ_{w} and on the coefficients A and B. In Table 4.2, some values of a and b are provided for different values of l_{mic} and λ_{w}. This demonstrates the strong influence of the solid thermal conductivity on the coefficients, and so on the ghost temperature $T_{\mathrm{w},i,N_y^{\mathrm{w}}+1}$. In particular, it is noticeable that for $\lambda_{\mathrm{w}} \to \infty$, $a \to 1$ and $b \to 0$, which means $T_{\mathrm{w},i,N_y^{\mathrm{w}}+1} \to T_{\mathrm{w},i,N_y^{\mathrm{w}}}$. This corresponds to an almost isothermal wall which is consistent with the asymptotic condition $\lambda_{\mathrm{w}} \to \infty$. On the other hand, for a given local heat flux a lower value of the solid thermal conductivity will involve larger variations in the solid temperature field. From equation (4.3), the following expression of the temperature derivative in the solid domain at the contact line can be deduced:

$$\left.\frac{\partial T_{\mathrm{w}}}{\partial y}\right|_{i,N_y^{\mathrm{w}}+1/2} = \frac{(a-1)T_{\mathrm{w},i,N_y^{\mathrm{w}}} + b}{\Delta y} \tag{4.19}$$

As this expression of the temperature derivative in the cell containing the contact line is linear, it can be directly injected in the linear system resulting from the spatial and implicit temporal discretization of equation (4.1). The modification in the discretization is described below.

$$\begin{aligned} a_{y_{i,N_y^{\mathrm{w}}}}(T_{i,N_y^{\mathrm{w}}}^{n+1} - T_{i,N_y^{\mathrm{w}}+1}^{n+1}) + a_{y_{i,N_y^{\mathrm{w}}-1}}(T_{i,N_y^{\mathrm{w}}}^{n+1} - T_{i,N_y^{\mathrm{w}}-1}^{n+1}) + a_{x_{i,N_y^{\mathrm{w}}}}(T_{i,N_y^{\mathrm{w}}}^{n+1} - T_{i+1,N_y^{\mathrm{w}}}^{n+1}) \\ + a_{x_{i-1,N_y^{\mathrm{w}}}}(T_{i,N_y^{\mathrm{w}}}^{n+1} - T_{i-1,N_y^{\mathrm{w}}}^{n+1}) + (T_{i,N_y^{\mathrm{w}}}^{n+1} - T_{i,N_y^{\mathrm{w}}}^{n})\rho C_p V_{i,j} = 0 \end{aligned} \tag{4.20}$$

Then the value of $T_{N_y^{\mathrm{w}}+1}^{n+1}$ is developed as previously

$$\begin{aligned} a_{y_{i,N_y^{\mathrm{w}}}}(T_{i,N_y^{\mathrm{w}}}^{n+1} - aT_{i,N_y^{\mathrm{w}}}^{n+1} - b) + a_{y_{i,N_y^{\mathrm{w}}-1}}(T_{i,N_y^{\mathrm{w}}}^{n+1} - T_{i,N_y^{\mathrm{w}}-1}^{n+1}) + a_{x_{i,N_y^{\mathrm{w}}}}(T_{i,N_y^{\mathrm{w}}}^{n+1} - T_{i+1,N_y^{\mathrm{w}}}^{n+1}) \\ + a_{x_{i-1,N_y^{\mathrm{w}}}}(T_{i,N_y^{\mathrm{w}}}^{n+1} - T_{i-1,N_y^{\mathrm{w}}}^{n+1}) + (T_{i,N_y^{\mathrm{w}}}^{n+1} - T_{i,N_y^{\mathrm{w}}}^{n})\rho C_p V_{i,j} = 0 \end{aligned} \tag{4.21}$$

Terms are reorganized:

$$T_{i,N_y^{\mathrm{w}}}^{n+1}\left(\rho C_p V_{i,j} + a_{y_{i,N_y^{\mathrm{w}}}}(1-a) + a_{y_{i,N_y^{\mathrm{w}}-1}} + a_{x_{i,N_y^{\mathrm{w}}}} + a_{x_{i-1,N_y^{\mathrm{w}}}}\right) - a_{y_{i,N_y^{\mathrm{w}}-1}} T_{i,N_y^{\mathrm{w}}-1}^{n+1} - a_{x_{i,N_y^{\mathrm{w}}}} T_{i+1,N_y^{\mathrm{w}}}^{n+1} - a_{x_{i-1,N_y^{\mathrm{w}}}} T_{i-1,N_y^{\mathrm{w}}}^{n+1} = T_{i,N_y^{\mathrm{w}}}^{n} \rho C_p V_{i,j} + a_{y_{i,N_y^{\mathrm{w}}}} b \quad (4.22)$$

Then, the energy balance at the contact line cell is solved by changing the local coefficients in the matrix. The contribution of the micro-region in the temperature field is solved implicitly. Afterwards, to account for the model in the fluid domain, the heat flux computed previously with the temperature field in the wall below the contact line is converted into an evaporation mass flow rate injected in the liquid domain. To assure this contribution is not counted twice, the conduction flux from the wall in the cell of the contact line is neutralized. To do so, the ghost cell of the liquid mesh below the contact line is set to T_{sat}, the temperature of the interface. Investigations showed a very weak influence of this boundary condition on the evaporation flux at the interface.

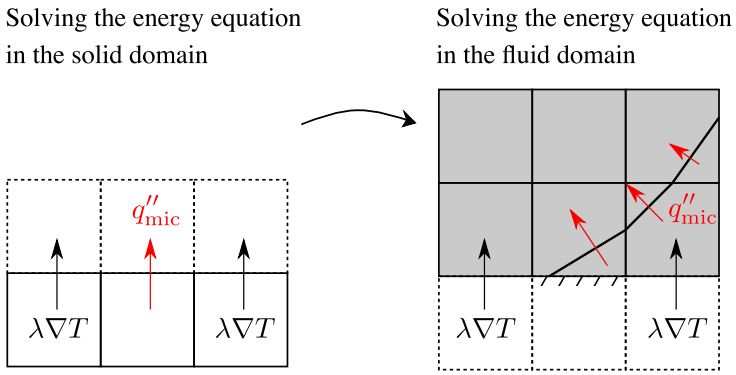

Figure 4.4: Implementation of the solid/fluid micro-region coupling. The flux is here spread near the contact line

Furthermore, the apparent contact angle can be deduced from the micro-region model as well, as can be observed in figure 3.11 since they are both function of the superheat. It is directly used in the solver, and is recalculated at every time step, providing a dynamic evolution of its value.

The first part of the coupling has been described. From now on, the difficulty lies in the handling of the fluid domain. Three different methods are described below on how to distribute the mass flux.

4.3 Micro-region coupling in the fluid domain

The heat flux, now extracted from the wall, must be redistributed in the fluid domain accurately. The most pragmatic way to account for the contribution of the micro-region flux would be to integrate the evaporation mass flow rate in the single cell of the contact line, as the micro-region size is far smaller than the smallest computed mesh. However, several attempts showed that a singularity leads to parasitic currents and discontinuities in the fields, as will be described below. Hence, different methods have been studied to alleviate these continuity issues.

4.3.1 Incorporation in a single cell at the contact line - DNS LMR

This method is the simplest but suffers from stability issues. It simply consists in substituting the computed mass flow rate in the cell of the contact line with the heat flux of the micro-region

model converted in an evaporation flux. This method is referred as DNS-LMR for Local Micro-Region model. As the micro-model is computed on a size equal to the mesh size, the substitution seems justified instead of the addition of the mass flux. Hence in the contact line cell,

$$\dot{m}_{\mathrm{cl}} = \frac{q'_{\mathrm{mic}}}{\Delta x_i L_{\mathrm{vap}}} \tag{4.23}$$

Therefore, a mass flow rate spot is generated at the contact line. From this discontinuity emerge difficulties to handle the contact line motion precisely, and to generate an accurate evaporation rate in the bubble. Especially, for high solid thermal conductivity with respect to the fluid conductivity, the mass flow rate spot is of uppermost importance and leads to numerical inconsistencies at the contact line.

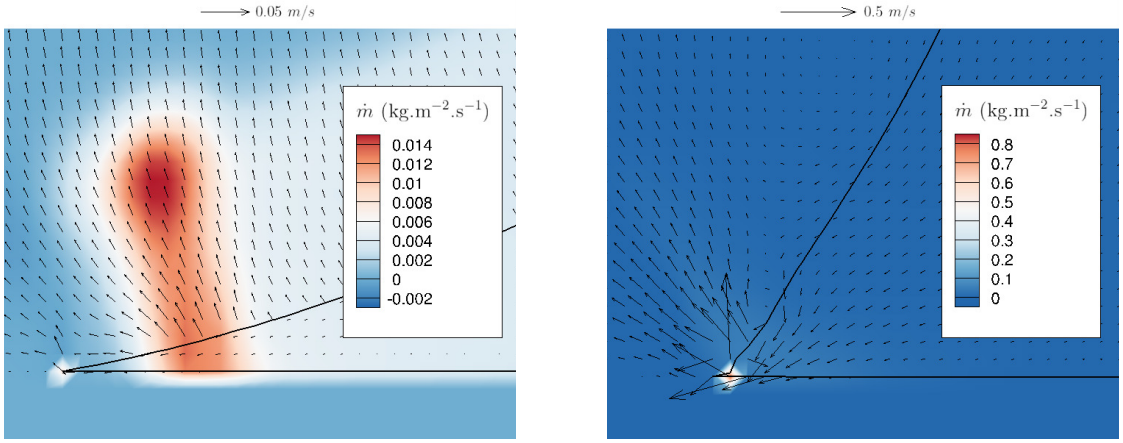

(a) $\lambda_{\mathrm{w}} = 1$ W/mK (b) $\lambda_{\mathrm{w}} = 50$ W/mK

Figure 4.5: Contact line behavior for two different solid wall conductivity
It should be emphasized that both mass flow rate and velocity scales are different. The mass flux is extrapolated away from the interface.

In figure 4.5, the contact line behavior for two different solid thermal conductivities is displayed. For low value, the micro-region contribution is small compared to the overall evaporation rate, the spot at the contact line is of the same order of magnitude as the evaporation rate computed by the DNS. The velocity field at the contact line seems not to be disturbed, as the flow resulting from the local evaporation in the contact line cell is consistent with a Stokes flow. At the opposite for a high solid thermal conductivity, the method shows erratic behavior with a contact line oscillating between adjacent cells and a contact angle not in accordance with the imposed one. The velocity field in this region is extremely unstable from an iteration to the next one hence the variable contact line position. In figure 4.5(b), one can observe a thin liquid layer close to the micro-region spot, due to numerical flaws. This behavior is regularly observed with this method coupled with high solid/liquid thermal conductivity ratio. Thus, the method is not considered as valid as the singularity of the source term causes obvious inconsistencies. By removing the thermal singularity at the contact line, we create another one. This method, obviously simple, cannot accurately describe the growth of a bubble with a micro-region model and needs to be improved.

4.3.2 Integrated in the volumic divergence term - DNS IMR

In the previous section, the source term has been injected in the contact line cell, generating a singularity. To alleviate the issue due to a single source term, the opposite method would be to consider the contribution of the microregion flux term in the whole bubble [44]. To account for

it, a source term is integrated in the divergence term of the mass balance equation. Indeed, the mass balance in the bubble allow us to write:

$$\dot{M}_\mathrm{b} = \frac{d}{dt}\iiint_{\mathcal{V}_b} \rho \,\mathrm{d}V = \iiint_{\mathcal{V}_b} \frac{\partial \rho}{\partial t} + \nabla\cdot(\rho\mathbf{V})\,\mathrm{d}\mathcal{V} \underbrace{=}_{\text{incompressible}} \rho_\mathrm{vap}\iiint_{\mathcal{V}_b} \nabla\cdot\mathbf{V}\,\mathrm{d}\mathcal{V} \tag{4.24}$$

To account for the microregion flux, we add a term in the velocity divergence term, which coincide with the mass gain due to the microregion:

$$\dot{M}_\mathrm{mic} = \frac{q'_\mathrm{mic}\times 2\pi r_\mathrm{cl}}{L_\mathrm{vap}} \tag{4.25}$$

With q'_mic in W/m of contact line. Hence $\dot{M}_\mathrm{tot} = \dot{M}_\mathrm{b} + \dot{M}_\mathrm{mic}$. The following contribution is added in the Poisson equation:

$$\dot{M}_\mathrm{tot} = \rho_\mathrm{vap}\iiint_{\mathcal{V}_b}\left(\nabla\cdot\mathbf{V} + \frac{2\pi r_\mathrm{cl} q'_\mathrm{mic}}{\rho_\mathrm{vap} L_\mathrm{vap}\mathcal{V}_\mathrm{b}}\right)\mathrm{d}\mathcal{V} \tag{4.26}$$

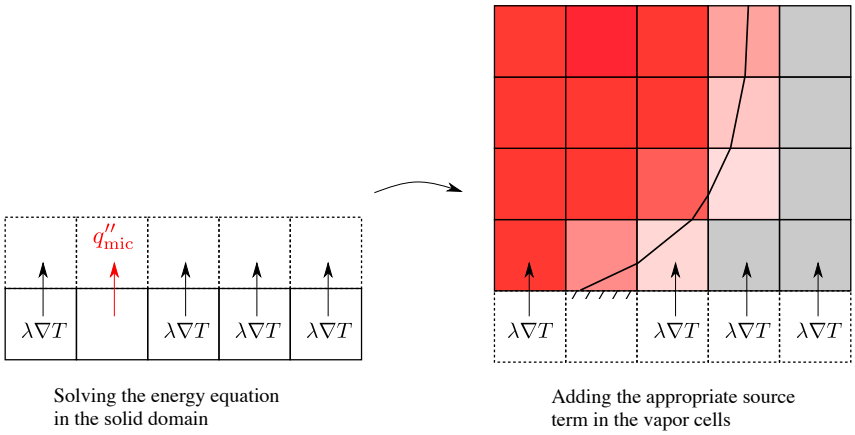

Figure 4.6: Accounting for the microregion heat flux in the vapor cells. In the red cells, the contribution is computed in accordance with the vapor fraction.

This contribution is added in the vapor cells, the value depending on the volume of the cell.

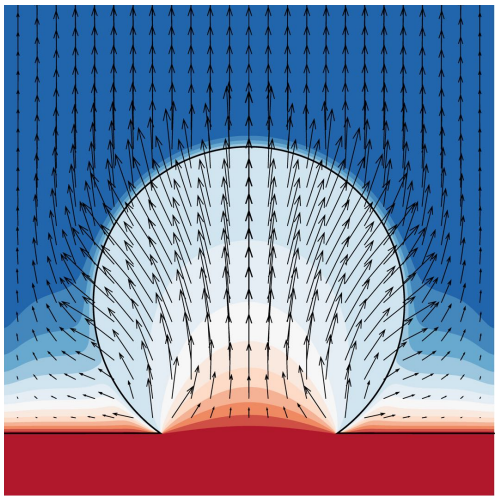

Figure 4.7: Snapshot of the bubble with divergence volume method

With this method, the microregion source term is not only accounted for in the interface cells but in the whole vapor, which makes it a much smoother process. However, the singularity of the phenomenon is entirely lost, especially the Stokes flow entails by the confined evaporation at the contact line. In figure 4.7, the velocity field is inconsistent, as the flow is generated artificially and the evaporation process generates vapor and do not withdraw liquid, which is visible by the important velocity above the bubble. The liquid is pushed off by the interface and not redirected to the contact line.

Therefore, this method is not appropriate in the analysis of the effect of the contact line and will not be studied further. Yet, it could be useful to model a less discrete source term. This coupling method will be refered in the rest of the paper as DNS-IMR for DNS with Integrated Micro-Region model.

4.3.3 Spread at the interface - DNS SMR

As both methods described in the previous subsections exhibit some deficiencies, i.e., stability issues for the first one, and the loss of local effect of the micro-region mass flow rate for the second one, we propose, in this subsection, an alternative method to overcome these shortcomings. As it has been identified that the strong spurious currents at the contact line originate from the discontinuity of the local mass flow rate along the interface, we propose to spread out the micro-region mass flow rate from the contact line to a given distance along the interface.

This can be achieved by carrying out the following steps:

- At first, a curvilinear abscissa s is defined as the distance from the contact line along the liquid/vapor interface. This field is generated, starting at the contact line and its values is 0 in every cell not crossed by the interface. As the microregion contribution is confined in a limited area, the curvilinear abscissa is not computed above a specific height. A typical field of s can be visualized in figure 4.8(a) for a given interface shape.
- Afterward, an arbitrary function of the curvilinear abscissa $u(s)$ is defined in the cells crossed by the interface, as plotted in figure 4.8(b), for instance, we chose $u(s) = e^{-\frac{s^2}{l^2}}$, with l is a given spreading length.
- The function is extended across the interface to ensure the continuity along the normal direction, as it can be observed in figure 4.8(c). This step is required for stability reasons, and is performed following the Aslam extensions [104].

For a 2D case, this procedure can be applied by defining the following smoothed $\dot{m}$,

$$\dot{m}_{\text{mic}}(s) = A_0 e^{-\frac{s^2}{l^2}}, \tag{4.27}$$

where A_0 is a normalization factor that ensured the overall conservation of the micro-region mass flow rate, such as,

$$\dot{M}_{\text{mic}} = \int_0^\infty \dot{m}_{\text{mic}}(s)\,\mathrm{d}s = \int_0^\infty A_0 e^{-\frac{s^2}{l^2}}\,\mathrm{d}s. \tag{4.28}$$

This condition leads to

$$A_0 = \frac{2\dot{M}_{\text{mic}}}{l\sqrt{\pi}} \tag{4.29}$$

This method is valid to perform a 2D computation. Its extension to axisymmetric simulations is now briefly detailed. At a first step, similarly to the curvilinear abscissa used above, a curvilinear surface S is defined on which a smoothing Gaussian function is spread. Then, the micro-region mass flux can be written as,

$$\dot{m}_{\text{mic}}(S) = A_0 e^{-\frac{S^2}{a^2}}, \tag{4.30}$$

where S is the integrated surface along the curvilinear abscissa s, defined as

$$S(s) = \int_0^s 2\pi r(s')\,\mathrm{d}s', \tag{4.31}$$

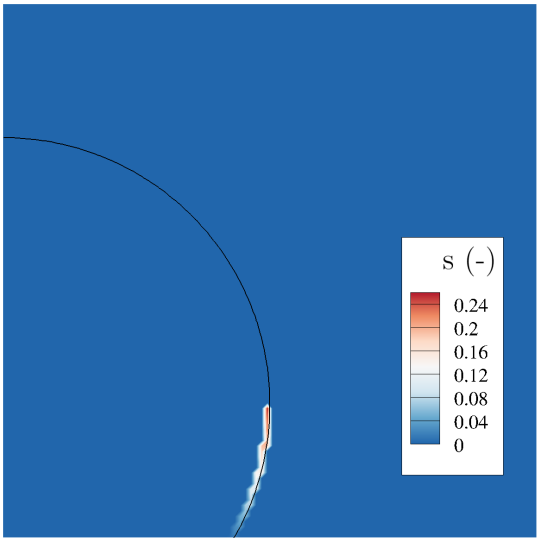

(a) Curvilinear abscissa s, without unit

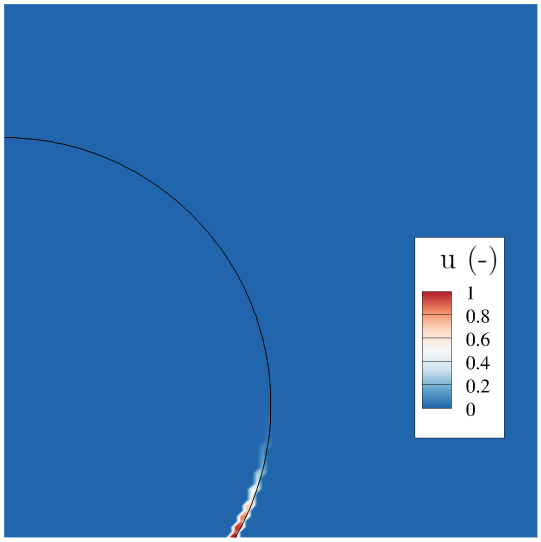

(b) Arbitrary function u, without unit

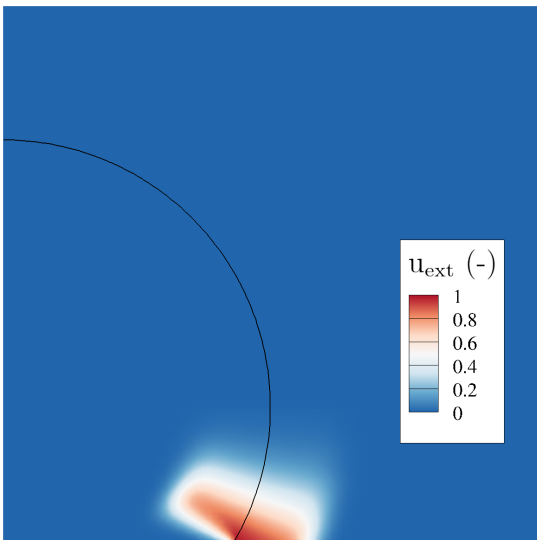

(c) Arbitrary function extended u_{ext}, without unit

Figure 4.8: Example of curvilinear abscissa and spreading function, dimensionless here

which comes from $\mathrm{d}S = 2\pi r(s)\,\mathrm{d}s$. a is an arbitrary smoothing surface expressed as $a = 2\pi r_{\mathrm{cl}} l$, with l a smoothing length similar to the 2D case, and r_{cl} the radial coordinate of the contact line. Therefore, the normalization factor A_0 is obtained from,

$$\dot{M}_{\mathrm{mic}} = \int_0^\infty \dot{m}_{\mathrm{mic}}(S)\,\mathrm{d}S = \int_0^\infty A_0 e^{-\frac{S^2}{a^2}}\,\mathrm{d}S = \frac{2\pi r_{\mathrm{cl}} q'_{\mathrm{mic}}}{L_{\mathrm{vap}}}, \tag{4.32}$$

which leads to,

$$A_0 = \frac{2\dot{M}_{\mathrm{mic}}}{a\sqrt{\pi}}. \tag{4.33}$$

In this work, the spreading surface a is taken equal to $2\pi r_{\mathrm{cl}} \times 5dx$, but this value is discussed further. With 5 mesh sizes, the micro-region mass flow rate is distributed on approximately ten cells along the interface.

The new field is now computed along the interface, and extended in the normal direction to build a continuous field in the whole computation domain. This extrapolation is carried out by solving the following PDE:

$$\frac{\partial \dot{m}_{\mathrm{mic}}}{\partial \tau} + H(\phi)\mathbf{n}.\nabla \dot{m}_{\mathrm{mic}} = 0\,. \tag{4.34}$$

In practise, this extension is only required on a few cells across the interface as the mass flow rate has no physical sense further away. Once computed, is added to the global evaporation mass flux as regularly calculated by the DNS solver. Both fields can be observed in figure 4.9.

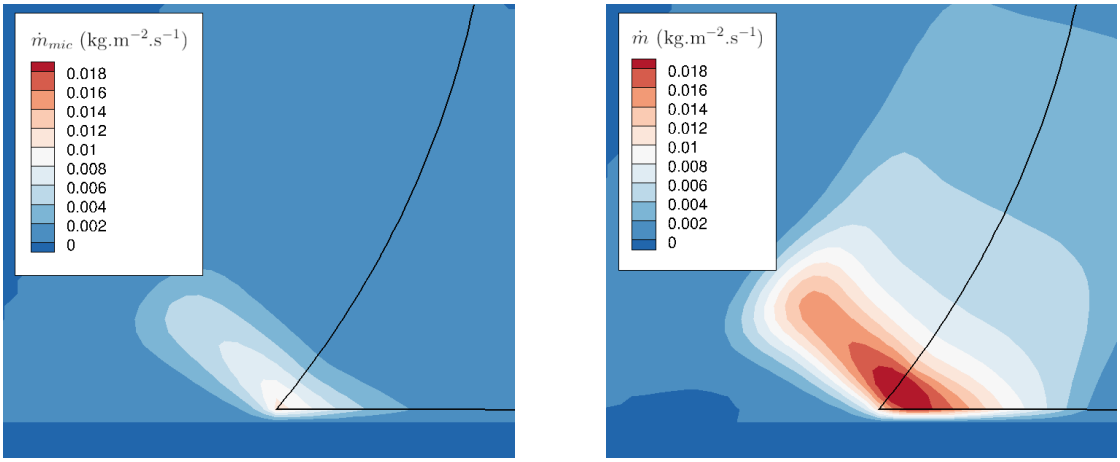

(a) Micro-region mass flow rate (b) Mass flow rate

Figure 4.9: Micro-region mass flow rate fields calculated and extended, and then added to the global mass flow rate

Different integrating surfaces have been tried to measure the influence of this parameter to the final bubble growth. This aspect is discussed further, as it is a critical criteria in terms of convergence.

Besides, one can observe in figure 4.10 that focusing the micro-region flow rate in a closer part of the contact line entails greater velocities in its region. This result is expected, as a smaller surface for the same global evaporation flux (assuming the same superheat) requires higher surfacic mass flow rate hence faster velocities of the liquid flow in the corner of the dihedral where the triple line lies. In the figure 4.10(a), the velocity field seems to be almost identical to a Stokes flow in a dihedral, with a source term in the corner. However, what can be highlighted here is the impoverishment of the global evaporation flux as computed by the micro-region model. The scattering of the flux on too few mesh cells deteriorates the precision of

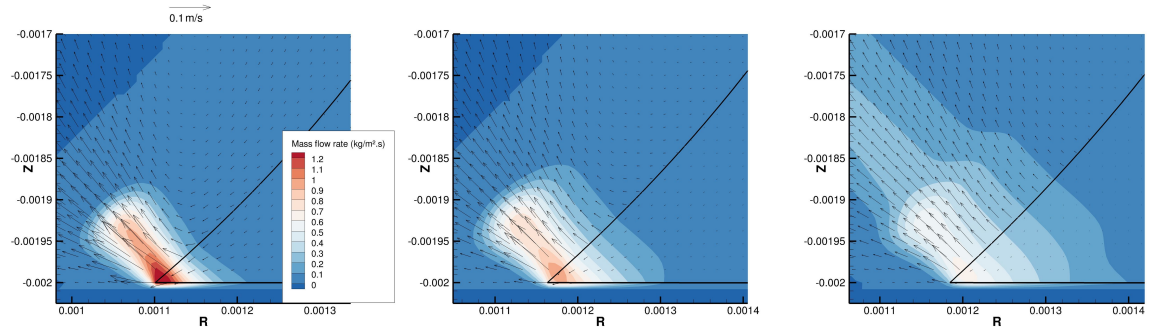

$a = 4 \times 10^{-5} \times 2\pi r_{\mathrm{cl}}$ $a = 8 \times 10^{-5} \times 2\pi r_{\mathrm{cl}}$ $a = 16 \times 10^{-5} \times 2\pi r_{\mathrm{cl}}$

Figure 4.10: Velocity and mass flow rate at the contact line for 3 different spreading surfaces. Mesh size is 8 µm.

the extension hence on the global mass flow rate. This last method will be referred as DNS-SMR for DNS with Smoothed Micro-Region model.

4.3.4 Choice of the accurate spreading length for DNS-SMR

The question of the correct surface to expand the micro-region is investigated in this part. Indeed, the physical phenomenon of the micro-region should only display an area of dozens to hundreds of nanometers, far shorter than the single mesh size used in the present simulations. On one hand, areas of 20 or 40 mesh size seems unreasonable to correctly depict the micro-region effect on the bubble growth as the local effects are lost. On the other hand, stretching the micro-region on too few cells is nearly similar to the first method described in subsection 4.3.1 and lead to numerical instabilities.

Different spreading lengths (l_{sp}) for the micro-region mass flow rate have been tried and the convergence of the computation examined.

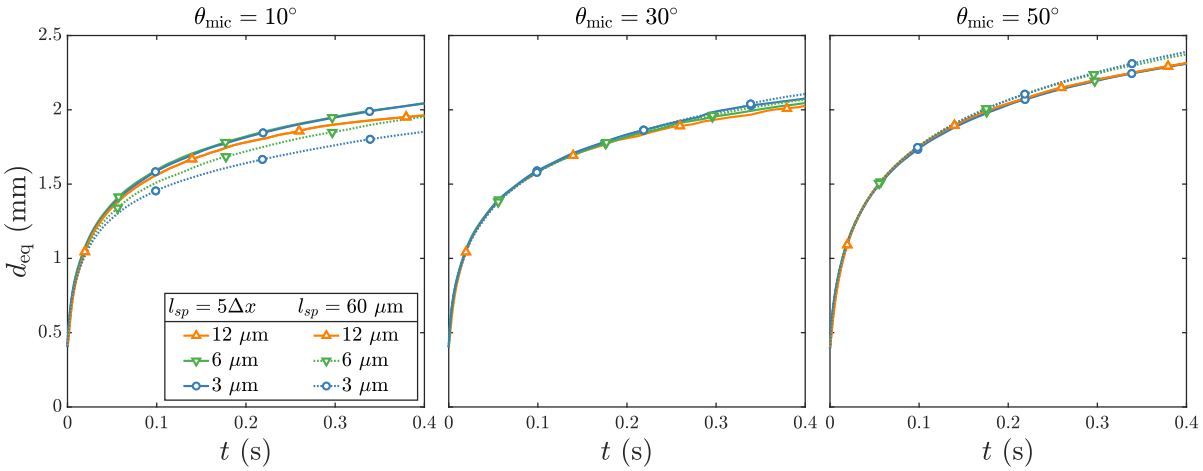

Figure 4.11: Convergence of the bubble diameter for different spreading lengths and different meshes. It should be noted that the spreading length is the same for both 12 µm simulations, and therefore the result displayed accounts for both methods.

In figure 4.11 is drawn the bubble diameter evolution for three different contact angles, for 3 consecutive meshes and with different spreading lengths. The continuous line is for constant l_{sp} in terms of **mesh number**, whereas dotted lines if for constant spreading **length**. For relatively high contact angle, the diameter evolution is almost independent of the length of spread. With

contact angle of 30 and 50°, the results are converged for 6 and 3 µm, with slightly different results between both methods.

Hence, the method with constant mesh number for the spreading length will be considered, since it provides better treatment of the singularity. Indeed, a constant length would not be fitted for the coarsest mesh, as a divergence is observed for a length of three cell size or lower. Furthermore, it appears crucial not to have a dependence on the mesh size in our results.

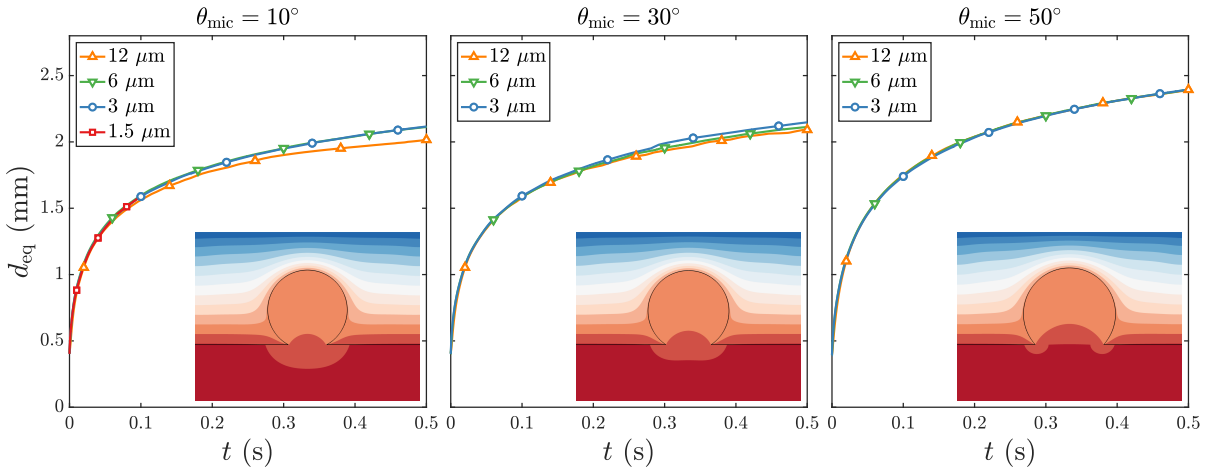

Figure 4.12: Diameter evolution at different contact angle for consecutive cell sizes and a spreading length of 5 cell size.

In figure 4.12, the evolution of the diameter for a $l_{sp} = 5\Delta x$ is displayed. For high microscopic contact angle, the evolution is perfectly converged for the three consecutive cell sizes of 12, 6 and 3 µm for this length. On the other hand for low microscopic angle, the convergence on the equivalent diameter is obtained for finer mesh, the 12 µm mesh seems insufficient. The 6 µm is converged. Therefore, thinner mesh are required for lower contact angle.

The heat flux balance has been evaluated in the dihedral for the chosen l_{sp}. The aim is to check that the heat flux is still balance despite the addition of a source term.

4.3.5 Heat Balance in the dihedral

Heat balance in the dihedral at the contact line is studied for high solid thermal conductivity ($\lambda_{\text{w}} = 50$ W.m^{-1}.K^{-1}). The different contributions for the heat balance are

- The liquid advection flux at the right part of the dihedral

$$\int -2\pi r_l \rho_{\text{liq}} C_{p,\text{liq}} (T - T_{\text{sat}})(\mathbf{v} \cdot \boldsymbol{n_x} + v_{\text{cl}})\, \mathrm{d}l \tag{4.35}$$

- The conduction in the liquid at the right part of the dihedral

$$\int 2\pi r_l \lambda_{\text{liq}} \nabla T \cdot \boldsymbol{n_x}\, \mathrm{d}l \tag{4.36}$$

- The conduction between the wall and the fluid at the bottom of the dihedral

$$\int 2\pi r(w) \lambda_{\text{harm}} \nabla T \cdot \boldsymbol{n_y}\, \mathrm{d}w \tag{4.37}$$

Where λ_{harm} is the harmonic conductivity between the fluid and the wall.

- The evaporation heat flux at the liquid/vapor interface

$$\int 2\pi r(s)\dot{m}L_{\text{vap}}\,\mathrm{d}s \tag{4.38}$$

- The dihedral expansion due to the contact line motion

$$\frac{d}{dt}\iiint_{\mathcal{V}_b}\rho_{\text{liq}}C_{p,\text{liq}}(T-T_{\text{sat}})\,\mathrm{d}\mathcal{V} \tag{4.39}$$

This study is conducted on a stabilized bubble, which allows to neglect the contact line velocity in (4.35) as well as the unstationary dihedral expansion (4.39).

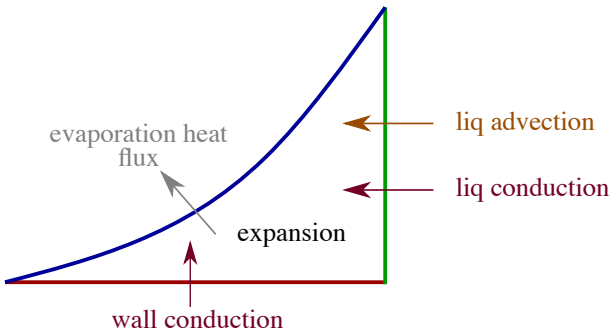

Figure 4.13: Enthalpy balance in the dihedral

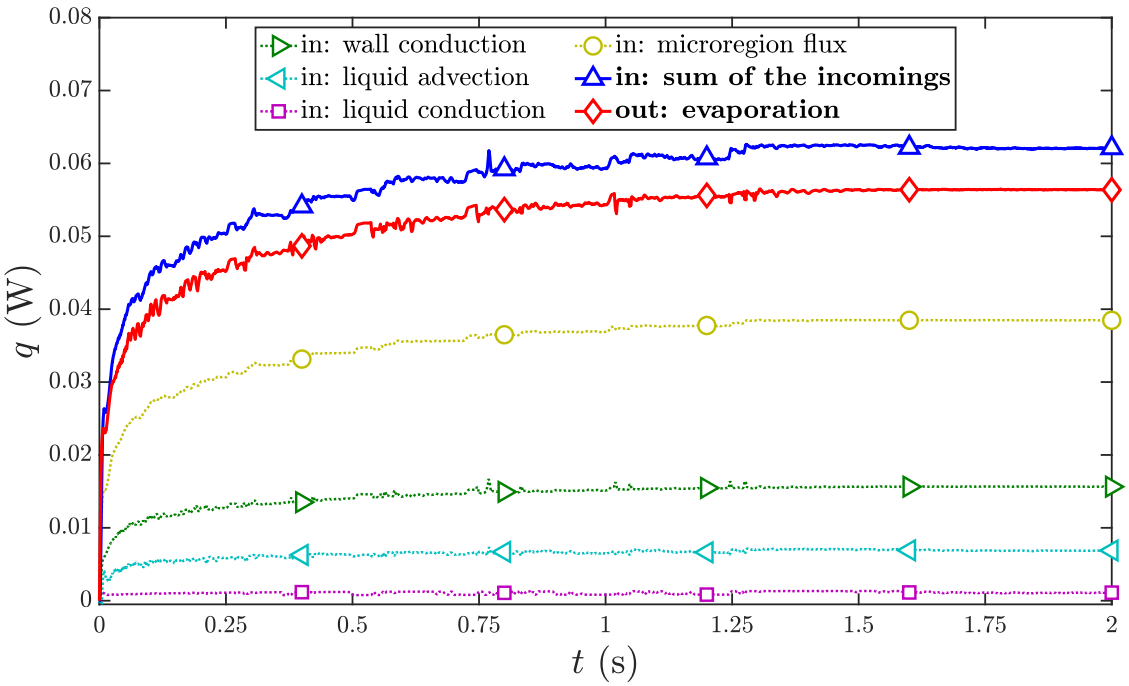

Figure 4.14: Energy balance for simulation 6 µm, $\theta = 10°$, $a = 30.10^{-6} \times 2\pi r_{\text{cl}}$, $\lambda_{\text{w}} = 50$ W.m^{-1}.K^{-1}.. Dihedral length is 15 mesh size (90 µm). 9.2% difference between incoming and outgoing flux.

In figure 4.14, the energy balance for a simulation is drawn all along the bubble growth. The incoming flux is the sum of the liquid convection flux (4.35), the liquid conduction (4.36), the solid conduction (4.37), and the micro-region heat flux computed with the local superheat of the contact line. The outgoing flux is the evaporated heat flux at the interface (4.38). The dihedral

size in which the heat flux is integrated is 15 mesh size wide, corresponding to a size of 90 µm. For a dihedral of this size, the whole micro-region heat flux has been spread.

	Contact angle	Error in heat balance (%)
DNS-NMR (No Micro-Region)	10°	5.9
	30°	7.5
	50°	37.6
DNS-SMR	10°	9.2
	30°	11.6
	50°	15.2

Table 4.3: Error in heat flux balance for different configuration. Mesh size is constant equal to 6 µm. Spreading length is $l_{sp} = 5\Delta x = 30$ µm. Length of the dihedral is 15 mesh size (90 µm)

Table 4.3 contains the heat balance in the dihedral for different contact angle and high solid thermal conductivity. It should be noted simulations with high conductivity ratio have the worst balance in term of heat flux. We here display the limit cases. At first, one can observe that without micro-region, the heat balance is never perfectly close, especially for high contact angle where little oscillations of the contact line positions induce complications of the calculations, hence the high value for the 50° NMR simulation.

For the reference case of 6 µm, at low microscopic contact angle and for $l_{sp} = 5 \times \Delta x$, the balance between the incoming and the outgoing flux is estimated to about 9%. This value is consistent with the values obtained without micro-region model. These results are more qualitative than quantitative, and show no major variations of the balance with the addition of a source term. The coupling handles the heat flux correctly despite the micro-region mass flow.

		ΔT		θ_{app}	
		$t = 0.1$ s	$t = 0.2$ s	$t = 0.1$ s	$t = 0.2$ s
10°	12 µm	1.194 K	1.174 K	14.034°	13.990°
	6 µm	1.201 K	1.189 K	14.028°	13.995°
	3 µm	1.153 K	1.162 K	13.869°	13.889°
30°	12 µm	1.447 K	1.440 K	30.367°	30.365°
	6 µm	1.441 K	1.429 K	30.363°	30.365°
	3 µm	1.442 K	1.423 K	30.361°	30.356°
50°	12 µm	1.597 K	1.587 K	50.108°	50.108°
	6 µm	1.581 K	1.571 K	50.107°	50.106°
	3 µm	1.568 K	1.557 K	50.106°	50.105°

Table 4.4: Values of superheat and apparent contact angle for three consecutive mesh size and three microscopic contact angles. The spreading length is $l_{sp} = 5\Delta x$ for all cases.

The superheat and contact angle convergence has also been studied. Table 4.4 describes the evolution of these values for three contact angle cases at $t = 0.1$ s and $t = 0.2$ s. The variation of superheat is about 1% between the consecutive meshes, except one case for 10° at 4%, which demonstrate a satisfactory convergence. The contact angle variation should be

considered more thoroughly. Indeed, variations for high microscopic contact angle are very low with the superheat, as observed in figure 3.12.

The micro-region coupling with the DNS has been displayed, and the convergence established. The spreading length will be kept equal as $5\Delta x$, since it it is thought that it is the best compromise between keeping an accurate balance in heat transfer at low scale, and reproducing the physical phenomenon in the vicinity of the contact line. A larger spreading would indeed make the fluid flow at the contact line vanish, and the micro-region would not be captured accurately.

4.4 Validation case: Multiscale Boiling experiment (RUBI)

First, the simulations have been compared to the Multiscale Boiling Experiment. Indeed, the RUBI experiment is a perfect database for comparing the results. As described in section 1.1.4, it provides an important number of configurations and includes large parameter scales. Several different experiments have been computed, and are described.

4.4.1 Simulation setup

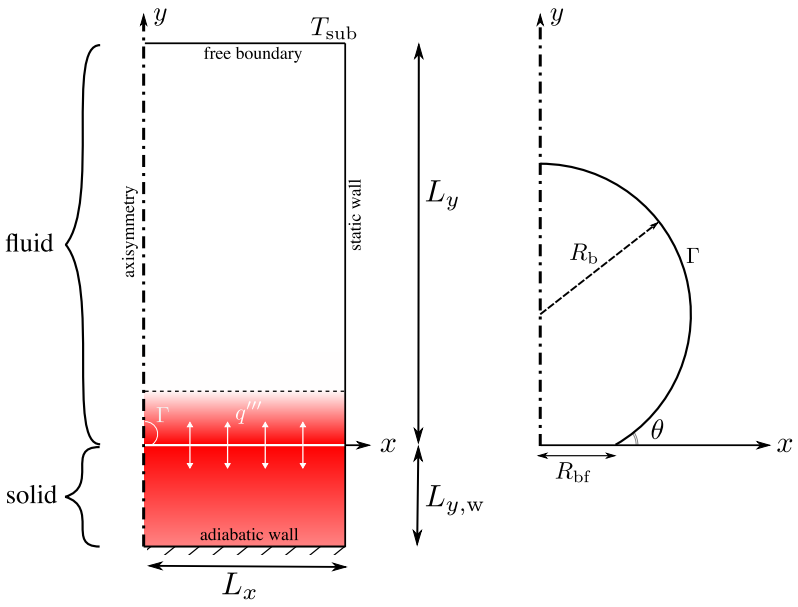

Figure 4.15: RUBI numerical setup

The RUBI test-cell is too large to be entirely modeled with DNS. We chose to simulate an axisymmetric box, with a domain size of $L_x \times L_y = 4{\times}8$ mm^2, with a wall $L_{y,w} = 5$ mm thick. Simulation with reduced wall thickness have been performed, but important dependency on this parameter has been observed. Thus, the experimental size has been simulated. The bottom of the wall is adiabatic, the top of the domain has free boundary conditions since the fluid is not entirely considered in the simulation. The fluid is FC-72. Its properties as well as the wall are described in Appendix C. The top of the wall is covered by a chromium thin coating (400 nm) where the Joule effect q'' creates a thermal boundary layer. This thickness is far lower than the thinnest mesh possibly used. Therefore, a density heat flux has been considered in the first wall cell to account for the surfacic effect generated by the chromium layer. If the heat flux is considered constant equal to q'' (depending on the configuration), the wall cell at the top of the solid domain is set with a density flux equal to $q''' = \frac{q''}{\Delta y}$. The distribution of the flux between the wall and the fluid is directly computed by the DNS. Due to the high difference in thermal conductivity, the energy is mainly directed toward the solid wall. Therefore, the thickness of

the wall is an important parameter.
The initial conditions need to be carefully set as well. The nucleation of the bubble occurs after a specific time t_{wait} during which a thermal boundary layer is developed. The whole analytical solution is described in Appendix A. It consists in the solution of the thermal field in two solid infinite media with a surfacic heat source at their interface.
However, this analytical solution is limited. Indeed, in some cases where the heater is set on several seconds before the nucleation, the infinite property assumed in the analytical solution becomes incorrect and edge effects are observed.

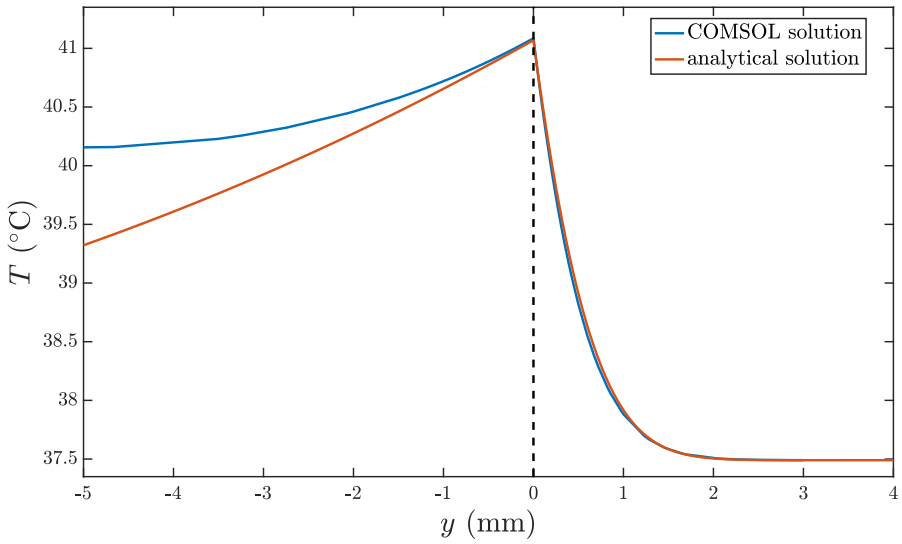

Figure 4.16: Initial condition in RUBI for configuration with $t_{\text{wait}} = 10$ s. Wall is denoted in dashed line.

In figure 4.16, the COMSOL solution and the analytical solution for the initial thermal field are depicted. One can observe that the left side condition (in the wall) underestimate the temperature, as the wall is finite and energy is stored. In the liquid, as the thermal diffusivity is lower, no difference occur within this low time scale. The COMSOL result is also consistent with an adiabatic condition at the bottom of the wall, as the zero derivative can be noticed.

4.4.2 Limitations of the experiment

In order to have consistent results, and to be numerically reproduced, the requirement for every experiments have been strictly defined beforehand. To avoid any parasitic bubble, a single nucleation site of 50 µm of diameter with a L-shape has been designed. The heat flux distribution of the chromium heater is required homogeneous. The temperature and pressure are regulated to ensure the nucleation occurs in the adequate conditions. However, the temperature regulation faced difficulties. Indeed in microgravity, with no natural convection to homogenize the fluid, the temperature distribution is sometimes stratified, and without flow the liquid cannot be stirred. In some cases where the thermocouple rack is close to the wall, some discrepancies in terms of experimental temperatures compared to theoretical ones as imposed by the B.USOC (Belgian User Support and Operations Centre) have been observed. An example is given below.

In figure 4.17, the evolution of the thermocouple temperatures are displayed. On the first moments of the experiment, before the nucleation that occurs for $t = 0$ s, the temperature is constant in the three upper thermocouples, whereas the one near the wall increases as the thermal boundary layer develops due to the Joule effect set a few seconds before. After the nucleation, the bubble disturbs the thermal field and a variation is observed. The difference in the thermocouple temperature before the triggering of the Joule effect should be less than

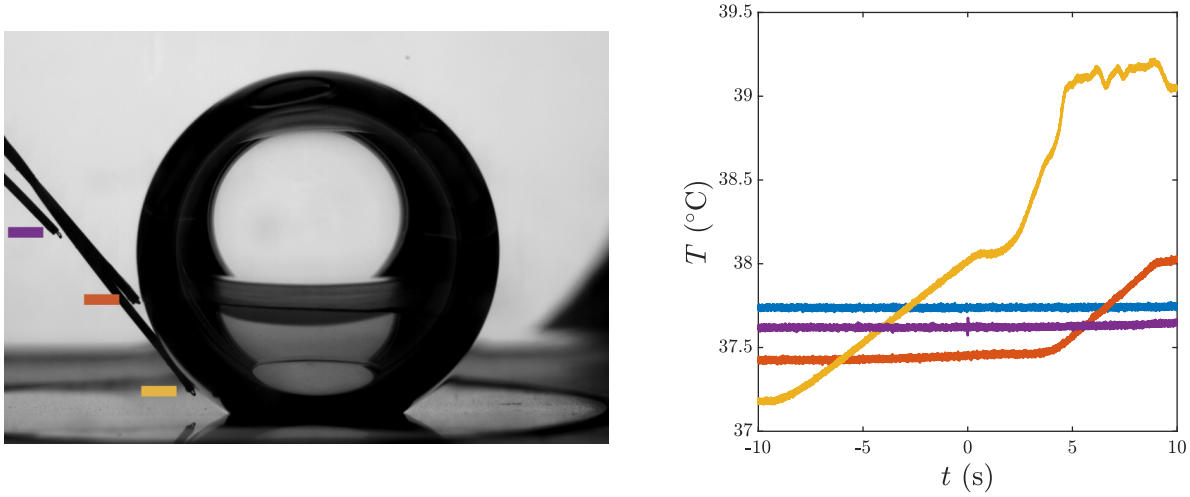

Figure 4.17: Black & White image of the bubble with the four thermocouples (only three visible) (left); Temperature variation in the thermocouples for a given configuration (the blue one is not visible, further away from the wall) (right)

0.1 K, which is larger here (see figure 4.17, right). The liquid should be homogenized. This gap has caused difficulties for simulations, since the initial temperature conditions are uncertain. Discussions with other research groups working on the RUBI experiments have be opened on the issue. A study of the adequate initial temperature field has been performed for some of the test cases, in collaboration with the group of the Université Libre de Bruxelles. On the case described further, it was agreed to decrease the value of the liquid subcooling of 1.5 K.

4.4.3 Comparison with the experimental results

The different methods introduced previously are now compared to the experimental results obtained with the RUBI experiment. For the sake of illustration, some snapshots of the bubble shape and thermal field are shown in figure 4.18, for different times. These snapshots have been obtained with the DNS-SMR solver, and they enable to visualize the bubble growth with time and the temperature field in the fluid and solid domains.

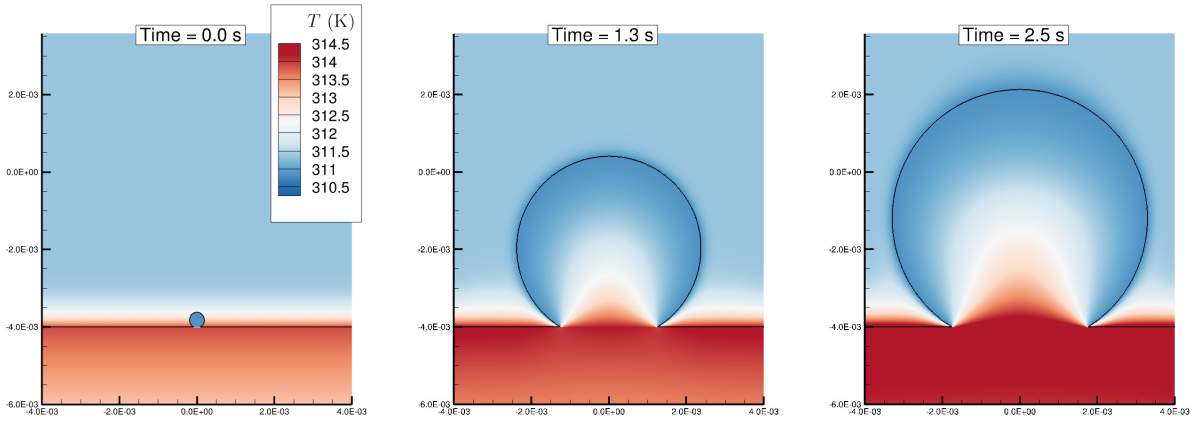

Figure 4.18: Interface location and temperature field of the bubble at different times.

For the case presented on figure 4.19, the thermal field has been increased (equivalent to reduce the saturation temperature) by 1.5 K.

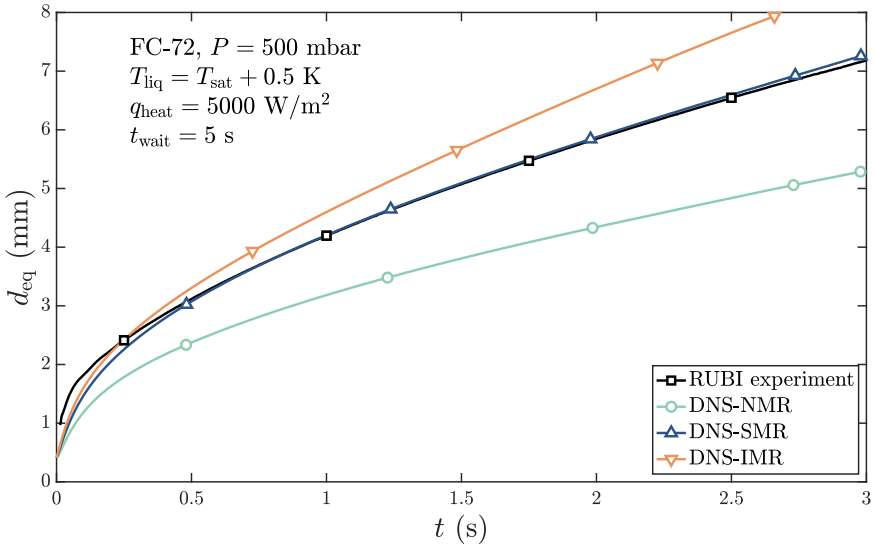

Figure 4.19: Comparison with RUBI experiment. In SMR and IMR, $f = 1$, $\theta_{mic} = 8°$. With NMR, θ_{app} is chosen constant, equal to 27°. Mesh size is 16 µm.

In figure 4.19 has been plotted the temporal evolution of the equivalent bubble diameter d_{eq} obtained with the different methods, i.e. DNS-NMR, DNS-SMR and DNS-IMR. Due to stability issues, the results with the DNS-LMR are not shown. One can observe that the results obtained with DNS-SMR matches very well with the experimental results, even on long range of time. The DNS-NMR solver strongly underestimates the bubble growth, which demonstrates the strong impact of the micro-region heat flux on the overall bubble growth. On the opposite, the DNS-IMR overestimates the bubble growth rate which suggests that this coupling method suffers from a flaw to describe the flow around the bubble due to the loss of locality when accounting for the micro-region mass flux. To highlight this, the streamlines of the velocity field are plotted in the vicinity of the contact line at a given time in figure 4.20 for both DNS-SMR and DNS-IMR.

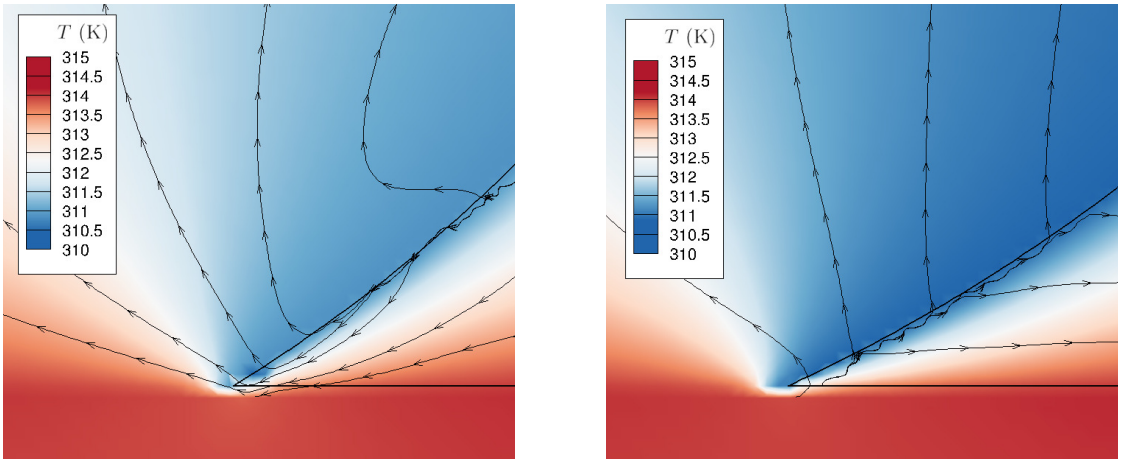

(a) DNS-SMR (b) DNS-IMR

Figure 4.20: Interface location, temperature field and streamlines near the contact line for the two methods at a given time.

In the case of the DNS-SMR solver, as the mass flux is increased near the contact line, an aspiration of the liquid is observed in the corner formed between the liquid interface and the solid wall, where the phase change mass flow rate is stronger. On the other hand, no aspiration

of the liquid is observed in the vicinity of the contact line with the DNS-IMR solver, since the streamlines show clearly that the liquid flows outward of the corner. This can be explained by the loss of locality of the DNS-IMR method since the micro-region mass flux is just integrated as an average volume source term spread out at any point of the bubble. For this reason, it cannot reproduce the effect of local liquid aspiration due to the strong vaporization in the vicinity of the contact line. Consequently, as it reproduces a better agreement with the experimental results and enables a better physical description of the flow in the vicinity of the contact line, the DNS-SMR solver will be considered as more accurate for the coupling between a micro-region model and a nucleate boiling DNS solver, and it will be kept for the numerical investigations in the coming chapters.

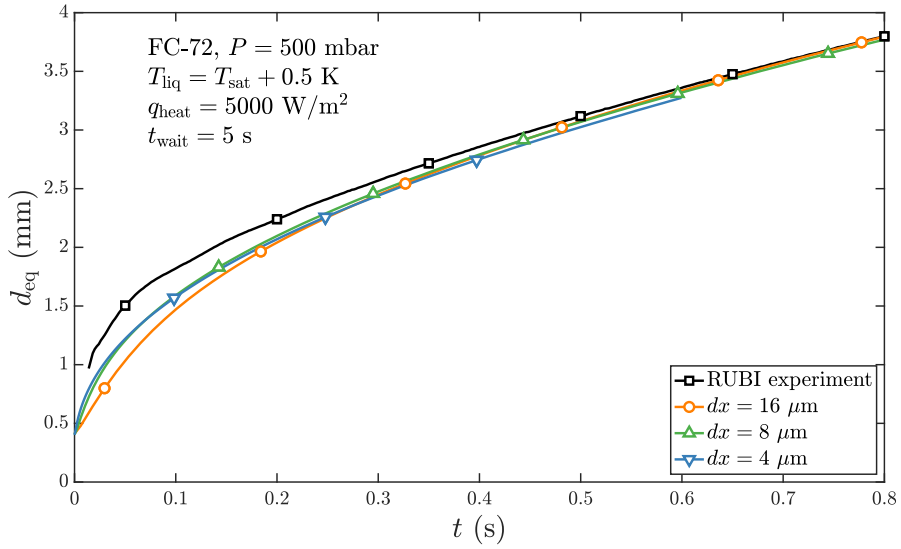

Figure 4.21: Convergence for three consecutive mesh.

The grid convergence is verified on figure 4.21. The evolution is accurately captured for 8 µm, the initial growth is slightly missed for coarser mesh. Validation of the code with the RUBI experiment has also been carried-out with other experimental data, i.e the bubble foot radius r_{cl}, the apparent contact angle θ_{app} and the wall temperature below the contact line $T_w - T_{sat}$. The three first are obtained with post-processing of the B&W images. The oscillations observed on the plots are due to the not-so-good pixel resolution of the camera and the difficulty to spot the interface accurately. The local superheat has been obtained with post-processing of the IR images, the routine is detailed in Appendix D.

In particular, there are uncertainties concerning the temperature profile of the liquid (as mentioned above), but also on the value of the accommodation coefficient which we supposed high for FC-72. Three simulations have been performed, changing f, but also the value of the heat flux, as the Joule effect in the experiment is not supposed to be constant all along the substrate. In the middle of the layer, at the nucleation site, the flux is supposed to be 20% higher than around. As the domain simulated with $\mathcal{DIVA}$ is small compared to the real experimental setup, we compute a whole simulation with increased heat flux, with therefore a different initial thermal field, calculated with Appendix A.1.

Figure 4.22 shows that the impact of changing f for a constant flux is low. The contact angle decreases a little, which slightly reduces the contact line radius. The impact on the global diameter is very narrow, and invisible on the local superheat. If the heat flux increases, so does the local superheat and hence the apparent contact angle. On the larger scale, the bubble diameter variation is not significant. We recall that the bulk fluid is at the same temperature in all three simulations, only the thermal boundary layer is different when heat flux is increased.

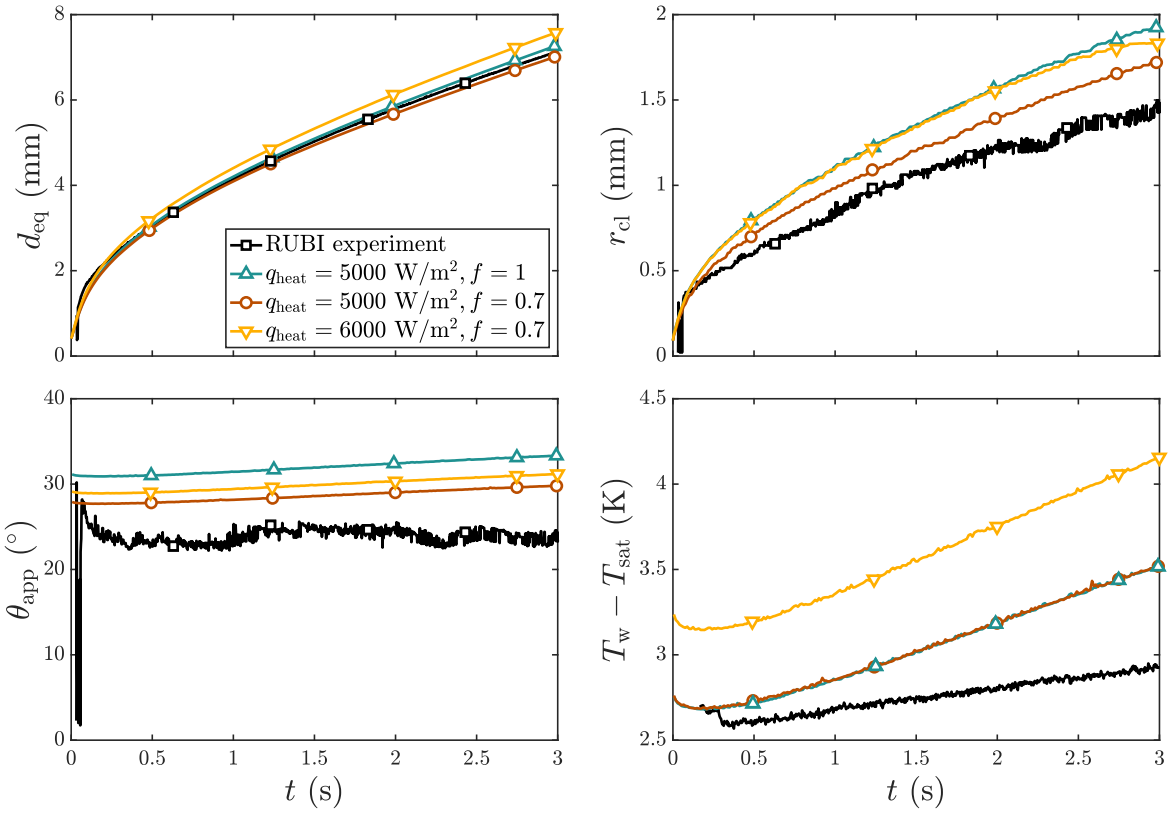

Figure 4.22: Comparison of d_{eq}, r_{cl}, θ_{app} and T_w with post-processed data. An offset have been set on the experimental temperature evolution.

It could be noted that the experimental contact angle evolution is not visible, despite the temperature variation (we also recall that due to issues in the IR camera calibration, an offset is taken on the measured temperature, but the evolution is accurately captured). It is supposed that the B&W camera resolution (20 µm/pixel) is barely sufficient to accurately capture the contact angle. The difference between experimental result and simulations lays in this contact angle which is difficult to capture, and has direct consequences on the contact line radius. These first comparison with the RUBI experiment are promising.

4.5 On the importance of the model dependency on the physical properties

With refrigerant like FC-72, the value of f is expected to take values close to 1. This leads to a large micro-region contribution for the RUBI experiment. For other fluid, the value is an open question. Paul [111] gather experimental results for this accommodation coefficient but the values are scattered and difficult to unify. The fluid purity may also have an impact on its value. Moreover, the thermal conductivities are crucial for the heat transfer. The local superheat is affected and so is the micro-region heat flux.

Therefore, we address in this section a pragmatic study on the influence of these parameters on the model.

4.5.1 Qualitative influence of the accommodation coefficient

Gravity case

The accommodation coefficient f entails variation in the model through the interfacial resistance R_Γ. The investigation is performed with a configuration of nucleate pool boiling in terrestrial conditions. Nucleation occurs in water at saturation temperature, above a superheated wall. Solid and fluid properties are identical to [77]. A thermal boundary layer is considered in the liquid using usual Kays and Crawford correlation [99]. In this layer, we set a linear gradient, and the fluid is at saturation temperature above. In the solid, a linear thermal gradient is set as well, and the temperature boundary condition at the bottom imposes a 7 K superheat between the fluid and the solid. The Jakob number in this case is equal to 21, which is usual for nucleate pool boiling regime. The microscopic contact angle of the fluid is 50°.

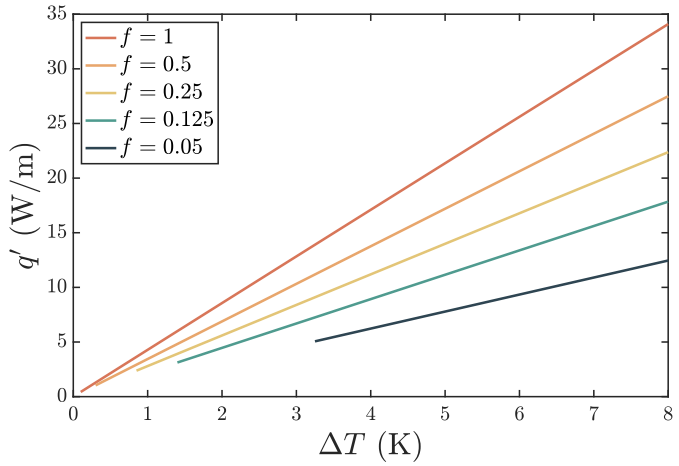

Figure 4.23: Micro-region heat flux for water with different f. Fluid is water, P_{atm}, $\theta_{\text{mic}} = 50°$, integration length 8 µm.

For this case, the model has been computed with the experimental contact angle, for different accommodation coefficient and the result in terms of heat flux is shown on figure 4.23. The dependence of the flux on the accommodation coefficient is more important for water than for FC-72, see figure 3.16 (right).

The fluid domain is a 4×4 mm^2, the solid 1.33 mm thick. The simulations have been performed with a grid $512 \times (512 + 166)$ for $L_x \times (L_y + L_{y,\text{w}})$, which corresponds to a 8 µm cell size, for which converged simulations have been already presented in [77] with the DNS-NMR solver. As the numerical results obtained show a good agreement with the experimental data, this suggests that the micro-region may not have a significant impact in this configuration.

Figure 4.24 displays an increasing bubble growth rate with f, with a lowering of the departure time. This result is consistent, since the departure diameter is imposed by the buoyancy. However, it should be noticed that the wall temperature dependence on the accommodation coefficient is very low in these conditions of high solid thermal conductivity. For variations in range [0.05 - 1] in f, the range of variation of R_Γ is [1686 nm - 43 nm] (we recall that $f \nearrow$, $R_\Gamma \searrow$), and yet the variation of ΔT is below 5%. On the opposite, the heat flux is highly dependent on f, as for the same temperature, the flux increases with f, figure 4.23. This has a direct impact on the global micro-region heat flux injected in the domain, on the bottom right plot. This case shows that lowering the accommodation would lead, ultimately, to the simulation without considering the micro-region model. The value would require to be lowered more than it is computationally possible, since low superheat with low f are difficult to obtain. Therefore, it may be expected that very low values of f do not bring significant contribution to the overall bubble growth.

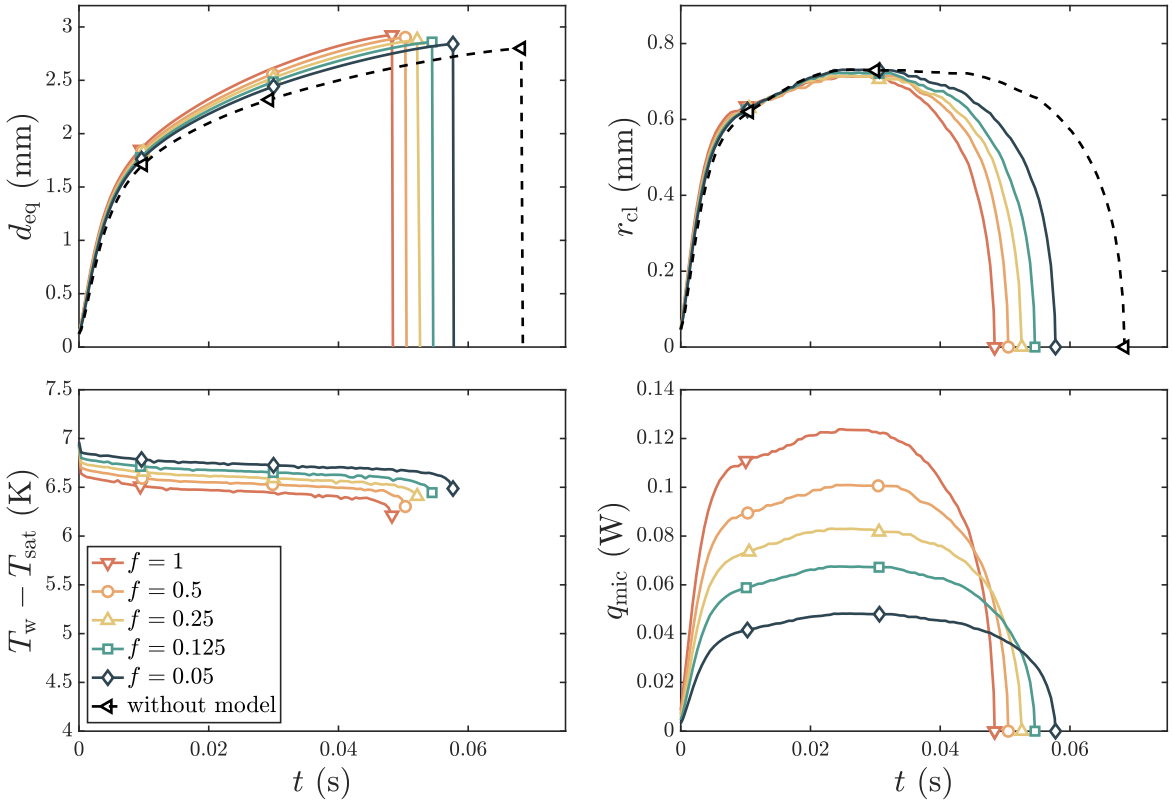

Figure 4.24: First bubble detachment for water at P_{atm} in terrestrial conditions.

Microgravity case

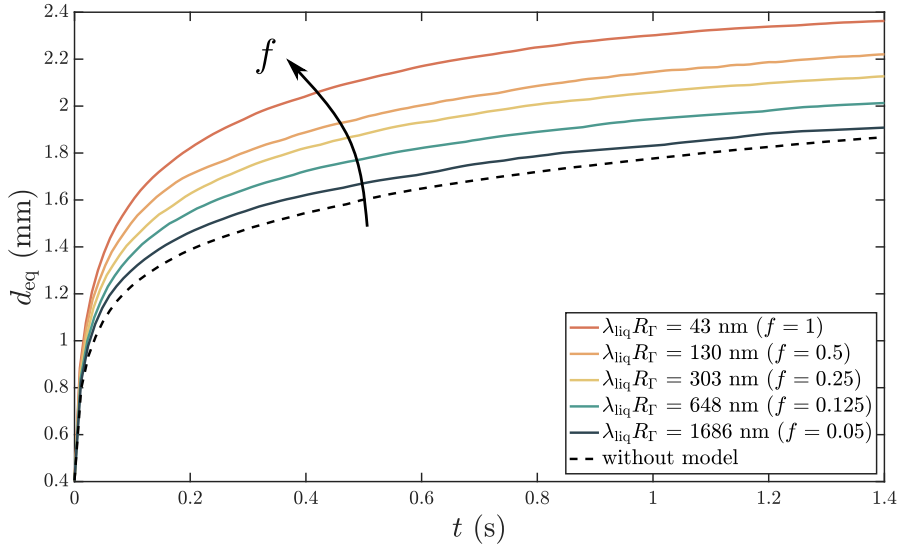

Figure 4.25: Bubble growth in microgravity conditions.

A similar case, in microgravity has also been considered. The full setup is described further in section 5.1, the result is presented here for qualitative observation. A subcooling of 10 K is imposed at the top of the domain, a superheating of 2 K at the bottom. A high solid thermal conductivity $\lambda_w = 50$ W.m^{-1}.K^{-1} and a contact angle $\theta_{mic} = 10°$.

In figure 4.25 the bubble equivalent diameter with different f are compared to the simulation

without micro-region. Again, it is interesting to observe that the simulation with the highest interfacial resistance (low f) is about to match the result without micro-region model. Indeed and as studied in subsection 3.4.3, a great interfacial resistance leads to a low micro-region heat flux and therefore negligible contribution in the overall evaporation process. This result is consistent and expected. As intermediate conclusion, for a fluid with low value for its accommodation coefficient, the contribution of the micro-region is negligible.

4.5.2 Qualitative influence of the thermal conductivity ratio λ_w/λ_{liq}

The influence of the solid thermal conductivity on the bubble growth rate has already been noticed by Nukiyama [123]. Moreover, its impact is even more important considering a micro-region model, as the contact line temperature is a driving parameter on the bubble global growth, hence the importance of the coupling previously described. Considering a micro-region model, Mann et al [81] showed that for equivalent heat flux, the local superheat is more important with a copper plate compared to the steel and ceramic one. The cold spot in the wall below the contact line shrinks with the wall conductivity. With high solid thermal conductivity, the wall temperature tends to be more homogeneous, leading to an increase the wall superheat and micro-region heat flux. However, the coupling between the micro-region and the solid solver was hidden, and the impact of one another is not straightforward.

The study of Urbano et al [83] has been conducted without micro-region. The bubble equilibrium dependence on the wall properties has been noticed but not quantified. Moreover, simulation on wetting fluid ($<30°$) has not been performed, due to the absence of coupling with micro-region model, which was expected to be of great importance since it involves higher heat fluxes and contact angle variations.

Nonetheless, the key point should not be the solid thermal conductivity, but rather the conductivity ratio between the solid and the liquid λ_w/λ_{liq}, since the important parameter is the temperature at the solid and fluid interface. Therefore, the study below will consider the ratio rather than the value of the wall.

In figure 4.26, the influence of the micro-region model in the overall bubble growth is displayed for different wall properties. For low thermal conductivity ratio, both low and high contact angle show very little dependence on the micro-region model. In these conditions, the local superheat is very low, as the wall is cooled down by the fluid and not heated enough by the cell in the neighbourhood of the contact line cell. As a consequence, the micro-region heat flux is very low. The difference of equilibrium diameter, and is less than 5% for both cases. On the opposite for high conductivity ratio, a high superheat is induced and the contribution of the micro-region becomes of uppermost importance, up to 20% on the equilibrium diameter. The superheat increases, and so does the heat flux and the apparent contact angle. If the global contribution of the micro-region is more important for the 50° case, it is due to a higher bubble foot radius, which induces a bigger global micro-region heat flux since $q_{mic} = 2\pi r_{cl} q'_{mic}$. It should be recalled that for a given temperature, the micro-region heat flux integrated on a specific length is always bigger for low contact angle, see figure 3.13.

The conductivity ratio plays a major role on the significance of the micro-region consideration. With low conductivity ratio, it can be nearly neglected, whatever the wetting properties of the fluid and the accommodation coefficient.

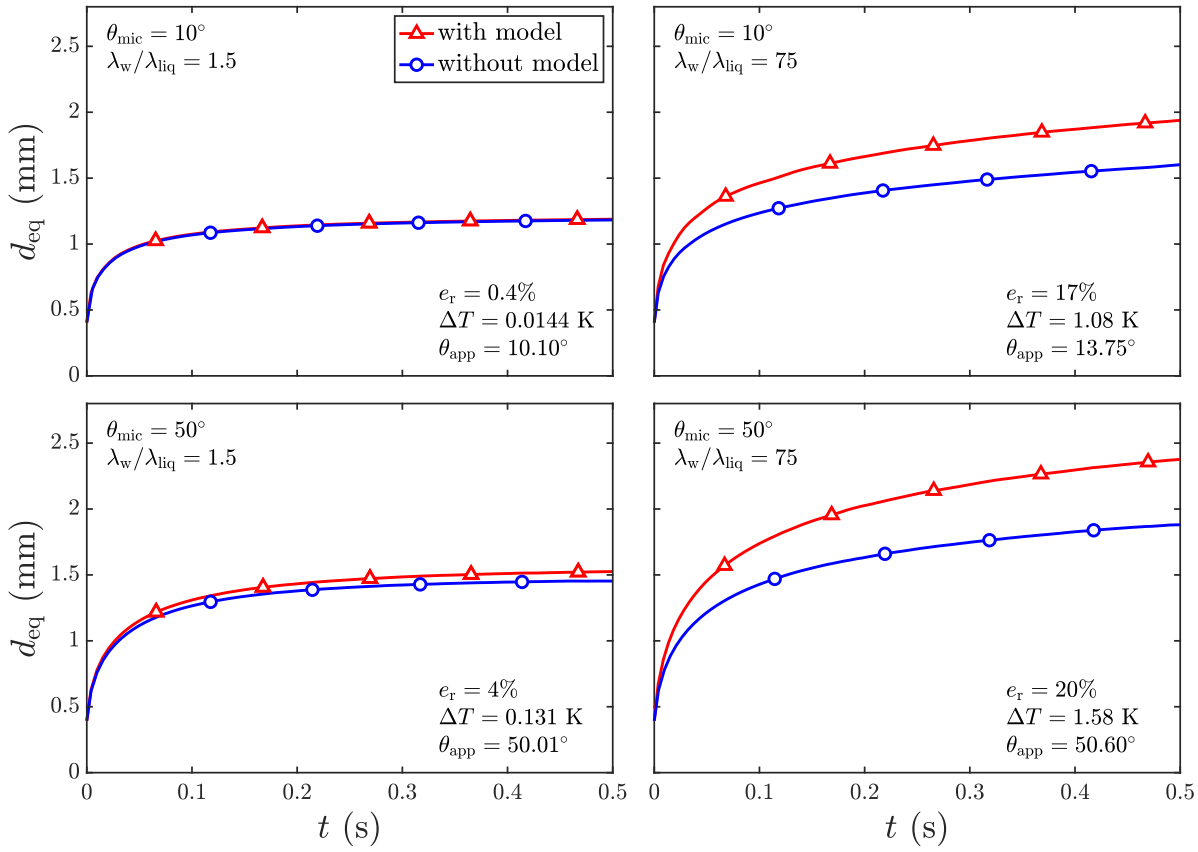

Figure 4.26: Equivalent diameter for different microscopic contact angle and solid thermal conductivity. Simulation with model are for $f = 1$.

4.6 Conclusion of the coupling between micro-region and DNS

In this chapter, a new method to account for micro-region models in DNS has been described. The linearization of the heat flux with the superheat can be directly used to modified the linear systems of the DNS, which provide a stable (and implicit) coupling with the wall. In the fluid, a spread of the micro-region heat flux in the vicinity of the contact line was found to be the best compromise to keep the local effect of the flow in the vicinity of the contact line. The grid convergence of the method has been demonstrated.

The results with the coupling show satisfactory agreement with the experimental data, despite the uncertainties in the RUBI configuration. Bubble evolution and local superheat are well captured. This coupling between micro and macro phenomena provide great improvement of the DNS for wetting fluids, and more generally for simulations of bubble attached to a heated wall. The contribution of the micro-region is of uppermost importance to accurately capture the bubble growth.

Nonetheless, a pragmatic study on the importance of the micro-region depending on the fluid and solid properties has been carried out. It has been shown that the micro-region only makes sense in the case of high thermal conductivity ratio, otherwise the micro-region vanishes due to low local superheat. Moreover, if the micro-region is considered with very low accommodation coefficient, the heat flux it brings is negligible. Thus, numerical results obtained with the DNS-SMR solver considering $f \to 0$ tend to previous results obtained with the DNS-NMR solver.

For now on, simulations with coupling will be investigated. In the next chapter, the influence of the parameters of the model will be studied.

Chapter 5

Results of nucleate boiling with micro-region

The micro-region model has been implemented and validated against the RUBI configuration. The previous chapter has shown that the micro-region model can be negligible in cases of low conductivity ratio or low accommodation coefficient. A more quantitative study is now performed, with the configuration of Urbano et al [83]. Nucleate boiling in zero-gravity under subcooled conditions is considered. In such configuration, an equilibrium radius is reached when the condensation at the top of the bubble due to the subcooling balances the vaporization at its bottom due to the wall superheat.
The influence of the micro-region model will be investigated, and a parametric analysis will be performed to show the influence of the parameters of the model on the overall bubble growth. In particular, and as shown in section 3.4, the microscopic contact angle and accommodation coefficient have a great influence on the heat flux. Moreover, the coupling with the simulation will highlight the importance of considering the wall as it will drive the superheat and, therefore, the micro-region contribution.

Contents

5.1 Parametric analysis 90
5.1.1 Configuration setup 92
5.1.2 Parameters studied and ranges of variation 93
5.2 Results 94
5.2.1 Evolution of the equilibrium diameter 94
5.2.2 Evolution of the contact line superheat and micro-region fluxes 97
5.2.3 Construction of the correlation for R_{eq} 101
5.2.4 Study of the Nusselt number 104
5.2.5 Global variations 107
5.3 Limitations for non-static configurations 107
5.4 Conclusion of the chapter 110

5.1 Parametric analysis

In this section, we take interest to the configuration of nucleate boiling in microgravity conditions presented by Urbano et al in [83]. It consists in a bubble in microgravity conditions which is immersed in a stratified thermal field so that the bottom of the bubble is vaporizing whereas the top of the bubble is condensing. As a consequence, an equilibrium radius is reached when the condensation at the top of the bubble, due to the subcooling, balances the vaporization at its bottom, due to the wall superheat. In the study of Urbano, this benchmark has been carried-out with the DNS-NMR solver while accounting for the thermal conduction in the solid domain. It is reported that a steady state of the bubble volume is reached after sufficient time, as it was expected. The setup is displayed in figure 5.1.

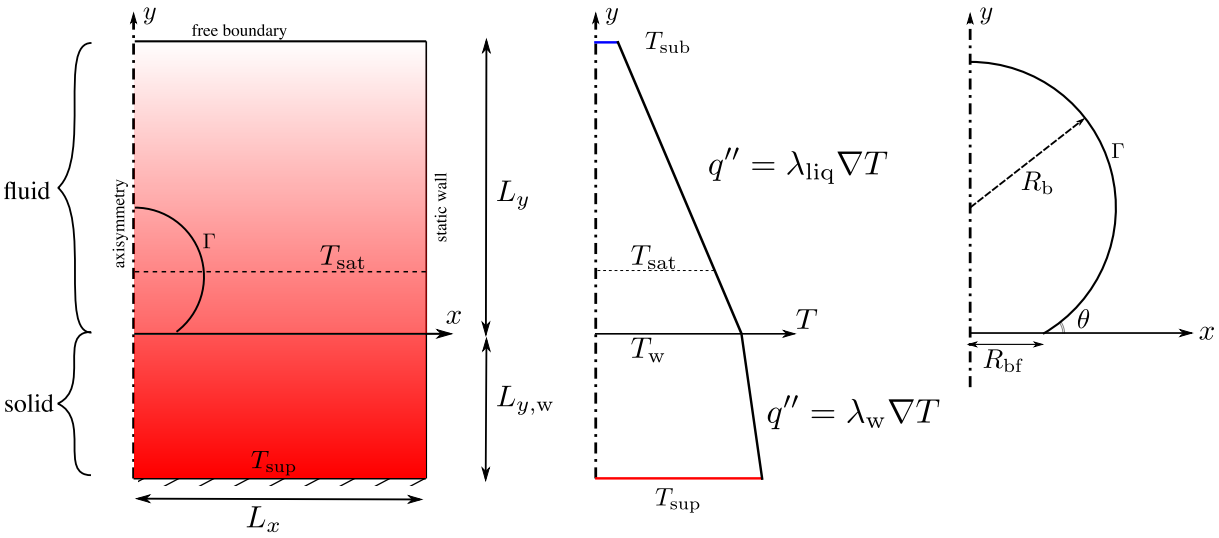

Figure 5.1: Setup of [83]

Under the assumption of a linear stratification of the thermal field, for a spherical bubble and by neglecting the wall influence, an analytical solution has been deduced from the energy balance. The detail is developed in Appendix B, and recalled here:

$$\frac{R_b}{L_y} = \frac{1}{1 + \frac{Ja_c}{Ja_e}} \left(\frac{1 + \cos\theta_A}{\cos\theta_A \left(1 + \cos\theta_A\right) + \frac{1}{2}\sin^2\theta_A} \right) \tag{5.1}$$

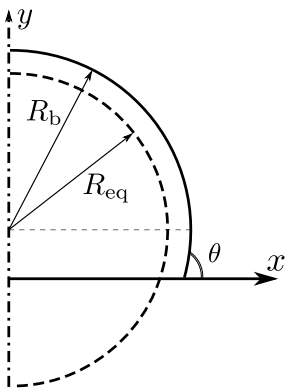

Figure 5.2: Scheme of apparent and equivalent radius. Bubble have similar volume.

Equation (5.1) can be transformed to be linked to the equivalent radius R_{eq} with the following relation

$$R_{eq} = R_b \left(\frac{4 - (2 + \cos\theta_A)\left(1 - \cos\theta_A\right)^2}{4} \right)^{1/3} \tag{5.2}$$

The volume of the truncated sphere of apparent radius R_b and the full bubble of equivalent radius R_{eq} is the same. In the further developments, we only use R_{eq}. The following correlation is obtained:

$$\frac{R_{\mathrm{eq}}}{L_y} = \frac{1}{1+\frac{\mathrm{Ja_c}}{\mathrm{Ja_e}}}\left(\frac{1+\cos\theta_A}{\cos\theta_A\left(1+\cos\theta_A\right)+\frac{1}{2}\sin^2\theta_A}\right)\left(\frac{4-\left(2+\cos\theta_A\right)\left(1-\cos\theta_A\right)^2}{4}\right)^{1/3} = g\left(\frac{\mathrm{Ja_c}}{\mathrm{Ja_e}},\theta\right) \tag{5.3}$$

The study conducted by Urbano et al investigated on the influence of the superheat and subcooling through variations of the Jakob number ratio between condensation and evaporation:

$$\frac{\mathrm{Ja_c}}{\mathrm{Ja_e}} = \frac{T_{\mathrm{sat}}-T_{\mathrm{sub}}}{T_{\mathrm{w,eq}}-T_{\mathrm{sat}}} \tag{5.4}$$

with $T_{\mathrm{w,eq}}$ the equilibrium temperature of the wall, which is the temperature that would reach the solid/liquid interface without bubble. For low conductivity ratio between the wall and the liquid ($\lambda_{\mathrm{w}}/\lambda_{\mathrm{liq}} = 1.5$), a prefactor $C = 1.15829$ has been found and provides a satisfactory fit to equation (5.3). Yet, higher conductivities have not been investigated by Urbano, since convergence issues have been reported if $\lambda_{\mathrm{w}}/\lambda_{\mathrm{liq}} > 5$. Diameter evolution as a function of the mesh size, for DNS-NMR and DNS-SMR and with high conductivity ratio is displayed in figure 5.3.

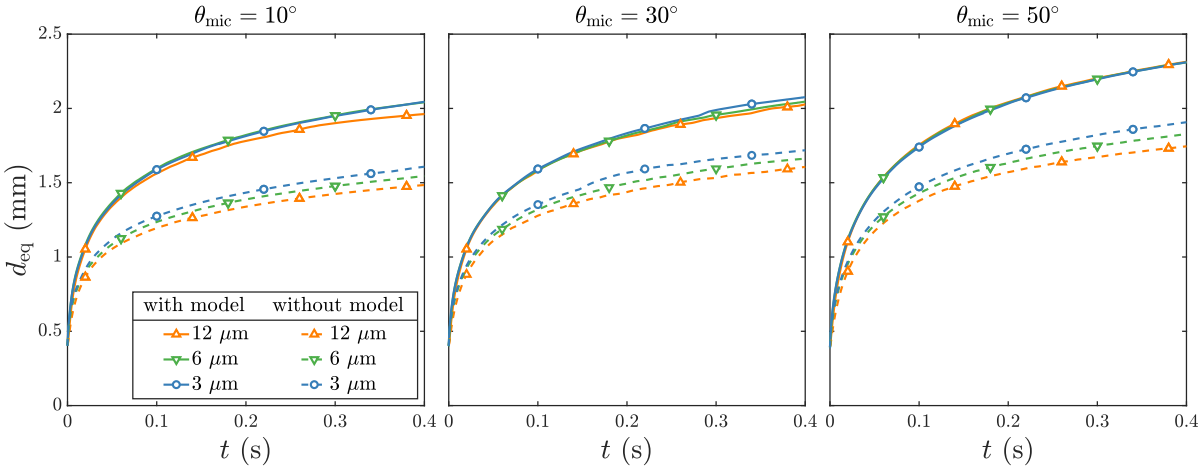

Figure 5.3: Convergence of the equilibrium diameter for different contact angles with and without micro-region model. $\lambda_{\mathrm{w}}/\lambda_{\mathrm{liq}} = 75$, $\mathrm{Ja_c}/\mathrm{Ja_e} = 5$. Simulations with model are for $f = 1$.

Indeed, the DNS-NMR solver forces a cold spot at the contact line because the saturation temperature is imposed, and this tends to thermalize locally the solid wall, see figure 5.4. However, for high value of thermal conductivity ratio, the cold spot region in the vicinity of the contact line is so tiny that space convergence can hardly be achieved. One may expect to converge with the use of much more refined grids, but this could not be reached with reasonable meshes.

On the other hand, figure 5.3 clearly demonstrates the convergence of the DNS-SMR even for high conductivity ratios. The wall temperature at the contact line is implicitly computed by the micro-region model and grid convergence has also been shown in the previous chapter.

Therefore, the objective of the present chapter is to investigate on the impact of the micro-region model on the overall bubble growth, and also to assess the effect of the solid thermal conductivity, since DNS-NMR does not bring satisfactory results for high values contrary to DNS-SMR. The configuration setup and the parameters studied will now be introduced.

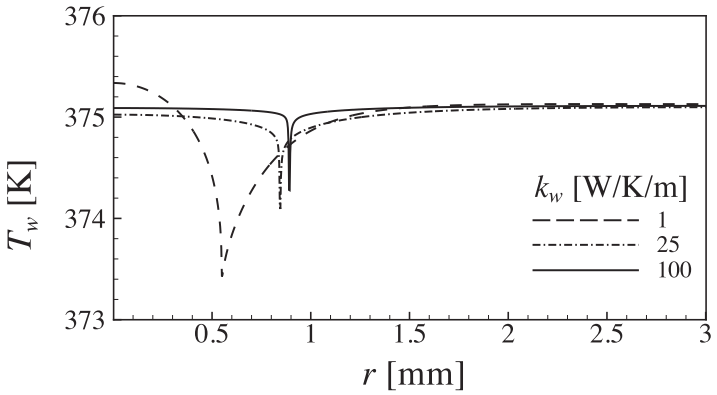

Figure 5.4: Wall temperature along the x-axis. With increasing wall thermal conductivity, the cold spot shrinks. Image from Urbano et al [83].

5.1.1 Configuration setup

The aim of these simulations is to observe the equilibrium of a bubble, for nucleate boiling in a zero-gravity environment in subcooled conditions. The setup is shown in figure 5.1. The domain size is of $L_x \times L_y = 3{\times}3$ mm^2 for the fluid, with a wall $L_{y,\mathrm{w}} = 1.5$ mm thick. The fluid domain is cooled at its top since a temperature $T_{\mathrm{sub}} < T_{\mathrm{sat}}$ is imposed, and superheated at its bottom by a solid, with a T_{sup} condition at the bottom. Therefore, the bubble can reach an equilibrium diameter when the condensation at its top is equal to the evaporation at its bottom. At equilibrium in the absence of bubble, we have two linear gradients depending on the respective liquid and wall conductivities, and $T_{\mathrm{w,eq}}$ is the temperature that would be reached at the solid/fluid interface. If a bubble is present, the solid/fluid interface temperature T_{w} would be equal to $T_{\mathrm{w,eq}}$ only far from the bubble.

Three different values of Jakob ratio will be imposed,

$$\frac{\mathrm{Ja_c}}{\mathrm{Ja_e}} = \frac{T_{\mathrm{sat}} - T_{\mathrm{sub}}}{T_{\mathrm{w,eq}} - T_{\mathrm{sat}}} = 2, 5, 10 \tag{5.5}$$

For every Jakob ratio, different couples of superheat/subcooling can be imposed. For instance, the Jakob ratio of 5 may be simulated with different couples of $(T_{\mathrm{w,eq}} - T_{\mathrm{sat}}; T_{\mathrm{sat}} - T_{\mathrm{sub}})$ such as $(1, 5)$ or $(2, 10)$.

As we do not want to impose the temperature at the solid/fluid interface, the bottom solid wall condition is imposed instead. The temperature is chosen so as to obtain $T_{\mathrm{w}} = T_{\mathrm{w,eq}}$ at the solid interface at initialisation. The temperature at the bottom of the solid domain is T_{sup}.

As we impose the value of T_{sub} depending on the Jakob ratio and the superheat $T_{\mathrm{w,eq}}$, we know the heat flux q''. Hence, we deduce the temperature at the bottom of the domain by conservation of the flux.

$$q'' = \lambda_{\mathrm{liq}} \nabla T|_{\mathrm{liq}} = \lambda_{\mathrm{w}} \nabla T|_{\mathrm{w}} \tag{5.6}$$

$$q'' = \lambda_{\mathrm{liq}} \frac{T_{\mathrm{w,eq}} - T_{\mathrm{sub}}}{L_y} = \lambda_{\mathrm{w}} \frac{T_{\mathrm{sup}} - T_{\mathrm{w,eq}}}{L_{y,\mathrm{w}}} \tag{5.7}$$

We have

$$T_{\mathrm{sup}} = T_{\mathrm{w,eq}} + \frac{\lambda_{\mathrm{liq}}}{\lambda_{\mathrm{w}}} \frac{L_{y,\mathrm{w}}}{L_y} (T_{\mathrm{w,eq}} - T_{\mathrm{sub}}) \tag{5.8}$$

Therefore during the simulation only the two boundary conditions T_{sub} and T_{sup} are imposed. Initially, the thermal gradients are set according to the wall and liquid thermal conductivities,

and an initial nucleus with a radius $R_0 = 200$ µm is considered. Far from the bubble, the wall temperature does not evolve during the simulation.

5.1.2 Parameters studied and ranges of variation

For this parametric study, the influence of five factors are investigated:

- The microscopic contact angle θ_{mic}. The whole study is carried out with the water properties, with only the contact angle variable to observe the influence of wetting conditions.
- The Jakob ratio $\text{Ja}_\text{c}/\text{Ja}_\text{e}$, which defines how the subcooled and superheated liquid is distributed in the domain. High values indicates that most of the liquid is subcooled, whereas low values are for predominantly superheated domain.
- The superheat/subcooling temperatures ($T_{\text{w,eq}} - T_{\text{sat}}$; $T_{\text{sat}} - T_{\text{sub}}$) imposed at the boundaries, for a given Jakob ratio. As the micro-region is considered and depends on the local superheat, this parameter may have an impact on the overall bubble growth.
- The ratio between solid and liquid thermal conductivities $\lambda_\text{w}/\lambda_\text{liq}$. This influence has not been studied in the article of Urbano [84], since convergence issues were encountered for high values. Moreover, the impact on the micro-region model is expected to be of uppermost importance. It must be mentioned that we will be interested in the steady state, when the bubble reaches its equilibrium radius. Therefore, other properties of the wall, such as thermal diffusivity will only play a role in the transient phase and are not considered here.
- Finally, the accommodation coefficient f, which reflects the influence of the micro-region model.

The range of these parameters are displayed in Table 5.1.

Parameter	Range of variation
θ_{mic}	10 - 30 - 50 (°)
$\text{Ja}_\text{c}/\text{Ja}_\text{e}$	2 - 5 - 10
$T_{\text{w,eq}} - T_{\text{sat}}$	1 - 1.5 - 2 (K)
$\lambda_\text{w}/\lambda_\text{liq}$	1.5 - 7.5 - 15 - 75 - 150
f	0.125 - 1

Table 5.1: Parameter variations for the parametric study

The study is conducted with water, which properties are displayed in Appendix C. When the conductivity ratio varies, only λ_w is changed, with values between 1 and 100. The wall thermal capacity and density are set to $C_{p,\text{w}} = 1500$ J.kg^{-1}.K^{-1}, and $\rho_\text{w} = 1400$ kg.m^{-3}.

More than 150 simulations have been performed for the parametric analysis, with mesh of 512×(512+256) for $L_x \times (L_y + L_{y,\text{w}})$, with constant mesh size of 6 µm. To reach equilibrium, simulations are performed with a time of 2.5 s. Simulation time highly depends on the parameters, but is estimated about $\sim$ 2000 h_CPU, hence about 300 000 h_CPU for the whole study. Each simulation has been performed with 16 or 32 cores, with approximately 4 or 2 days, respectively. Computations have been carried out at IMFT local clusters, and with CALMIP (Toulouse Regional Computational Center).

5.2 Results

5.2.1 Evolution of the equilibrium diameter

Most of the simulations performed are depicted in figures 5.5 and 5.6. The diameter evolution is shown on 2.5 s range. On each plot, six curves are drawn, for 3 different superheat/subcooling couples (colors) and for two accommodation parameter (markers). The ratio of thermal conductivity changes with the lines, while the Jakob number ratio changes with columns. Two plots, for two contact angles are depicted.

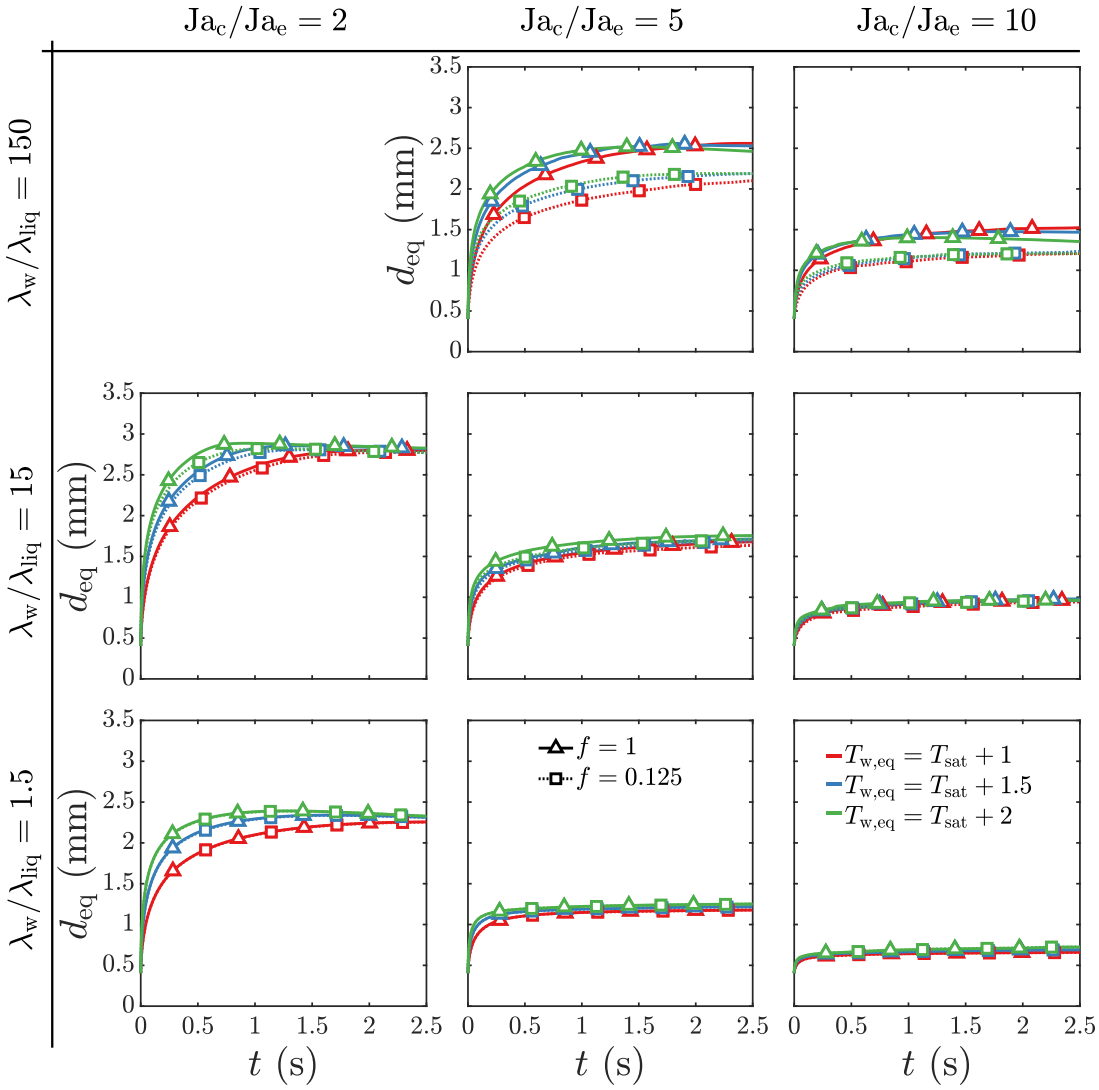

Figure 5.5: Bubble equivalent diameter for many configurations. $\theta_\mathrm{mic} = 10°$.

Prior early interpretation, a limitation in the simulations must be pointed out. It can be observed in left-middle plot ($\lambda_\mathrm{w}/\lambda_\mathrm{liq} = 15$, $\mathrm{Ja_c/Ja_e} = 2$) that all simulations converge on a same equilibrium radius whatever f and $T_\mathrm{w,eq}$. A snapshot of the bubble at equilibrium is displayed in figure 5.7. One can observe that the bubble reaches the size of the domain, and then is limited by it. This is not the case for higher Jakob ratio, as seen in figure 5.8. The boundary conditions at the top are imposed, and then the iso-temperature line are limited numerically by the boundaries, and are not physically consistent. The validity of these simulations can be

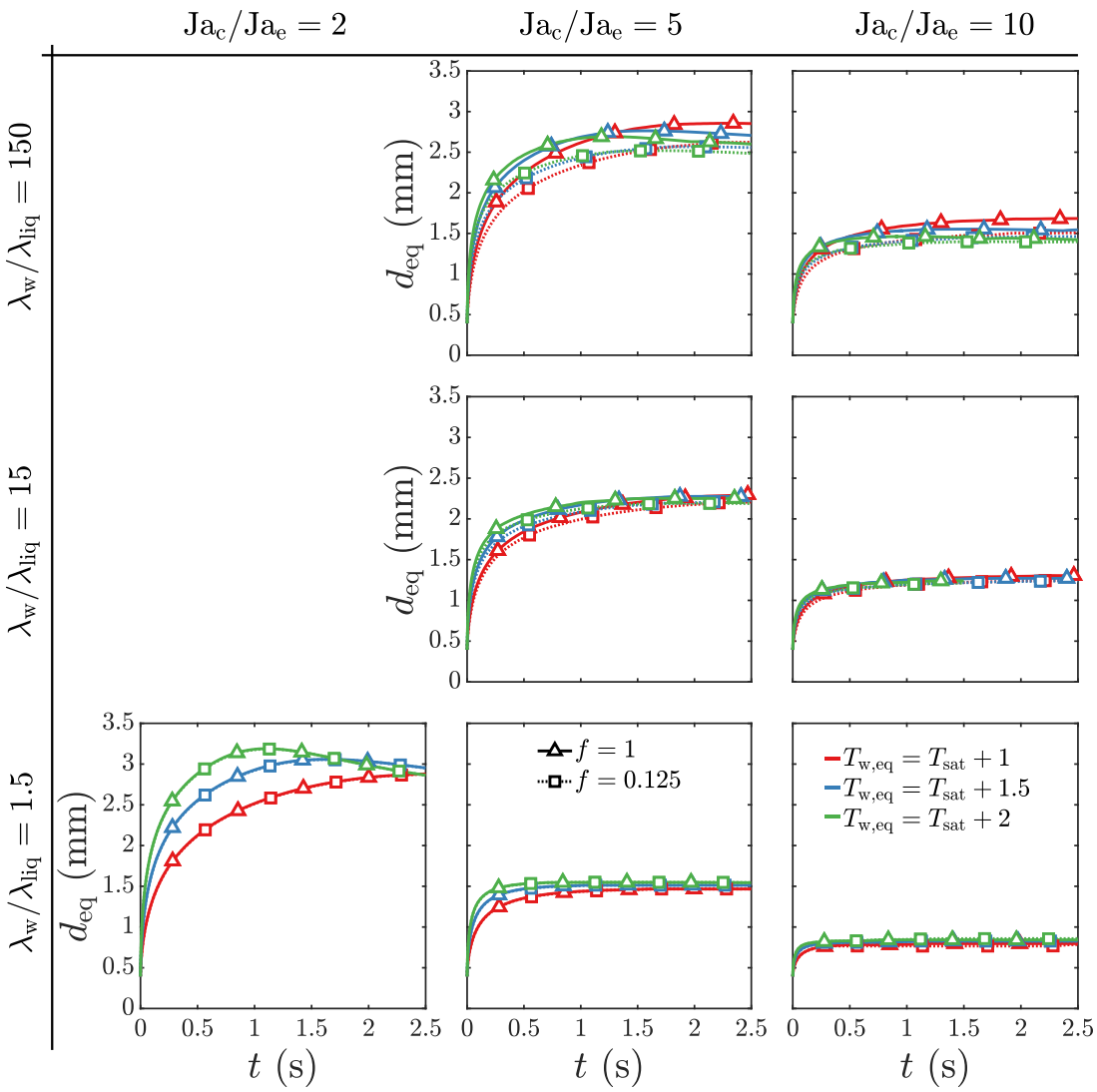

Figure 5.6: Bubble equivalent diameter for many configurations. $\theta_\mathrm{mic} = 50°$.

questioned, and therefore they will not be accounted for in the further interpretation. In light of these results, the simulations at high conductivity and low Jakob ratio have not been performed.

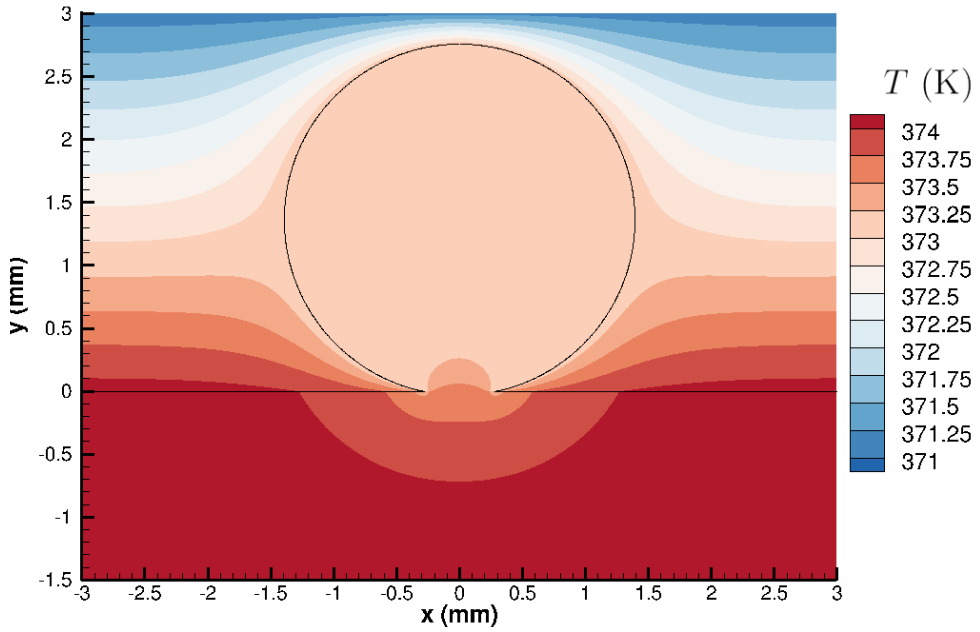

Figure 5.7: Snapshot of the bubble at equilibrium. $\lambda_w/\lambda_{liq} = 15$, $Ja_c/Ja_e = 2$.

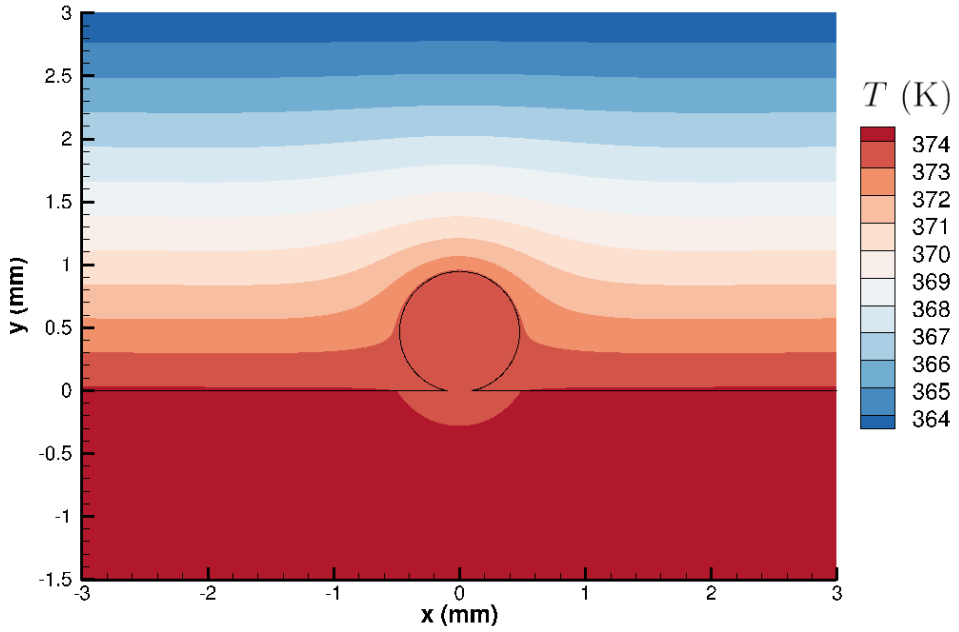

Figure 5.8: Snapshot of the bubble at equilibrium. $\lambda_w/\lambda_{liq} = 15$, $Ja_c/Ja_e = 10$.

On the global figures 5.5 and 5.6, the following tendencies can be deduced:

- Figure 5.5 is for $\theta_{mic} = 10°$, and figure 5.6 for $\theta_{mic} = 50°$. Globally, the values for high contact angles are slightly higher, which is consistent with the previous result and a consequence of the bubble geometry, since the surface in the superheated area is bigger.
- The subcooling/superheated couple for a given configuration only impacts the dynamic of the growth. Among a single plot, the higher the imposed superheat the faster the initial

growth. On longer time ranges, the three (for $T_{w,eq} = 1, 1.5, 2$) full (or dotted) lines lead to the same final equilibrium diameter. Such observations are consistent with the results of Urbano [83], which states that the bubble final radius does not depend on the temperature value but only on the Jakob number ratio. The result has been recalled in equation (5.3).

- With increasing the Jakob number ratio (left to right), the subcooling becomes more predominant compared to the superheating. As a consequence, the condensation is more important and the equilibrium diameter decreases.

- The thermal conductivity ratio has a strong impact on the bubble equilibrium diameter. The ratio increases from the bottom to the top plots, so that the value of d_{eq} is doubled between $\lambda_w/\lambda_{liq} = 1.5$ and $\lambda_w/\lambda_{liq} = 150$ for $Ja_c/Ja_e = 10$ (right plots, bottom and top).

- Finally, the impact of the accommodation coefficient is coupled with the thermal conductivity. For low values of λ_w/λ_{liq} (bottom), the influence of f is negligible, since full and dotted lines lead to the same equilibrium diameter. On the opposite, high values of conductivity ratio entails an increasing impact of f, with up to 20% difference in the equilibrium diameter between low and high values.

These five parameters are entangled with each other, and individual conclusions are difficult to draw. In the next part, these local effects are investigated, and influence of the parameters described more thoroughly.

5.2.2 Evolution of the contact line superheat and micro-region fluxes

Impact of λ_w/λ_{liq} and of f on the local superheat

Prior interpretation in this section, we believe useful to recall:

- T_w is the local superheat observed at the contact line: it is given as an output by the micro-region coupled with the DNS.

- $T_{w,eq}$ is the equilibrium temperature that will reach the whole solid/fluid interface in the absence of the bubble. It does not depend on the computation but only the evaporation Jakob Ja_e imposed.

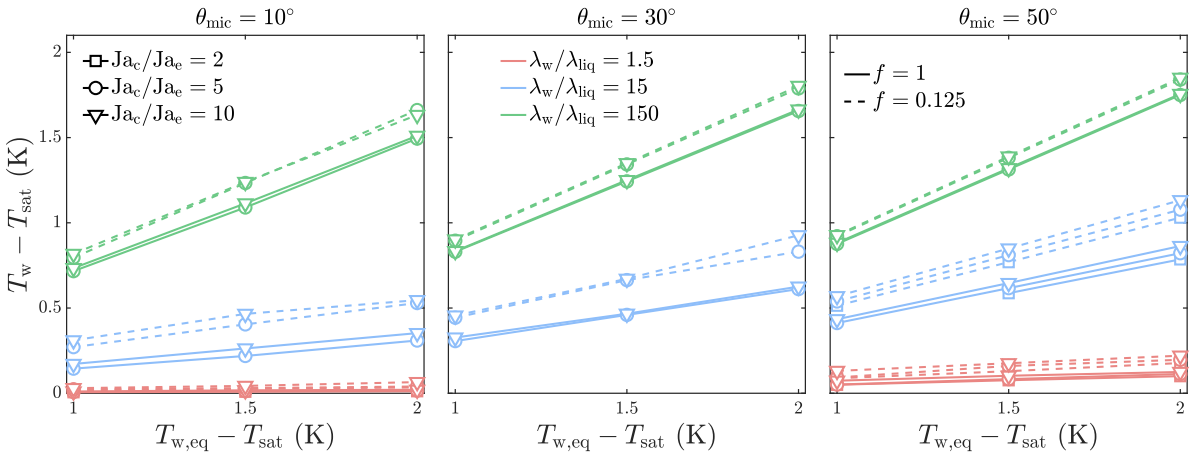

Figure 5.9: Evolution of the local superheat $T_w - T_{sat}$ given by the micro-region model with the imposed superheat $T_{w,eq} - T_{sat}$(or evaporation Jakob Ja_e). Since it has been observed soon that the influence of the micro-region model for low conductivity ratio was low, simulations for $\theta_{mic} = 30°$, $\lambda_w/\lambda_{liq} = 1.5$ have not been performed.

Figure 5.9 displays the evolution of the local **contact line** superheat with the **imposed** superheat.

The red points correspond to low values of λ_w/λ_{liq}, and it can be observed that the contact line superheat is always close to 0 for all Jakob number ratio, contact angle and imposed temperature. In this case, the wall has such a low conductivity that it is cooled down by the interface at the contact line, and therefore nearly reaches the liquid saturation temperature. Since the superheat is very low, so is the micro-region heat and mass fluxes. The nano-scale phenomenon becomes negligible. As λ_w/λ_{liq} increases, the local superheat gets more important, and as a result the heat flux increases (blue and green curves), and so does the bubble equivalent diameter d_{eq}.

The conductivity ratio is the main driver of the micro-region superheat and heat flux. On the other hand, one can observe that the values of the local superheat obtained with the model are higher for low value of f. This effect must be put into perspective: if the absolute value of the superheat is indeed higher, the associate heat flux is lower since the interfacial resistance for $f = 0.125$ is much larger, see figure 4.23. As a consequence, the impact of the micro-region is lowered. The impact on the heat flux is studied below.

Impact of λ_w/λ_{liq} and of f on the mass flux at the interface

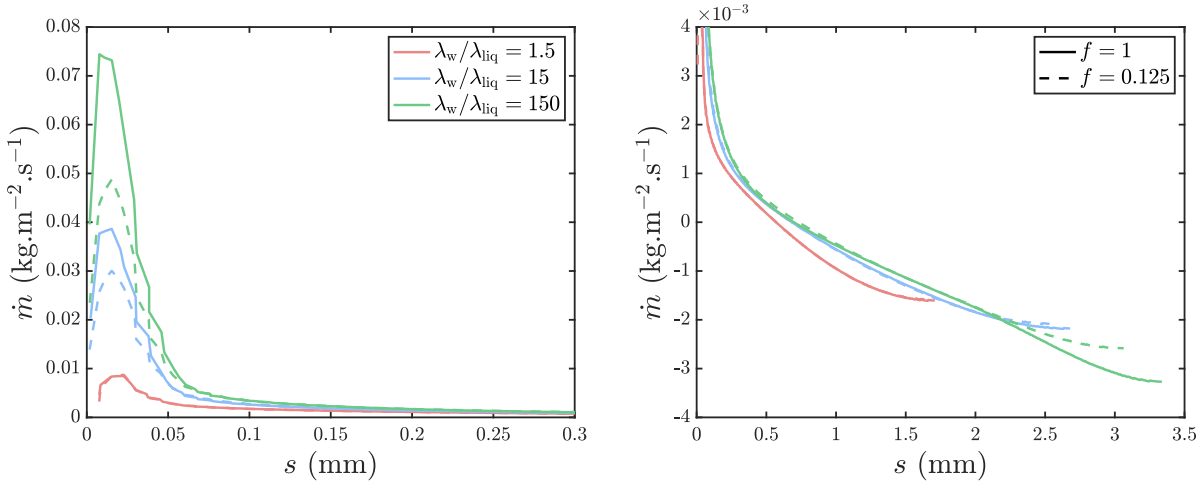

Figure 5.10: Mass flux along the interface. $\theta_{mic} = 50°$, $Ja_c/Ja_e = 5$, $T_{w,eq} - T_{sat} = 1$ K

Figure 5.10 shows the evolution of the mass flux along the interface, for the same fluid thermal conditions, with only variations of λ_w/λ_{liq} and f. The local heat flux in the vicinity of the contact line is increasing with the thermal conductivity ratio and the accommodation coefficient. This is consistent with the previous observation, as the increasing contact line temperature leads to an increase of the micro-region heat flux. Again, we observe that the contribution of the micro-region vanishes for low solid thermal conductivity, since the curves for $f = 1$ and 0.125 are identical.

On the left plot, the mass flux in the vicinity of the contact line is displayed; on the right plot, it is its value along the whole bubble interface. The mass flux decreases quickly with the distance, and reaches negative values on the top half of the bubble, where condensation occurs.

A deeper focus on the flux in the micro-region is displayed in figures 5.11 and 5.12, for $f = 1$ and 0.125, respectively.

In full (or dashed) line is shown the total evaporation mass flux along the curvilinear abscissa s, and in dotted line the total mass flux minus the micro-region. It must be first noted that both curves merge after about ~ 50 µm, corresponding to about 8 cells size in the present case ($\Delta x = 6$ µm). This is consistent with the spreading of the model described in part 4.3.3.

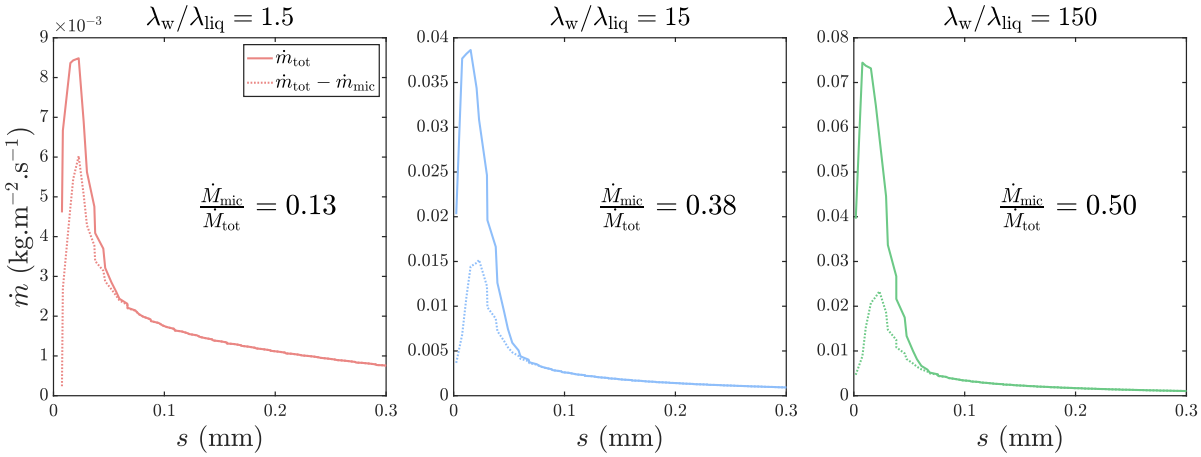

Figure 5.11: Contribution of the micro-region in the evaporation mass flux. $\theta_{mic} = 50°$, $Ja_c/Ja_e = 5$, $T_w - T_{sat} = 1$ K, $f = 1$.

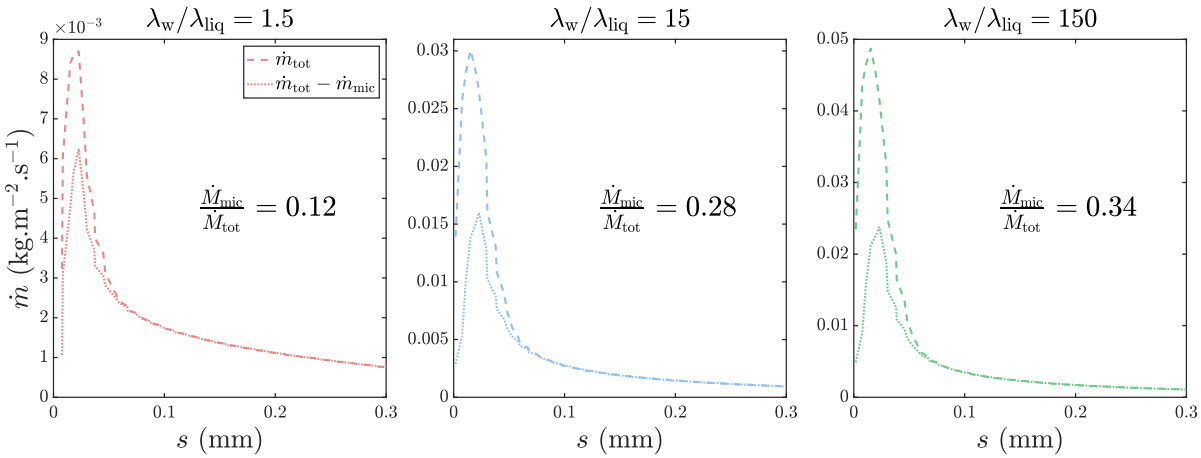

Figure 5.12: Contribution of the micro-region in the evaporation mass flux. $\theta_{mic} = 50°$, $Ja_c/Ja_e = 5$, $T_w - T_{sat} = 1$ K, $f = 0.125$.

Looking separately to figures 5.11 and 5.12, the same tendency is observed, with an increasing contribution of the micro-region mass flux to the global evaporation mass flux: for $f = 1$, this contribution raises from 13% at $\lambda_w/\lambda_{liq} = 1.5$ to 50% for $\lambda_w/\lambda_{liq} = 150$. Indeed, since increasing the conductivity ratio leads to higher values of the contact line superheat (see 5.2.2), the micro-region mass flux gets bigger. Moreover, high values of f lead to higher micro-region mass flux. Comparison between figures 5.11 and 5.12 shows that the contribution of the micro-region mass flux is higher for $f = 1$: for $\lambda_w/\lambda_{liq} = 150$, it is 50% against 34% for $f = 0.125$.

Therefore, the larger the solid thermal conductivity ratio, the higher the local superheat and hence the heat flux. The effect is increased if the accommodation coefficient is large. This study has been conducted for one local superheat, now is investigated the influence of its variation.

Impact of $T_{w,eq} - T_{sat}$ on the mass flux

It has been observed that the equilibrium diameter seemed independent of the imposed superheat in figures 5.5 and 5.6 (three line ending at the same value), in spite of obviously increasing micro-region contribution. In figure 5.13, the mass flux along the interface is displayed, for the same Jakob number ratio, but for two different superheat.

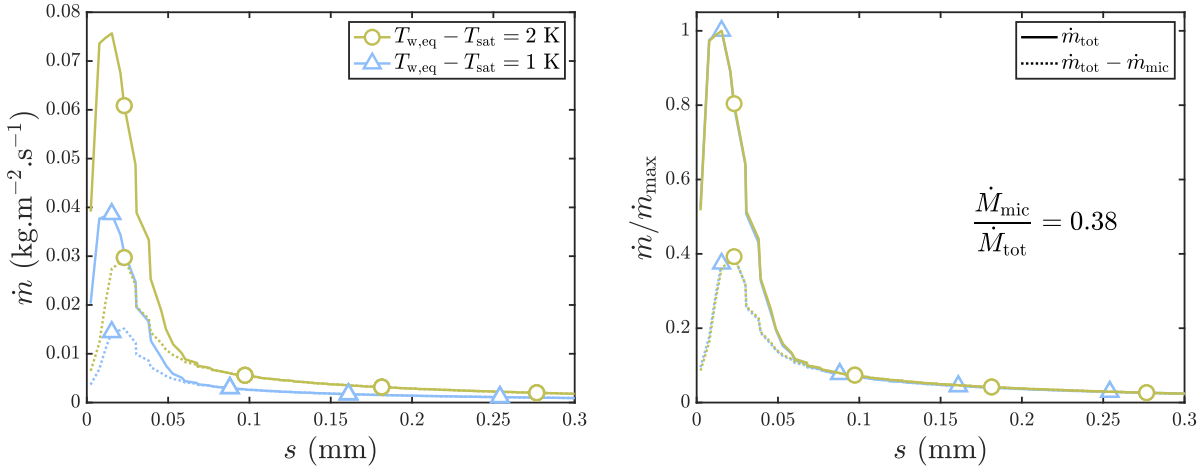

Figure 5.13: Contribution of the micro-region in the evaporation mass flux, with only a variation of $T_w - T_{sat}$ (or Ja_e). The case is the same as in figure 5.11, second plot. ($\theta_{mic} = 50°$, $Ja_c/Ja_e = 5$, $\lambda_w/\lambda_{liq} = 15$).

The blue curve is the same as shown in figure 5.11. The result for the simulation of the same λ_w/λ_{liq}, Ja_c/Ja_e and f, but with increased superheat is added in yellow. With a higher temperature, it is straightforward that the evaporation is improved, as the thermal gradients are. The total mass flux is about twice higher if the superheat is doubled, and so is the micro-region mass flux. If we normalize the curves by the maximum value of the evaporation mass flux (right plot), both curves perfectly superpose. This means the relative contribution of the micro-region to the total evaporation mass flux remains constant. When integrated all along the interface, the contribution of the micro-region to the overall evaporation is constant with the imposed superheat (or with evaporation Jakob Ja_e). It stays equal to 38% in the present case, which is medium conductivity ratio (10) and Jakob ratio (5). This means that, despite the increasing mass flux from the model, it is always balanced by the condensation at the top of the bubble. The micro-region contribution stays proportional to the superheat imposed.

All tendencies described above are the same for all contact angles. The values in term of local superheat at the contact line do not differ much, and are slightly higher for non-wetting fluids. However, attention should be paid to the contribution on bubble growth, which is different.

Indeed, as can be observed in figure 3.13 (left for water), for a given superheat, the micro-region heat flux highly depends on the contact angle value. Moreover, as the contact line radius is different, so is the integrated micro-region heat flux. Conclusions on the impact of contact angle on the overall bubble growth are not straightforward.

5.2.3 Construction of the correlation for R_{eq}

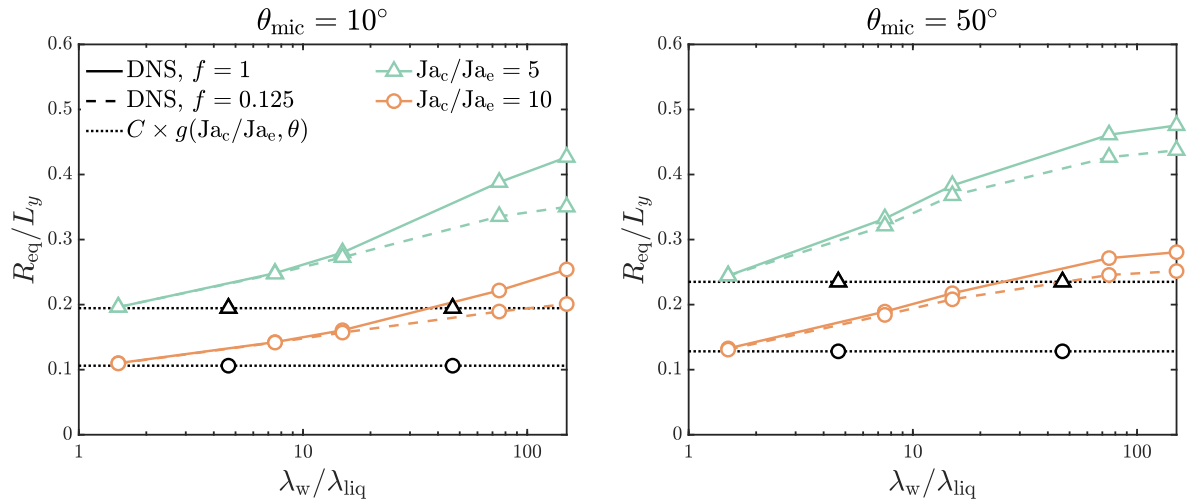

Figure 5.14: Evolution of bubble equivalent radius with λ_w/λ_{liq} and f. The correlation of [83] is depicted with dotted line.

In order to account for f and to the conductivity ratio λ_w/λ_{liq}, a correction for the correlation (5.3) is now investigated. In figure 5.14, the variation of the R_{eq}/L_y is shown for different conductivity ratio and accommodation coefficient. The correlation of Urbano is also displayed, and, as expected, matches well for low solid thermal conductivity since it was drawn with the same wall properties. It should also be noted that it is in this case unrelated to the accommodation coefficient. Therefore, the correction we are looking for cannot be separated into two independent contribution of λ_w/λ_{liq} and f. However, figure 5.14 clearly shows linear dependence of R_{eq}/L_y on $\log_{10}(\lambda_w/\lambda_{liq})$. The slopes slightly vary with f, θ_{mic} and $\mathrm{Ja_c/Ja_e}$. Due to the non-linearity expected with the micro-region contribution and the only two values used, we think more reasonable to remove f from the correlation, and create two separate functions, for $f = 1$ and 0.125. Then, we assume equation (5.3) can be modified into

$$\frac{R_{eq}}{L_y} = C \times g\left(\frac{\mathrm{Ja_c}}{\mathrm{Ja_e}}, \theta\right) \times \left(1 + h_f\left(\frac{\mathrm{Ja_c}}{\mathrm{Ja_e}}, \theta\right) \times \left(\log_{10}\left(\frac{\lambda_w}{\lambda_{liq}}\right) - r_\lambda\right)\right) \tag{5.9}$$

The function h_f aims to correct the correlation of Urbano, which has been established for $\lambda_w/\lambda_{liq} = 1.5$. We will therefore consider $r_\lambda = \log_{10}(1.5) = 0.1761$ so that both correlations match. The function h_f will be called h_1 for $f = 1$ and h_0 for $f = 0.125$. The value of h is plotted on figure 5.15.

Globally, the influence of f on the slope is straightforward comparing left and right plots. The value is lowered if the accommodation coefficient is low. This result is expected as the micro-region heat flux is reduced and so goes the bubble radius. On the other hand, the influence of both $\mathrm{Ja_c/Ja_e}$ and θ are more subtle. The slope only slightly varies. Data fitting finds a very low dependency on the contact angle, so that it has been neglected on the correlation: $h_f\left(\frac{\mathrm{Ja_c}}{\mathrm{Ja_e}}, \theta\right) \to h_f\left(\frac{\mathrm{Ja_c}}{\mathrm{Ja_e}}\right)$. With this simplifying, we are able to find h_f for $f = 1$:

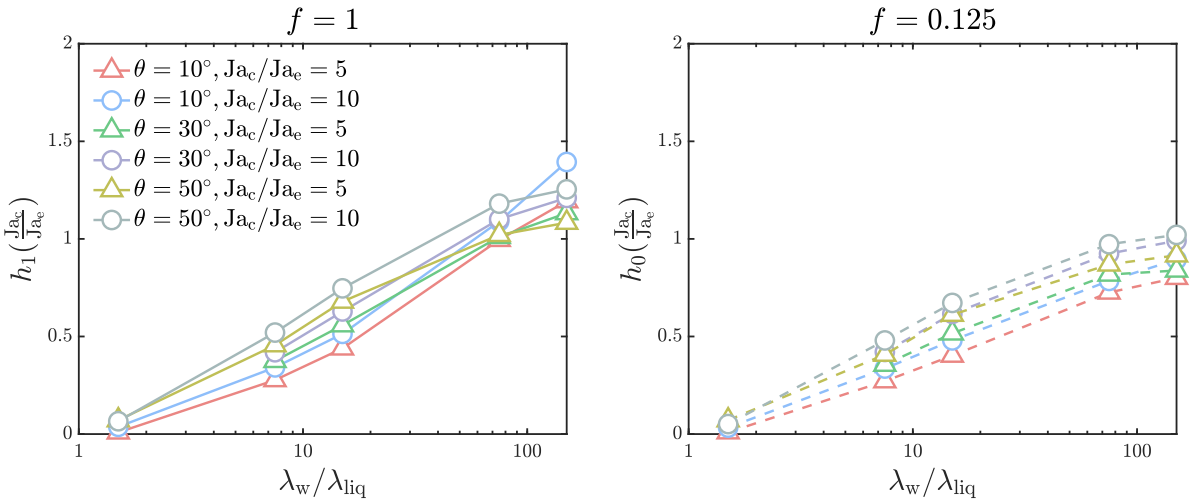

Figure 5.15: Evolution of h function.

$$h_1\left(\frac{\mathrm{Ja_c}}{\mathrm{Ja_e}}\right) = C_1 \times \left(C_{\mathrm{Ja},1} + \frac{\mathrm{Ja_c}}{\mathrm{Ja_e}}\right) \tag{5.10}$$

With

$$\begin{cases} C_1 = & 1.457.10^{-2} & (5.11a) \\ C_{\mathrm{Ja},1} = & 34.33 & (5.11b) \end{cases}$$

And for $f = 0.125$:

$$h_0\left(\frac{\mathrm{Ja_c}}{\mathrm{Ja_e}}\right) = C_0 \times \left(C_{\mathrm{Ja},0} + \frac{\mathrm{Ja_c}}{\mathrm{Ja_e}}\right) \tag{5.12}$$

With

$$\begin{cases} C_0 = 1.228.10^{-2} & (5.13a) \\ C_{\mathrm{Ja},0} = 32.13 & (5.13b) \end{cases}$$

Which gives full correlations:

$$\left.\frac{R_{\mathrm{eq}}}{L_y}\right|_{f=1} = 1.158 \times g\left(\frac{\mathrm{Ja_c}}{\mathrm{Ja_e}}, \theta\right) \times \left(1 + C_1\left(C_{\mathrm{Ja},1} + \frac{\mathrm{Ja_c}}{\mathrm{Ja_e}}\right) \times \left(\log_{10}\left(\frac{\lambda_w}{\lambda_{liq}}\right) - r_\lambda\right)\right) \tag{5.14}$$

$$\left.\frac{R_{\mathrm{eq}}}{L_y}\right|_{f=0.125} = 1.158 \times g\left(\frac{\mathrm{Ja_c}}{\mathrm{Ja_e}}, \theta\right) \times \left(1 + C_0\left(C_{\mathrm{Ja},0} + \frac{\mathrm{Ja_c}}{\mathrm{Ja_e}}\right) \times \left(\log_{10}\left(\frac{\lambda_w}{\lambda_{liq}}\right) - r_\lambda\right)\right) \tag{5.15}$$

The coefficients found by data fitting are consistent with the dependency on f since $C_1 > C_0$. Values of $C_{\mathrm{Ja},1}$ and $C_{\mathrm{Ja},0}$ are close. A plot for the correlation (5.14) is displayed in figure 5.16, for a given $\theta_{\mathrm{mic}} = 50°$. The different conductivity ratios are shown with 5 colored curves.

Both correlations show good agreement with the simulated results, as observed in figure 5.17. However, the limitations for this correlation are important. The influence of θ has been neglected since it is low, but its influence could be noticed. By looking closely to plots 5.17, a pattern can be observed, with a slight underestimation of the bubble radius for low contact angle, and slight overestimation at high contact angles, which could be corrected. Moreover, the correlation of

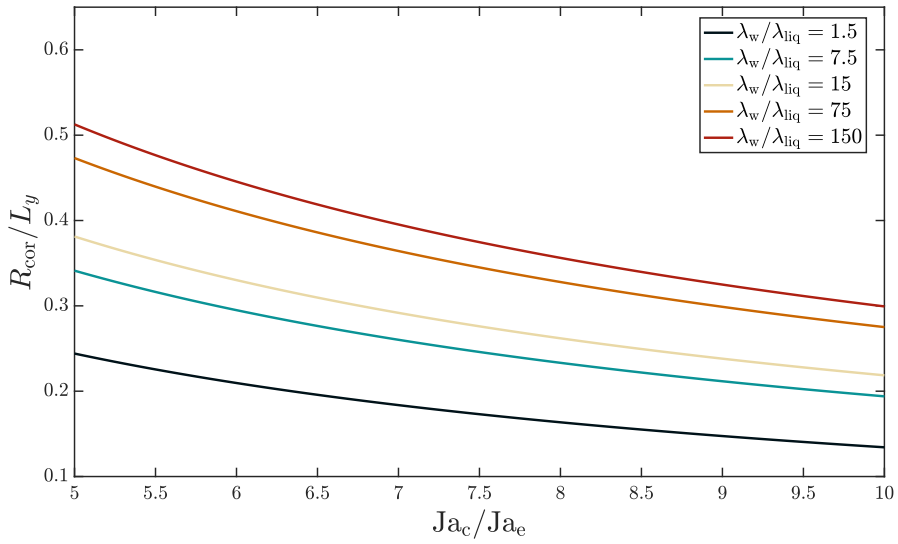

Figure 5.16: Correlation result for different λ_w/λ_{liq}. Case for $f = 1$ and $\theta_{mic} = 50°$.

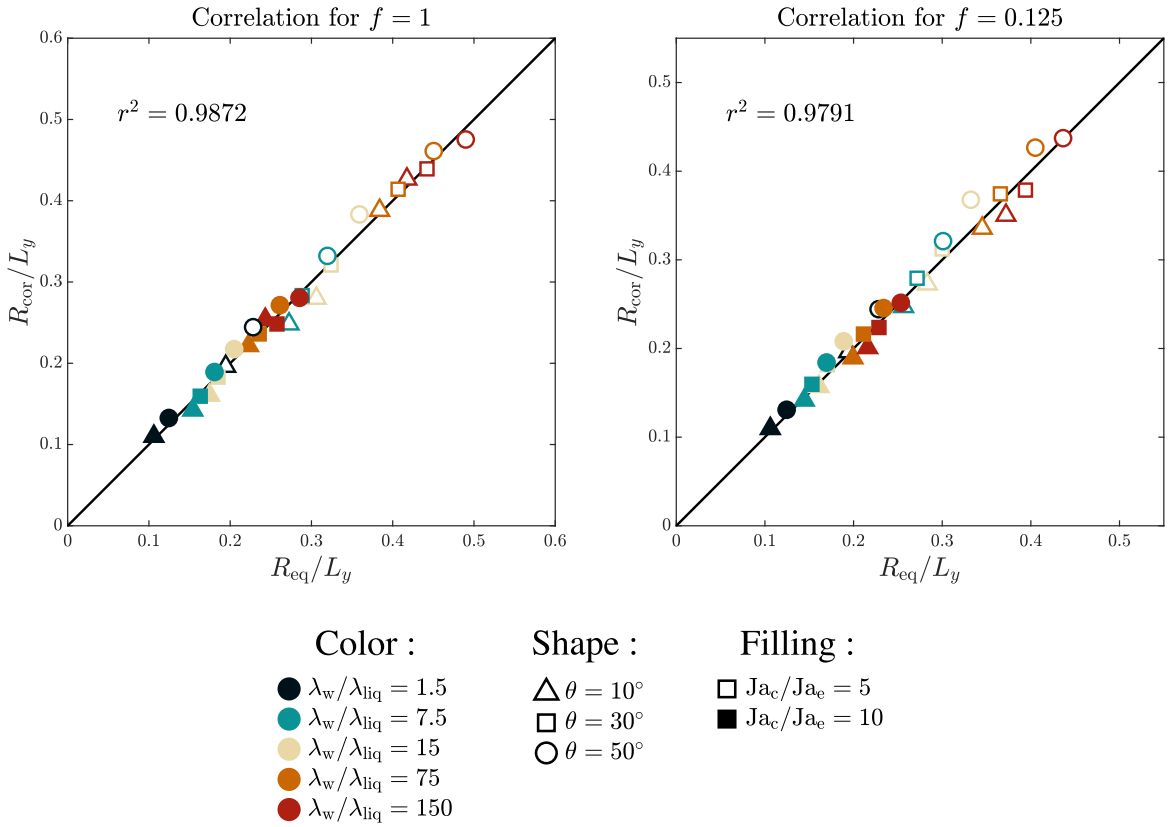

Figure 5.17: Correlation vs simulation results for two values of f.

Urbano is based on the apparent contact which does not vary with DNS-NMR ($\theta_{app} = \theta_{mic}$). In the present case, the value used for the correlation is based on the microscopic contact angle θ_{mic}, and do not account for the variations due to the superheat. Nevertheless, since the superheat considered is always low, only slight variations have been observed: in the worst case for $\theta_{mic} = 10°$, the output value for the apparent contact angle is 14.7°, reached for the highest conductivity ratio, whereas most of the case entails variations lower than 1° and are negligible. Therefore, if more important superheat are considered, a correction will be required.

Finally, the Jakob number ratio limited values must be highlighted. Only two values 5 and 10 have been used. However, a few cases out of the range of the correlation have been tried and show good agreement. As an example, the equilibrium radius of a bubble for $\lambda_w/\lambda_{liq} = 15$, $\theta = 50°$, $f = 1$, but with $Ja_c/Ja_e = 20$ is 0.310 mm, which displays only 2% difference with the expected value from the correlation even though the Jakob ratio is far from the values used to create the correlation.

5.2.4 Study of the Nusselt number

At the wall, the heat transfer is strongly affected by the bubble, as seen in figure 5.18. On the left ($x \to 0$), the heat flux is strongly reduced due to the vapor, which insulates the wall: the flux drops of about one order of magnitude because of the low conductivity of the vapor compared to the liquid. A peak is reached at the contact line position. Then, the heat flux decreases, reaching its stationary value $q''_{w,0}$ when $x \to \infty$. It is the heat flux we would obtain without nucleate boiling. It is independent from the solid conductivity, and its value is given by

$$q''_{w,0} = \lambda_{liq} \frac{T_{w,eq} - T_{sub}}{L_y} \tag{5.16}$$

To compute the Nusselt number Nu, we compute the total heat flux crossing the wall with

$$q_{tot} = \int_0^{L_x} \lambda \frac{dT}{dy}\bigg|_w 2\pi r \, dr \tag{5.17}$$

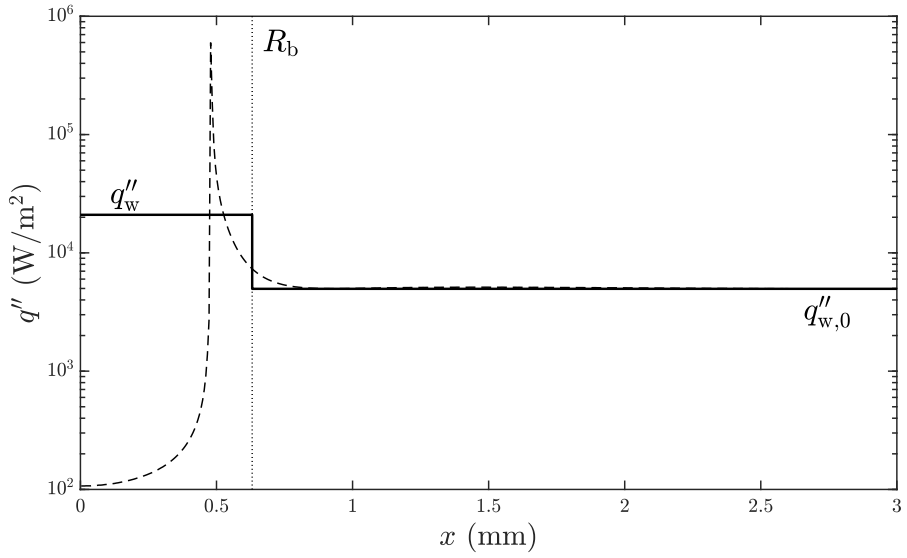

Figure 5.18: Heat flux across the wall

The Nusselt number correspond to the ratio between the real heat flux with the bubble and the heat flux without nucleate boiling. Question on how to compute the heat flux must be asked. Indeed, as the heat flux is disturbed only in the vicinity of the contact line, taking a too

long integration length would lose the local effect and would lead to Nu $\to$ 1. In our case, the length is chosen equal to the bubble radius R_b (different from the equivalent bubble radius R_eq, see Appendix B). Afterwards, we can separate the two contributions q''_w and $q''_{\mathrm{w},0}$ which acts on different surfaces:

$$q_\mathrm{tot} = q''_\mathrm{w}\pi R_\mathrm{b}^2 + q''_{\mathrm{w},0}\pi\left(L_x^2 - R_\mathrm{b}^2\right) \tag{5.18}$$

In this equation, only q''_w is unknown and computed with the post-process, by straightforward deduction of equation (5.18)

$$q''_\mathrm{w} = \frac{q_\mathrm{tot}}{\pi R_\mathrm{b}^2} - q''_{\mathrm{w},0}\frac{L_x^2 - R_\mathrm{b}^2}{R_\mathrm{b}^2} \tag{5.19}$$

Figure 5.18 shows the heat flux distribution along the wall (dash line), and the model of equation (5.18).

Then, we define the Nusselt number as the ratio between the two heat fluxes:

$$\mathrm{Nu} = \frac{q''_\mathrm{w}}{q''_{\mathrm{w},0}} \tag{5.20}$$

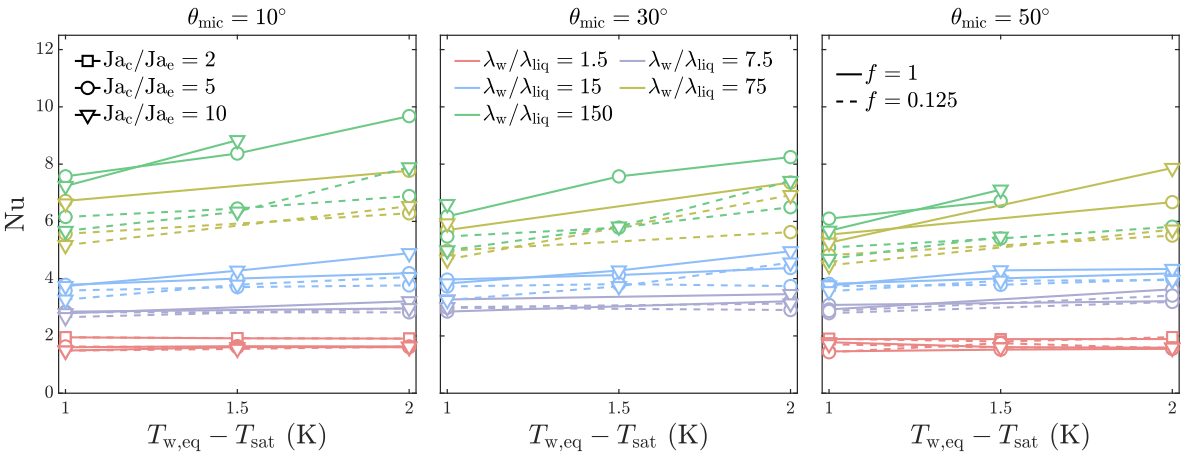

Figure 5.19: Evolution of the Nusselt number.

The values of the Nusselt numbers are displayed in figure 5.19. The conductivity ratio $\lambda_\mathrm{w}/\lambda_\mathrm{liq} = 7.5$ and 75 have been added for some cases. The variations are a bit more complex to analyse compared to the bubble radius. The establishment of a correlation, due to some instabilities in the Nusselt numerical computation, has not been performed. Instead, the global variations with the parameters are described:

- The microscopic contact angle has very low influence on the Nusselt number variations. The values are slightly reduced at high conductivity if the contact angle increases.

- The main driver of the Nusselt number is the conductivity ratio. As a first approximation, ten times more conductive wall doubles the heat exchange compared to a fluid without bubble. At low conductivity, the heat is twice as effective as a purely conductive flux; it rises to eight times for very high conductivity ratio.

- The accommodation coefficient has an influence only at high conductivity. The micro-region is negligible for $\lambda_\mathrm{w}/\lambda_\mathrm{liq} \sim 1.5$, but for 150 it increases the flux by about 20% between $f = 0.125$ and $f = 1$.

- The Nusselt number is nearly independent on $\mathrm{Ja_c}/\mathrm{Ja_e}$, despite large dependence of the equilibrium radius on this parameter. For a given value of $\lambda_\mathrm{w}/\lambda_\mathrm{liq}$ and f, the curves cross each other, but in average, it is hard to spot a regular behavior.

- A linear evolution of the Nu with $T_\mathrm{w,eq} - T_\mathrm{sat}$ (or $\mathrm{Ja_e}$) is always observed. The slope is zero for low conductivity, but increases with it. In this study, only low values have been considered. Since on such reduced scales, the heat flux increases linearly with the superheat, this result is consistent. Therefore, this may not be the case on larger superheat.

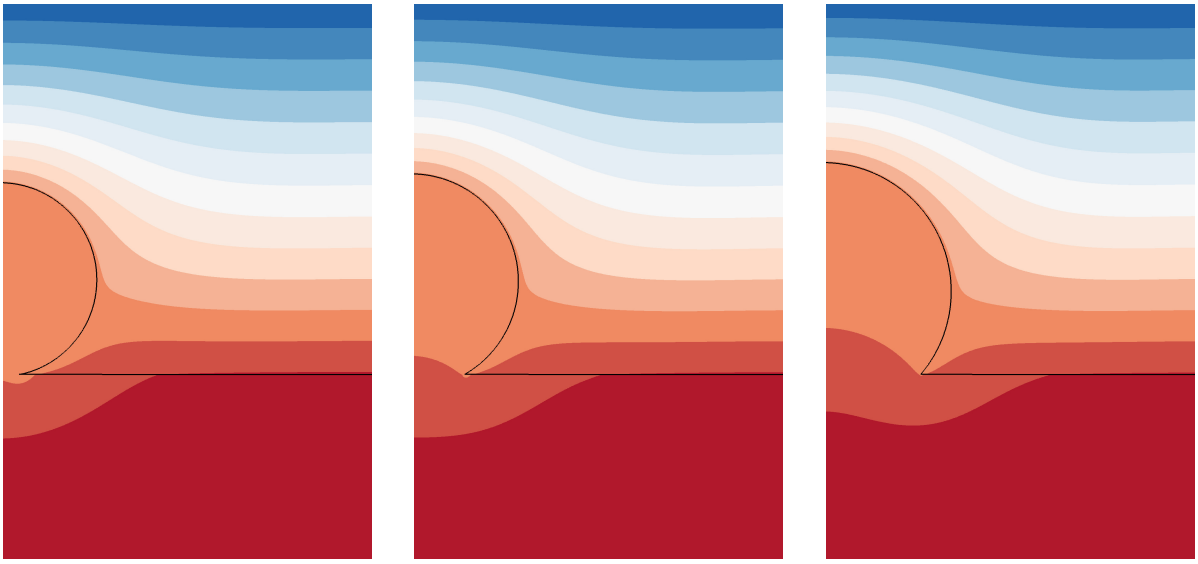

$\theta_\mathrm{mic} = 10°$ $\theta_\mathrm{mic} = 30°$ $\theta_\mathrm{mic} = 50°$

Figure 5.20: Configuration $\lambda_\mathrm{w}/\lambda_\mathrm{liq} = 7.5$, $\mathrm{Ja_c}/\mathrm{Ja_e} = 5$, $T_\mathrm{w,eq} - T_\mathrm{sat} = 2$ K, $f = 1$ for different contact angle.

Figure 5.20 displays snapshots of bubble at equilibrium for different contact angle. The configuration is specified in caption. The Nusselt number in three cases is nearly the same, despite obviously different bubble radius and contact line radius. In such case, it is surprising that the Nusselt number does not vary. In practise, as we calculate it, the Nusselt number is based on a model depending of the surface πR_b^2, so they are all computed on a different basis. This must be kept in mind when using this correlation. As we obtained equations (5.14) and (5.15):

$$\begin{cases} \left.\dfrac{R_\mathrm{eq}}{L_y}\right|_{f=1} = \psi_1\left(\theta, \dfrac{\mathrm{Ja_c}}{\mathrm{Ja_e}}, \dfrac{\lambda_\mathrm{w}}{\lambda_\mathrm{liq}}\right) & \text{(5.21a)} \\ \left.\dfrac{R_\mathrm{eq}}{L_y}\right|_{f=0.125} = \psi_0\left(\theta, \dfrac{\mathrm{Ja_c}}{\mathrm{Ja_e}}, \dfrac{\lambda_\mathrm{w}}{\lambda_\mathrm{liq}}\right) & \text{(5.21b)} \end{cases}$$

And considering R_b can be found out using the following equation:

$$R_\mathrm{eq} = R_\mathrm{b}\left(\frac{4 - (2+\cos\theta)\,(1-\cos\theta)^2}{4}\right)^{1/3} \tag{5.22}$$

We obtain the following equation for the bubble radius R_b

$$\begin{cases} \left.\dfrac{R_\mathrm{b}}{L_y}\right|_{f=1} = \psi_1\left(\theta, \dfrac{\mathrm{Ja_c}}{\mathrm{Ja_e}}, \dfrac{\lambda_\mathrm{w}}{\lambda_\mathrm{liq}}\right)\left(\dfrac{4}{4-(2+\cos\theta)\,(1-\cos\theta)^2}\right)^{1/3} & \text{(5.23a)} \\ \left.\dfrac{R_\mathrm{b}}{L_y}\right|_{f=0.125} = \psi_0\left(\theta, \dfrac{\mathrm{Ja_c}}{\mathrm{Ja_e}}, \dfrac{\lambda_\mathrm{w}}{\lambda_\mathrm{liq}}\right)\left(\dfrac{4}{4-(2+\cos\theta)\,(1-\cos\theta)^2}\right)^{1/3} & \text{(5.23b)} \end{cases}$$

From the bubble radius, we can deduce the equivalent projected surface of the bubble on the wall. Thus, for a given nucleate site density, the heat transfer coefficient between the heat wall and the fluid can be determined directly, and does not require DNS of the whole surface and all the bubbles. This result is of utmost importance for a partition model, since it is how is defined the evaporation contribution of the global heat transfer:

$$q''_{\mathrm{w,tot}} = n\pi R_\mathrm{b}^2 q''_\mathrm{w} + (1 - n\pi R_\mathrm{b}^2) q''_{\mathrm{w},0} \tag{5.24}$$

with n the density of nucleation site. If $T_{\mathrm{w,eq}}$ is known, R_b, q''_w can be calculated. q''_w is known by single phase flow correlation.

5.2.5 Global variations

From the observation previously described, the global variations of the equilibrium diameter, Nusselt number and local superheat as function of the input can be summarized in the following table:

		d_eq	Nu	T_w
↗	$\lambda_\mathrm{w}/\lambda_\mathrm{liq}$	↗	↗	↗
	θ_mic	↗	↘	↗
	f	↗	↗	↘
	$\mathrm{Ja_c}/\mathrm{Ja_e}$	↘	→	→
	$T_{\mathrm{w,eq}} - T_\mathrm{sat}$	→	↗	↗

Table 5.2: Table of variations, summary of the parametric study.

The influence of all the parameters on the equilibrium diameter and Nusselt number have been described in details. The dependency of the Nusselt number on the Jakob ratio has not been observed in our case, or at least neglected. In the work or Urbano [83], a very low influence has been noticed. Yet, we consider here fewer variation. The absence of change of the equilibrium diameter with the imposed superheat was not expected as well. It may also be due to the low variations observed in our cases (between 1 and 2 K).

5.3 Limitations for non-static configurations

In all the simulations presented previously, as we were investigating on the equilibrium diameter, the aspect of contact line velocity has not been considered. Even in the RUBI experiment, the contact line velocities were very low ($\sim 1-2$ mm/s, leading to capillary number of about 10^{-4}). In the case of usual gravity conditions and due to buoyancy, the contact line is expected to move faster. Here is quickly investigated its influence on the micro-region model and on the overall bubble growth.

In figure 5.21, the equivalent diameter and bubble contact line radius evolution are shown, in a configuration with gravity conditions, at high contact angle. This simulation is the same as [77], mentioned earlier in section 4.5.1, and here considered with $f = 1$, with the assumption of static contact line (brown), and dynamic contact line (yellow). In this case, accounting for the

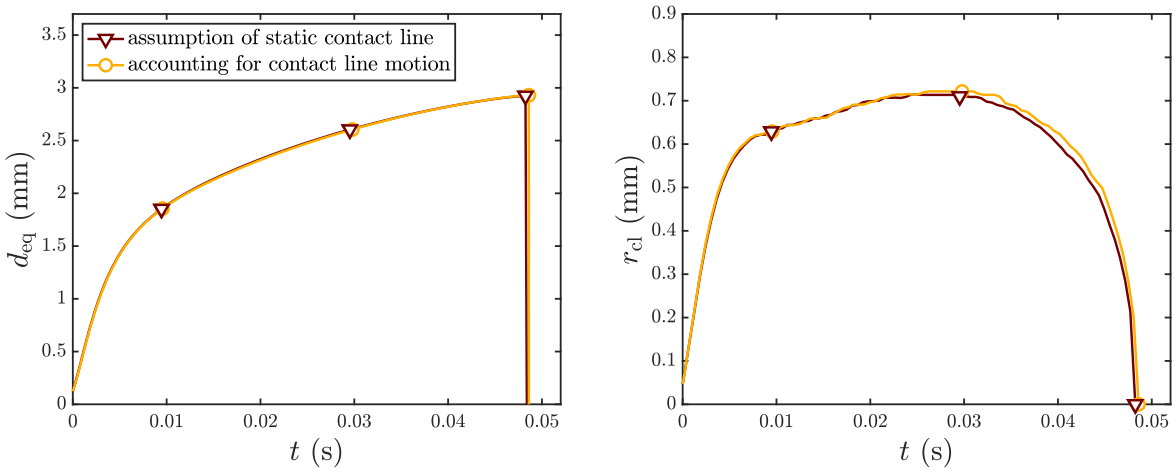

Figure 5.21: Simulation of DNS-SMR, with assumption of static contact line, and with dynamic model.

motion of the contact line does not bring any improvement, as the contact angle is not modified with both superheat or velocity. Hereafter in figure 5.22 is displayed the apparent contact angle evolution with the superheat, for $\theta_{mic} = 10°$ and $50°$. Note that scales are very different.

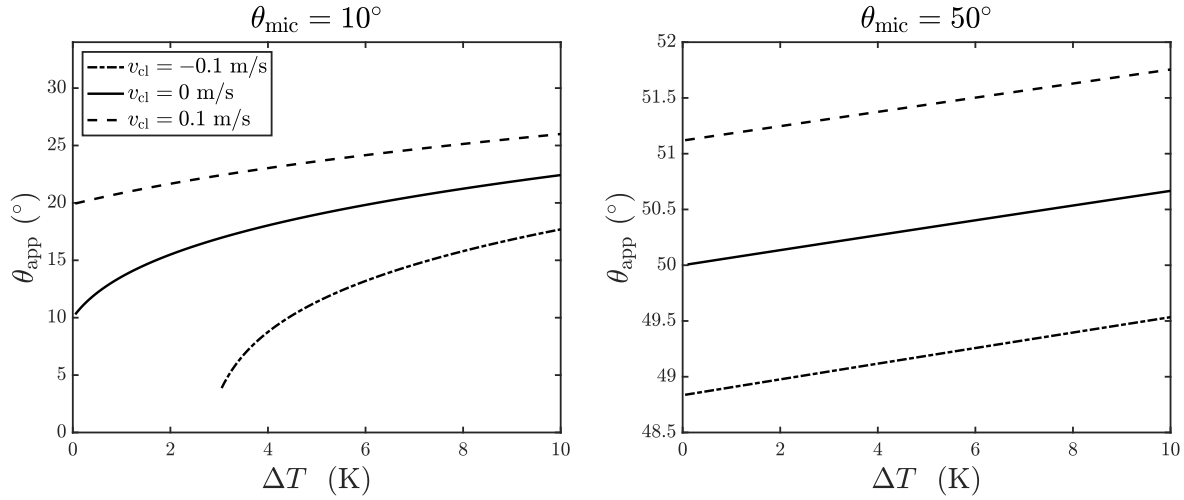

Figure 5.22: Influence of the contact line velocity on the apparent contact angle for two θ_{mic}. Scales are very different between the two.

It is straightforward to see that the contact angle variation is negligible in the 50° case. The very low difference observed in figure 5.21 is only explained by the heat flux variation with contact line velocity, which is low as well. On the other hand, due to the very high dependency of the contact angle on the velocity for more wetting fluids, the 10° case is expected to have more important variations. Results are shown in figure 5.23.

In this case, the equilibrium diameter variation is low and the detachment time is slightly reduced. In both cases, the solid thermal conductivity is high compared to water conductivity, hence the wall temperature is nearly constant. With the static case, the contact angle only depends on the temperature, and is therefore constant. With the dynamic consideration, it is the opposite: the contact angle is mainly influenced by the velocity, and vary from 25° (advancing contact line) to 15° (receding). The drop of the contact angle value in the receding phase of the bubble life explains the acceleration of the detachment.

Therefore, with partially wetting fluid and for dynamic configurations, attention must be paid to the contact line velocity. Mathieu's model is able to account for it since the velocity can

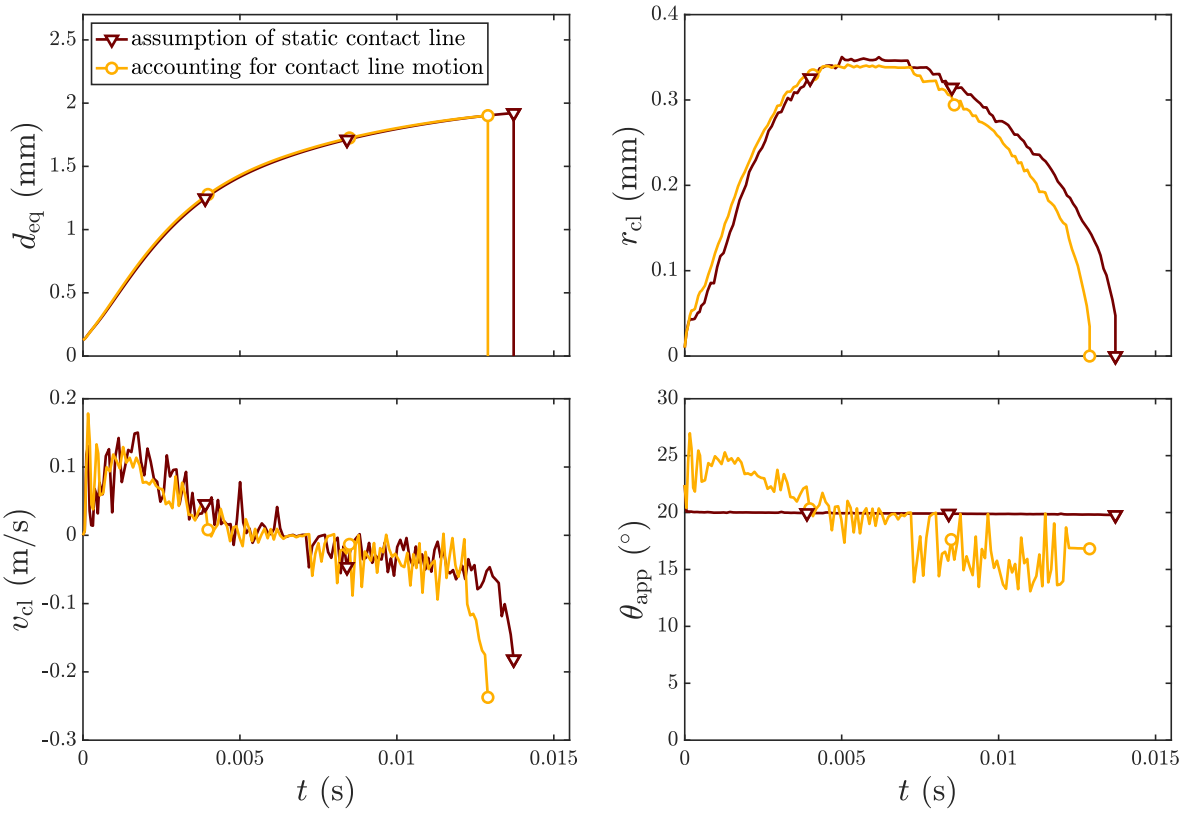

Figure 5.23: Same simulation as in figure 5.21, with $\theta_{mic} = 10°$, $f = 1$.

easily be inserted as one more input parameter. The details has not been presented, but the coupling has been improved to account for the contact line velocity, as shown in the simulation of figures 5.21 and 5.23.

5.4 Conclusion of the chapter

In this chapter, the influence of the micro-region on simulations has been investigated. The study carried out by Urbano et al has been continued, and the impact of the different parameters of the models quantified. Moreover, the influence of the wall properties, usually disregarded, is displayed of uppermost importance on the bubble dynamics.

To highlight these aspects, a correlation on the bubble equilibrium diameter has been computed. The heat flux, through the Nusselt number has been investigated despite no correlation has been clearly established . They provide a major tool to predict the heat transfer between a bubble and a superheated wall. However and as mentioned in the previous chapter, the variability of major parameters, such as the accommodation coefficient, is difficult to assess. That is why two correlations have been established for the two f tested. Yet, further works should require more value to improve the correlation.

Chapter 6

Outlooks: Simulation of boiling in micro-layer regime

These recent years, numerous numerical simulations of boiling in micro-layer regime have been performed [84, 85, 87, 90, 93, 94]. In some of the studies, since the computational cost of low scale simulation is expensive, empirical models of Cooper on the film thickness were used. To our knowledge, no complete simulation of the micro-layer flow dynamics, accounting for micro-region heat flux has been performed. As the contact line also exists in the micro-layer (whereas it can't be separated from the micro-layer heat flux in the experiments) and considering that both phenomena act at different scales one can assume they are spatially decoupled. This suggests that a micro-region could exist inside the micro-layer since the latter is much thicker that the micro-region. Therefore, preliminary simulations are performed to investigate on the influence of the micro-region in boiling in the micro-layer regime. In the present chapter, a first comparison with numerical simulation with micro-region model and the experiment of Bucci [22] is performed.

Contents

6.1 Experiment of Bucci 112
6.1.1 Configuration setup 112
6.1.2 Simulation results 114
6.2 Conclusion on micro-layer simulations 119

6.1 Experiment of Bucci

6.1.1 Configuration setup

The configuration of the simulations is described in Bureš [95], and corresponds to an experiment carried out by Bucci [22]. This experiment shows some similarities with the Multiscale Boiling Experiment described in subsection 1.1.4 and used for the validation of the micro-region models 4.4. the setup is shown in figure 6.2.

A Joule heat flux is set on in a titanium layer along the simulation, generating a thermal layer in both liquid and solid. The heat flux q'' is imposed at the interface between the fluid and the wall, via the volumic heat flux q'''. The solid is a sapphire plate for the IR-transparent properties, and the fluid is water, initially at saturation temperature. After a short time ($t = 88.1$ ms), a spherical bubble with a radius of 10 µm is nucleated. This heat flux is variable in the r-coordinate, and is calculated so that it analytically matches the temperature values of the experiment.

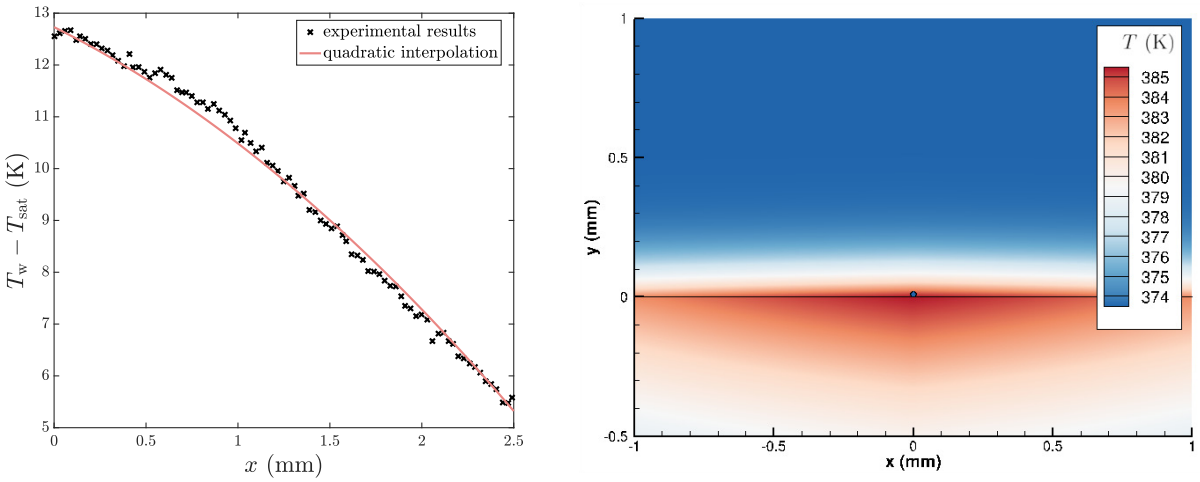

Figure 6.1: Initial temperature profile at the wall (left), and deduction of the fluid profile (right)

In figure 6.1 is shown the initial temperature profile, and the quadratic interpolation performed which leads to the initial condition used in the DNS. Moreover, from this initial profile is computed the heat flux, which therefore is x-dependent, similarly as in Appendix A.1. A quadratic interpolation for the heat used is deduced, and imposed as a density heat flux, as in the RUBI simulation. However, the heat fluxes involved are much bigger, as the latent heat of vaporization of water is about 25 times more important than FC-72. The initial superheat observed at nucleation time is about 12.56 K above saturation temperature, which corresponds to a value of $\mathrm{Ja_e} = 37.6$. Such value refers to micro-layer regime, as highlighted by Urbano [84].

Our simulations are performed on a square fluid domain $1{\times}1$ mm^2, and a 0.5 mm thick sapphire wall of thermal conductivity $\lambda_w = 25.1$ W.m^{-1}.K^{-1}. Due to the thin micro-layer thickness that has to be captured, simulations are performed with very refined uniform grid of $4096{\times}(4096{+}2048)$ elements for $L_x \times (L_y + L_{y,w})$, which corresponds to a cell size of 250 nm for which space convergence has been demonstrated for micro-layer simulations presented in [84]. Simulations have been performed with both DNS-SMR and DNS-NMR in order to evaluate the impact of the micro-region heat flux in such a configuration. The microscopic contact angle is taken at $\theta_{mic} = 30°$. The previous study in section 4.5.1 has demonstrated that for water, the accommodation should be lowered. In this chapter for micro-layer computation, f is taken equal to 0.005 in order to have the accurate coupling with the wall and not to account for a too high micro-region heat flux in the vicinity of the contact line. The result of the model for a superheat

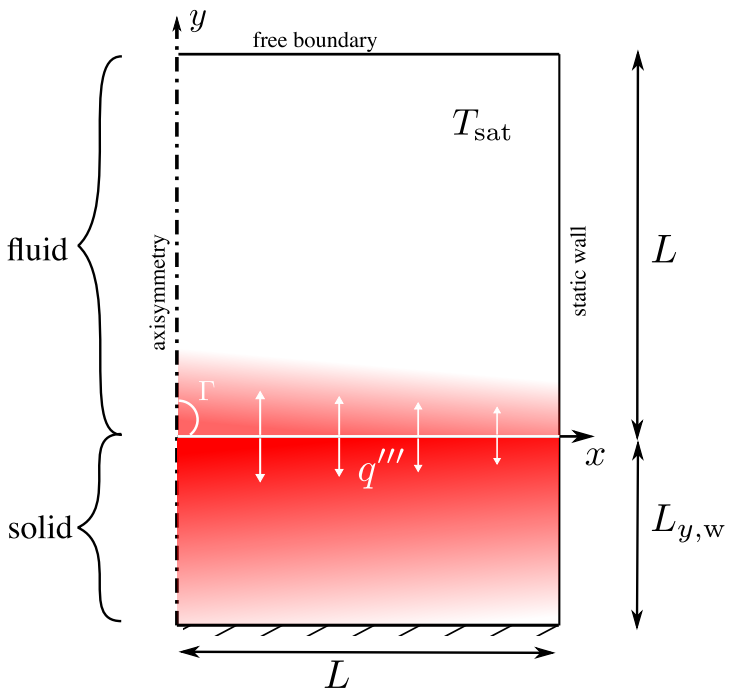

Figure 6.2: Setup used for the simulations

of 20 K with this accommodation coefficient is shown in figure 6.3.

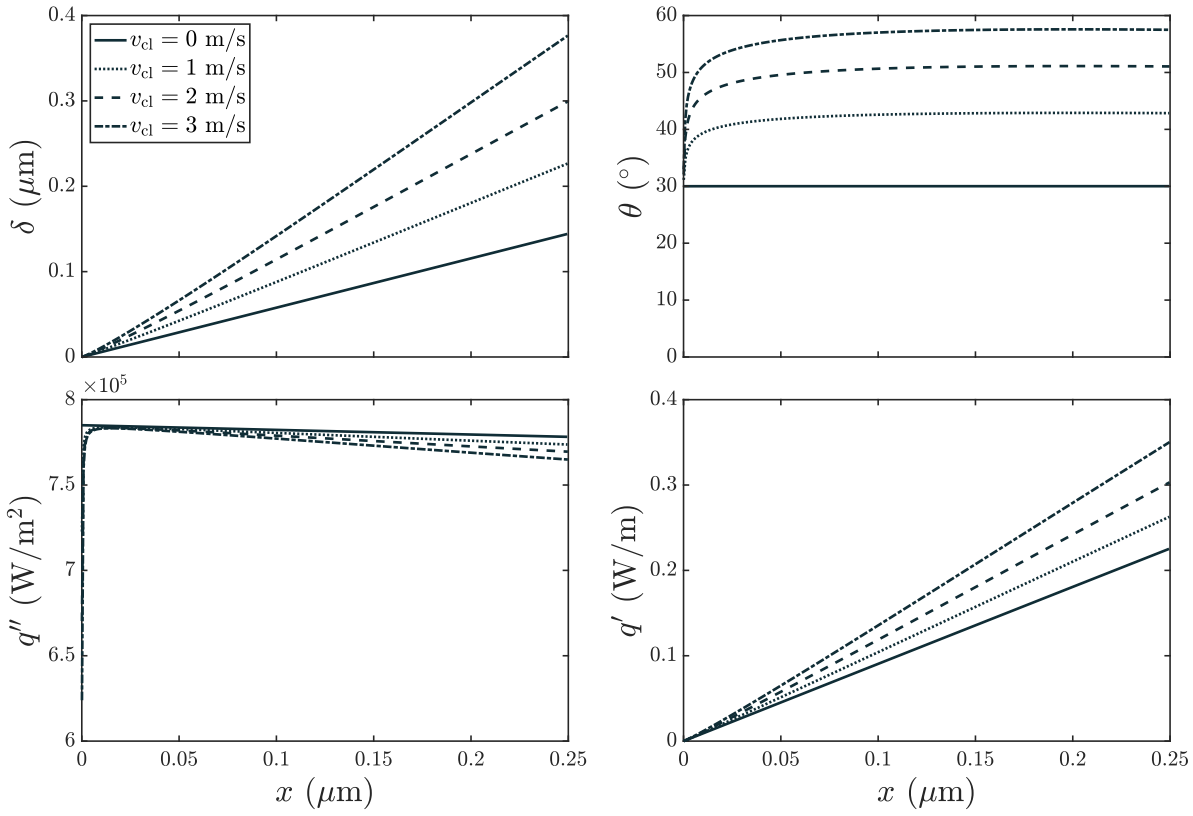

Figure 6.3: Influence of the contact line velocity for water. ΔT=20 K, $f = 0.005$, $\theta_{\mathrm{mic}} = 30°$, $l_{\mathrm{int}} = 250$ nm.

The variations of apparent contact angle and integrated heat flux are also displayed in

figure 6.4.

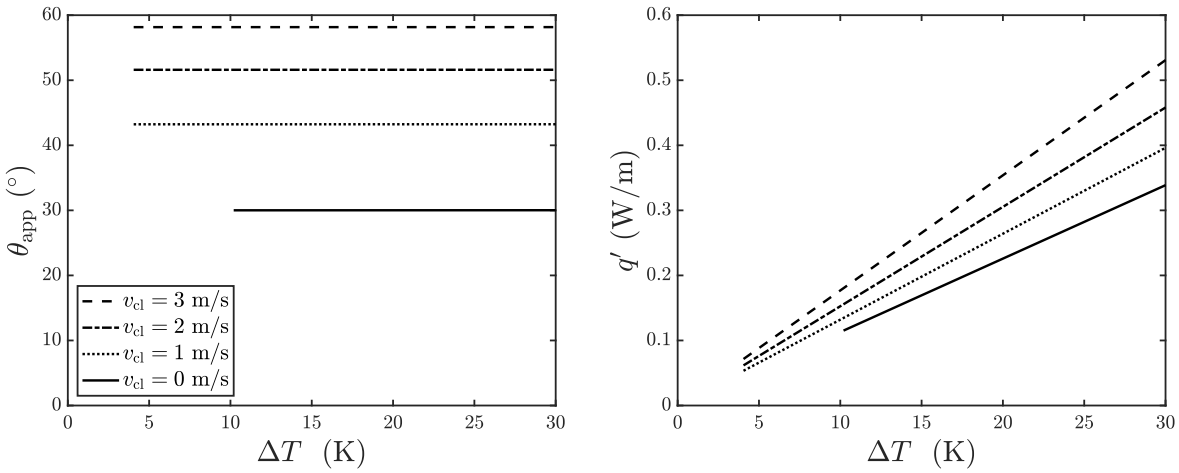

Figure 6.4: Water, $\theta_{mic} = 30°$, $f = 0.005$, for different v_{cl}, integrated on 250 nm.

In figure 6.5, are plotted snapshots of the overall bubble shape and of the temperature field on which a very thin liquid film between the bubble and the solid wall is computed. This liquid film is typical of the micro-layer regime. In figure 6.6, a zoom of the liquid film is plotted in order to visualize the interface shape, the temperature and velocity fields inside the micro-layer. This enables to highlight the intense vaporisation in the micro-layer, and especially in the vicinity of the contact line, along the liquid rim where the micro-region heat flux is spread.

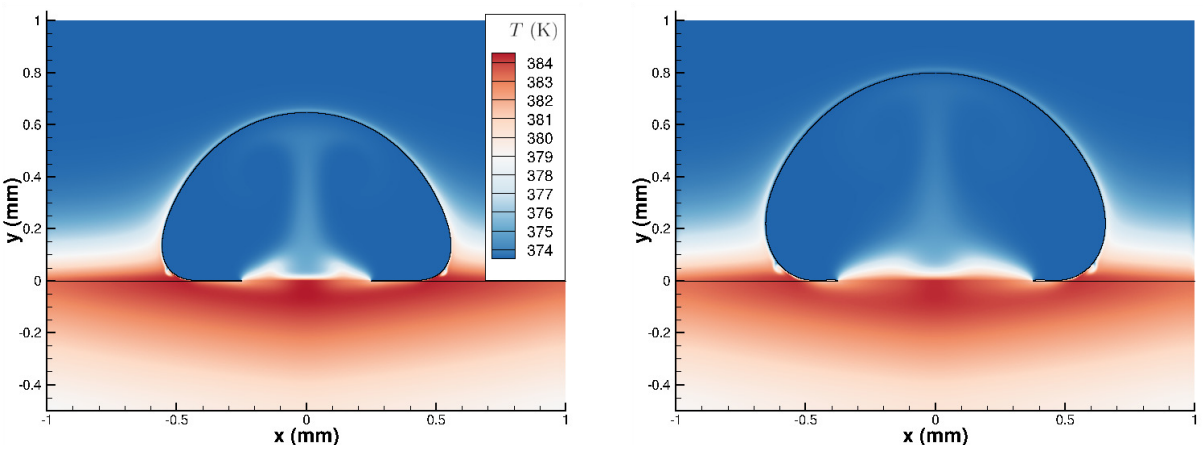

Figure 6.5: Interface shape and temperature field at $t = 0.15$ and 0.30 ms, with a grid 4096×(4096+2048), mesh size is 250 nm.

6.1.2 Simulation results

In figure 6.7, the comparison between experimental data and two simulations is drawn in terms of bubble volume (left) and bubble lateral radius (right). One can observe that without micro-region model (DNS-NMR), the bubble volume is overestimated, whereas DNS-SMR shows a better agreement with the experimental results, and thus a lower bubble growth rate. It may seem contradictory that by adding a micro-region heat flux at the contact line, a decrease of the bubble growth rate is observed. However, the effect of the micro-region on the contact line tends to increase the contact line velocity and to shorten the micro-layer total length. Consequently, the evolution of the bubble radius is slowed down. Indeed, as in the micro-layer regime a large

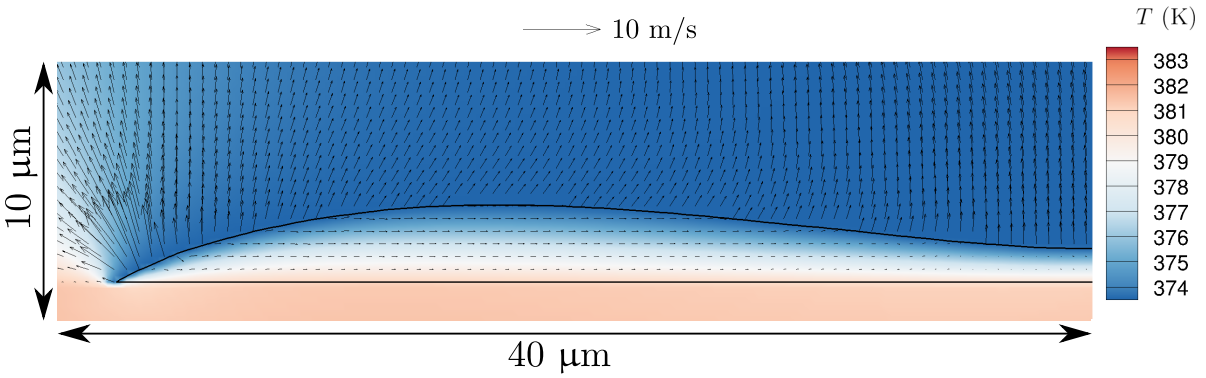

Figure 6.6: Interface shape, velocity and temperature fields inside the micro-layer in the vicinity of the contact line, at $t = 0.15$ ms.

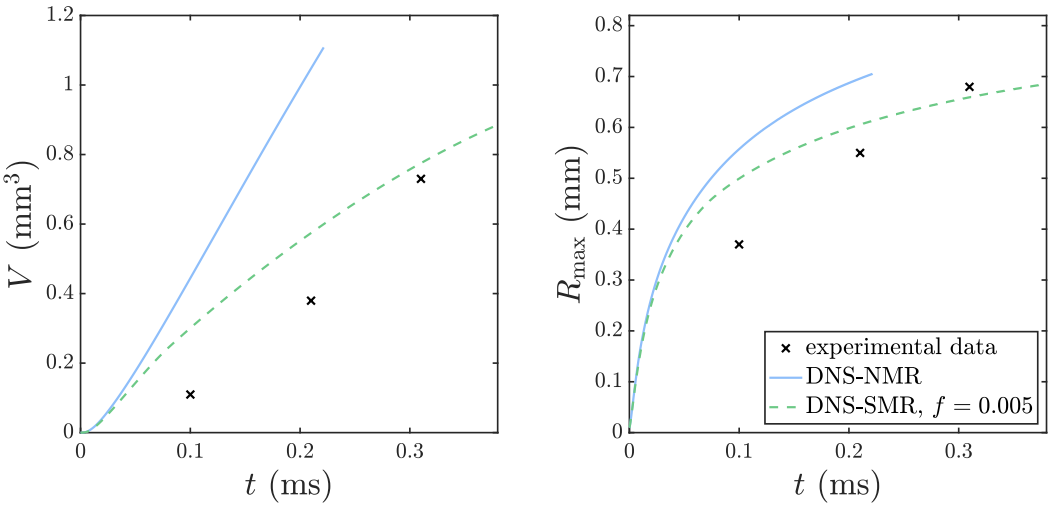

Figure 6.7: Comparison between experimental results of Bucci [22], DNS-NMR and DNS-SMR, on the total bubble volume (left) and on the maximum bubble radius (right).

part of the vaporization mass flux is related to the micro-layer, if its length decreases the bubble growth rate also decreases. Although the micro-region heat flux has a significant impact on the contact line velocity, its contribution to the overall vaporization mass flux is less than 0.5%, whereas the micro-layer contribution is between 30 to 50%. Therefore, in such a regime the micro-region heat flux is negligible in comparison to the micro-layer heat flux, but it can have a significant impact on the micro-layer length, and so on the micro-layer heat flux. To strengthen this analysis, the temporal evolution of the micro-layer length and an instantaneous snapshot of the interface at a given time are plotted in figure 6.8 for both solvers.

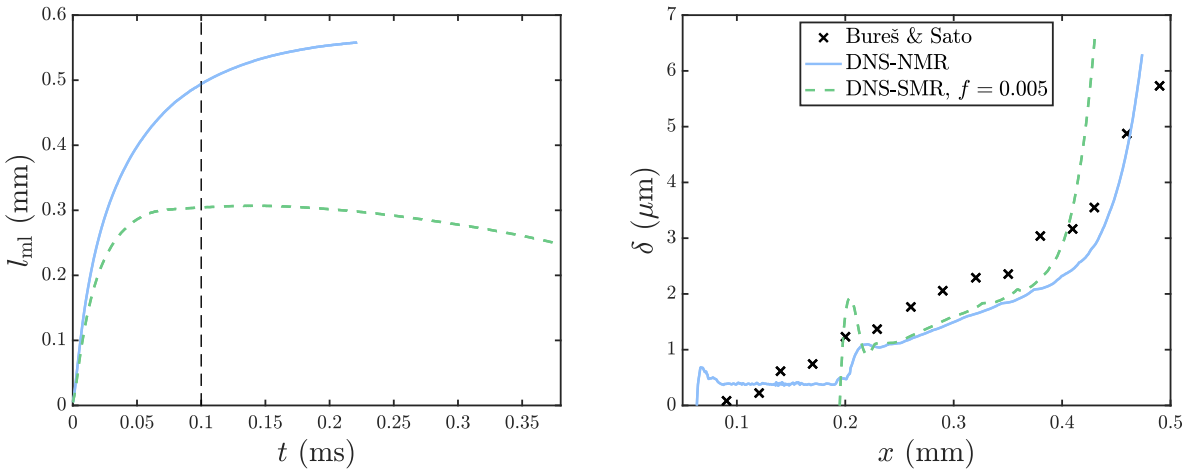

Figure 6.8: Temporal evolution of the micro-layer length (left), and a snapshot of the interface profile in the micro-layer with DNS-SMR (green dashed line) and DNS-NMR (blue line) at $t = 0.1$ ms (right). Experimental data post-processed by Bureš & Sato are taken at a different time on the right plot since they aim to show the agreement in terms of micro-layer thickness.

The DNS-NMR and SMR solvers lead to differences in the micro-layer length (figure 6.8, left) whereas the thickness is similar (right). This result seems to indicate that the physical phenomena of the micro-layer is captured, but the contact line motion requires further study. The subgrid model accounting for the contact line phenomenon tends to increase the contact line velocity, which as a consequence reduces the micro-region length.

The temporal evolution of the bubble shape is drawn on figure 6.9. The case is the same as presented above, with $\theta_{\mathrm{mic}} = 30°$, and $f = 0.005$. The simulation is stopped at $t = 0.5$ ms, time at which the bubble begins to be influenced by the boundaries of the domain. A zoom on the micro-layer thickness can be observed in figure 6.10. With the DNS-SMR the contact line velocity can be estimated to around ~ 2 m/s. With such high speeds, the influence of the micro-region on the apparent contact angle should be large, as seen in figure 6.4. Even though the accommodation coefficient value is low, the variation of θ_{app} with v_{cl} is major. If the contact line velocity is considered, the variation in contact angle would be about 30°, leading to high macroscopic values. In such case, the micro-layer is expected to vanish quickly: according to the simulations of Urbano [84], for a contact angle of 50° and $\mathrm{Ja_e} = 37.6$, this is an intermediate between micro-layer and contact line regimes. However, we do not know the microscopic angle, which may be lower than the 30° chosen here, as this value is usually used for water simulation. Then, as we lack information, we chose to neglect the effect of v_{cl} and to only use the micro-region model obtained for $v_{\mathrm{cl}} = 0$ m/s.

Despite this simplification to avoid non realistic contact angle, the micro-layer tends to vanish quickly. The rim just after the contact line gets bigger over time with micro-layer evaporation. Within 0.5 ms, the contact line has moved far enough to evaporate the whole layer, and the bubble evaporation turns into a contact line regime. Moreover, the liquid velocity inside the micro-layer seems mainly radial, and lead to Peclet value ($\mathrm{Pe} = \frac{v\delta}{\alpha_{\mathrm{liq}}} \sim 20$), which indicates that

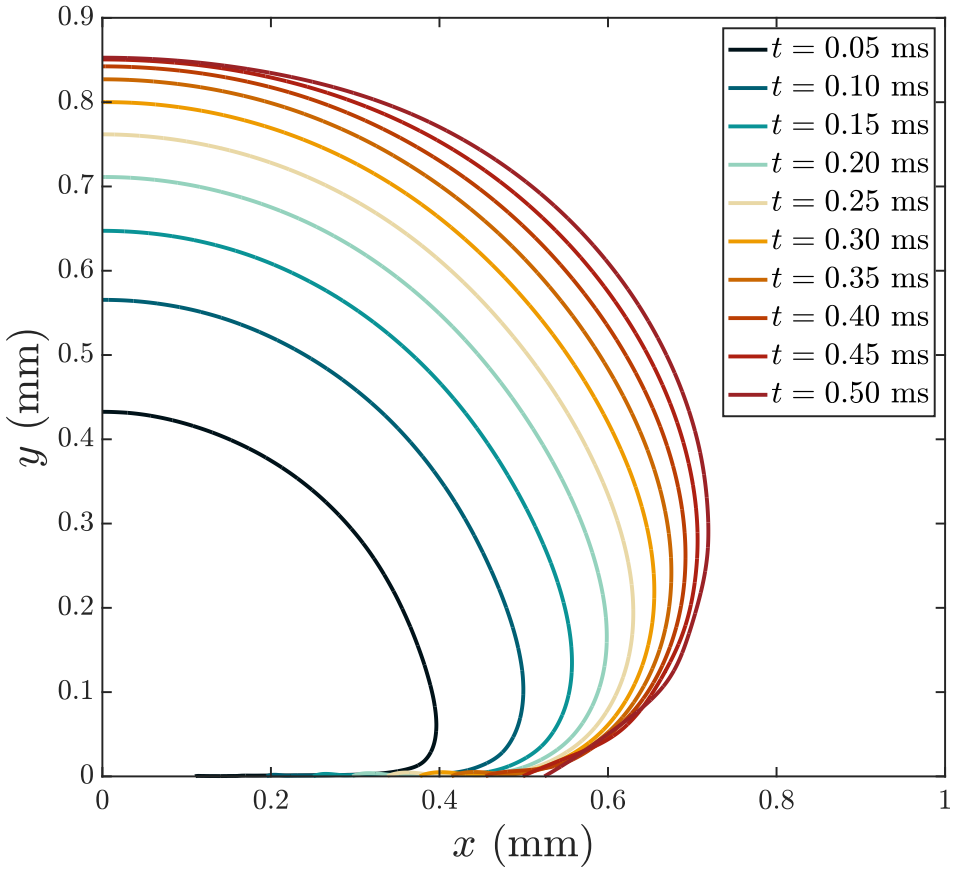

Figure 6.9: Bubble evolution at different time

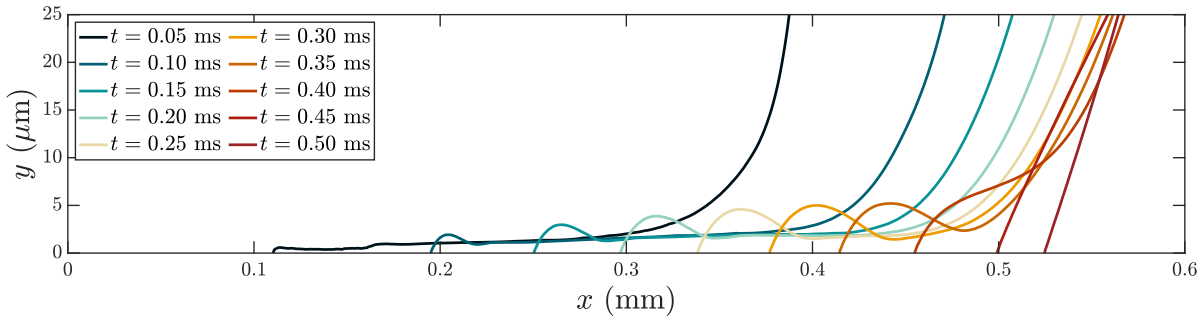

Figure 6.10: Micro-layer evolution with time. Scales are stretched.

in our case the micro-layer is dewetted and not evaporated as in Zhang model [92]. Therefore, a deeper study is required to accurately capture the contact line motion in the DNS.

Thus, the results obtained do not fit with the simulation of Bureš and his post-processed data from the experiment of Bucci, at least for the couples of parameters used here. It is expected that a better estimation of the accommodation coefficient could improve the comparison. Due to the simulation cost ($\sim$ 80000 h_{CPU}, on 1024 cores, for 0.5 ms), only a few values of f have been tried, the best fit obtained for a very low value of the accommodation coefficient, is presented above. Some improvements are expected in further works, especially on the contact line motion, which is too fast. With DNS-SMR, the contact line velocity can be estimated to $\sim$ 2 m/s, whereas the experiment of Bucci seems to indicate velocity one order of magnitude slower (see [22], figure 4.5). The evolution of the dry front has been captured, as the local heat flux clearly denotes the distinction between very low values in the dry zone, and very high values in the micro-layer. To perform more accurate simulations of the micro-layer, further work on the contact line motion are required.

6.2 Conclusion on micro-layer simulations

Despite the lack of conclusive evidence with the experimental comparison, these preliminary observations demonstrate the interest to account for the micro-region heat flux, even in configurations involving the formation of a micro-layer. Its formation, depletion and therefore heat flux are related to the contact line velocity. Development are still to be made to accurately describe the micro-region influence in such unsteady configurations. In particular, future works should focus on accurate comparisons between experiments and numerical simulations on the contact line velocity and on the micro-layer length. In particular, the contact line motion would require a model to couple the large scale interface velocity and the local value at the contact line. An implicit coupling has been performed on the temperature and heat flux, the next step is to apply a similar treatment for the velocity.

General conclusion and outlooks

In this thesis, the mechanisms involved in two-phase flows and their modelling with DNS have been studied in the framework of nucleate boiling. First, a bibliographic study has been carried out to provide a quick overview on the existing works on the subject. The physics of nucleate pool boiling has been introduced, from the first study of the XXth century to the most recent experiments focusing on isolated bubble vaporization. Simulations results have been presented, and the difference between the micro-layer, which can be directly observed experimentally, and the micro-region, too small to be directly observed, emphasized. The distinction between both phenomena is crucial in this thesis.

Afterwards, the methods used for the computation of two-phase flows, main algorithms of the DNS solver and the interface tracking have been described. They consist in the $\mathcal{DIVA}$ code used to perform two-phase flow simulations in many different cases, from nucleate boiling to Leidenfrost simulations. The most known micro-region models have been presented in the third chapter. In particular, Stephan & Busse's model has been fully detailed. The main specificities and the distinction with Mathieu's model have been highlighted. Nevertheless, the results do not differ much, and Mathieu's model has been adopted because of its ability to handle partially-wetting fluids. For a given fluid and local superheat, the computation of the micro-model provides outputs such as the apparent contact angle and the heat flux.

Therefore, in order to have more accurate simulations of nucleate boiling on superheated walls, a proper method to couple these micro-region models with a DNS solver has been developed. The important point is the coupling between the micro-region heat flux, which is imposed as a boundary condition to the solid heat conduction solver. However, the micro-region heat flux depends on the temperature at the contact line and thus on the temperature of the solid frontier. Only an implicit coupling can be successfully achieved. It is carried out by proposing a suitable Robin boundary condition in the cells containing the contact line. Indeed, an explicit coupling based on a Neumann boundary condition imposing the heat flux computed from the previous iteration would not maintain a temperature discontinuity in the cell containing the contact line, which would result in a artificial vanishing of the micro-region effect. Moreover, an important point is the coupling method between the boiling mass flow rate related to the micro-region to the overall numerical solver. A rough implementation of this mass flow rate in the cells containing the contact line systematically leads to numerical instabilities and local inconsistencies on the contact angle, especially for high micro-region heat flux. This method can not be used. On the other hand, another method which integrates the micro-region into the whole bubble has been tested, but does not capture accurately the local flow in the vicinity of the contact line, and therefore has been abandoned. Finally, a compromise, which is based on a local smoothing of the boiling mass flow rate along the interface is proposed and shows satisfactory results both from the point of view of the numerical stability and of the accuracy. The interest of the proposed developments are highlighted on several benchmarks, including comparisons with experiments in micro-gravity conditions, detailed investigations on the solid thermal conductivity and accommodation coefficient.

Moreover, since some of the parameters involved in the model remain unknown, a parametric study has been conducted to investigate on their influence on bubble growth. The case of one bubble in subcooled liquid in microgravity has been chosen, since a steady state can be reached.

The thermal conductivity ratio between the solid wall and the liquid is found to be the driving parameter. The micro-region influence on the growth also depends on it, as conductive walls tends to restrain the temperature drop usually observed at the contact line. As a consequence the flux which must be accounted for in the simulation increases, and is missing without model. Correlations have been established to evaluate the bubble equilibrium diameter submitted to superheated wall and subcooled fluid environment. The heat transfer has also been investigated through the Nusselt number. These information are crucial for the prediction of heat transfer at larger scale, and the establishment of heat flux partitioning model.

Finally, the first simulations of micro-layer regime accounting for the micro-region heat flux at the contact line have been performed. It is shown that, even in the micro-layer regime, the micro-region can have a significant impact on the overall bubble growth since it tends to shorten the micro-layer length and modify the liquid flow inside it. Nonetheless, these are preliminary results to demonstrate the ability to model micro-region inside micro-layer, but the comparison with experimental results must be improved.

The micro-region model has some unknown parameters, such as the microscopic contact angle or the accommodation coefficient, mainly discussed in this whole thesis. Its value, at this time, can hardly be measured accurately. One of the approach is an inverse method, as the one used with the RUBI experiment on part 4.4.3, where the overall results on the contact angle and bubble diameter are compared with the experiments to adjust the value of f, but this remains limited and imprecise. This parameter, which has been shown to be of uppermost importance, should first be tackled. Moreover, it has been speculated that the value of f may be dependent of the fluid purity, with decreasing value as the fluid is contaminated. In such a case, the prediction of the micro-region heat flux contribution becomes more complex. Considering the influence of this coefficient on micro-layer simulation, there is still future work and improvements to accurately perform simulations of bubble growth in micro-layer regimes with micro-region model.

In particular, the question of the contact line velocity should be assessed. First because it should be accounted for in the micro-region model. The outputs, like the contact angle and heat flux, widely vary with it. If this dependence has been neglected in microgravity cases due to the low values expected, the micro-layer regime entails high contact line velocity. More than the impact on the model itself, the numerical treatment of the contact line needs to be improved for future works. It is today only accounted for with a boundary condition on the ϕ function, but the viscosity and stress effects, which should act on the contact line motion, have no specific treatment at the contact line cell. Similarly as the implicit coupling performed on the heat flux (chapter 4), a coupling between the low and large scales on the velocity may be performed in future works. A first improvement on this point should be considered.

Appendix A

Analytical solution of the temperature of two walls with heat source at the interface

At first, we consider a one-side infinite wall with imposed temperature. The heat equation for a homogeneous media with constant properties and without heat source is

$$\frac{\partial T}{\partial t} = \alpha \frac{\partial^2 T}{\partial x^2} \tag{A.1}$$

With T the temperature at the position x and the time t and α its thermal diffusivity. If we suppose that the wall is initially at the temperature T_i so that $T(x > 0, t = 0) = T_\mathrm{i}$, we can easily state that $\theta(x,t) = T(x,t) - T_\mathrm{i}$. Then, the heat equation become:

$$\frac{\partial \theta}{\partial t} = \alpha \frac{\partial^2 \theta}{\partial x^2} \tag{A.2}$$

With $\theta(x,0) = 0$. By using the Laplace transform, we get

$$p\bar{\theta} - \underbrace{\theta(x,0)}_{=0} = \alpha \frac{\partial^2 \bar{\theta}}{\partial x^2} \tag{A.3}$$

The previous equation then is simplified in

$$\frac{\partial^2 \bar{\theta}}{\partial x^2} = \frac{p}{\alpha}\bar{\theta} \tag{A.4}$$

With a general solution:

$$\bar{\theta}(x,p) = A(p)\exp^{-qx} + B(p)\exp^{qx} \tag{A.5}$$

With $q = \sqrt{\frac{p}{\alpha}}$. For a semi-infinite wall, it can easily be stated that $\lim_{x \to +\infty} \theta(x,p)$ is finite $\forall p$, hence $B(p) = 0$.

Thus, the general solution of the Laplace transform is

$$\bar{\theta}(x,p) = A(p)\exp^{-qx} \tag{A.6}$$

With $A(p)$ the Laplace transform of the temperature imposed at the wall in $x = 0$:

$$A(p) = \mathscr{L}\{\theta(0,t)\} \tag{A.7}$$

Henceforth, we consider the heat source at the interface between two wall which induces

variation in the interface temperature. The energy conservation equation at $x = 0$ can then be written:

$$-\lambda_1 \frac{\partial T_1}{\partial x}\bigg|_{x=0^-} + q'' = -\lambda_2 \frac{\partial T_2}{\partial x}\bigg|_{x=0^+} \tag{A.8}$$

With q'' the heat source at the interface, supposed to be constant. We then applied the Laplace transform, and supposed the initial temperature in both walls are equal

$$\lambda_1 \frac{\partial \bar{\theta_1}}{\partial x}\bigg|_{x=0^-} = \lambda_2 \frac{\partial \bar{\theta_2}}{\partial x}\bigg|_{x=0^+} + \frac{q''}{p} \tag{A.9}$$

$$\iff \lambda_1 \sqrt{\frac{p}{\alpha_1}} \bar{\theta}(0,p) = -\lambda_2 \sqrt{\frac{p}{\alpha_2}} \bar{\theta}(0,p) + \frac{q''}{p} \tag{A.10}$$

Hence we have

$$\bar{\theta}(0,p) = \frac{q''}{b_1 + b_2} \times \frac{1}{p^{\frac{3}{2}}} \tag{A.11}$$

By noticing that

$$A(p) = \mathscr{L}\{\theta(0,t)\} = \bar{\theta}(0,p) \tag{A.12}$$

We obtain the general solution with the inverse Laplace transform

$$\theta(x,t) = \frac{2q''\sqrt{t}}{b_1 + b_2} \operatorname{ierfc} \frac{|x|}{2\sqrt{\alpha t}} \tag{A.13}$$

$$\operatorname{ierfc} z = \frac{e^{-z^2}}{\sqrt{\pi}} - z\,(1 - \operatorname{erf} z) \tag{A.14}$$

When we consider the initial temperature T_i and the associated physical properties of the two walls:

$$T_1(x,t) = \frac{2q''\sqrt{t}}{b_1 + b_2} \left(\frac{e^{-\frac{x^2}{4\alpha_1 t}}}{\sqrt{\pi}} - \frac{|x|}{2\sqrt{\alpha_1 t}} \left(1 - \operatorname{erf} \frac{|x|}{2\sqrt{\alpha_1 t}} \right) \right) + T_\mathrm{i} \tag{A.15a}$$

$$T_2(x,t) = \frac{2q''\sqrt{t}}{b_1 + b_2} \left(\frac{e^{-\frac{x^2}{4\alpha_2 t}}}{\sqrt{\pi}} - \frac{|x|}{2\sqrt{\alpha_2 t}} \left(1 - \operatorname{erf} \frac{|x|}{2\sqrt{\alpha_2 t}} \right) \right) + T_\mathrm{i} \tag{A.15b}$$

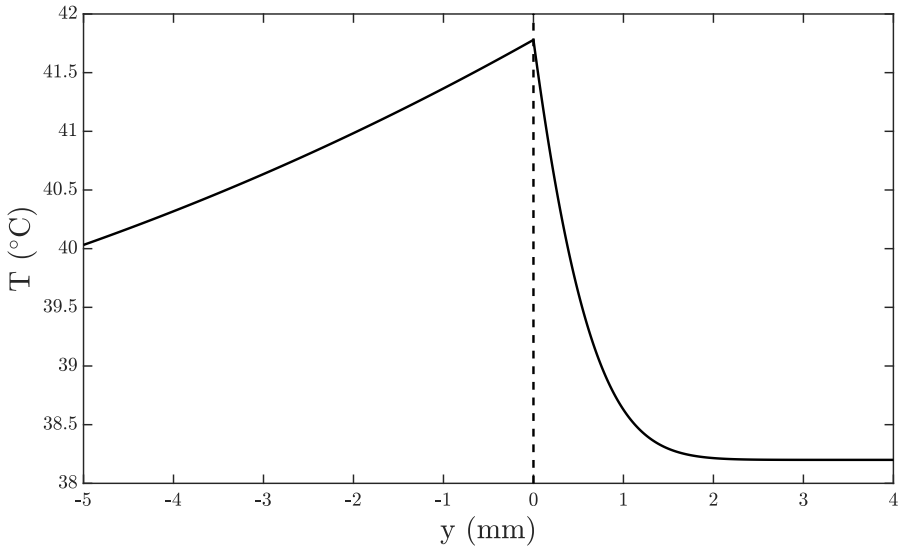

Figure A.1: Thermal field in two wall with different properties with a heat source at their interface at ($y = 0$). Given at $t = 10$ s, $q'' = 1$ W/cm^2, with properties of Sapphire and FC-72 from tables C.1 and C.3. T_i taken equal to 38.3°C.

Appendix B

Analytical solution of the bubble equilibrium radius in microgravity

In microgravity, in absence of buoyancy, we suppose a linear temperature gradient in the liquid domain. Therefore,

$$T(y) = T_{\text{sup}} - (T_{\text{sup}} - T_{\text{sub}})\frac{y}{L_y} \tag{B.1}$$

The bubble is assumed to be spherical with radius R_{b}, the contact angle is noted θ_A. Therefore, we have

$$y = R_{\text{b}}\cos\theta_A + R_{\text{b}}\sin\theta \tag{B.2}$$

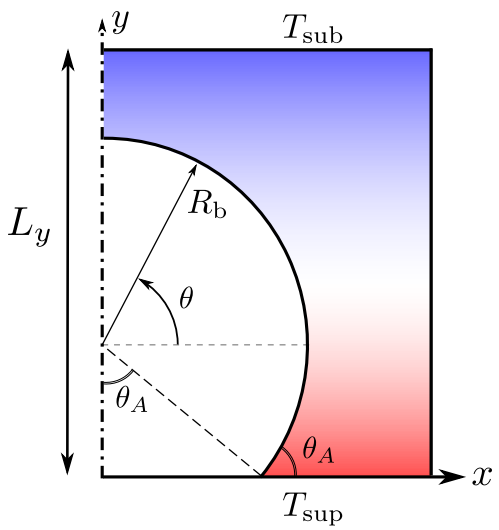

Figure B.1: Schematic of the bubble for analytical solving.

Therefore,

$$T(\theta) = T_{\text{sup}} - (T_{\text{sup}} - T_{\text{sub}})\,\frac{R_{\text{b}}}{L_y}(\cos\theta_A + \sin\theta) \tag{B.3}$$

If the equilibrium is reached, it means that the integral of the heat flux between the interface at saturation temperature and the superheated liquid is equal to zero. The heat flux from the wall to the vapor is neglected.

$$\lambda_{\mathrm{liq}} \int_{\theta_A-\pi/2}^{\pi/2} \left(T(\theta) - T_{\mathrm{sat}}\right) 2\pi R_{\mathrm{b}} \cos\theta \,\mathrm{d}\theta = 0 \tag{B.4}$$

$$\int_{\theta_A-\pi/2}^{\pi/2} \left((T_{\mathrm{sup}} - T_{\mathrm{sat}}) - (T_{\mathrm{sup}} - T_{\mathrm{sub}}) \frac{R_{\mathrm{b}}}{L_y} (\cos\theta_A + \sin\theta) \right) \cos\theta \,\mathrm{d}\theta = 0 \tag{B.5}$$

$$\begin{aligned} (T_{\mathrm{sup}} - T_{\mathrm{sat}}) \left(1 - \sin\left(\theta_A - \frac{\pi}{2}\right)\right) - (T_{\mathrm{sup}} - T_{\mathrm{sub}}) \frac{R_{\mathrm{b}}}{L_y} \cos\theta_A \left(1 - \sin\left(\theta_A - \frac{\pi}{2}\right)\right) \\ - (T_{\mathrm{sup}} - T_{\mathrm{sub}}) \frac{R_{\mathrm{b}}}{L_y} \int_{\theta_A-\pi/2}^{\pi/2} \sin\theta \cos\theta \,\mathrm{d}\theta = 0 \end{aligned} \tag{B.6}$$

$$\begin{aligned} (T_{\mathrm{sup}} - T_{\mathrm{sat}}) \left(1 - \sin\left(\theta_A - \frac{\pi}{2}\right)\right) \\ - (T_{\mathrm{sup}} - T_{\mathrm{sub}}) \frac{R_{\mathrm{b}}}{L_y} \left(\cos\theta_A \left(1 - \sin\left(\theta_A - \frac{\pi}{2}\right)\right) + \frac{1}{4}\left(1 + \cos\left(\pi - 2\theta_A\right)\right) \right) = 0 \end{aligned} \tag{B.7}$$

The ratio between the equilibrium radius and the size of the domain is

$$\frac{R_{\mathrm{b}}}{L_y} = \frac{T_{\mathrm{sup}} - T_{\mathrm{sat}}}{T_{\mathrm{sup}} - T_{\mathrm{sub}}} \left(\frac{1 - \sin(\theta_A - \frac{\pi}{2})}{\cos\theta_A \left(1 - \sin\left(\theta_A - \frac{\pi}{2}\right)\right) + \frac{1}{4}(1 + \cos(\pi - 2\theta_A))} \right) \tag{B.8}$$

$$\frac{R_{\mathrm{b}}}{L_y} = \frac{T_{\mathrm{sup}} - T_{\mathrm{sat}}}{T_{\mathrm{sup}} - T_{\mathrm{sub}}} \left(\frac{1 + \cos\theta_A}{\cos\theta_A \left(1 + \cos\theta_A\right) + \frac{1}{2}\sin^2\theta_A} \right) \tag{B.9}$$

The prefactor can be rearranged in

$$\frac{T_{\mathrm{sup}} - T_{\mathrm{sat}}}{T_{\mathrm{sup}} - T_{\mathrm{sub}}} = \frac{\mathrm{Ja_e}}{\mathrm{Ja_e} + \mathrm{Ja_c}} = \frac{1}{1 + \frac{\mathrm{Ja_c}}{\mathrm{Ja_e}}} \tag{B.10}$$

Therefore

$$\frac{R_{\mathrm{b}}}{L_y} = \frac{1}{1 + \frac{\mathrm{Ja_c}}{\mathrm{Ja_e}}} \left(\frac{1 + \cos\theta_A}{\cos\theta_A \left(1 + \cos\theta_A\right) + \frac{1}{2}\sin^2\theta_A} \right) \tag{B.11}$$

The bubble radius only depend on the ratio between the condensation and the evaporation Jakob. The volume of this truncated sphere is given with basic geometry, and can be linked to the equivalent bubble radius R_{eq}:

$$\mathcal{V}_{\mathrm{b}} = \frac{4}{3}\pi R_{\mathrm{b}}^3 - \frac{\pi}{3} R_{\mathrm{b}}^3 \left(2 + \cos\theta_A\right) \left(1 - \cos\theta_A\right)^2 = \frac{4}{3}\pi R_{\mathrm{eq}}^3 \tag{B.12}$$

$$R_{\mathrm{eq}} = R_{\mathrm{b}} \left(\frac{4 - \left(2 + \cos\theta_A\right)\left(1 - \cos\theta_A\right)^2}{4} \right)^{1/3} \tag{B.13}$$

Equation (B.11) becomes

$$\frac{R_{\mathrm{eq}}}{L_y} = \frac{1}{1 + \frac{\mathrm{Ja_c}}{\mathrm{Ja_e}}} \left(\frac{1 + \cos\theta_A}{\cos\theta_A \left(1 + \cos\theta_A\right) + \frac{1}{2}\sin^2\theta_A} \right) \left(\frac{4 - \left(2 + \cos\theta_A\right)\left(1 - \cos\theta_A\right)^2}{4} \right)^{1/3} \tag{B.14}$$

Appendix C

Physical Properties

In this appendix are given the usual properties for the fluid used. For FC-72, properties are provided by the LOw gravity and THermal Advanced Research laboratory (LOTHAR), from the University of Pisa.

If not precised otherwise, the dimensions for all the physical properties are given in the next table:

P	T	ρ	C_p	σ	L_{vap}	λ	α	μ
Pa	K or °C	kg.m^{-3}	$\text{J.kg}^{-1}\text{.K}^{-1}$	N.m^{-1}	J.kg^{-1}	$\text{W.m}^{-1}\text{.K}^{-1}$	$\text{m}^2\text{.s}^{-1}$	Pa.s

Table C.1: Physical properties of N-perfluorohexane (FC-72)

P_{sat} (mbar)	T_{sat} (°C)	ρ_{liq}	ρ_{vap}	$C_{p,\text{liq}}$	σ	L_{vap}	λ_{liq}	μ_{liq}
400	32	1665.0	5.69	1060.0	1.04×10^{-2}	91.28×10^{3}	5.50×10^{-2}	5.87×10^{-4}
500	37.7	1653.9	7.02	1069.2	9.91×10^{-3}	89.77×10^{3}	5.44×10^{-2}	5.49×10^{-4}
537	39.5	1650.5	7.49	1072.0	9.75×10^{-3}	89.28×10^{3}	5.41×10^{-2}	5.38×10^{-4}
1000	56.6	1619.8	13.4	1098.4	8.27×10^{-3}	84.52×10^{3}	5.22×10^{-2}	4.53×10^{-4}

Table C.2: Physical properties of water P_{atm}, $T_{\text{sat}} = 373.12$ K

	ρ	C_p	σ	L_{vap}	λ	μ
Liquid	958	4216	5.8×10^{-2}	2.256×10^{6}	0.677	2.82×10^{-4}
Vapor	0.594	2034	/	/	0.0246	1.22×10^{-5}

Table C.3: Physical properties of the wall in RUBI

	ρ	C_p	λ	α	δ
Chromium	7190	448	94	2.918×10^{-5}	400 nm
Sapphire	4890	410	10.9	5.437×10^{-6}	5 mm

Appendix D

Post treatment of the infrared camera of RUBI

The RUBI experiment is provided with an infrared camera to monitor the temperature of the substrate. The resolution of the camera is 640x120 pixels, which correspond to a domain of 26.5x5 mm^2, for a resolution of 41.5 µm/pixel. This value is far larger than the micro-region as described in Chapter 3. As a consequence, the post-processing can only depict the overall outcomes of the micro-region on the substrate.

The camera has a frame rate of 240 Hz, resulting in 2400 images for each experiment. The post-processing has been operated with *Matlab*, and aim to monitor the evolution of the substrate temperature along with time, and especially the cooling of the contact line on the surface. The solid part is in saphirre, which is transparent to infrared light, and covered with a chromium substrate which heat both the fluid and the saphirre by Joule effect. The layer is opaque to the IR light, hence what is observed by the camera is the temperature of the chromium substrate, 400 µm thick, and is considered isothermal along this dimension.

First, it should be reminded that the Joule effect is not perfectly constant everywhere in the substrate, but merely has a Gaussian distribution as can be seen in figure D.1. It is absent 8 mm away from the center of the domain.

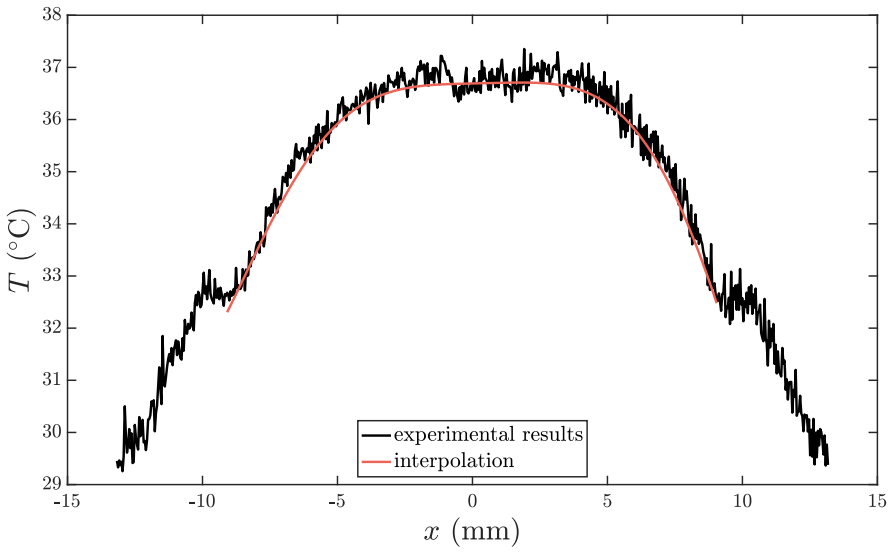

Figure D.1: Temperature distribution at mid-height of the domain.

It should be observed that the signal is noisy, henceforth the accurate position of the contact

line cannot be directly denoted for a single image. As we acknowledge the heat flux is gaussian, the first step of the processing is to interpolate the temperature with the appropriate function and substract the mean value. Figure D.1 displays the interpolation, only computed on the domain where the joule heating is effective.

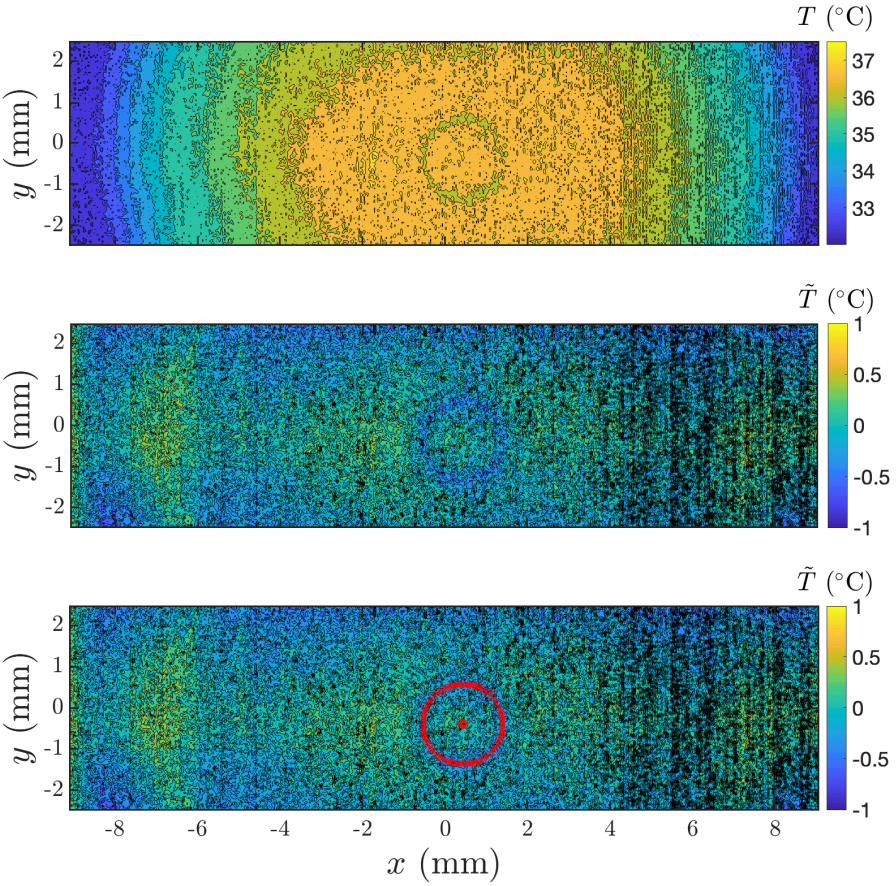

Figure D.2: top: raw image; middle: with removed gaussian function; bottom: with center o and cells crossed by the contact line x denoted

The interpolation is substrated to the global temperature, and remains a noisy temperature field denoted $\tilde{T}$ which mean value is zero. The contact line can be differentiated more easily as the local difference is the minimum. Afterwards, we need to find the most accurate circle corresponding to the cooling of the contact line. Due to absence of shear flow, we chose to approximate the shape of the bubble as spherical, hence a circle for the contact line, which seems visually reasonable, as is observed on figure D.2.

The first image is treated carefully: we need to accurately find the initial center and radius which we have no information about. We scour all the pixels in a large vicinity of the center, run through all the reasonable initial radius, and measure for all the concentric circles (varying the diameter), the one with the minimum mean temperature. The coldest circle correspond to the contact line. The initial position of the center is not known, and thus we have to run though many potential center and radius. Afterwards, due to the high frequency of the IR camera, we assume the position of the center do not vary more than a couple of pixel, and so does the radius. Hence, these two values are saved for every image, and for the next one, the range of values covered by the process is largely reduced.

The different steps of the work on a single image is displayed on figure D.2. The evolution of the process with time in figure D.3. The mean diameter and temperature can also be drawn, as they have been shown in part 4.4.

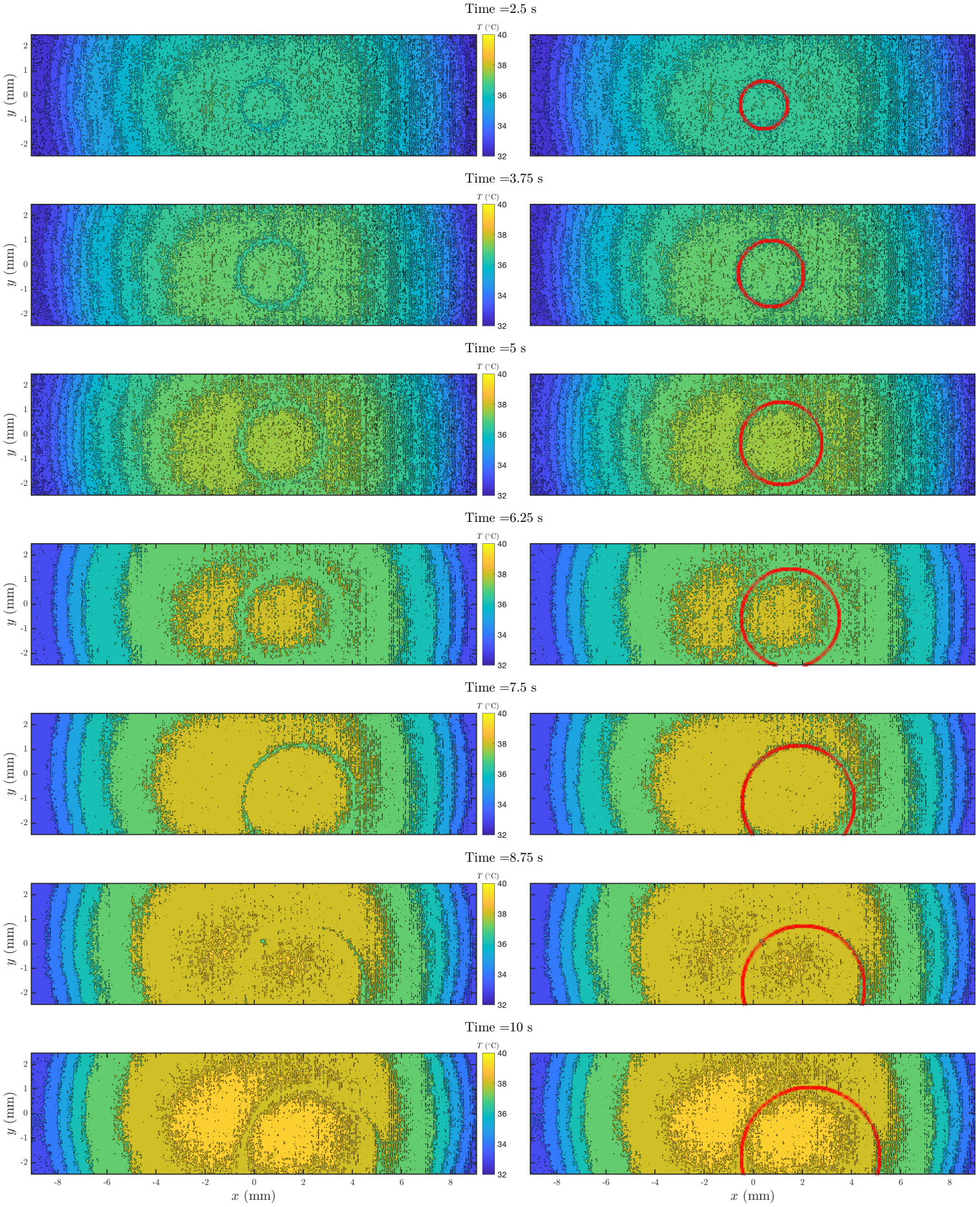

Figure D.3: Raw images vs after after post-processing to find the contact line position

Nomenclature

Numbers

Ca	Capilary number
Ja	Jakob number
Nu	Nusselt number
Pe	Péclet number
Pr	Prandtl number
Re	Reynolds number

Symbols

α	thermal diffusivity [$m^2.s^{-1}$]
δ	thickness [m]
$\dot{m}$	mass flow rate [$kg.m^{-2}.s^{-1}$]
κ	curvature [m^{-1}]
λ	thermal conductivity [$W.m^{-1}.K^{-1}$]
μ	dynamic viscosity [Pa.s]
ϕ	Level Set distance [m]
ρ	density [$kg.m^{-3}$]
$\bar{\bar{D}}$	strain rate tensor [s^{-1}]
$\bar{\bar{S}}$	stress tensor [Pa]
σ	surface tension [$N.m^{-1}$]
θ	contact angle [°] or [rad]
A	Hamaker constant [$Pa.m^3$]
b	thermal effusivity [$W.K^1.m^{-2}.s^{-1/2}$]
C_p	heat capacity [$J.kg^{-1}.K^{-1}$]
d	diameter [m]
f	accommodation coefficient
L_{vap}	latent heat [$J.kg^{-1}$]
l_s	slip length [m]
l_{sp}	spreading length [m]
p	pressure [Pa]
q	total flux [W]
q'	lineic flux [$W.m^{-1}$]
q''	heat flux [$W.m^{-2}$]
q'''	volumetric heat flux [$W.m^{-3}$]
R	radius [m]
R_λ	interfacial thermal resistance [$K.W^{-1}$]
R_g	specific gaz constant [$J.kg^{-1}.K^{-1}$]
T	temperature [K]
t	time [s]
v_s	slip velocity [$m.s^{-1}$]
$\mathbf{g}$	gravity [$m.s^{-2}$]
$\mathbf{n}$	normal to the interface
$\mathbf{v}$	velocity [$m.s^{-1}$]
$\mathbf{x}$	cartesian coordinates [m]

Subscripts

Γ	liquid/vapor interface
θ	azimutal
ads	adsorbed
app	apparent
atm	atmospheric
b	bubble
cl	contact line
c	condensation
eq	equivalent
ext	exterior
e	evaporation
liq	liquid
mic	microscopic
ml	micro-layer

r	radial
sat	saturation
sub	subcooling
sup	superheat
vap	vapor
w	wall
d	disjonction

Bibliography

[1] N. Kurul and M.Z. Podowski. Multidimensional effects in forced convection subcooled boiling. Begel House Inc., 1990. 2

[2] N. Basu, G. Warrier, and V.K. Dhir. Wall Heat Flux Partitioning During Subcooled Flow Boiling: Part 1—Model Development. *Journal of Heat Transfer*, 127(2):131–140, March 2005. 2

[3] N Basu, G Warrier, and V.K Dhir. Wall Heat Flux Partitioning During Subcooled Flow Boiling: Part II—Model Validation. *Journal of Heat Transfer*, 127(2):141–148, March 2005. 2

[4] A. Richenderfer, A. Kossolapov, J.H. Seong, G. Saccone, E. Demarly, R. Kommajosyula, E. Baglietto, J. Buongiorno, and M. Bucci. Investigation of subcooled flow boiling and CHF using high-resolution diagnostics. *Experimental Thermal and Fluid Science*, 99:35–58, December 2018. 2

[5] E. Baglietto, E. Demarly, and R. Kommajosyula. Boiling crisis as the stability limit to wall heat partitioning. *Applied Physics Letters*, 114(10):103701, March 2019. 2, 3

[6] V.P. Carey. *Liquid - Vapor Phase Change Phenomena*. CRC Press, 3 edition, 1982. Num Pages: 82. 3

[7] M. S. Plesset and S. A. Zwick. The Growth of Vapor Bubbles in Superheated Liquids. *Journal of Applied Physics*, 25(4):493–450, April 1954. Number: 4. 3

[8] H.K. Forster and N. Zuber. Dynamics of vapor bubbles and boiling heat transfer. *AIChE Journal*, 1(4):531–535, December 1955. 3

[9] L.E. Scriven. On the dynamics of phase growth. *Chemical Engineering Science*, 10(1):1–13, April 1959. 3

[10] D. Legendre, J. Borée, and J. Magnaudet. Thermal and dynamic evolution of a spherical bubble moving steadily in a superheated or subcooled liquid. *Physics of Fluids*, 10(6):1256–1272, June 1998. 4

[11] B.B. Mikic, W.M. Rohsenow, and P. Griffith. On bubble growth rates. *International Journal of Heat and Mass Transfer*, 13(4):657–666, April 1970. 4

[12] R. Mei, W. Chen, and J.F. Klausner. Vapor bubble growth in heterogeneous boiling—I. Formulation. *International Journal of Heat and Mass Transfer*, 38(5):909–919, March 1995. 4

[13] N. Zuber. Nucleate boiling. The region of isolated bubbles and the similarity with natural convection. *International Journal of Heat and Mass Transfer*, 6(1):53–78, January 1963. 4

[14] S.J.D. Van Stralen. The mechanism of nucleate boiling in pure liquids and in binary mixtures—part I. *International Journal of Heat and Mass Transfer*, 9(10):995–1020, October 1966. 4

[15] S.J.D. Van Stralen. The mechanism of nucleate boiling in pure liquids and in binary mixtures—part II. *International Journal of Heat and Mass Transfer*, 9(10):1021–1046, October 1966. 4

[16] S.J.D. Van Stralen. The mechanism of nucleate boiling in pure liquids and in binary mixtures—part III. *International Journal of Heat and Mass Transfer*, 10(11):1469–1484, November 1967. 4

[17] M.G. Cooper and A.J.P. Lloyd. The microlayer in nucleate pool boiling. *International Journal of Heat and Mass Transfer*, 12(8):895–913, August 1969. 4

[18] T. Yabuki and O. Nakabeppu. Heat transfer mechanisms in isolated bubble boiling of water observed with MEMS sensor. *International Journal of Heat and Mass Transfer*, 76:286–297, September 2014. 4

[19] T. Yabuki and O. Nakabeppu. Microscale wall heat transfer and bubble growth in single bubble subcooled boiling of water. *International Journal of Heat and Mass Transfer*, 100:851–860, September 2016. 4

[20] Y. Utaka, Y. Kashiwabara, M. Ozaki, and Z. Chen. Heat transfer characteristics based on microlayer structure in nucleate pool boiling for water and ethanol. *International Journal of Heat and Mass Transfer*, 68:479–488, January 2014. 5, 15

[21] C. Gerardi, J. Buongiorno, L. Hu, and T. McKrell. Study of bubble growth in water pool boiling through synchronized, infrared thermometry and high-speed video. *International Journal of Heat and Mass Transfer*, 53(19-20):4185–4192, September 2010. 5

[22] M. Bucci. A theoritical and experimental study of vapor bubble dynamics in separate effect pool boiling conditions. September 2020. 5, 16, 111, 112, 115, 118

[23] H.H. Jawurek. Simultaneous determination of microlayer geometry and bubble growth in nucleate boiling. *International Journal of Heat and Mass Transfer*, 12(8):843–848, August 1969. 5

[24] M. Gao, L. Zhang, P. Cheng, and X. Quan. An investigation of microlayer beneath nucleation bubble by laser interferometric method. *International Journal of Heat and Mass Transfer*, 57(1):183–189, January 2013. 5

[25] Z. Chen, X. Hu, K. Hu, Y. Utaka, and S. Mori. Measurement of the microlayer characteristics in the whole range of nucleate boiling for water by laser interferometry. *International Journal of Heat and Mass Transfer*, 146:118856, January 2020. 5, 6

[26] C. Tecchio, X. Zhang, B. Cariteau, G. Zalczer, P.R. Cabarrocas, P. Bulkin, J. Charliac, S. Vassant, and V.S. Nikolayev. Microlayer in nucleate boiling seen as Landau-Levich film with dewetting and evaporation, June 2023. 6

[27] A. Kossolapov, B. Phillips, and M. Bucci. Can LED lights replace lasers for detailed investigations of boiling phenomena? *International Journal of Multiphase Flow*, 135:103522, February 2021. 6

[28] A. Kossolapov. *Experimental Investigation of Subcooled Flow Boiling and CHF at Prototypical Pressures of Light Water Reactors*. PhD thesis, 2021. 6

[29] T. Chen, J. Klausner, and J. Chung. Subcooled boiling heat transfer and dryout on a constant temperature microheater. *International Journal of Heat and Fluid Flow*, 25:274–287, April 2004. 6

[30] F. Demiray and J. Kim. Microscale heat transfer measurements during pool boiling of FC-72: effect of subcooling. *International Journal of Heat and Mass Transfer*, 47(14-16):3257–3268, July 2004. 6

[31] C.D. Henry and J. Kim. A study of the effects of heater size, subcooling, and gravity level on pool boiling heat transfer. *International Journal of Heat and Fluid Flow*, 25(2):262–273, April 2004. 6

[32] S. Moghaddam and K. Kiger. Physical mechanisms of heat transfer during single bubble nucleate boiling of FC-72 under saturation conditions-I. Experimental investigation. *International Journal of Heat and Mass Transfer*, 52(5-6):1284–1294, February 2009. 6

[33] C. Sodtke, J. Kern, N. Schweizer, and P. Stephan. High resolution measurements of wall temperature distribution underneath a single vapour bubble under low gravity conditions. *International Journal of Heat and Mass Transfer*, 49(5-6):1100–1106, March 2006. 6

[34] E. Wagner and P. Stephan. High-Resolution Measurements at Nucleate Boiling of Pure FC-84 and FC-3284 and Its Binary Mixtures. *Journal of Heat Transfer*, 131(12), October 2009. 7

[35] R. Siegel. Effects of Reduced Gravity on Heat Transfer. In J.P. Hartnett and T.F. Irvine, editors, *Advances in Heat Transfer*, volume 4, pages 143–228. Elsevier, January 1967. 7

[36] J. Straub. The role of surface tension for two-phase heat and mass transfer in the absence of gravity. *Experimental Thermal and Fluid Science*, 9(3):253–273, October 1994. 7

[37] N. Schweizer. *Multi-Scale Investigation of Nucleate Boiling Phenomena in Microgravity*. phd, Technische Universität, Darmstadt, December 2010. 7

[38] H. Ohta. Experiments on microgravity boiling heat transfer by using transparent heaters. *Nuclear Engineering and Design*, 175(1):167–180, November 1997. 7

[39] P. Stephan and N. Schweizer. Experimental study of bubble behavior and local heat flux in pool boiling under variable gravitational conditions. *Multiphase Science and Technology*, 21(4):329–350, 2009. 7

[40] P. Di Marco, R. Raj, and J. Kim. Boiling in variable gravity under the action of an electric field: Results of parabolic flight experiments. *Journal of Physics: Conference Series*, 327:012039, December 2011. 7

[41] G. Duhar, G. Riboux, and C. Colin. Vapour bubble growth and detachment at the wall of shear flow. *Heat and Mass Transfer*, 45(7):847–855, May 2009. 7

[42] M. Lebon. *Etude de la dynamique de bulles formées en paroi par injection ou ébullition : effet de la gravité et des forces hydrodynamiques*. PhD thesis, Institut National Polytechnique de Toulouse (INP Toulouse), November 2016. 8

[43] A. Sielaff, D. Mangini, O. Kabov, M.Q. Raza, A.I. Garivalis, M. Zupančič, S. Dehaeck, S. Evgenidis, C. Jacobs, D. Van Hoof, O. Oikonomidou, X. Zabulis, P. Karamaounas, A. Bender, F. Ronshin, M. Schinnerl, J. Sebilleau, C. Colin, P. Di Marco, T. Karapantsios, I. Golobič, A. Rednikov, P. Colinet, P. Stephan, and L. Tadrist. The multiscale boiling investigation on-board the International Space Station: An overview. *Applied Thermal Engineering*, 205:117932, March 2022. 9

[44] G. Son, V. K. Dhir, and N. Ramanujapu. Dynamics and Heat Transfer Associated With a Single Bubble During Nucleate Boiling on a Horizontal Surface. *Journal of Heat Transfer*, 121(3):623–631, August 1999. 10, 13, 61, 68

[45] F.H. Harlow and J.E. Welch. Numerical Calculation of Time-Dependent Viscous Incompressible Flow of Fluid with Free Surface. *The Physics of Fluids*, 8(12):2182–2189, December 1965. Publisher: American Institute of Physics. 10

[46] B.J. Daly. Numerical Study of Two Fluid Rayleigh-Taylor Instability. *The Physics of Fluids*, 10(2):297–307, February 1967. Publisher: American Institute of Physics. 10

[47] J. Glimm, C. Klingenberg, O. McBryan, B. Plohr, D. Sharp, and S. Yaniv. Front tracking and two-dimensional Riemann problems. *Advances in Applied Mathematics*, 6(3):259–290, September 1985. 10

[48] D. Juric and G. Tryggvason. Computations of Boiling Flows. *International Journal of Multiphase Flow*, 24(3):387–410, 1998. 10

[49] S. Popinet and S. Zaleski. A front-tracking algorithm for accurate representation of surface tension. *International Journal for Numerical Methods in Fluids*, 30(6):775–793, 1999. Publisher: Wiley. 10

[50] C.W. Hirt and B.D Nichols. Volume of fluid (VOF) method for the dynamics of free boundaries. *Journal of Computational Physics*, 39(1):201–225, January 1981. 11

[51] C. Josserand, L. Lemoyne, R. Troeger, and S. Zaleski. Droplet impact on a dry surface: triggering the splash with a small obstacle. *Journal of Fluid Mechanics*, 524:47–56, February 2005. Publisher: Cambridge University Press. 11

[52] S. Popinet. An accurate adaptive solver for surface-tension-driven interfacial flows. *Journal of Computational Physics*, 228:5838 – 5866, 2009. 11

[53] S. Osher and J.A. Sethian. Fronts propagating with curvature-dependent speed: Algorithms based on Hamilton-Jacobi formulations. *Journal of Computational Physics*, 79(1):12–49, November 1988. 11, 25

[54] J. Sethian. Turbulent combustion in open and closed vessels. *Journal of Computational Physics*, 54(3):425–456, June 1984. 11

[55] M. Sussman, P. Smereka, and S. Osher. A Level Set Approach for Computing Solutions to Incompressible Two-Phase Flow. *Journal of Computational Physics*, 114:146–159, October 1994. 11, 26

[56] F. Gibou, L. Chen, D. Nguyen, and S. Banerjee. A level set based sharp interface method for the multiphase incompressible Navier–Stokes equations with phase change. *Journal of Computational Physics*, 222(2):536–555, March 2007. 11, 30

[57] D.Q. Nguyen, R.P. Fedkiw, and M. Kang. A Boundary Condition Capturing Method for Incompressible Flame Discontinuities. *Journal of Computational Physics*, 172(1):71–98, September 2001. 11, 29

[58] R. Scardovelli and S. Zaleski. Direct Numerical Simulation of Free-Surface and Interfacial Flow. *Annual Review of Fluid Mechanics*, 31(1):567–603, January 1999. 11

[59] R.P. Fedkiw, T. Aslam, B. Merriman, and S. Osher. A Non-oscillatory Eulerian Approach to Interfaces in Multimaterial Flows (the Ghost Fluid Method). *Journal of Computational Physics*, 152(2):457–492, July 1999. 11, 26

[60] B. Lalanne, L. Villegas, S. Tanguy, and F. Risso. On the computation of viscous terms for incompressible two-phase flows with Level Set/Ghost Fluid Method. *Journal of Computational Physics*, 301:289–307, November 2015. 11

[61] S. Tanguy, M. Sagan, B. Lalanne, F. Couderc, and C. Colin. Benchmarks and numerical methods for the simulation of boiling flows. *Journal of Computational Physics*, 264:1–22, May 2014. 11, 31, 34

[62] G. Sahut, G. Ghigliotti, G. Balarac, M. Bernard, V. Moureau, and P. Marty. Numerical simulation of boiling on unstructured grids. *Journal of Computational Physics*, 432:110161, May 2021. 11

[63] B.M. Ningegowda, Z. Ge, G. Lupo, L. Brandt, and C. Duwig. A mass-preserving interface-correction level set/ghost fluid method for modeling of three-dimensional boiling flows. *International Journal of Heat and Mass Transfer*, 162:120382, December 2020. 11

[64] L.M. Hocking. A moving fluid interface. Part 2. The removal of the force singularity by a slip flow. *Journal of Fluid Mechanics*, 79(2):209–229, February 1977. Publisher: Cambridge University Press. 12

[65] E. B. Dussan V., E. Ramé, and S. Garoff. On identifying the appropriate boundary conditions at a moving contact line: an experimental investigation. *Journal of Fluid Mechanics*, 230:97–116, September 1991. 12

[66] P. Wayner, Y.K. Kao, and L.V. LaCroix. The Interline Heat Transfer Coefficient of an Evaporating Wetting Film. *International Journal of Heat and Mass Transfer*, 19:487–492, May 1976. 12, 38

[67] P.C. Stephan and C.A. Busse. Analysis of the heat transfer coefficient of grooved heat pipe evaporator walls. *International Journal of Heat and Mass Transfer*, 35(2):383–391, February 1992. 12, 37, 38

[68] B. Mathieu. *Études Physique, Expérimentale et Numérique des mécanismes de base intervenant dans les écoulement diphasiques en micro-fluidique*. PhD thesis, Université de Provence - CNRS - UMR 6595, 2003. 12, 37, 42

[69] V.S. Nikolayev. Dynamics of the triple contact line on a nonisothermal heater at partial wetting. *Phys. Fluids*, page 13, 2010. 12, 37

[70] A.Y. Rednikov and P. Colinet. Truncated versus Extended Microfilms at a Vapor-Liquid Contact Line on a Heated Substrate. *American Chemical Society*, page 12, 2011. 12, 48

[71] R. Raj, C. Kunkelmann, P. Stephan, J. Plawsky, and J. Kim. Contact line behavior for a highly wetting fluid under superheated conditions. *International Journal of Heat and Mass Transfer*, 55(9-10):2664–2675, April 2012. 12, 38, 40

[72] R.W. Schrage. *A theoretical study of interphase mass transfer*. Columbia University Press, New York, 1953. OCLC: 574619311. 12, 39

[73] V. Janeček. *Evaporation à l'échelle microscopique et à haut Flux thermique*. PhD thesis, UPMC, 2012. 12, 13, 48, 50, 51

[74] C. Kunkelmann. *Numerical Modeling and Investigation of Boiling Phenomena*. PhD thesis, Darmstadt, September 2011. 13, 41

[75] S. Batzdorf. *Heat transfer and evaporation during single drop impingement onto a superheated wall*. PhD thesis, Darmstadt, 2015. 13, 42, 46

[76] G. Son and V.K. Dhir. Numerical simulation of nucleate boiling on a horizontal surface at high heat fluxes. *International Journal of Heat and Mass Transfer*, 51(9-10):2566–2582, May 2008. 13

[77] G. Huber, S. Tanguy, M. Sagan, and C. Colin. Direct numerical simulation of nucleate pool boiling at large microscopic contact angle and moderate Jakob number. *International Journal of Heat and Mass Transfer*, 113:662–682, October 2017. 13, 14, 37, 83, 107

[78] G. Son and V.K. Dhir. Numerical Simulation of Film Boiling Near Critical Pressures With a Level Set Method. *Journal of Heat Transfer*, 120(1):183–192, February 1998. 13

[79] S. Shin, S.I. Abdel-Khalik, and D. Juric. Direct three-dimensional numerical simulation of nucleate boiling using the level contour reconstruction method. *International Journal of Multiphase Flow*, 31(10-11):1231–1242, October 2005. 13, 14

[80] G. Kocamustafaogullari and M. Ishii. Interfacial area and nucleation site density in boiling systems. *International Journal of Heat and Mass Transfer*, 26(9):1377–1387, September 1983. 14

[81] M. Mann, K. Stephan, and P. Stephan. Influence of heat conduction in the wall on nucleate boiling heat transfer. *International Journal of Heat and Mass Transfer*, 43(12):2193–2203, June 2000. 14, 85

[82] E. Aktinol and V.K. Dhir. Numerical Simulation of Nucleate Boiling Phenomenon Coupled with Thermal Response of the Solid. *Microgravity Science and Technology*, 24(4):255–265, September 2012. 14

[83] A. Urbano, S. Tanguy, and C. Colin. Direct numerical simulation of nucleate boiling in zero gravity conditions. *International Journal of Heat and Mass Transfer*, 143:118521, November 2019. 15, 85, 89, 90, 92, 97, 101, 107

[84] A. Urbano, S. Tanguy, G. Huber, and C. Colin. Direct numerical simulation of nucleate boiling in micro-layer regime. *International Journal of Heat and Mass Transfer*, 123:1128–1137, August 2018. 15, 17, 18, 93, 111, 112, 116

[85] L. Bureš and Y. Sato. On the modelling of the transition between contact-line and microlayer evaporation regimes in nucleate boiling. *Journal of Fluid Mechanics*, 916:A53, June 2021. 15, 16, 18, 111

[86] Z. Chen and Y. Utaka. On heat transfer and evaporation characteristics in the growth process of a bubble with microlayer structure during nucleate boiling. *International Journal of Heat and Mass Transfer*, 81:750–759, February 2015. 15

[87] Y. Sato and B. Niceno. A depletable micro-layer model for nucleate pool boiling. *Journal of Computational Physics*, 300:20–52, November 2015. 15, 111

[88] Y. Utaka, Y. Kashiwabara, and M. Ozaki. Microlayer structure in nucleate boiling of water and ethanol at atmospheric pressure. *International Journal of Heat and Mass Transfer*, 57(1):222–230, January 2013. 15

[89] X. Duan, B. Phillips, T. McKrell, and J. Buongiorno. Synchronized High-Speed Video, Infrared Thermometry, and Particle Image Velocimetry Data for Validation of Interface-Tracking Simulations of Nucleate Boiling Phenomena. *Experimental Heat Transfer*, 26(2-3):169–197, March 2013. 15

[90] A. Guion, S. Afkhami, S. Zaleski, and J. Buongiorno. Simulations of microlayer formation in nucleate boiling. *International Journal of Heat and Mass Transfer*, 127:1271–1284, December 2018. 15, 111

[91] X. Zhang and V.S. Nikolayev. Liquid film dynamics with immobile contact line during meniscus oscillation. *Journal of Fluid Mechanics*, 923:A4, September 2021. 15, 18

[92] X. Zhang and V.S. Nikolayev. Dewetting acceleration by evaporation. *Journal of Fluid Mechanics*, 948:A49, October 2022. Publisher: Cambridge University Press. 15, 18, 118

[93] Z. Chen, F. Wu, and Y. Utaka. Numerical simulation of thermal property effect of heat transfer plate on bubble growth with microlayer evaporation during nucleate pool boiling. *International Journal of Heat and Mass Transfer*, 118:989–996, March 2018. 16, 111

[94] S. Hänsch, S. Walker, and C. Narayanan. Mechanistic studies of single bubble growth using interface-tracking methods. *Nuclear Engineering and Design*, 321:230–243, September 2017. 16, 111

[95] L. Bureš and Y. Sato. Comprehensive simulations of boiling with a resolved microlayer: validation and sensitivity study. *Journal of Fluid Mechanics*, 933:A54, February 2022. 16, 112

[96] S. Fischer, T. Gambaryan-Roisman, and P. Stephan. On the development of a thin evaporating liquid film at a receding liquid/vapour-interface. *International Journal of Heat and Mass Transfer*, 88:346–356, September 2015. 16

[97] K. Schweikert, A. Sielaff, and P. Stephan. On the transition between contact line evaporation and microlayer evaporation during the dewetting of a superheated wall. *International Journal of Thermal Sciences*, 145:106025, November 2019. 17

[98] L. Landau and B. Levich. Dragging of a Liquid by a Moving Plate. In *Dynamics of Curved Fronts*, pages 141–153. Elsevier, 1988. 17

[99] W.M. Kays and M.E. Crawford. *Convective Heat and Mass Transfer*. Mcgraw-hill edition, 1993. 17, 83

[100] C. Min and F. Gibou. A second order accurate level set method on non-graded adaptive cartesian grids. *Journal of Computational Physics*, 225(1):300–321, July 2007. 26

[101] M. Sussman, K.M. Smith, M.Y. Hussaini, M. Ohta, and R. Zhi-Wei. A sharp interface method for incompressible two-phase flows. *Journal of Computational Physics*, 221(2):469–505, February 2007. 29

[102] S. Tanguy, T. Ménard, and A. Berlemont. A Level Set Method for vaporizing two-phase flows. *Journal of Computational Physics*, 221(2):837–853, February 2007. 30

[103] F. Gibou, R.P. Fedkiw, L. Cheng, and M. Kang. A Second-Order-Accurate Symmetric Discretization of the Poisson Equation on Irregular Domains. *Journal of Computational Physics*, 176(1):205–227, February 2002. 30

[104] T. Aslam. A partial differential equation approach to multidimensional extrapolation. *Journal of Computational Physics*, 193(1):349–355, January 2004. 31, 70

[105] M. Lepilliez, E.R. Popescu, F. Gibou, and S. Tanguy. On two-phase flow solvers in irregular domains with contact line. *Journal of Computational Physics*, 321:1217–1251, September 2016. 32

[106] R. Borges, M. Carmona, B. Costa, and W.S. Don. An improved weighted essentially non-oscillatory scheme for hyperbolic conservation laws. *Journal of Computational Physics*, 227(6):3191–3211, March 2008. 32

[107] J.E. Dendy. Black box multigrid. *Journal of Computational Physics*, 48(3):366–386, December 1982. 32

[108] B.P. Van Poppel, O. Desjardins, and J.W. Daily. A ghost fluid, level set methodology for simulating multiphase electrohydrodynamic flows with application to liquid fuel injection. *Journal of Computational Physics*, 229(20):7977–7996, October 2010. 32

[109] S.P. MacLachlan, J.M. Tang, and C. Vuik. Fast and robust solvers for pressure-correction in bubbly flow problems. *Journal of Computational Physics*, 227(23):9742–9761, December 2008. 32

[110] V. Janeček and V.S. Nikolayev. Contact line singularity at partial wetting during evaporation driven by substrate heating. *EPL (Europhysics Letters)*, 100(1):14003, October 2012. 38, 50, 51

[111] B. Paul. Compilation of Evaporation Coefficients. *ARS Journal*, 32(9):1321–1328, September 1962. 39, 53, 82

[112] L.D. Landan and E.M. Lifshitz. *Statistical Physics*, volume 5 of *Course of Theoretical Physics*. Pergamon International Library, 3rd edition, 1980. 39

[113] J.R. Winkler. Numerical recipes in C: The art of scientific computing, second edition. *Endeavour*, 17(4):201, January 1993. 40

[114] H.K. Moffatt and B.R. Duffy. Local similarity solutions and their limitations. *Journal of Fluid Mechanics*, 96(2):299–313, January 1980. 42

[115] J.H. Lay and V.K. Dhir. Shape of a Vapor Stem During Nucleate Boiling of Saturated Liquids. *Journal of Heat Transfer*, 117(2):394–401, May 1995. 48

[116] V. Janeček and V.S. Nikolayev. Apparent-contact-angle model at partial wetting and evaporation: Impact of surface forces. *Physical Review E*, 87(1):012404, January 2013. 50

[117] V. Janeček and V.S. Nikolayev. Triggering the Boiling Crisis: A Study of the dry spot spreading mechanism. *Interfacial Phenomena and Heat Transfer*, 2(4):363–383, 2014. 50

[118] V. Janeček and D.M. Anderson. Microregion Model of a contact line including evaporation, kinetics and slip length. *Interfacial Phenomena and Heat Transfer*, 4(2-3):93–107, 2016. 50

[119] Y. Sato and B. Ničeno. A sharp-interface phase change model for a mass-conservative interface tracking method. *Journal of Computational Physics*, 249:127–161, September 2013. 61

[120] C. Kunkelmann and P. Stephan. Numerical simulation of the transient heat transfer during nucleate boiling of refrigerant HFE-7100. *International Journal of Refrigeration*, 33(7):1221–1228, November 2010. 61

[121] M. Vahab, M. Sussman, and K. Shoele. Fluid-structure interaction of thin flexible bodies in multi-material multi-phase systems. *Journal of Computational Physics*, 429:110008, March 2021. 61

[122] L. Torres, A. Urbano, C. Colin, and S. Tanguy. On the coupling between Direct Numerical Simulation of Nucleate boiling and a Micro-Region model at the contact line. *Journal of Computational Physics*, page 112602, November 2023. 61

[123] S. Nukiyama. The maximum and minimum values of the heat Q transmitted from metal to boiling water under atmospheric pressure. *International Journal of Heat and Mass Transfer*, 9(12):1419–1433, December 1966. 85